



UNIVERSITÀ DEGLI STUDI DELL'AQUILA

DIPARTIMENTO DI SCIENZE FISICHE E CHIMICHE

DOTTORATO DI RICERCA IN SCIENZE FISICHE E CHIMICHE

XXXIII CYCLE

SSD FIS/04

---

# High-Energy Neutrinos and Gamma-rays from the Milky Way

---

*Author:*  
Maddalena Cataldo

*Supervisor:*  
Prof. Francesco L. Villante  
Dr. Giulia Pagliaroli

*Coordinator:*  
Prof. Antonio Meozzi

A.Y. 2019/2020



UNIVERSITÀ DEGLI STUDI DELL'AQUILA

## *Abstract*

Dipartimento di Scienze Fisiche e Chimiche

Doctor of Philosophy

### **High-Energy Neutrinos and Gamma-rays from the Milky Way**

by Maddalena Cataldo

Hadronic interactions of high energy protons (or nuclei) with ambient medium represent one of the main processes that produce high-energy neutrinos and TeV gamma-rays in our Galaxy. They occur both within the sources where cosmic rays (CR) are accelerated and/or in the interstellar gas contained in our Galaxy. Being gamma and neutrino production strictly related, it is natural to adopt a multimessenger approach in which their observations are explained within the same framework.

We present updated calculations of the diffuse emission produced by the interaction of CR with the gas contained in the Galactic disk considering also the possibility of CR spectral hardening in the inner Galaxy, recently emerged from the analysis of Fermi-LAT data at lower energies. Above TeV energies diffuse and source components are expected to provide comparable contributions and it is difficult to separate them on observational grounds. Hence we compare our estimates with the total (diffuse + sources) observed fluxes: IceCube HESE signal for neutrinos, and fluxes from the Galactic plane measured by Argo-YBJ, H.E.S.S., HAWC and Milagro for the gamma counterpart. We provide a limit to the fraction of the high energy neutrino signal observed by IceCube that can be ascribed to a Galactic origin. We demonstrate that the TeV gamma-ray sky can be used to probe the distribution of Galactic cosmic rays. We state that a potential tension exists between the CR spectral hardening hypothesis and observational results.

The constraints can be strengthened if the contribution of sources not resolved by H.E.S.S. is taken into account. The analysis of H.E.S.S. Galactic Plane Survey allows to infer the properties of Galactic TeV source population. Evaluating the cumulative flux expected at Earth by the considered population, we show that the H.E.S.S. unresolved sources provide a relevant contribution to the diffuse Galactic emission. By the population study we infer general information on the total Milky Way such as its high-energy gamma-ray luminosity and total flux. Finally, in the hypothesis that the majority of bright sources detected by H.E.S.S. are powered by pulsar activity, like e.g. pulsar wind nebulae or TeV halos, we estimate the main properties of the pulsar population.



# Contents

|   |            |
|---|------------|
| <b>Abstract</b>   | <b>iii</b> |
| <b>1 Cosmic Neutrinos and Gamma-rays</b>                      | <b>3</b>   |
| 1.1 Cosmic Neutrinos and Gamma-ray production                 | 4          |
| 1.1.1 p-p interaction   | 4          |
| 1.1.2 Secondary particle spectra                              | 5          |
| 1.1.3 p- $\gamma$ interaction                                 | 11         |
| 1.2 Leptonic gamma-ray production                             | 12         |
| 1.3 Gamma absorption  | 15         |
| 1.4 Neutrino/gamma spectrum relation                          | 16         |
| <b>2 Galactic Sources of High-Energy Neutrinos and Gammas</b> | <b>21</b>  |
| 2.0.1 Disk  | 22         |
| 2.0.2 Centre  | 23         |
| 2.0.3 Halo  | 24         |
| 2.0.4 Fermi Bubbles   | 25         |
| 2.1 Point-like and extended Galactic sources                  | 26         |
| 2.1.1 Supernova Remnants                                      | 26         |
| 2.1.2 Pulsars   | 29         |
| 2.1.3 Pulsar Wind Nebulae                                     | 31         |
| <b>3 High-Energy Neutrino and Gamma-ray detectors</b>         | <b>33</b>  |
| 3.1 IceCube   | 34         |
| 3.1.1 Event topology  | 34         |
| 3.1.2 Background  | 37         |
| 3.1.3 HESE dataset  | 38         |
| 3.1.4 Through-going muons                                     | 40         |
| 3.2 ANTARES   | 41         |
| 3.3 H.E.S.S.  | 42         |
| 3.3.1 H.E.S.S. Galactic Plane Survey and diffuse measurement  | 42         |
| 3.4 HAWC  | 46         |
| 3.4.1 Catalogue   | 47         |
| 3.5 ARGO-YBJ  | 48         |
| 3.5.1 Results   | 50         |
| 3.6 Milagro   | 50         |
| 3.6.1 Results   | 52         |
| 3.7 Future generation of detectors                            | 53         |
| <b>4 Diffuse Galactic emission</b>                            | <b>55</b>  |
| 4.1 Diffuse emission  | 56         |
| 4.1.1 Cosmic-ray distribution                                 | 56         |
| 4.1.2 Results   | 62         |
| 4.2 Resolved source contribution                              | 66         |

|          |  |            |
|----------|--|------------|
| 4.3      | Comparisons . . . . .                                      | 67         |
| 4.4      | Discussion . . . . .                                       | 70         |
| 4.5      | Unresolved sources . . . . .                               | 71         |
| <b>5</b> | <b>Source contribution to the VHE Galactic emission</b>    | <b>77</b>  |
| 5.1      | Why H.E.S.S.? . . . . .                                    | 78         |
| 5.2      | Model . . . . .  | 80         |
| 5.2.1    | Cumulative flux of H.E.S.S. sources . . . . .              | 82         |
| 5.3      | Unbinned Likelihood . . . . .                              | 83         |
| 5.4      | Best-fit values . . . . .                                  | 84         |
| 5.5      | Total flux and total luminosity of the Milky Way . . . . . | 86         |
| 5.6      | Unresolved source contribution . . . . .                   | 87         |
| 5.7      | Robustness of results . . . . .                            | 88         |
| 5.8      | Final considerations . . . . .                             | 90         |
| <b>6</b> | <b>Galactic TeV population of pulsar-powered sources</b>   | <b>93</b>  |
| 6.1      | Pulsar powered sources . . . . .                           | 93         |
| 6.1.1    | From PWN to TeV-halo . . . . .                             | 94         |
| 6.1.2    | Magnetic dipole model for pulsars . . . . .                | 96         |
| 6.1.3    | Gamma emission of pulsar-powered sources . . . . .         | 98         |
| 6.2      | Model in the fading-source interpretation . . . . .        | 99         |
| 6.3      | $P_0$ and $B_0$ dispersion . . . . .                       | 102        |
| 6.4      | Results . . . . .  | 103        |
| 6.5      | Conclusions . . . . .                                      | 108        |
| <b>7</b> | <b>Conclusions</b>   | <b>109</b> |
|          | <b>Bibliography</b>  | <b>111</b> |

# List of Figures

|     |   |    |
|-----|---|----|
| 1.1 | Energy spectra of pions and eta mesons for the numerical simulations (histograms) and their analytical approximations given by Eqs. (1.12) and (1.16). The plots are obtained for 4 different values of the incident proton energy: 0.1, 10, 100 and $10^3$ TeV. Figure taken from Kelner, Aharonian, and Bugayov, 2006. . . . .  | 7  |
| 1.2 | Plots of the energy ratio $x = E_\nu/E_p$ squared times the adimensional functions: $F_{\nu_e}$ (blue line), $F_{\nu_\mu,\mu} + F_{\nu_\mu,\mu}$ (orange line), and $F = F_{\nu_\mu,\mu} + F_{\nu_\mu,\mu} + F_{\nu_e}$ (green line), all evaluated in the incident proton energy: $E_p = 10^3$ TeV. Figure reproduced from Kelner, Aharonian, and Bugayov, 2006. . . . . | 8  |
| 1.3 | Differential cross section for the neutrino production in nucleon-nucleon interactions evaluated at the energy of proton: $E_p = 10^3$ TeV. Figure reproduced from results in Kelner, Aharonian, and Bugayov, 2006. . . . .   | 9  |
| 1.4 | The adimensional function $F_\gamma(x, E_p)$ times the energy ratio $x = E_\gamma/E_p$ squared, as a function of $x$ and plotted at energy of proton $E_p = 3 \cdot 10^3$ TeV. Figure reproduced from Kelner, Aharonian, and Bugayov, 2006. . . . .   | 11 |
| 1.5 | Differential cross section for the gamma ray production in nucleon-nucleon interactions at the proton energy of $E_p = 3 \cdot 10^3$ . Figure reproduced from results in (Kelner, Aharonian, and Bugayov, 2006). . . . .  | 12 |
| 1.6 | Gamma ray emission rate at the Sun position. The total emission and the single contributions of the three main mechanisms (hadronic, bremsstrahlung and inverse Compton scattering) are shown. Figure taken from Lipari and Vernetto, 2018. . . . .   | 14 |
| 1.7 | Energy distribution of soft photons in the solar neighborhood. Figure taken from Vernetto and Lipari, 2016. . . . .   | 16 |
| 1.8 | Absorption coefficient for gamma-rays in the solar neighborhood, as a function of energy, averaged over the direction of the photon. Figure taken from Vernetto and Lipari, 2016. . . . .   | 17 |
| 2.1 | Milky Way from Paranal, Chile in 2007. Credit: Astronomer Yuri Beletsky. . . . .  | 21 |
| 2.2 | Galaxy structure. Credit: Pearson Education, Inc., publishing as Pearson Addison-Wesley. . . . .  | 22 |
| 2.3 | Radial distribution of the gas density profiles in the Galaxy obtained using the public code GALPROP. . . . .   | 23 |
| 2.4 | Picture of the Sombrero galaxy captured by the Hubble telescope released in October 2004. Credit: Wikipedia. . . . .  | 24 |
| 2.5 | Fermi Bubble representation. Credit: Wikipedia. . . . .   | 26 |
| 2.6 | Left: The remnant of SN 1987A captured by NASA's Hubble Space Telescope (September, 2010). Right: mosaic image, one of the largest ever taken by NASA's Hubble Space Telescope, of the Crab Nebula (December, 2005). . . . .  | 27 |

|      |  |    |
|------|--|----|
| 2.7  | Frame of Vela pulsar movie captured by NASA's Chandra X-ray Observatory (June-September 2010). . . . .   | 29 |
| 3.1  | IceCube in-ice structure. Credit: <i>IceCube website</i> . . . . .   | 35 |
| 3.2  | Two real events observed in the first period of data taking. Figures taken from Aartsen et al., 2013. . . . .  | 36 |
| 3.3  | The observable fluxes are suppressed in the Northern sky ( $\cos \theta \leq 0.2$ , to the left of the vertical dashed line) by absorption in the Earth (at $\cos \theta < -0.8$ we see a major absorption in correspondence of the much denser core), and in the Southern sky ( $\cos \theta > 0.2$ , to the right of the line) by self-veto by accompanying muons. Figure taken from Aartsen et al., 2015b. . . . .  | 37 |
| 3.4  | IceCube lateral section (left) and horizontal section (right). Figure taken from Aartsen et al., 2013. The gray area is the veto region. In the left panel the shaded 80 meters area situated in the middle represents the impure layer that cannot be used for detection. . . . .   | 39 |
| 3.5  | Correlation map of 6-years HESE events. Figure taken from Collaboration, 2017. Arrival directions of the events in galactic coordinates. Shower-like events are marked with a + and those containing tracks with a $\times$ . Colors show the test statistics (TS) for the point-source clustering test at each location. . . . .  | 40 |
| 3.6  | Reconstructed arrival directions of observed events with estimated muon energies above 200 TeV. The color indicates the energy. The solid gray line indicates the galactic plane and the dashed black line the supergalactic plane. Figure taken from Collaboration, 2017. . . . .   | 41 |
| 3.7  | H.E.S.S. observatory site in Namibia. Credit: Wikipedia ( <i>H.E.S.S. gamma-ray experiment five telescope array</i> ). . . . .   | 42 |
| 3.8  | Illustration of HGPS region superimposed an all-sky image of Planck CO(1-0) data ((Ptuskin and Zirakashvili, 2005)) in Galactic coordinates. Figure taken from Abdalla et al., 2018a. See Abdalla et al., 2018a for all details. . . . .   | 43 |
| 3.9  | Integral source flux ( $E > 1$ TeV) vs. source size scatter plot with colors representing the different classes of firmly identified sources. Figure taken from Abdalla et al., 2018a. . . . .   | 44 |
| 3.10 | Illustration of the location of identified H.E.S.S. sources in the Galaxy with respect to HGPS completeness (sensitivity limits). The spiral arms are the gray bars. The HGPS horizons for source luminosities of $10^{33}$ and $10^{34}$ erg/s are depicted by light blue and light brown lines (and shaded regions therein), respectively. Figure taken from Abdalla et al., 2018a. . . . .  | 45 |
| 3.11 | Upper plot: the white regions depict the diffuse analysis region (DAR). Black are regions of significant $\gamma$ -ray emission. The horizontal dashed lines mark the latitudes: $b = -1.2^\circ$ and $b = 1.2^\circ$ . Middle plot: black crosses indicate the longitudinal profile of the differential flux data at 1 TeV in $ b  < 2^\circ$ including known sources. Red solid line represent the minimal hadronic $\gamma$ -ray emission expected in the same region. Bottom panel: same as middle panel but without the source contribution. Figure taken from Abramowski et al., 2014. . . . . | 46 |
| 3.12 | HAWC observatory in the national park Pico de Orizaba, Mexico ( <i>The High-Altitude Water Cherenkov Gamma-Ray Observatory</i> ). . . . .  | 47 |

|      |  |    |
|------|--|----|
| 3.13 | HAWC sources in part of the inner Galactic Plane region, in Galactic coordinates: $44^\circ < l < 4^\circ$ and $ b  < 6^\circ$ . Figure taken from Abeysekara et al., 2017b. . . . .   | 48 |
| 3.14 | ARGO-YBJ (Astrophysical Radiation with Ground-based Observatory at YangBaJing): the Yangbajing observatory in Tibet where the experiment ARGO-YBJ is located. Credit <i>INFN website: ARGO-YBJ</i> . . . . .   | 49 |
| 3.15 | Figure taken from Bartoli et al., 2015. Galactic longitude profile of the diffuse gamma-ray emission in the Galactic latitude interval $ b  < 5^\circ$ at an energy of 600 GeV obtained from the ARGO-YBJ data. The filled circles show the results after masking the sources, while the open circles show the results without the masking. The solid line represents the value quoted by the Fermi-DGE model at the same energy, smeared out with the ARGO-YBJ PSF (see Bartoli et al., 2015). . . . .  | 49 |
| 3.16 | Figure taken from Bartoli et al., 2015. Galactic latitude profile of the diffuse gamma-ray emission in the Galactic longitude interval $25^\circ < l < 100^\circ$ at an energy of 600 GeV obtained from the ARGO-YBJ data. See legend in Fig.3.15. . . . .   | 50 |
| 3.17 | Milagro detector on Jemez Mountains near Los Alamos, New Mexico. Credit: <a href="https://www.lanl.gov">https://www.lanl.gov</a> . . . . .   | 51 |
| 3.18 | Galactic longitude profile of the gamma-ray emission around 15 TeV in the Galactic plane as measured by Milagro. Upper plot: Red data points – no subtraction of source contributions, black data points – after subtraction. Lower plot: Source-subtracted profile overlaid with prediction of the optimized GALPROP model – the red line is the pion contribution, the green line the IC, and the blue line is the total flux prediction integrated in the latitude range $\pm 2^\circ$ . Figure taken from Abdo et al., 2008a. . . . .                    | 51 |
| 3.19 | Source-subtracted Galactic latitude profile of the gamma-ray emission around 15 TeV in the inner Galaxy (left plot), in the Cygnus region (middle plot), and in the region above Cygnus (right plot) as measured by Milagro (points with errors) and predicted by the optimized GALPROP model. The colors are as above. Figure taken from Abdo et al., 2008a. . . . .  | 52 |
| 3.20 | CTA prototype that shows all three classes of telescopes planned. Credit: <i>CTA/M-A. Besel/IAC (G.P. Diaz)/ESO</i> . . . . .  | 53 |
| 3.21 | Schematic view of IceCube Gen-2, comprising the existing IceCube array with its densely equipped inner region DeepCore, the high-energy array of Gen2, the super-densely equipped PINGU sub-detector, and an extended surface array (Spiering, 2018). . . . .  | 54 |
| 4.1  | All-particle flux (black thick solid line), the flux contributed by protons (red line solid line), helium (yellow dashed line), oxygen (gray dash-dotted line), and iron (blue dotted line). Bands around the model lines show a variation of one standard deviation. Error bars represent combined statistical and systematic uncertainties. Data points of composition measurements from air-showers are not shown without error bars for clarity. TA stands for Telescope Array, KG for KASCADE-Grande. Figure taken from Dembinski et al., 2018. . . . . | 59 |

- 4.2 **Upper Panel:** The black lines show the functions  $g(\mathbf{r})$  obtained from Eq.(4.13) for different smearing radii  $R$ . Going from top to bottom at  $r \simeq 2\text{kpc}$ , the different lines correspond to  $R = 1, 3, 5, 10, \infty$  kpc, respectively. The data points show the CR density at  $E \simeq 20\text{ GeV}$  Acero et al., 2016 (normalized to one at the Sun position) and the  $\gamma$ -ray emissivity above  $E_\gamma = 1\text{ GeV}$  (Yang, Aharonian, and Evoli, 2016; Pothast et al., 2018), as a function of the galactocentric distance obtained from Fermi-LAT data. **Lower Panel:** The black line gives the spectral index of CR at  $E_{\text{CR}} = 20\text{ GeV}$  adopted in this calculation. The data points show the CR spectral index obtained as a function of the galactocentric distance from Fermi-LAT data in Acero et al., 2016; Yang, Aharonian, and Evoli, 2016; Pothast et al., 2018. Figure taken from Cataldo et al., 2019. . . . . 63
- 4.3 The diffuse HE gamma-ray flux at  $E_\gamma = 1\text{ TeV}$  as a function of the Galactic longitude  $l$  (for  $b = 0$ ) (upper panel), and Galactic latitude for  $l = 0$  (lower panel) obtained by assuming that the CR spectrum is position-independent (blue lines) and by implementing CR spectral hardening in the inner Galaxy (red lines) as described by Eqs.(4.4),(4.15). Solid and dashed lines (in each group) are obtained by assuming that the CR spatial distribution follows that of SNR with smearing radius  $R = 1\text{ kpc}$  and  $R = \infty$ , respectively. Plots obtained with results published in Cataldo et al., 2019. . . . . 64
- 4.4 The diffuse HE neutrino flux at  $E_\gamma = 100\text{ TeV}$  as a function of Galactic longitude for  $b = 0$  (upper panel), and latitude for  $l = 0$  (lower panel) obtained by assuming that the CR spectrum is position-independent (blue lines) and by implementing CR spectral hardening in the inner Galaxy (red lines) as described by Eqs.(4.4),(4.15). Solid and dashed lines (in each group) are obtained by assuming that the CR spatial distribution follows that of SNR with smearing radius  $R = 1\text{ kpc}$  and  $R = \infty$ , respectively. . . . . 65
- 4.5 Upper panel: HGPS gamma-ray sources as parameterized in Abdalla et al., 2018b; lower panel: corresponding neutrino sources in the hypothesis of a dominant hadronic regime. . . . . 68
- 4.6 Longitudinal distribution of total neutrino flux at 100 TeV, in the range  $-65^\circ < l < 60^\circ$  ( $b = 0$ ), obtained for the 4 cases. Blue lines: standard cases, red lines: hardening cases. Solid and dotted lines correspond to the two diffusion radii  $R = 1\text{ kpc}$ , and  $R = \infty$  respectively. The green line represents the isotropic fit of the HESE signal measured by IceCube (Abbasi et al., 2020b). . . . . 69
- 4.7 The total gamma fluxes predicted as a function of the Galactic longitude  $l$  following the same color prescription as in Fig.4.3. The green dotted line represents the contribution of resolved sources. For a detailed description of the plots see the text. Figure taken from Cataldo et al., 2019. . . . . 75
- 4.8 The total gamma flux as a function of the energy for the four different cases considered. The same quantity as measured by H.E.S.S., HAWC, Argo-YBJ and Milagro is also displayed for a comparison. The green dotted line represents the contribution due to resolved sources. Figure taken from Cataldo et al., 2019 . . . . . 76

|     |  |     |
|-----|--|-----|
| 4.9 | The total neutrino flux as a function of the energy for the different cases. The same quantity as measured by IceCube for starting events and through-going muons events is displayed in green and purple respectively. . . . .  | 76  |
| 5.1 | Histograms of flux, longitude, latitude distributions in the HGPS. Blue blocks: over-threshold sources; pink blocks: below-threshold sources. . . . .  | 79  |
| 5.2 | Pie chart of the identification of 32 sources observed by H.E.S.S. above the flux threshold. . . . .   | 80  |
| 5.3 | Galactic pulsar distribution in cylindrical coordinates as in Lorimer et al., 2006, with a disk thickness $H = 200$ pc. . . . .  | 81  |
| 5.4 | The best fit and the 1 and 2 $\sigma$ allowed regions for the maximal luminosity $L_{\max}$ and the normalization $\mathcal{N}$ of the luminosity distribution of Galactic TeV sources. The dot represents the best fit value. The olive line corresponds to constant values of the total Milky Way luminosity, calculated according to Eq.(5.21). Figure taken from Cataldo et al., 2020. . . . .   | 85  |
| 5.5 | The cumulative distribution of the HGPS sources (gray line) compared with expectations for different values of the maximal luminosity $L_{\max}$ . The black line is obtained for the best-fit values in Eq.(5.20), the magenta dot-dashed line and the blue dotted one are obtained for the limit cases of $L_{\max} \rightarrow 0$ and $L_{\max} \rightarrow \infty$ , respectively, while the red dashed line shows an intermediate case of $L_{\max} = 30 \times L_{\text{CRAB}}$ . Figure taken from Cataldo et al., 2020. . . . .  | 87  |
| 6.1 | Sketch of the main evolutionary stages of a PWN. See text for more details. The key is in the lower left corner. In all three panels, the ISM density gradient is upwards, and the pulsar “kick” velocity towards the left. Figure taken from Giacinti et al., 2020. . . . .   | 95  |
| 6.2 | Table taken from Abdalla et al., 2018b that collects HGPS sources considered as firmly identified pulsar wind nebulae. The sources are sorted by decreasing $\dot{E}$ . $\lg \dot{E}$ stands for $\log_{10}(E/\text{erg s}^{-1})$ , $\tau_c$ is the pulsar characteristic age, $d$ is the pulsar distance, $R_{\text{PWN}}$ is the 1-sigma Gaussian extension, and $L_{1-10 \text{ TeV}}$ is the TeV luminosity. . . . .   | 100 |
| 6.3 | The best fit and the 1 and 2 $\sigma$ allowed regions in the plane $(P_0, B_0)$ , calculated in the assumption that the fraction of pulsar spin-down energy converted to TeV emission is $\lambda = 10^{-3}$ . The shaded regions correspond to $N(0.1\Phi_{\text{CRAB}}) \leq 10$ in the assumption $\lambda = 5 \times 10^{-2}$ . Figure taken from Cataldo et al., 2020. . . . .  | 104 |
| 6.4 | Upper panel: the best fit and the 1 $\sigma$ and 2 $\sigma$ allowed regions in the plane $(L_{\max}, \tau)$ . Lower panel: the best fit and the 1 $\sigma$ and 2 $\sigma$ allowed regions in the plane $(P_0, B_0)$ , calculated in the assumption that $\lambda = 10^{-3}$ . In both panels the red shaded area is excluded by the data because corresponds to $N(0.1\Phi_{\text{CRAB}}) \leq 10$ in the assumption of $\lambda = 5 \times 10^{-2}$ which is a large value for the fraction of pulsar spin-down energy converted to TeV emission. Figure taken from Cataldo et al., 2020. . . . . | 107 |



# List of Tables

- 5.1 The best fit values and the  $1\sigma$  allowed ranges for the maximal luminosity ( $L_{\max}$ ); the normalization factor of the luminosity function ( $\mathcal{N}$ ); the total TeV Milky Way luminosity ( $L_{\text{MW}}$ ); the total flux in the H.E.S.S. OW ( $\Phi_{\text{tot}}$ , expressed in  $10^{-10} \text{ cm}^{-2} \text{ s}^{-1}$ ). The different cases are described in the text. The  $\Delta\chi^2$  is calculated respect to our reference case (first row in the table.) . . . . . 90
- 6.1 The same as Table 5.1 but with best fit values and the  $1\sigma$  allowed ranges for the magnetic field of pulsars  $B_0$  (in Gauss and expressed logarithmically), and the spin-down period  $P_0$  in ms; the fading timescale  $\tau$  is expressed in ky. The different cases are described in the text in Chapter 5. . . . . 104



# List of Abbreviations

|               |   |
|---------------|---|
| <b>AGN</b>    | <b>A</b> ctive <b>G</b> alactic <b>N</b> uclei                          |
| <b>CMB</b>    | <b>C</b> osmic <b>M</b> icrowave <b>B</b> ackground                     |
| <b>CTA</b>    | <b>C</b> herenkov <b>T</b> elescope <b>A</b> rray                       |
| <b>EBL</b>    | <b>E</b> xtragalactic <b>B</b> ackground <b>L</b> ight                  |
| <b>GRB</b>    | <b>G</b> amma <b>R</b> ay <b>B</b> urst                                 |
| <b>HE</b>     | <b>H</b> igh <b>E</b> nergy   |
| <b>ICAT</b>   | <b>I</b> maging <b>A</b> tmospheric <b>C</b> herenkov <b>T</b> elescope |
| <b>IC</b>     | <b>I</b> nverse <b>C</b> ompton   |
| <b>ISM</b>    | <b>I</b> nter <b>S</b> tellar <b>M</b> edium                            |
| <b>VHE</b>    | <b>V</b> ery <b>H</b> igh <b>E</b> nergy                                |
| <b>UHECRs</b> | <b>U</b> ltra <b>H</b> igh <b>E</b> nergy <b>C</b> osmic <b>R</b> ays   |
| <b>SN</b>     | <b>S</b> uper <b>N</b> ova  |
| <b>SNR</b>    | <b>S</b> uper <b>N</b> ova <b>R</b> emnant                              |
| <b>PWN</b>    | <b>P</b> ulsar <b>W</b> ind <b>N</b> ebraska                            |



# Introduction

The high-energy part of our Universe is still for most part unknown. What we can understand of it is deduced from particle messengers that encounter our Earth and interact in our telescopes. The research is still widely open and for many topics we have a good understanding but many others are still quite enigmatic. A multimessenger study of different astrophysical particles gives a wider view on our matter of interest. At the same time a combination of information, resources and minds is fundamental for our common purpose. Nowadays a multitude of telescopes covering a large range of energies is observing the whole sky. We have available a number of measurements and catalogues that are year by year being enriched. The technology for these experimental facilities is constantly being refined and many are the projects for the construction of new high-energy telescopes.

Among the recent most remarkable results we find the ones provided by IceCube. The IceCube Collaboration reported the discovery of high-energy neutrinos of energies that reach tens of PeV. Follow-up analyses confirmed the astrophysical origins of the signal. The exact origin of this neutrino flux is still an unsolved mystery, that, if solved, could in turn bring more understanding on the whole high-energy sky. So far the registered signal appears to be well fitted by an isotropic flux. The only source correlation was observed from the extragalactic blazar in the Orion constellation: TXS 0506+056. In September 2017 it was first observed a muon neutrino event from TXS 0506+056 and subsequently were registered a number of photon signals at other wavelengths of light including radio, infrared, optical, X-rays and gamma-ray. The extensive multi-wavelength campaign that followed is a perfect example of how efficient combining different measurements from different messengers and ranges of energy can be.

One of the expectations for the upcoming data-takings is to be able to perform a similar combined neutrino/gamma-ray analysis also for Galactic sources. High energy neutrinos and TeV gamma-rays can be produced by hadronic interactions of high energy protons (or nuclei) with ambient medium, both within the sources where cosmic rays (CR) are accelerated and/or in the interstellar gas contained in our Galaxy. These particles propagate to Earth without being deflected, providing us with relevant information about their production sites. Being gamma and neutrino production strictly related, it is natural to adopt a multimessenger approach in which gamma and neutrino observations are explained within the same framework. In this thesis, we adopt this kind of approach to model Galactic neutrino and gamma emission.

The aim of this thesis is to provide an overview of the possible Galactic sources of both HE neutrinos and TeV gamma-rays and to give an estimation of the total Galactic HE fluxes of both these messengers.

In the first chapter is introduced the theoretical basis of high-energy neutrino-gamma multimessenger Physics. We describe the processes from which they take origin, their propagation, and their intrinsic connections, giving the models at the basis of our computations.

In the second chapter an overview of our Galaxy and all Galactic sources of both high-energy neutrinos and gamma-rays is presented. We describe the main sources both extended and point-like giving information on their properties.

The third chapter is dedicated to experimental facilities and their data-sets. We briefly illustrate the main detectors of our interest and we focus on the results useful for the discussion in the following chapters. These are: for neutrinos the largest telescope IceCube and for gamma-rays the detectors H.E.S.S., HAWC, Argo-YBJ, and Milagro. We finish with an overview on telescopes that will be built in the upcoming future and their promising expectations.

Chapter 4 is based on the original paper: Cataldo et al., 2019 and also presents other original results. This is focused on the study of the diffuse component of Galactic neutrinos and gamma-rays i.e. the ones originated in hadronic interactions of cosmic rays and the interstellar gas. Here we present our results for four models based on four different assumptions of the cosmic ray distribution in the Galaxy which appears to suffer of significant uncertainty. Including also the possibility of a dependence of the cosmic ray spectral index from the galactocentric distance in order to reproduce recent data-analysis in the gamma-ray sky of GeV energies. We perform comparisons of our expectations for Galactic TeV flux of neutrinos and gamma-rays with total fluxes measured by the mentioned experiments with the aim of constraining our models. We finally highlight the importance of a good estimation of the unresolved contribution to the total in order to obtain valid constraints. We improve the gamma-ray comparisons by giving a preliminary estimation of this term.

In Chapter 5 we propose a refinement of the unresolved flux estimation by operating a population study on the H.E.S.S. Galactic Plane Survey (HGPS). We start from this intention and infer general properties of the total Milky Way such as its high-energy gamma-ray Luminosity and total flux.

In Chapter 6 we apply the previous study to a particular category of Galactic sources already introduced in Chapter 2: fading sources which produce high-energy gamma-rays from being powered by pulsar activity. Under this category fall pulsar wind nebulae but also newly observed extended sources called "TeV halos", whose role in the total emission is worthy to investigate. In the end, from this study we also can to infer some general properties of the Galactic pulsar population which appear to be in good agreement with other estimations in literature. Both the last two chapters are based on the original paper Cataldo et al., 2020.

## Chapter 1

# Cosmic Neutrinos and Gamma-rays

With the name "Very High Energy" gamma-rays are intended photons at energies of order of  $10^9 - 10^{12}$  eV (GeV–TeV) and above. VHE gamma-rays are produced in our Galaxy and have several characteristic that make of them good messengers for the investigation of the Galaxy. They are not deflected in magnetic fields and, for energies  $E_\gamma \lesssim 1$  PeV they are negligibly absorbed in their path towards the Earth. Gamma-ray telescopes can reach therefore good pointing capability and also we expect to have good measurements of flux intensity from their VHE sources. Due to their peculiarities, gamma-rays have long been used for studies of Galactic sources.

The history of photon sky observations dates back to several decades ago. Many are the experiments that were built in order to detect photons produced in the remotest regions of the sky; covering several tens of orders of magnitude of the electromagnetic spectrum and wider and wider windows of observation.

In the recent years the largest neutrino telescope IceCube has provided many evidences of a high-energy cosmic neutrino signal. The all-flavor signal is fitted by an isotropic flux with an unbroken power-law distribution in energy (Aartsen et al., 2015a). Starting from these evidences, neutrino astronomy is becoming increasingly more interesting and the information that is providing is leading to new questions that need to be answered.

Astrophysical neutrino, just as gamma-rays, have the property of preserving their production direction and, at our energies of interest, they are not absorbed. However, their production mechanisms is entirely hadronic while for gamma-rays we have also a leptonic flux that, depending on the energy considered, might have to be taken into account. Due to the technical difficulties of constructing an optimal neutrino telescope, so far the reconstructed direction of neutrino events is not as good as the one provided in gamma-ray measurements. However, is fundamental to consider both kind of observations in order to have the most complete overview on phenomena. A combined observation of both messengers would confirm a hadronic production process inside that source. Our final purpose is to reach a good interpretation of all high-energy Galactic emission.

Multimessenger neutrino-gamma research is growing in interest in these years also due to recent extragalactic observations. This induces us to reasonably hope for a similar observational coincidence but from Galactic origins in the next future. In our Galaxy this kind of study is even more straightforward at energies of our interest since a large part of neutrinos and gamma-rays are produced in the same hadronic interactions. As we will see in this and next chapter, the combined production of neutrinos and gamma-rays is verified whether the proton-proton collision occurs in a (point-like or extended) Galactic source or in the interstellar regions of the Galaxy.

In this chapter we describe the main processes that occur in the Galaxy and that take to a combined production of neutrinos and gammas at high-energies. We give

all the phenomenological models for computations that we will use for our estimations in the upcoming chapters, such as primary particle spectra, cross-section functions, and we will define all the hypotheses environment in which we will perform our next calculations.

## 1.1 Cosmic Neutrinos and Gamma-ray production

The main astrophysical processes that produce both high-energy neutrinos and  $\gamma$ -rays are inelastic p-p interactions of cosmic rays with surrounding gas or p- $\gamma$  interactions with ambient photons. Given this distinction we can identify two channels of production and link them to different kind of sources. The first interaction is assumed to occur mainly in the regions of the Galaxy where there is a dominant presence of the Galactic gas which is rich in baryons. This production is therefore dominant in the interstellar regions of the disk and in Galactic sources such as SNRs and PWNe. The second interaction is mainly dominant in regions with an high gamma density, i.e. in areas close to extragalactic sources such as Active Galactic Nuclei, Blazars, and Gamma-Ray Bursts.

### 1.1.1 p-p interaction

The p-p interaction occurs very commonly in our Galaxy and we can state that whenever there is production of neutrinos by p-p interaction this will be accompanied by hadronic gamma-production. Inelastic collision of high-energy protons on non-relativistic protons produces mainly neutral and charged pions:  $\pi^+$ ,  $\pi^-$ ,  $\pi^0$ , and, in minor quantity, also kaons:  $K^+$ ,  $K^-$ ,  $K^0$ ,  $\bar{K}^0$  and eta-mesons:  $\eta$ . Due to the isospin symmetry, the three pions are created in almost equal amount. Charged pions decay in muons and neutrinos (B.R. = 0.999):

$$\pi^+ \rightarrow \mu^+ + \nu_\mu, \quad (1.1)$$

$$\pi^- \rightarrow \mu^- + \bar{\nu}_\mu. \quad (1.2)$$

From these two decays stems a secondary production of high-energy electronic and muonic neutrinos (or antineutrinos) by muons decay:

$$\mu^+ \rightarrow e^+ + \nu_e + \bar{\nu}_\mu, \quad (1.3)$$

$$\mu^- \rightarrow e^- + \bar{\nu}_e + \nu_\mu. \quad (1.4)$$

The main production of gamma rays by p-p interaction, instead, is due to neutral pions decay. Neutral pions most common decay channel is the two photons decay (B.R. = 0.988):

$$\pi^0 \rightarrow \gamma\gamma. \quad (1.5)$$

Along with neutral pions also eta-mesons are produced, which are responsible of gamma production as well, in a measure that is subdominant but not negligible. At energies around few TeV the fraction of  $\eta$  over  $\pi_0$  produced in p-p collisions is 20% – 40% (Acharya et al., 2018). The  $\eta$ -meson decay channels and their respective

branching ratios are:

$$\eta \rightarrow \gamma + \gamma \quad \text{B.R} = 39\%; \quad (1.6)$$

$$\eta \rightarrow 3\pi^0 \quad \text{B.R} = 32\%; \quad (1.7)$$

$$\eta \rightarrow \pi^+ + \pi^- + \pi^0 \quad \text{B.R} = 23\%; \quad (1.8)$$

$$\eta \rightarrow \pi^- + \pi^+ + \gamma \quad \text{B.R} = 4\%. \quad (1.9)$$

A small amount of neutrinos is also produced by charged kaons that decay as:

$$K^+ \rightarrow \mu^+ \bar{\nu}_\mu \quad \text{B.R.} \simeq 64\%;$$

$$K^+ \rightarrow \pi^0 \pi^+ \quad \text{B.R.} \simeq 21\%;$$

$$K^+ \rightarrow \pi^0 e^+ \bar{\nu}_e \quad \text{B.R.} \simeq 5\%.$$

The antiparticle  $K^-$  decays analogously. In general, the amount of kaons produced in p-p is around 10% to 20% the number of pions.

### 1.1.2 Secondary particle spectra

For our calculations we need detailed estimates of both nucleon-nucleon inelastic cross section and secondary particle spectral functions. A refined treatment of these functions is done in Kelner, Aharonian, and Bugayov, 2006. They present a parametrization of energy spectra of secondary particles: pions, electrons, neutrinos and gamma-rays produced by inelastic p-p collisions based on results of SIBYLL and QGSJET codes. These codes rely on methods of both theoretical and experimental Physics: they are based on phenomenological models of p-p interaction incorporated with comprehensive experimental data provided by particle accelerators. Their results obtain very good approximation of energy distribution of secondary particles in the energy range above 100 GeV, providing accuracies generally better than several percent. While the codes applied to the computations could also be directly used to compute the particle spectra, we instead rely on the analytical approximations of the codes' results given in the paper. The simple parameterizations used are intended to simplify and reduce the computation time.

Following Kelner, Aharonian, and Bugayov, 2006, the general expression for the total cross section of the p-p interaction that we use in our calculation is:

$$\frac{d\sigma_i(E_p, E_i)}{dE_i} = \frac{\sigma(E_p)}{E_p} F_i(x, E_p). \quad (1.10)$$

Where  $E_p$  is the energy of the incident proton,  $E_i$  is the energy of the secondary particle, and  $x = E_i/E_p$ . The term  $\sigma(E_p)$  represents the inelastic part of the total cross section of the p-p collision, while the adimensional functions  $F_i$  describe the secondary particle spectra, the index  $i$  indicates the particle considered: leptons or gamma. The energy dependent term  $\sigma(E_p)$  is calculated by fitting numerical data included in the SIBYLL code, and the approximation obtained is:

$$\sigma(E_p) = 34.3 + 1.88 \ln \left( \frac{E_p}{1 \text{ TeV}} \right) + 0.25 \ln \left( \frac{E_p}{1 \text{ TeV}} \right)^2 \text{ mb.} \quad (1.11)$$

The first important result that has to be defined is the inclusive spectra of pions. The data for the energy spectrum of  $\pi$ -mesons produced in p-p inelastic cross section can be obtained by both the SIBYLL and the QGSJET codes. However since the first

one seems to better approximate the accelerator data for a larger range of energies, only the SIBYLL code results are used. The analytical approximation obtained for the pion spectrum is:

$$F_{\pi}(x, E_p) = 4\alpha B_{\pi} x^{\alpha-1} \left( \frac{1-x^{\alpha}}{1+rx^{\alpha}(1-x^{\alpha})} \right)^4 \times \left( \frac{1}{1-x^{\alpha}} + \frac{r(1-2x^{\alpha})}{1+rx^{\alpha}(1-x^{\alpha})} \right) \left( 1 - \frac{m_{\pi}}{xE_p} \right)^{1/2}; \quad (1.12)$$

with the best fit parameters:

$$B_{\pi} = 3.92 + 0.83 \left( \ln \frac{E_p}{1 \text{ TeV}} \right) + 0.075 \left( \ln \frac{E_p}{1 \text{ TeV}} \right)^2; \quad (1.13)$$

$$\alpha = \frac{0.98}{\sqrt{3.67 + 0.83 \left( \ln \frac{E_p}{1 \text{ TeV}} \right) + 0.075 \left( \ln \frac{E_p}{1 \text{ TeV}} \right)^2}}; \quad (1.14)$$

$$r = \frac{2.6}{\sqrt{3.67 + 0.83 \left( \ln \frac{E_p}{1 \text{ TeV}} \right) + 0.075 \left( \ln \frac{E_p}{1 \text{ TeV}} \right)^2}}. \quad (1.15)$$

Note that due to the isospin symmetry in strong interaction, as expected, the spectra of the three pions are described by the same expression since they represent an isospin triplet.

In case we are considering the gamma-ray production we have to also take into account the eta-meson contribution, in this regard the expression found by the simulation for the  $F$  function is:

$$F_{\eta}(x, E_p) = (0.55 + 0.028 \ln x) \left( 1 - \frac{m_{\eta}}{xE_p} \right) F_{\pi}(x, E_p); \quad (1.16)$$

with the condition  $F_{\eta}(x, E_p) = 0$  for  $x < m_{\eta}/E_p$ .

Fig. 1.1 is reprinted from Kelner, Aharonian, and Bugayov, 2006, and represents the results of the simulations obtained by the SIBYLL code for the  $\pi$ -mesons and  $\eta$ -mesons (histograms), and their analytical approximations given by Eqs. 1.12 and 1.16. The plots are for four values of incident proton energy: 0.1, 10, 100 and  $10^3$  TeV. The approximation for pion spectra describes the data with an accuracy of 10% in the total energy range of protons considered, while the approximation for the  $\eta$ -mesons appears less accurate.

### Neutrino spectrum from p-p

In this section is presented spectra of high energy neutrinos obtained considering the p-p production process and consequent pion decay as in Eq. (1.2). These functions are obtained in Kelner, Aharonian, and Bugayov, 2006 by numerical computation and through the previous parameterizations of  $\pi$  spectrum. With the function  $d\sigma_{\ell}/dE_{\nu}$  we indicate the differential cross section for production of neutrinos and antineutrinos  $\nu_{\ell}, \bar{\nu}_{\ell}$  of energy  $E_{\nu}$  by a nucleon of energy  $E$  in nucleon-nucleon collision. The parameterization do not discern the neutrinos from the antineutrinos. Although in the p-p interactions the number of  $\pi^{-}$  produced slightly exceeds the number of  $\pi^{+}$ , this difference is below the accuracy of the data used for the computations. So for this model  $\nu = \bar{\nu}$ , the only distinction of neutrinos is between different flavours.

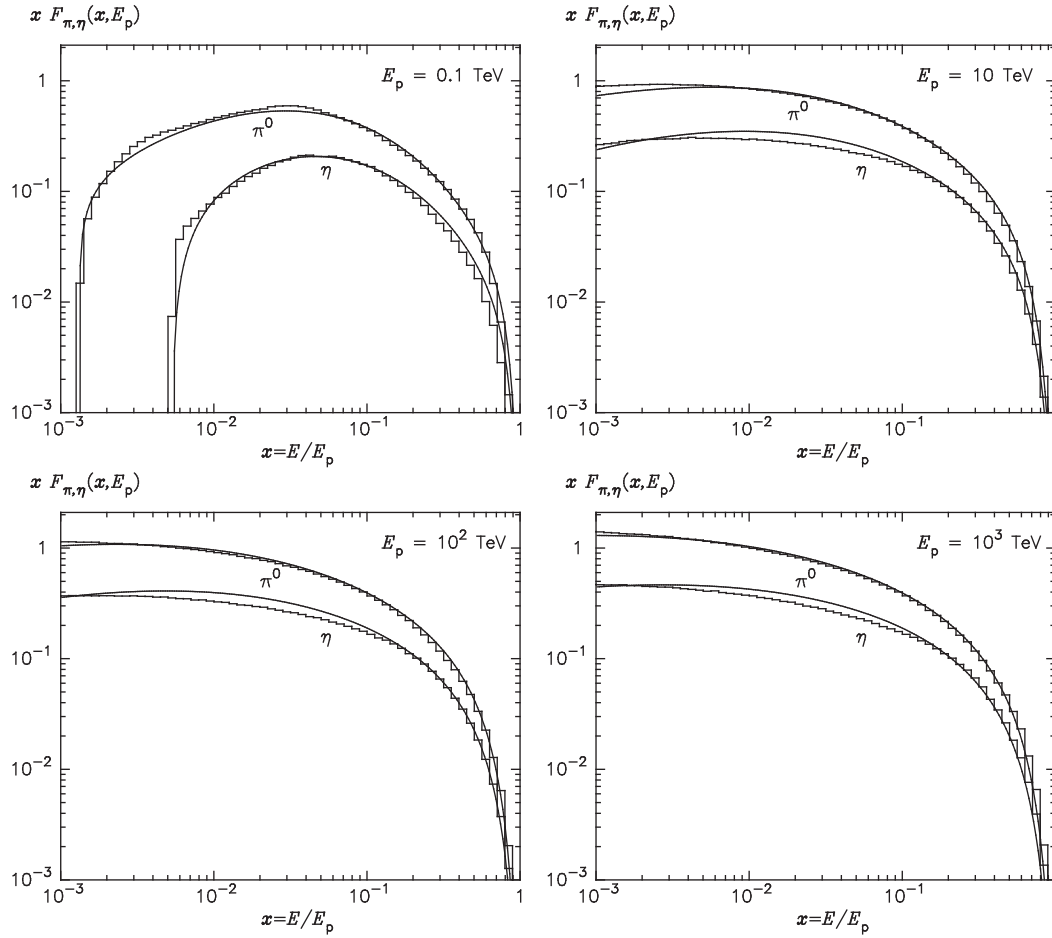


FIGURE 1.1: Energy spectra of pions and eta mesons for the numerical simulations (histograms) and their analytical approximations given by Eqs. (1.12) and (1.16). The plots are obtained for 4 different values of the incident proton energy: 0.1, 10, 100 and  $10^3$  TeV. Figure taken from Kelner, Aharonian, and Bugayov, 2006.

Using the above results the differential cross section can be expressed, with a very good approximation, as in Kelner, Aharonian, and Bugayov, 2006:

$$\sum_{\ell=e,\mu,\tau} \frac{d\sigma_{\ell}(E_p, E_v)}{dE_v} = \frac{\sigma(E_p)}{E_p} F_v(x, E_p). \quad (1.17)$$

The  $F_v$  function describes energy spectra of neutrinos produced:  $\nu_{\mu}$  in the pion decay, and  $\nu_{\mu}$  and  $\nu_e$  from the consequent muon decay.  $F_v$  is represented by the sum of the spectral functions of the muonic neutrinos and electronic neutrino (see Eq. (1.2)):

$$F_v(x, E_p) = F_{\nu_{\mu}}(x, E_p) + F_{\nu_e}(x, E_p), \quad (1.18)$$

where  $x = E_v/E_p$ . Since muonic neutrinos are produced both in the leptonic pion decay and in the following muon decay, the total muon function  $F_{\nu_{\mu}}$  is expressed by the sum of the two functions relative to the first and the second decays:

$$F_{\nu_{\mu}}(x, E_p) = F_{\nu_{\mu},\pi}(x, E_p) + F_{\nu_{\mu},\mu}(x, E_p), \quad (1.19)$$

while, the electronic neutrino function  $F_{\nu_e}(x, E_p)$  is only the one relative to the muon

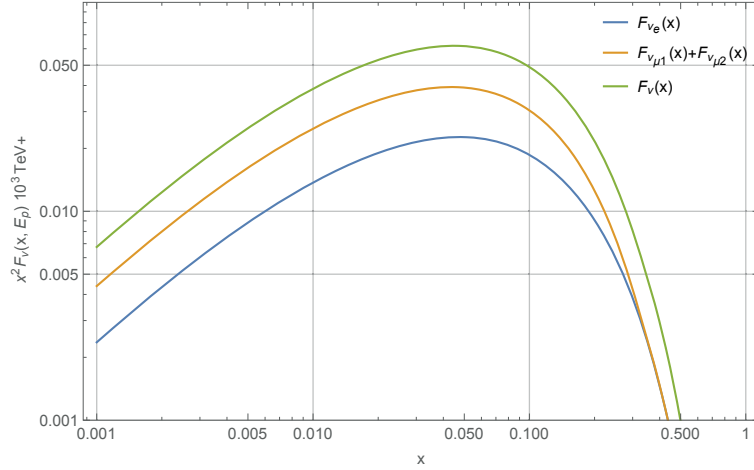


FIGURE 1.2: Plots of the energy ratio  $x = E_\nu/E_p$  squared times the adimensional functions:  $F_{\nu_e}$  (blue line),  $F_{\nu_{\mu,1}} + F_{\nu_{\mu,2}}$  (orange line), and  $F = F_{\nu_{\mu,1}} + F_{\nu_{\mu,2}} + F_{\nu_e}$  (green line), all evaluated in the incident proton energy:  $E_p = 10^3$  TeV. Figure reproduced from Kelner, Aharonian, and Bugayov, 2006.

decay. Furthermore, as described in Kelner, Aharonian, and Bugayov, 2006 the electronic neutrino and first muonic neutrino have approximately the same spectral distribution:

$$F_{\nu_{\mu,1}}(x, E_p) = F_{\nu_e}(x, E_p). \quad (1.20)$$

These functions obtained fitting results from the SIBYLL code are:

$$F_{\nu_{\mu,\pi}} = B_\pi \frac{\ln y}{y} \left( \frac{1 - y^{\beta_\pi}}{1 + k_\pi y^{\beta_\pi} (1 - y^{\beta_\pi})} \right)^4 \times \left[ \frac{1}{\ln y} - \frac{4\beta_\pi y^{\beta_\pi}}{1 - y^{\beta_\pi}} - \frac{4k_\pi \beta_\pi y^{\beta_\pi} (1 - 2y^{\beta_\pi})}{1 + k_\pi y^{\beta_\pi} (1 - y^{\beta_\pi})} \right]; \quad (1.21)$$

$$F_{\nu_{\mu,\mu}}(x, E_p) = F_{\nu_e}(x, E_p) = B_\mu \frac{(1 + k_\mu (\ln x)^2)^3}{x(1 + 0.3/x^{\beta_\mu})} (-\ln x)^5; \quad (1.22)$$

where  $y = x/0.427$  and  $L = \ln(E_p/1 \text{ TeV})$ . The respective coefficients are:

$$B_\pi = 1.75 + 0.204L + 0.010L^2, \quad (1.23)$$

$$\beta_\pi = \frac{1}{1.67 + 0.111L + 0.00038L^2}, \quad (1.24)$$

$$k_\pi = 1.07 - 0.086L + 0.002L^2. \quad (1.25)$$

$$B_\mu = \frac{1}{69.5 + 2.65L + 0.3L^2}, \quad (1.26)$$

$$\beta_\mu = \frac{1}{(0.201 + 0.062L + 0.00042L^2)^{1/4}}, \quad (1.27)$$

$$k_\mu = \frac{0.279 + 0.141L + 0.0172L^2}{0.3 + (2.3 + L^2)}. \quad (1.28)$$

Finally, Fig. 1.2 is reproduced from Kelner, Aharonian, and Bugayov, 2006 and shows the adimensional functions  $F_\nu$ : muonic (cyan line), electronic (orange line)

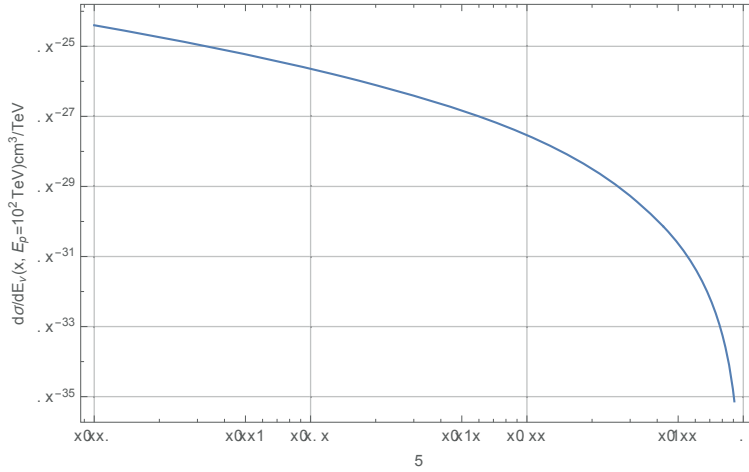


FIGURE 1.3: Differential cross section for the neutrino production in nucleon-nucleon interactions evaluated at the energy of proton:  $E_p = 10^3$  TeV. Figure reproduced from results in Kelner, Aharonian, and Bugayov, 2006.

and their sum (pink line) as function of  $x = E_\nu/E_p$ . While in Fig.1.3 is shown the product of the deep inelastic cross section and the total function  $F_\nu(E_p, x)$ .

An important phenomenon that characterizes neutrinos, and that one needs to take into account when computing neutrino fluxes, is the oscillation mechanism. Given a neutrino propagating in vacuum with a defined initial flavour at the moment of production  $a$ , the probability of oscillation into a flavor  $b$ ,  $P(a \rightarrow b) = P_{ab}$  (Bellini et al., 2014) is given by:

$$P_{ab} = \sum_i |k_i|^2 + \sum_{i < j} 2\text{Re}(|k_i k_j^*|) \cos(\phi_{ij}). \quad (1.29)$$

The first term in this expression only depends on the values of the mixing matrix  $U$  (since  $k_i = U_{bi}U_{ai}^*$ ), while the second term depends only on the oscillation phase  $\phi_{ij} = (m_i^2 - m_j^2)L/2E$  where  $\Delta m_{ij}^2 = m_i^2 - m_j^2$  is the mass differences of the mass eigenstates,  $L$  is the distance and  $E = |p|$  is the energy of neutrino. This is a general result, however in case of high-energy Galactic neutrinos this expression is simplified because coherency is lost due to the very large propagation distance:

$$\phi_{ij} = 1.27 \frac{L(\text{m})\Delta m_{ij}^2(\text{eV}^2)}{E_\nu(\text{MeV})} = 1.27 \frac{3.08 \cdot 10^{20} 10^{-5}(\text{eV}^2)}{100 \cdot 10^6 \text{ MeV}} \sim 4 \cdot 10^7 \gg 1.$$

In the case of an incoherent neutrino packet we need to calculate the mean oscillation probability  $\bar{P}_{ab}$  given by:

$$\bar{P}_{ab} = \sum_i |k_i|^2 = \sum_i |U_{ai}U_{bi}|^2.$$

Since it depends only on the squared modulus of the mixing matrix the probability is the same for antineutrinos:  $P(\nu_a \rightarrow \nu_b) = P(\bar{\nu}_a \rightarrow \bar{\nu}_b)$ , meaning that cosmic neutrino oscillation is CP invariant. Using this relation all the oscillation probability for cosmic neutrinos can be calculated for each couple of flavors  $ab$ . For a generic initial neutrino flux generated with three different fractions of neutrino for each flavor:  $F_a^i$ ,

$F_b^i, F_c^i$ , where:

$$F_a^i + F_b^i + F_c^i = 1, \quad (1.30)$$

We can infer the final flavor fractions by using the previous results. So the  $F_a^f$  is given by the sum of the probability that the initial fraction of  $a$  preserves its flavor, plus the sum of the probabilities that the other two fractions oscillate into the flavor  $a$ :

$$F_a^f = F_a^i \bar{P}_{aa} + F_b^i \bar{P}_{ba} + F_c^i \bar{P}_{ca}. \quad (1.31)$$

The flavour ratio at the Earth is in principle different according to the production process considered at the source, so according to the initial flavour fraction. Hence, the potential observation of the flavour ratio of high-energy neutrino might represent an interesting handle to determine the dominant production process at the source (such as charmed meson decay; neutron  $\beta$  decay; pion decay with damped muon) (Palladino et al., 2015, Vissani, Pagliaroli, and Villante, 2013). However, since we are considering high-energy Galactic neutrinos, the flavor oscillation phenomenon that occurs considering our energy range of interest and the Galactic distances, takes to a situation where the final flavor ratio are approximately equal:  $\nu_e : \nu_\mu : \nu_\tau = 1/3 : 1/3 : 1/3$ . In all our work we will make the reasonable assumption that the  $\pi$ -meson decay after nucleon-nucleon collision is the dominant process in the production of high-energy neutrinos from Galactic sources so it will always be assumed a full flavour mixing of the flux. Therefore to obtain the single neutrino flux from our estimation we will simply divide the total flux for 3.

### Gamma-ray spectrum from p-p

The main source of gamma production by p-p collision is the secondary neutral pion decay. However, for the calculation of the total gamma-ray spectrum one should include also the contribution from  $\eta$ -mesons. The calculation of the spectrum from the  $\eta \rightarrow \gamma + \gamma$  decay along similar lines of that of the  $\pi^0$  decay. To include the contributions of the other  $\eta$  decay modes ( $\eta \rightarrow 3\pi^0 \rightarrow 6\gamma, \eta \rightarrow \pi^+ + \pi^- + \pi^0 \rightarrow 2$ ) one should know the spectra of the produced  $\pi_0$  in the rest frame of  $\eta$ . However, in Kelner, Aharonian, and Bugayov, 2006, the calculations show that the final gamma-ray spectrum weakly depends on the specific form of the pion spectra: for different forms the result vary within 5%. In the following parameterization, which is reproduced from the paper, only the first  $\eta$  decay mode has been taken into account since it produces to the most energetic gammas.

The differential cross section is expressed with good approximation:

$$\frac{d\sigma_\gamma(E_p, E_\gamma)}{dE_\gamma} = \frac{\sigma(E_p)}{E_p} F_\gamma(x, E_p). \quad (1.32)$$

The term  $\sigma(E_p)$  represents the total inelastic cross section of p-p collisions and is the same used for the neutrino case, see Eq.(1.11). The  $F_\gamma$  function, as for the previous case, describes energy spectra of particles produced, with  $x = E_\gamma/E_p$  and  $E_p$  being the energy of the initial proton  $p$ . The total spectrum of gamma-rays based on the simulations of energy distribution of  $\pi$  and  $\eta$ -mesons by the SIBYLL code can be

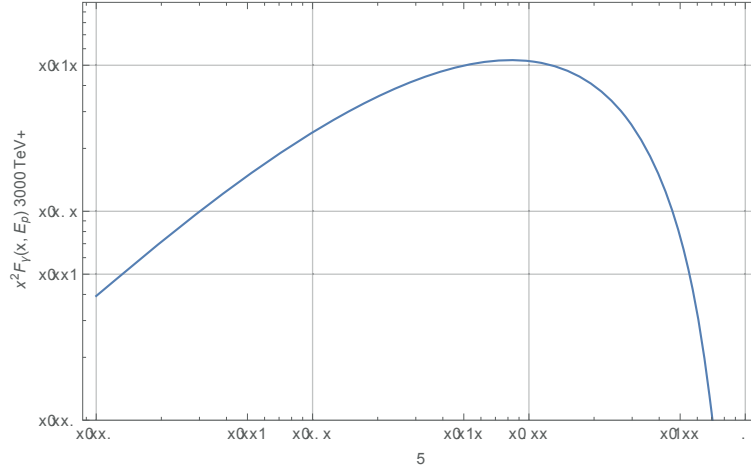


FIGURE 1.4: The adimensional function  $F_\gamma(x, E_p)$  times the energy ratio  $x = E_\gamma/E_p$  squared, as a function of  $x$  and plotted at energy of proton  $E_p = 3 \cdot 10^3$  TeV. Figure reproduced from Kelner, Aharonian, and Bugayov, 2006.

approximated by the following analytical form:

$$\begin{aligned}
 F_\gamma(x, E_p) &= B_\gamma \frac{d}{dx} \left[ \ln(x) \left( \frac{1 - x^{\beta_\gamma}}{1 + k_\gamma x^{\beta_\gamma} (1 - x^{\beta_\gamma})} \right)^4 \right] = \\
 & B_\gamma \frac{\ln(x)}{x} \left( \frac{1 - x^{\beta_\gamma}}{1 + k_\gamma x^{\beta_\gamma} (1 - x^{\beta_\gamma})} \right)^4 \times \\
 & \left[ \frac{1}{\ln(x)} - \frac{4\beta_\gamma x^{\beta_\gamma}}{1 - x^{\beta_\gamma}} - \frac{4k_\gamma \beta_\gamma x^{\beta_\gamma} (1 - 2x^{\beta_\gamma})}{1 + k_\gamma x^{\beta_\gamma} (1 - x^{\beta_\gamma})} \right].
 \end{aligned} \tag{1.33}$$

The parameters  $B_\gamma$ ,  $\beta_\gamma$  and  $k_\gamma$  depend only on the energy of the incident proton:

$$B_\gamma = 1.30 + 0.14L + 0.011L^2; \tag{1.34}$$

$$\beta_\gamma = \frac{1}{1.79 + 0.11L + 0.008L^2}; \tag{1.35}$$

$$k_\gamma = \frac{1}{0.801 - 0.049L + 0.0014L^2}. \tag{1.36}$$

where  $L = \ln(E/1 \text{ TeV})$ . Fig. 1.4 is reproduced from (Kelner, Aharonian, and Bugayov, 2006) and presents the total energy spectrum of gamma-rays; we note that around the peak, the relation between the energies of gamma produced in this processes and the energy of the primary particles is about 10%. In Fig. 1.5 is shown the gamma-ray production cross-section of Eq.(1.32).

### 1.1.3 p- $\gamma$ interaction

Since the p- $\gamma$  collision is dominant mainly in extragalactic sources which are not our matter of interest, we give here a simple overview of the process.

As already mentioned, the p- $\gamma$  interaction becomes principally dominant in regions where there is a high density of gammas. There are 3 possible results for the p- $\gamma$  interaction according to the energy: the Inverse Compton (IC), pair production,

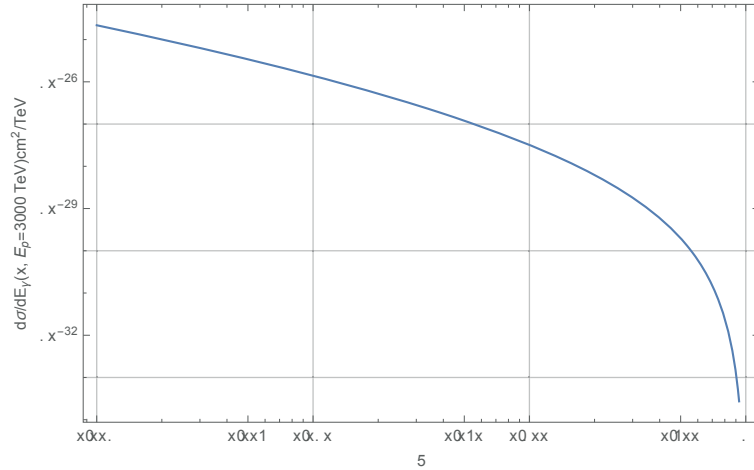


FIGURE 1.5: Differential cross section for the gamma ray production in nucleon-nucleon interactions at the proton energy of  $E_p = 3 \cdot 10^3$ . Figure reproduced from results in (Kelner, Aharonian, and Bugayov, 2006).

and photomeson production, respectively:

$$p\gamma \rightarrow p\gamma' \quad (1.37)$$

$$p\gamma \rightarrow p + e^+ + e^- \quad (1.38)$$

$$p\gamma \rightarrow N + k\pi \quad (1.39)$$

where  $k$  is an arbitrary number of pions depending on the energy of the collision.

Note that only the second and third processes have an energy threshold given by the masses of their secondary products. The process of inverse Compton of protons and electrons are identical, but the energy loss-rate of protons is more suppressed. At energies above the threshold of production of electron-positron pairs, the IC process is four orders of magnitude slower compared to the losses caused by pair-production. So the first channel is always subdominant at these energies. The pair production instead do not give origin to gamma-rays. The only channel that significantly produces gammas, and also neutrinos, is the hadronic result. In the paper by Kelner and Aharonian, 2008 is given a clear and exhaustive analytical presentation of the energetic distribution of the gammas and neutrinos produced in this interaction.

## 1.2 Leptonic gamma-ray production

Besides the hadronic one, different mechanisms for gamma-ray emission at high energy are also present. They are generated by leptonic processes where gamma rays are radiated by cosmic-ray electrons and positrons via bremsstrahlung and inverse Compton scattering. These production processes being electromagnetic do not have neutrinos as an outcome, but only gamma-rays. Nevertheless, they have to be well understood in order to give the proper estimation of the total gamma-ray astrophysical flux.

Bremsstrahlung emission occurs in presence of charged atomic nuclei (indicated by  $Z$ , i.e. their atomic number). Hence, as in the hadronic case, the interstellar gas

represents the target. The interaction is the following:

$$e + Z \rightarrow e + Z + \gamma. \quad (1.40)$$

While, the target for inverse Compton scattering is the ensemble of soft photons that constitute the radiation field in space. This process is referred to as "inverse Compton" (IC), to differentiate from the "normal" Compton process in which is the photon to have a larger energy and the electron is the target. The interaction is:

$$e + \gamma_{\text{soft}} \rightarrow e + \gamma. \quad (1.41)$$

The leptonic mechanisms for gamma-ray production are purely electromagnetic and therefore have exactly calculable cross sections. Many derivations of the leptonic gamma-ray emissivity at high-energies can be found in literature. The study of the leptonic component of HE gamma-rays is not strictly matter of this work so we will not present here the total derivation, one of the most complete treatment is given for example in Blumenthal and Gould, 1970. As already mentioned, bremsstrahlung radiation is emitted when electrons interact with the electric field of ions. In astrophysical environments this occurs for example when a flux of electrons encounters plasma. The emissivity of bremsstrahlung process is given by the integral:

$$q_{\text{brem}}(E_\gamma, \vec{r}) = \int \frac{d\sigma_{e \rightarrow \gamma}(E_\gamma, E_e)}{dE_\gamma} n(\vec{r}) \times 4\pi \phi_e(E_e) dE_e; \quad (1.42)$$

where  $d\sigma_{e \rightarrow \gamma}/dE_\gamma$  is the differential cross section,  $\phi_e$  is the differential spectrum of electrons (meaning electrons plus positrons),  $n(\vec{r})$  is the target spatial number density, and the term  $4\pi$  accounts for the isotropy of the electron flux. The bremsstrahlung cross section can be written as (see Gaisser, Engel, and Resconi, 2016):

$$\frac{d\sigma_{e \rightarrow \gamma}(E_\gamma, E_e)}{dE_\gamma} = \frac{1}{E_e} \frac{\varphi(v)}{N_A X_0}, \quad (1.43)$$

where  $X_0$  is the radiation length,  $\varphi(v)$  is an adimensional function dependent on the ratio:  $v = E_\gamma/E_e$ , and  $N_A$  is the Avogadro number. So the resulting emissivity is dependent on the initial electron spectrum. The simplest case is obtained assuming a simple power law with index  $\alpha$  for the differential spectrum  $\phi_e(E_e)$ . The resulting emissivity in this case can be shown to be (Gaisser, Engel, and Resconi, 2016):

$$q_{\text{brem}}(E_\gamma) \sim \frac{4\pi\rho}{X_0} \phi_e(E_\gamma) \left( \frac{1}{\alpha + 1} + \frac{1.35}{\alpha - 1} - \frac{1.35}{\alpha} \right). \quad (1.44)$$

Where  $\rho$  is the target mass density. It is evident how the emissivity directly reflects the initial electron spectrum. At energies around few GeV, and assuming a simple power law electron spectrum, the ratio of bremsstrahlung and hadronic photo-emission is  $\sim 10\%$ . The nuclear interaction is dominant at high energies. See Fig. 1.6.

The inverse Compton interaction is important in regions of high photon density and is an efficient acceleration mechanism of soft photons up to high energies. This phenomenon can indeed promote in energy an X-ray into a gamma-ray. The energy distribution of photons produced via IC starting from an infrared/X-ray photon population can peak indeed at GeV-TeV energies.

The calculation of gamma-ray emissivity by IC is not a trivial procedure (see Blumenthal and Gould, 1970). Assuming an isotropic photon field at a single frequency

$\nu_0 = E_0/h$ , the emissivity dependent on the gamma energy  $E_\gamma$  is:

$$q_{\text{IC}}(E_\gamma) = \frac{3\sigma_{\text{T}}cn_{\text{rad}}(E_0)}{16\gamma^4E_0^2}E_\gamma \left[ 2E_\gamma \ln \left( \frac{E_\gamma}{4\gamma^2E_0} \right) + E + 4\gamma^2E_0 - \frac{E^2}{2\gamma^2E_0} \right]; \quad (1.45)$$

where  $\gamma$  represents the Lorentz factor,  $n_{\text{rad}}(E_0)$  is the soft photon number density, and  $\sigma_{\text{T}}$  is the Thompson interaction cross section. At low energies ( $\gamma E_\gamma \ll m_e c^2$ ), in the so called "Thompson regime", the term in square brackets is constant and the scattered radiation emissivity has the form  $q_{\text{IC}}(E_\gamma) \propto E_\gamma$ . Moreover, the spectrum has the characteristic to be peaked around the energy corresponding to head-on collisions in which the photon gets scattered back on its original direction. At high-energies ( $\gamma E_\gamma \gg m_e c^2$ ) the interaction reaches the so called "Klein-Nishina regime" and the spectrum has a decreasing trend. Considering also in this case the simplest assumption of an initial power law spectrum of electrons with spectral index  $\alpha$ , this results in an intensity spectrum of the scattered radiation of the form  $E_\gamma^{-(\alpha-1)/2}$ .

This might be a good assumption for approximated calculations, however, the real energy spectrum of the summed fluxes of electrons and positrons is not strictly a power law. The full calculation of the leptonic emission requires a full description of this initial flux. The leptonic fluxes in the energy range 10–10<sup>4</sup> GeV are well measured by several telescopes (land-based or satellite) such as PAMELA, Fermi, DAMPE, MAGIC, H.E.S.S. and others. In Lipari and Vernetto, 2018 is presented a clarifying plot of the fit of the two main leptonic components of the gamma-ray flux using the fit of the data of the aforementioned experiments. In Fig. 1.6 is reported the plot where the hadronic, inverse Compton, and bremsstrahlung resulting spectra are shown.

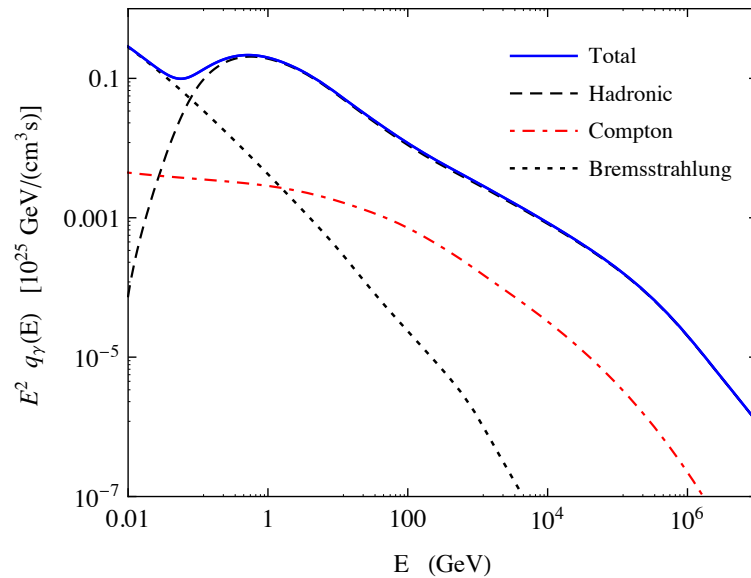


FIGURE 1.6: Gamma ray emission rate at the Sun position. The total emission and the single contributions of the three main mechanisms (hadronic, bremsstrahlung and inverse Compton scattering) are shown. Figure taken from Lipari and Vernetto, 2018.

What is evident from the plot is that in the case of bremsstrahlung,  $e^-$  and  $e^+$  radiate photons with an energy independent cross section. If the primary electrons have a power law spectrum, the emission is then also a power law with the same

spectral index. It is evident that the bremsstrahlung spectrum softens at higher energy, and this is because there is a break in the ( $e^- + e^+$ ) spectrum around 1 TeV. While for the inverse Compton we can see that starts with a harder spectrum. At energies around 100 GeV instead, the spectrum changes since it switches to the Klein–Nishina regime and has a softening (Blumenthal and Gould, 1970). This is also due to the softening of the ( $e^- + e^+$ ) spectrum around 1 TeV. The result is that at these energies the inverse Compton emission of gamma rays gives a maximum contribution of order 5% respect to the hadronic one (Lipari and Vernetto, 2018).

### 1.3 Gamma absorption

The process responsible of the gamma-ray absorption during the propagation in the interstellar gas of the Galaxy is the "pair production" mechanism. In this case we have the electromagnetic interaction of high-energy photons with soft radiation producing electron-positron pairs:

$$\gamma + \gamma \rightarrow e^- + e^+. \quad (1.46)$$

The target in the Galaxy is made of cosmic microwave background radiation (CMBR), infrared radiation, stellar light, and Extragalactic Background Light (EBL). The largest source of target photons is the cosmic microwave background radiation (CMBR) with a homogeneous density around  $400 \text{ cm}^{-3}$  (Vernetto and Lipari, 2016). The other target is generated by the emission of all radiation sources in the Universe and is called the extragalactic background light (EBL), it is also uniformly distributed in space and has an average density of around  $1.5 \text{ cm}^{-3}$  of higher energy photons (Vernetto and Lipari, 2016). In the Galaxy, the other large source of target photons is the infrared emission of dust when heated by stellar light. The radiation field generated by the dust emission is not homogeneous in space and have space and angular distributions that must be carefully modeled to compute the absorption effects. Furthermore, starlight photons have a smaller number density and their effects on gamma ray absorption are therefore negligible. In Vernetto and Lipari, 2016 there is a thorough treatment of this problem. Fig. 1.7 represents the plot of the soft photons background energy distribution at the Sun position, broken down into its main components. It is interesting to observe the energy-dependence of the angle-averaged absorption coefficient in the Sun position (Fig.1.8) computed starting from the soft radiation distribution (Fig.1.7). Each contribution given by the four components is shown in the plots; note that the CMBR operates the largest absorption in the energy range in which we are interested. While at energies around 1 TeV the main absorption is given by the starlight. It is evident how the absorption by EBL and CMBR precludes the possibility of gamma-ray extragalactic Astrophysics at energies over 30 TeV.

Both the presence of leptonic gamma-ray production and the absorption process that interests the high-energy gamma-rays once they are produced at the source, make the link with neutrino flux and in general the multimessenger approach more difficult. This is because, due to these two phenomena, the calculation of the neutrino flux counterpart starting from gamma-ray sources observations is not straightforward. In our following computations (Chapter 4) we make the hypothesis that all sources are in hadronic regime, so when converting gamma-ray flux in neutrino flux the estimate is considered as an upper bound. The gamma-ray absorption is considered negligible since our study is focused at energies around 1 TeV (see Fig.1.8).

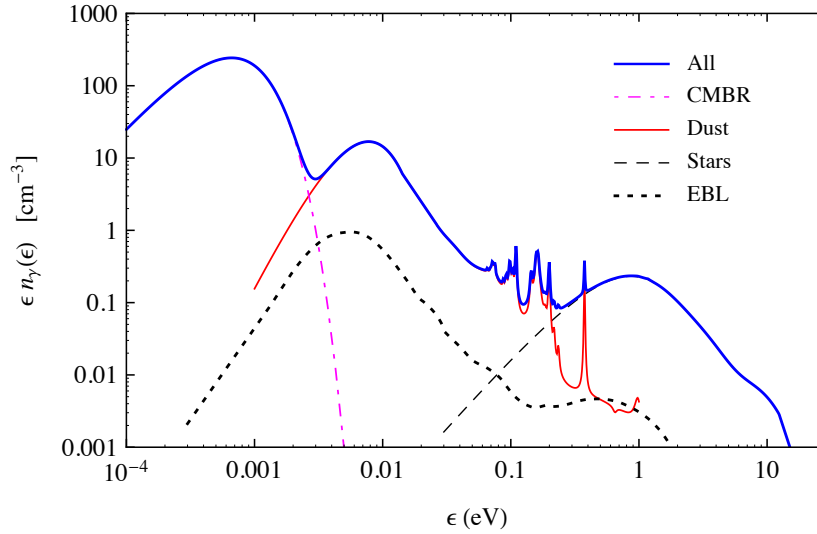


FIGURE 1.7: Energy distribution of soft photons in the solar neighborhood. Figure taken from Vernetto and Lipari, 2016.

## 1.4 Neutrino/gamma spectrum relation

In the astrophysical sources where the hadronic production of gamma-rays by p-p interaction is dominant over the leptonic one, the measurements of gamma-ray flux can give direct information on the neutrino flux expected. To obtain the relation between the two fluxes, the simplest case is obtained for a simple power-law spectrum and has been widely treated (recently: Costantini and Vissani, 2005; Lipari, 2006).

A primary estimation of the energy ratio between neutrinos and gamma-rays from pion decay can be a useful result that might become handy in the future discussion. By cinematic considerations we can assume that in average neutrinos obtain approximately 1/4 of the charged pion energy. This estimation is valid for neutrinos produced directly by pion decay and by those subsequently produced in muon decay. For gammas the consideration is even more straightforward, the  $\pi^0$  decay is a two body decay in two identical particles, so each gamma gains in average 1/2 of the pion energy. In general the neutrino and gamma that are produced by 2 pions with the same initial energy have an energy ratio of:

$$E_\gamma \simeq 2 E_\nu, \quad (1.47)$$

In our case, considering that the leading pions produced by p-p collisions, regardless of their charge, gain  $\sim 1/5$  of the initial proton energy, we infer that neutrinos gain in average 1/20 of the initial proton energy, while gammas gain 1/10. In other words, if we are observing a neutrino (or gamma) at a certain energy, we should suppose a primary proton with an initial energy 20 (10) times the observed energy:

$$E_p \simeq 20 \times E_\nu \simeq 10 \times E_\gamma. \quad (1.48)$$

One of the most commonly used hypotheses is the case in which the initial spectrum of protons is a power law. Under the assumption of the Feynman scaling approximation of the inclusive cross sections of the hadronic interaction, the spectrum of secondary particles is still a power law with same spectral index. In general the spectrum of a p-p neutrino obtained by a proton spectrum with power law with

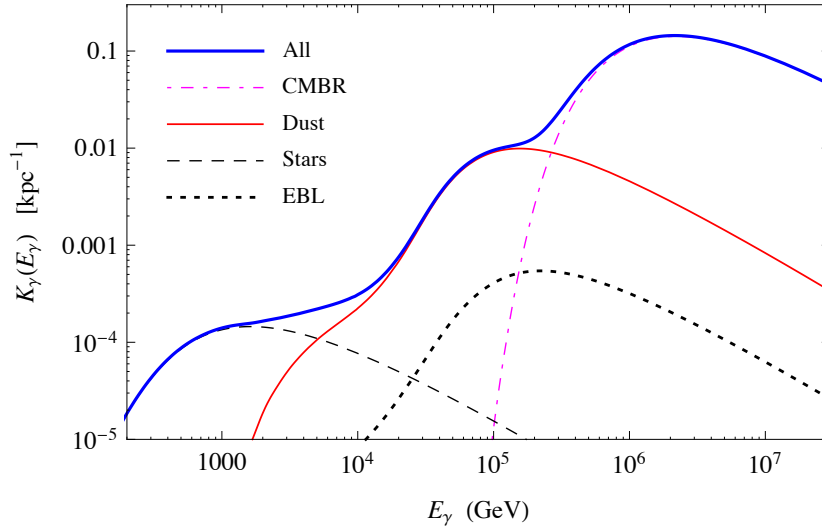


FIGURE 1.8: Absorption coefficient for gamma-rays in the solar neighborhood, as a function of energy, averaged over the direction of the photon. Figure taken from Vernetto and Lipari, 2016.

spectral index  $\alpha$  can be expressed by (Kelner, Aharonian, and Bugayov, 2006):

$$\varphi_{\nu_\ell}(E_{\nu_\ell}) = NE_{\nu_\ell}^{-\alpha} a_{\nu_\ell}(\alpha); \quad (1.49)$$

where  $N$  is the normalization factor. The coefficient  $a_{\nu_\ell}(\alpha)$  depends on the flavour considered and can be expressed through the functions  $f_{\nu_\ell}(x)$  that describe the fraction of energy carried by a neutrino with respect to the pion energy  $x = E_{\nu_\ell}/E_\pi$  in the laboratory frame:

$$a_{\nu_\ell}(\alpha) = \int_0^1 f_{\nu_\ell}(x) x^{\alpha-1} dx. \quad (1.50)$$

The  $f_\nu(x)$  functions are indeed probability functions and their analytical expression along with their derivation can be found in Kelner, Aharonian, and Bugayov, 2006. In this case the spectral distribution would depend on the flavour considered and the sum of the total neutrino flux produced in a p-p collision:

$$\varphi_\nu = \varphi_{\nu_\mu} + \varphi_{\bar{\nu}_\mu} + \varphi_{\nu_e} = NE_\nu^{-\alpha} (a_{\nu_\mu}(\alpha) + a_{\bar{\nu}_\mu}(\alpha) + a_{\nu_e}(\alpha)). \quad (1.51)$$

Analogously the spectral distribution of a gamma-ray obtained by the same interaction is expressed by:

$$\varphi_\gamma(E_\gamma) = NE_\gamma^{-\alpha} a_\gamma(\alpha); \quad (1.52)$$

with:

$$a_\gamma(\alpha) = \int_0^1 f_\gamma(x) x^{\alpha-1} dx. \quad (1.53)$$

This last computation is easier since the distribution  $f_\gamma(x)$  in the laboratory frame for the 2-gamma decay is  $f_\gamma(x) = 1$ , due to the fact that the energy distribution of each particle in a 2 identical particle decay is uniform. Therefore:

$$a_\gamma = \frac{1}{\alpha}.$$

Note that the ratio between neutrinos and gammas produced by the same interaction is variable and is a function of the spectral index of the primary spectrum:

$$\frac{\varphi_\nu}{\varphi_\gamma} = \alpha(a_{\nu_\mu}(\alpha) + a_{\bar{\nu}_\mu}(\alpha) + a_{\nu_e}(\alpha)). \quad (1.54)$$

However, for more refined experimental observations the power law is not always the best approximation since the proton spectrum appears to have several features. For instance, in cases in which the proton spectrum is better approximated to a power law with a cutoff, the spectra of secondary neutrinos and gammas is more complex and do not follow a simple power law with cutoff.

In Kappes et al., 2007 is presented a derivation of the neutrino/gamma spectra relation assuming a spectrum of incident hadrons as power-law with exponential cutoff with arbitrary parameters. This is also based on results from the SIBYLL event generator. The expression for proton spectrum has index  $\alpha$  and cutoff value  $\epsilon_p$ :

$$\varphi_p(E_p) = k_p \left( \frac{E_p}{1 \text{ TeV}} \right)^{-\alpha} \exp\left(-\frac{E_p}{\epsilon_p}\right), \quad (1.55)$$

where  $k_p$  is a normalization constant. Considering spectra indices in the range  $1.8 < \alpha < 3.0$ , and an energy cut-off range  $10 \text{ TeV} < \epsilon_p < 1 \text{ PeV}$ , the neutrino and gamma-ray spectra obtained are:

$$\varphi_{\nu,\gamma}(E_{\nu,\gamma}) \approx k_{\nu,\gamma} \left( \frac{E_{\nu,\gamma}}{1 \text{ TeV}} \right)^{-\Gamma_{\nu,\gamma}} \exp\left(-\sqrt{\frac{E_{\nu,\gamma}}{\epsilon_{\nu,\gamma}}}\right), \quad (1.56)$$

with the following relations between the neutrino and gamma parameters and the primary proton parameters:

$$k_\nu \approx (0.71 - 0.16\alpha)k_\gamma, \quad (1.57)$$

$$\Gamma_\nu \approx \Gamma_\gamma \approx \alpha - 0.1, \quad (1.58)$$

$$\epsilon_\nu \approx 0.59\epsilon_\gamma \approx \frac{\epsilon_p}{40}. \quad (1.59)$$

The obtained neutrino flux is calculated as the sum of electron and muon neutrino spectrum, assuming a flavour ratio ( $\nu_e : \nu_\mu : \nu_\tau = 1/3 : 2/3 : 0$ ) at the source. Assuming full mixing of the flux, the single flavour neutrino spectrum at Earth is then given by one-third of the total flux at the source. As mentioned before, a full mixed neutrino flux is a valid approximation for astrophysical Galactic distances and energies considered.

The main assumptions under which are obtained these results are the following:

1. a negligible contribution of non-hadronic production processes to the measured gamma-ray emission;
2. no significant  $\gamma$ -ray absorption in the nearby area around the source;
3. low magnetic fields, so that muons decay without significant energy loss;
4. a fully mixed flux of neutrinos at Earth ( $\nu_e : \nu_\mu : \nu_\tau = 1/3 : 1/3 : 1/3$ );
5. the nucleus-nucleus and p-p interactions produce similar pion spectra, so that can be studied in the same way.

Except for the first one, all these conditions are valid for all high-energy gamma-ray sources that we will examine in the following part of the work (see H.E.S.S. Galactic Plane Survey in Chapter 5), so we will often rely on this tool for linking together the neutrino and gamma fluxes (Kappes et al., 2007).

Another interesting gamma/neutrino relation that is worth to be mentioned is presented in the paper by Villante and Vissani, 2008. Here it is provided a simple analytic expression for the neutrino fluxes which can be applied directly to gamma-ray data without the need for a previous parameterization of the photon spectrum. This allows to propagate easily the observational errors in the gamma-ray flux and, thus, to understand how well the neutrino flux and the signal in neutrino telescopes can be constrained by  $\gamma$ -ray data. In the paper this procedure is applied to the case of known SNRs in order to estimate their neutrino flux counterpart and expected events.



## Chapter 2

# Galactic Sources of High-Energy Neutrinos and Gammas

Our Galaxy is called the Milky Way originally because of its appearance as a bright white stripe in the dark sky (Fig.2.1). The Milky Way is a barred spiral galaxy with an estimated disk radius of about 20 kpc, and a disk thickness of about 100-300 pc (Fig. 2.2) (Gaisser, Engel, and Resconi, 2016). Spiral galaxies are estimated to be the two thirds of the total galaxies in the Universe. Unlike a regular spiral, a barred spiral contains a bar across its center region, and presents two major arms.

Our Galaxy is estimated to contain 100–400 billions stars and at least the same number of planets. At the centre is located a Super Massive Black Hole called Sagittarius A\*. This is surrounded by a bulge of particles and stars characterized by strong photon emission in a wide range of energies. From that central area, depart the arms of the spiral. On the inner edge of the Orion Arm is located the Solar System, at a distance of around 8.5 kpc from the Galactic centre. The Orion arm is located between two major arms, Perseus and Sagittarius.

In the upcoming paragraphs we will describe the main sources (both extended and point-like) of neutrinos and gamma-rays in all galaxies in general, and, of course, also in the Milky Way. We will give an overview on all their main properties and categories in order to have a clear panorama on their variety which will be useful to keep in mind for our next discussion.

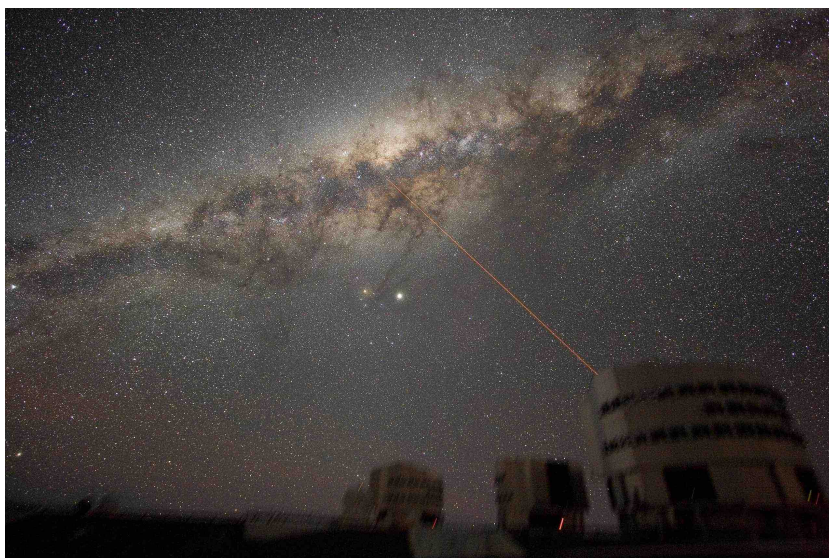


FIGURE 2.1: Milky Way from Paranal, Chile in 2007. Credit: Astronomer Yuri Beletsky.

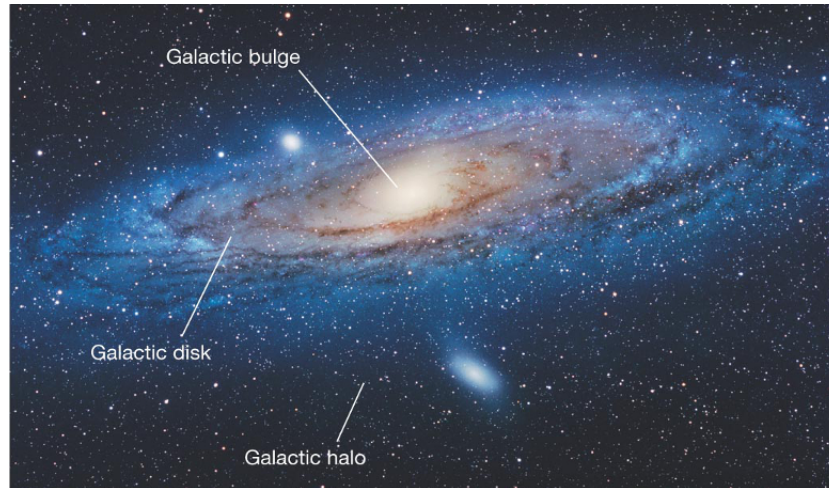


FIGURE 2.2: Galaxy structure. Credit: Pearson Education, Inc., publishing as Pearson Addison-Wesley.

### 2.0.1 Disk

The Galactic disk is permeated by a gas of particles, mainly Hydrogen and Helium, floating in the interstellar regions. It accounts for  $\sim 10\text{--}15\%$  of the total mass of the Galactic disk and is mainly concentrated near the Galactic plane and along the spiral arms, while being inhomogeneously distributed at small scales. The gas density is approximately 1 nucleon per  $\text{cm}^3$  (Gaisser, Engel, and Resconi, 2016). Despite its very low density it constitutes the target of the cosmic rays that in the nucleon-nucleon inelastic collisions produce a prominent part of the total high-energy  $\nu/\gamma$  flux. This is commonly called the *diffuse* flux component.

The amount of tenuous matter contained in the Galactic disk exists in the form of gas (atoms, molecules, ions, and electrons), and dust, composed of tiny solid particles. The chemical composition of interstellar matter by number is: 90.8% of hydrogen, 9.1% of helium, and 0.12% of heavier elements called "metals", such as C, N, O (Ferrière, 2001). This is close to the "cosmic composition" inferred from abundance measurements in the Sun, in stars, and in meteorites.

This tenuous matter is not homogeneously distributed in the interstellar space. In fact, half the interstellar mass is confined to discrete clouds occupying only  $\sim 1\text{--}2\%$  of the interstellar volume (Ferrière, 2001). These clouds can be divided into three types. Firstly, there are the *dark clouds*, which are essentially made of very cold molecular gas and block off the light from background stars, with a temperature  $T$  around  $10\text{--}20\text{K}$ . Then there are the *diffuse clouds*, which consist of cold ( $T \sim 100\text{K}$ ) atomic gas and are almost transparent to the light of the stars, except at a number of specific wavelengths where they give origin to absorption lines observable at Earth. Lastly there are *translucent clouds* which contain molecular and atomic gas and have intermediate visual absorption features. The rest of the remaining interstellar matter, spread out between the clouds, can be found in three different forms: warm (mostly neutral) atomic, warm ionized, and hot ionized (Ferrière, 2001).

In order to model the diffuse component of the neutrino and gamma-ray Galactic fluxes a knowledge of the spatial distribution of the density and composition of the interstellar medium is required. For our models we will use the distributions of both molecular and atomic hydrogen, and of helium, since, they are the most abundant elements in the ISM. The model that we will use is obtained from the public GALPROP code (GALPROP). This is given as a sum of atomic (H) and molecular ( $\text{H}_2$ ) hydrogen.

Molecular hydrogen cannot be observed directly, but its spatial distribution can be inferred through the observation of the emission lines of carbon monoxide (CO). For this we adopt a conversion factor with respect to the CO density as given by Yang, Aharonian, and Evoli, 2016 from a fit of the diffuse  $\gamma$  emission. Finally, the minor Helium contribution to the Galactic gas is taken into account by assuming a constant density ratio of 0.11 with respect to total hydrogen amount. Our model is cylindrically symmetrical. In Fig. 2.3 is shown the total gas distribution along the radial cylindrical coordinate which was used for all our work. As we can see, it presents a large number of structures, while see Ferrière, 2001 for a simple analytical parameterization of all the components. For the distribution along the coordinate  $z$  the data report a very steep, almost exponential, decrease.

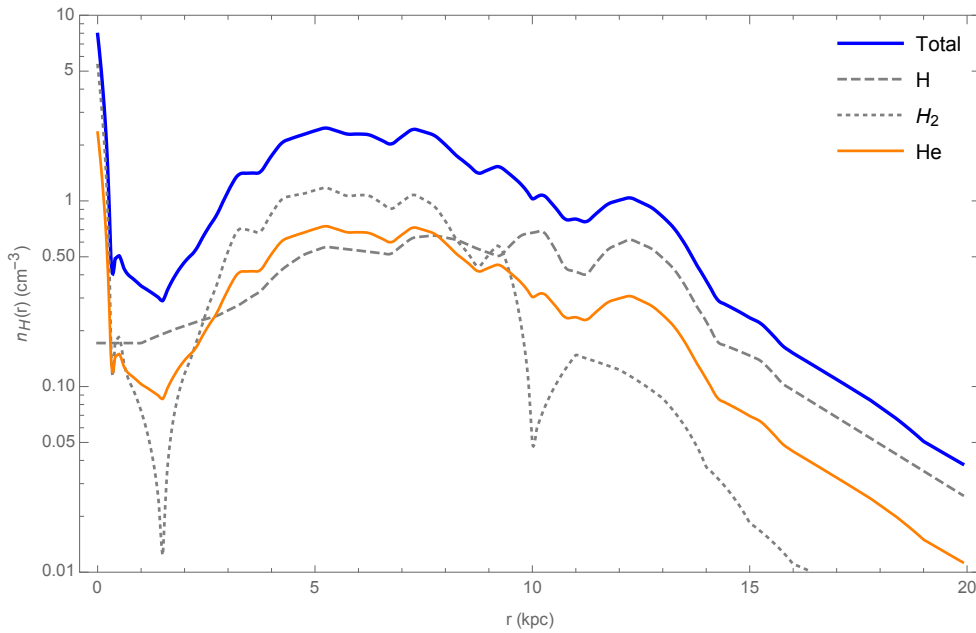


FIGURE 2.3: Radial distribution of the gas density profiles in the Galaxy obtained using the public code GALPROP.

To have an estimation of the diffuse contribution to the total fluxes of both neutrinos and gammas, the last term that we should be in possession of is detailed information on the distribution of the cosmic rays in the Galaxy, or at least in every position where the interstellar gas density is different from zero. This estimation could become quite uncertain since it reflects the uncertainty of this term. In Chapter 4 we will treat this problem in detail starting from this gas distribution, and we will give our estimations based on different assumptions of cosmic ray energy and spatial distribution.

## 2.0.2 Centre

The Galactic centre (also called "bulge") is a spherical central region with radius 2-3 kpc. The centre of the Milky Way has been long investigated as it is a region of high stellar activity. Indeed this is the largest density region of the Galaxy. Here is located the black hole Sagittarius A\* classified as a Supermassive Black Hole having a mass of  $4 \times 10^6 M_{\odot}$ . This region around the Milky Way bulge was hypothesized to be the location of the so called PeVatron: the accelerating engine that gives origin to UHE-CRs that are confined in our Galaxy and that reach energies up to PeV. The H.E.S.S.

collaboration investigated the nearby area and confirmed this region to host cosmic rays accelerated to PeV (Abramowski et al., 2016). This was inferred by measurements of gamma-ray spectrum in this area. Here the H.E.S.S. observatory registered one intense  $\gamma$ -ray point-like source: HESS J1745-290, which is located close by the position of the Galactic Centre PeVatron, however the current data cannot answer whether there is a link between the two objects. Moreover, this source still remains unidentified.

The Galactic bulge hosts also a molecular cloud. This region surrounding the Galactic Centre contains predominantly molecular gas and extends out to a distance in projection of around 250 pc at positive galactic longitudes and around 150 pc at negative longitudes. Here the production of the gamma rays observed is believed to be dominantly hadronic. Indeed, although the inverse Compton mechanism is active in this region the electrons suffer of a severe radiative loss of energy at TeV energies and are therefore prevented from propagating to distances comparable to the size of the central zone. Moreover the shape of the VHE  $\gamma$ -ray brightness distribution is compatible with the shape and extension of the molecular gas, and that suggests an hadronic production due to the interaction of the cosmic-rays and the gas of the gas-rich complexes. Therefore we would expect to have also a production of high-energy neutrinos in this region.

We will give a detailed estimation of the diffuse flux and longitudinal distribution of both neutrinos and gamma-rays in Chapter 4, where the large contribution of the Galactic bulge will be clear.

### 2.0.3 Halo

The galactic halo is a roughly spherical area that surrounds most galaxies and it can extend of hundreds of times the dimension of the contained galaxy. However, the actual dimension of the galactic halo is hard to determine because its borders are faint and dissolve in the outer medium. The halo is commonly believed to be composed mainly of gas, but there are also many globular clusters of stars disseminated in its volume. In Fig. 2.4 is shown a picture of the Sombrero galaxy captured by the Hubble telescope in which the bright part of its surrounding halo is evident.



FIGURE 2.4: Picture of the Sombrero galaxy captured by the Hubble telescope released in October 2004. Credit: Wikipedia.

The halo emission is generally considered subdominant and negligible respect to the disk. However, Taylor, Gabici, and Aharonian, 2014 presented an interesting

estimation that shows that, although its gas density is very low, due to its large extension the halo diffuse emission could be in fact comparable to the disk one. If this is the case, the halo can have therefore a significant role in the total neutrino flux that reaches the Earth. By assuming a constant CR distribution in the whole disk and halo, in Taylor, Gabici, and Aharonian, 2014 is given for both a first order estimation of the expected number of diffuse neutrinos  $N_\nu$  detected by a given telescope from a region subtending a solid angle  $\Delta\Omega$ . The ratio between the two is given by:

$$\frac{N_\nu^{\text{halo}}}{N_\nu^{\text{disk}}} = \left( \frac{n_p^{\text{halo}}}{n_p^{\text{disk}}} \right) \left( \frac{L^{\text{halo}}}{L^{\text{disk}}} \right) \left( \frac{\Delta\Omega^{\text{halo}}}{\Delta\Omega^{\text{disk}}} \right);$$

where  $n_p^{\text{halo}}$  and  $n_p^{\text{disk}}$ ,  $L^{\text{halo}}$  and  $L^{\text{disk}}$  are respectively the gas densities and sizes of halo and disk.  $\Delta\Omega^{\text{halo}} = 2\pi$  sr and  $\Delta\Omega^{\text{disk}} = 0.1$  sr ( $-40^\circ < l < 40^\circ$ ,  $|b| < 2^\circ$ ) are the assumed solid angles subtended by the telescope. The typical gas density and dimension values considered for the disk are:  $n_p^{\text{disk}} = 1n_{p,0}^{\text{disk}} \text{cm}^{-3}$ ,  $L^{\text{disk}} = 10L_1^{\text{disk}}$  kpc. For the halo the following reference values are adopted:  $n_p^{\text{halo}} = 10^{-3}n_{p,3}^{\text{halo}} \text{cm}^{-3}$  and  $L^{\text{halo}} = 10L_1^{\text{halo}}$  kpc. So the ratio between the expected neutrino numbers is:

$$\frac{N_\nu^{\text{halo}}}{N_\nu^{\text{disk}}} \sim 0.05 \left( \frac{n_{p,-3}^{\text{halo}}}{n_{p,0}^{\text{disk}}} \right) \left( \frac{L_1^{\text{halo}}}{L_1^{\text{disk}}} \right) \left( \frac{0.1}{\Delta\Omega^{\text{disk}}} \right).$$

In conclusion, under the constant CR intensity assumption, the diffuse neutrino fluxes emitted by disk and halo can be comparable assuming a very extended halo so that:  $L_1^{\text{halo}} \gg L_1^{\text{disk}}$ . This appears supported by the recent detection of a large gas reservoir around our Galaxy which extends to  $\sim 100$  kpc (Gupta et al., 2012).

For what concerns high-energy gamma-rays instead, they are supposed to be absorbed over distances comparable to the dimensions of the halo so they are not expected to reach the Earth.

Finally, there is also another component of the galactic halo which is the dark matter halo and that is supposed to surround all the galaxies. Their extension and form are not clear also because their presence has not been directly observed but only inferred by their effect on gas distribution and star motions.

## 2.0.4 Fermi Bubbles

Analysis of the Fermi-LAT data revealed two extended spherical zone of gamma-rays above and below the Galactic centre that took the name of Fermi Bubbles (Su, Slatyer, and Finkbeiner, 2010), see Fig. 2.5 for a schematic representation. The Fermi-LAT telescope observes energies in the range 1–100 GeV, but consequently it was also found a microwave (Finkbeiner, 2004) and X-ray counterpart of the bubbles (Kataoka et al., 2013, Kataoka et al., 2018). They extend for 50 degrees above and below the Galactic center, with a width of about 40 degrees in longitude and their intensity appears to be uniform for the almost the whole extension. The Fermi bubble spectrum is harder respect to the one generated by IC and pp interaction in the Galactic disk, and has a spectral index of  $\sim -2$ . Moreover, there is no significant difference between the southern and northern fluxes, nor in the intensity neither in the spectrum.

Many models for the explanation of these two structures were proposed. In (Su, Slatyer, and Finkbeiner, 2010) it is argued that they were created by some extended episode of energy injection in the Galactic center, such as past accretion events onto

the central massive black hole, or a nuclear starburst. In Crocker and Aharonian, 2011 is hypothesized an hadronic model for the bubbles as due to the interaction of a population of relic cosmic ray protons injected by processes associated with extremely long timescale (more than 8 Gyr). In Boer et al., 2015 it is proposed that the bubbles outflow from the plane with the gamma-rays arising from hadronic interactions of protons trapped in a plasma of advected gas. In any of these models the neutrino counterpart is expected. However, there are also leptonic models or even dark matter models that explain the Fermi bubble formation. In these cases the neutrino produced would be negligible or absent. For this reason a future observation of a neutrino signal coming from the Fermi-bubble areas would be crucial in order to give an understanding of the innermost astrophysical mechanisms.

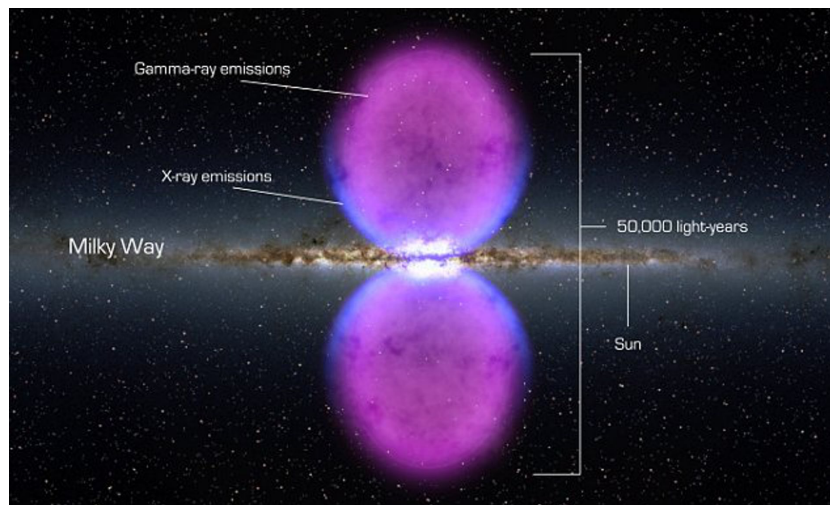


FIGURE 2.5: Fermi Bubble representation. Credit: Wikipedia.

## 2.1 Point-like and extended Galactic sources

The most common point-like known Galactic sources of neutrinos and/or very-high energy radiation are Supernova Remnants (SNRs), pulsars, Pulsar Wind Nebulae (PWNe). There is also a new kind of extended source that was recently observed which is the TeV-halo (Abeysekara et al., 2016). This source appears as a large area of about a 30 – 40 pc radius with an intense TeV gamma-ray production. The conditions under which this kind of objects form, and the precise definition of what a TeV-halo is, are still debated and we will go more in detail about it in Chapter 6. What is commonly believed is that a TeV-halo can take origin in the last phase of the formation of a Pulsar Wind Nebula and can be responsible for a large fraction of the total high-energy gamma-ray Galactic flux.

### 2.1.1 Supernova Remnants

The death of massive stars or when a white dwarf is triggered into runaway nuclear fusion, results in a disruptive explosion that is called "supernova" (SN). Supernova explosions are extremely energetic events that emit a large optical luminosity with a peak that can be comparable to that of an entire galaxy before fading away over several weeks or months. The death of a massive star leads to a so called "core-collapse" supernova, while the nuclear fusion of a white dwarf, a more rare phenomenon,

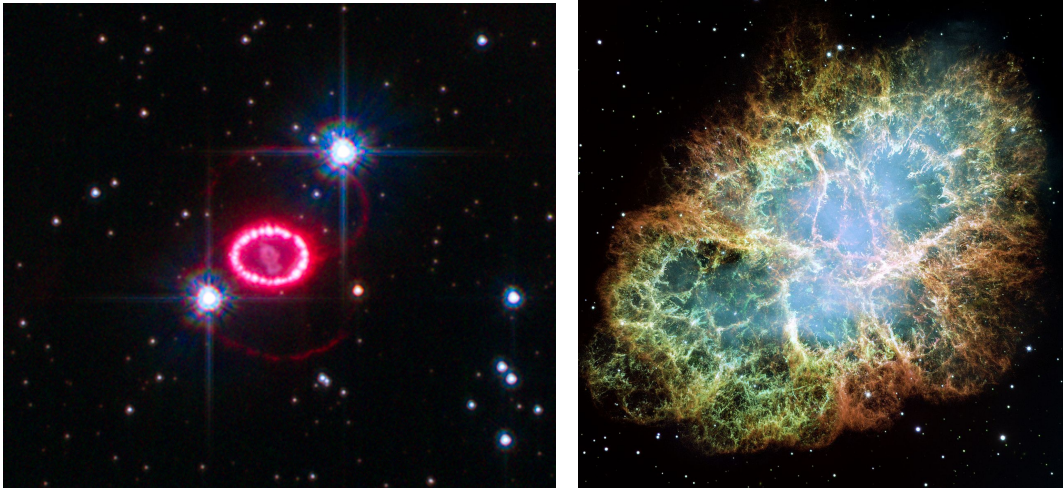


FIGURE 2.6: Left: The remnant of SN 1987A captured by NASA's Hubble Space Telescope (September, 2010). Right: mosaic image, one of the largest ever taken by NASA's Hubble Space Telescope, of the Crab Nebula (December, 2005).

takes to a supernova usually classified as "Type I". The whole taxonomy of supernovae is more complex, however, and is generally based on the absorption lines of different chemical elements that appear in their spectra.

In our work we are only interested in core-collapse SNe which we will simply call SN from now on. After the explosive phase, core-collapse supernovae either become neutron stars or black holes. In any case, however, the remaining structure around it is called "Supernova Remnant" (SNR). This is bounded by an expelled shock wave and consists of ejected material expanding from the initial explosion that sweeps up the ambient gas and provokes turbulent magnetic fields.

SNRs can be classified in three types: shell type, filled or plerionic type, and composite type. With shell type is indicated the SNRs presented without any other feature. When the supernova explosion plows through space, it heats and stirs up any interstellar material, this produces a big almost spherical structure of hot material in space. In this case a ring-like structure is formed, which takes the name of "shell". The filled and the composite types, instead, are different because powered by a pulsar in the center that produces high-energy electrons. These electrons emit synchrotron radiation in the X-rays, optical, and radio frequencies by interacting with the magnetic field. According to the emission observed, the SNRs takes the name of plerions or pulsar wind nebulae (PWNe) when appears with an undefined "blob" shape and more faint borders, while is called composite when is characterized by a mixed shell-type and nebular morphology.

One of the best observed ring-like young supernova remnants was formed by SN 1987A, a supernova in the Large Magellanic Cloud that was observed in February 1987, see Fig. 2.6, left panel. Another well-known supernova remnant is the plerionic SNR that includes the Crab Nebula, see Fig. 2.6, right panel.

Theoretical arguments developed to explain extensive observations of cosmic rays and Galactic radiations favor the hypothesis that cosmic-ray acceleration takes place at supernova remnant shocks below PeV energies (Ginzburg and Syrovatskii, 1964).

In principle, most of the particle acceleration occurs when the ejecta has swept

up its own mass in surrounding material so during the first phases of the SNR evolution, since most of the initial energy of the remnant is dissipated during this period.

However, the maximum energy reached by cosmic-rays in the SNR environment doesn't appear to be sufficient to produce VHE  $\nu$  and  $\gamma$  in interaction with the ISM. The question on the origin of particles above the knee energy limit is still an open issue. There is also a number of other possibilities suggested, i.e. a variety of supernovae and hypernovae, pulsars, a Giant Galactic Halo, and extragalactic origin (Erlykin and Wolfendale, 2005). One of the hypothesis is that the best conditions where they can be generated are found especially in molecular clouds. Here the youngest SNRs are supposed to give origin to higher energy cosmic-rays and therefore to the very energetic neutrinos and gammas. SNRs are naturally produced in star-forming regions rich in gas, so they have a high probability of being spatially close to molecular clouds. Indeed, these particular SNRs are supposed to produce intense enough fluxes that are observable in the present experiments at Earth (such as IceCube that observes neutrinos up to few PeV of energy). Moreover, another hypothesis are the remnants of very energetic supernovae, called "Hypernovae" (HN). The required CR energy of 20 – 30 PeV for the production of 1 PeV neutrinos can be reached by hypernovae (HN) with kinetic energy  $E \geq 10^{52}$  erg. The estimations of neutrino fluxes expected by both these types of sources are done in Ahlers and Murase, 2014. Assuming a homogeneous SNR distribution with radius  $\simeq 17$  kpc and height  $\simeq 0.1$  kpc; a source spectrum of CR as a power law with index  $-2.2$ ; the obtained cumulative diffuse neutrino flux from SNRs in a solid angle  $\Delta\Omega \simeq 0.44$  sr ( $-180^\circ < l < 180^\circ$ ,  $|b| < 2^\circ$ ) is:

$$E_\nu^2 \phi_{\nu_\alpha}^{\text{SNR}} \simeq 2.5 \times 10^{-8} \text{ GeV cm}^{-2} \text{ s}^{-1} \text{ sr}^{-1} \left( \frac{E_\nu}{0.1 \text{ PeV}} \right)^{-0.2}; \quad (2.1)$$

with exponential cutoff at  $E_{\nu, \text{max}} = 0.1$  PeV. This result is obtained assuming a supernova birth rate of  $\sim 0.03 \text{ yr}^{-1}$ . The result for hypernovae is obtained for a lower rate (being much rarer phenomena):  $\sim 1 - 2$  % of the SN rate, hence for a lower number of sources but a larger ejecta energy. The result given for hypernovae is:

$$E_\nu^2 \phi_{\nu_\alpha}^{\text{HNR}} \simeq 6.2 \times 10^{-9} \text{ GeV cm}^{-2} \text{ s}^{-1} \text{ sr}^{-1} \left( \frac{E_\nu}{0.1 \text{ PeV}} \right)^{-0.2}; \quad (2.2)$$

with exponential cutoff at  $E_{\nu, \text{max}} = 2$  PeV. So having an higher cutoff they represent possible candidates for the acceleration of CRs at 20 – 30 PeV which in turn can produce  $\geq 1$  PeV neutrinos.

However, observations show that the distribution of SNRs is not uniform. The parameterization that we use in our work is based on the one obtained in Green, 2015 by fitting the catalogue Green, 2014. This is the updated catalogue of known Galactic supernova remnants (mostly detected at radio wavelengths) which currently collects 294 objects. The fit of the Galactic surface density of SNRs is a power law/exponential model respect to the Galactocentric radius,  $r$ :

$$\rho_{\text{SNR}}(r) \propto \left( \frac{r}{r_\odot} \right)^{\alpha_{\text{SNR}}} \exp \left( -\beta_{\text{SNR}} \frac{r - r_\odot}{r_\odot} \right); \quad (2.3)$$

where  $r_\odot = 8.5$  kpc (i.e. a cylindrically symmetrical distribution about the Galactic Centre), and parameters:  $\alpha_{\text{SNR}} = 2.00 \pm 0.67$ ,  $\beta_{\text{SNR}} = 3.53 \pm 0.77$ . The author, however, does not make any constraint on the vertical distribution respect to the Galactic plane because of the limited number of bright SNRs.

### 2.1.2 Pulsars

As the black hole, one of the end points of the life of a massive star after it explodes in a supernova, is a neutron star. These are very compact objects, highly magnetized, and rotating that emit beams of electromagnetic radiation and relativistic particles out of their magnetic poles. From this characteristic comes the widely used denomination of "pulsar". Since neutron stars are very dense, and have regular and short rotational periods, they can produce a very precise interval between pulses that ranges from milliseconds to seconds for an individual pulsar.



FIGURE 2.7: Frame of Vela pulsar movie captured by NASA's Chandra X-ray Observatory (June-September 2010).

We are able to observe these pulses of radiation whenever the magnetic pole is visible. They have been found to emit in visible light, X-ray, and gamma ray wavelengths. A very clear picture of the Vela pulsar is captured in Fig. 2.7 which is an X-ray emission observation. We can clearly see the central neutron star and the two beams of particles and radiation along the axis.

Due to their rapidly-rotating, hugely-intense magnetic fields, pulsars are very efficient natural particle accelerators. The accelerated particles (mostly electrons and positrons) are delivered into a highly-magnetized surrounding, ideal to make them radiate high-energy gamma rays that bear the timing signature of their parent object.

The pulsars are divided into three macro-classes according to the source that fuels their electromagnetic emission. Although the three classes of objects are all neutron stars, their observable behavior and the underlying physics are very different:

1. **Rotation-powered pulsars.** In these objects the emission is powered by the rotational energy of the neutron star itself. They are usually radio pulsars. Over 99% of radio pulsars are single objects emitting in the form of relativistic particles and magnetic dipole radiation and lighting up any nearby nebula that surrounds them. Their observed periods are in the range of the order of milliseconds to seconds, and all radio pulsars are slowing down in their rotation by losing angular momentum.
2. **Accretion-powered pulsars.** They are also identified as *X-ray* pulsars. They consist of magnetized neutron stars in orbit with a normal stellar companion and thus represent a type of binary star system. In this case the energy is fueled by the matter accretion that enhances the gravitational potential energy.

Indeed, in these pulsars the mass is accreted from the stellar companion by stellar winds or accretion disks. The gas of particles is channeled by the neutron star's magnetic field on to the magnetic poles producing localized X-ray spots. While rotation-powered pulsars appear to always slow down, X-ray pulsars show a variety of spin behaviors. It is thought that X-ray pulsars are probably old rotationally-powered pulsars located in a binary system and that have lost most of their power.

3. **Magnetars.** In these objects the decay of an extremely strong magnetic field provides the electromagnetic power. Magnetars have magnetic fields of  $\sim 10^{13} - 10^{15}$  G, while the typical magnetic fields of other pulsars and neutron stars is  $\sim 10^{10} - 10^{12}$  G. The magnetic field decay powers the emission of high-energy electromagnetic radiation, particularly strong and characteristic X-rays and gamma-rays. Magnetars rotate more slowly in comparison to other neutron stars. Most magnetars rotate once every two to ten seconds. Moreover, the duration of their active life is quite short compared to the lifetime of other pulsars. They live for only 10000 years since their magnetic field decays very rapidly. Given the number of magnetars observable today, one estimate puts the number of inactive magnetars in the Milky Way around 30 million.

Nevertheless, there are several other sub-categories of pulsars that have hybrid or different characteristics (Kaspi, 2010). For instance, a pulsar with a rotational period smaller than about 40 milliseconds is called *millisecond-pulsar* (MSPs). In addition, several other types of pulsars have also been observed and classified, such as X-ray bright compact central objects (CCOs), and rotating radio transients (RRATs), see Kaspi, 2010 for a complete treatment.

Nowadays there is a large number of pulsars catalogues that collect all Galactic pulsars observed so far. Around 2300 pulsars were discovered in our Galaxy:  $\sim 1000$  of which are radio pulsars (*ATNF*); while Fermi-Lat observed 253 gamma-ray pulsars in the GeV range (*LAT-Detected Gamma-Ray Pulsars*) of energy and 345 have been identified as millisecond pulsars (*D. Lorimer's catalogue*). It was estimated however that the number of pulsars contained in our Galaxy is several orders of magnitude larger, reaching a number  $> 1 \times 10^6$  (Kaspi, 2010).

A useful approximation of the pulsars distribution in the Galaxy is given by Lorimer et al., 2006. This is obtained by fitting two catalogues of pulsars observed in the radio wavelength. The sample used is made of 1008 pulsars obtained by the two surveys called "Parkes multi-beam survey" (PMB) and the "high-latitude pulsar survey" (PH) of the region  $-140^\circ < l < -100^\circ$  and  $|b| < 60^\circ$  (Burgay et al., 2006). Both surveys were carried out using the same observing system, so it represent a reasonably homogeneous sample from which to proceed. The function, in cylindrical coordinates, is defined by the radial analytical profile:

$$\rho_{\text{Lorimer}}(r) = A \left( \frac{r}{r_\odot} \right)^B \exp \left( -C \frac{r - r_\odot}{r_\odot} \right); \quad (2.4)$$

and along the  $z$  axis as:

$$N(z) = D \exp -\frac{|z|}{E}; \quad (2.5)$$

where  $r_\odot = 8.5$  kpc (i.e. a cylindrically symmetrical distribution about the Galactic Centre). The parameters  $A, B, C, D, E$  are obtained by fitting the data about the pulsars positions contained in the sample. We will use this same functional form to

define the distribution for our model and we will rely on some of the results for the parameters values obtained in Lorimer et al., 2006.

In our work we will extensively discuss the role of Galactic pulsars in the VHE Galactic gamma-ray emission observed by present experiments (Chapter 6).

### 2.1.3 Pulsar Wind Nebulae

With the name Pulsar Wind Nebula (PWN, plural PWNe), sometimes called *plerion*, is indicated a type of nebula that can form inside the shells of supernova remnants. These nebulae were discovered in 1976 as small depressions at radio wavelengths near the centre of supernova remnants (Weiler and Panagia, 1978). They have been found to be X-ray emitters and are likely gamma-ray sources.

These nebulae are powered by pulsar winds generated by its central pulsar. As we already saw, the explosion of a supernova triggered by the collapse of a massive star produces several solar masses of stellar ejecta expanding into surrounding circumstellar and interstellar material. On a timescale of thousands of years the nebula expands, adiabatically powered by the pulsar. Then, as the shock sweeps up material, the deceleration drives a reverse shock back into the cold ejecta. The resulting forward shock compresses and heats the ambient gas. On a timescale of  $10^4$  years, the reverse shock travels back to the center of the remnant. As a consequence of the interaction with the reverse shock, the PWN starts oscillating between contraction and expansion. Energy is lost mainly via synchrotron radiation usually observed in the radio or X-ray band.

Pulsar winds are mainly composed of electrons and positrons, with little ion component. PWNe are created entirely by a confined magnetic wind produced by an energetic pulsar. At early times, the confining material is supernova ejecta, but at later times it can simply be the ISM (Slane, 2017).

The relic nebula created can assume different shapes, it can be visible as a wind bubble, shell nebula, or also as a bow-shock. New PWNe appear within the first few thousands of years of a pulsar's creation, and often look like a series of shells inside the supernova remnants. See for example the small pulsar wind nebula within the inner region of the Crab Nebula, or the nebula within the large Vela Supernova Remnant and its associated Vela Pulsar. The criteria on which PWNe can be observationally identified are several and sometimes their distinction with a SNR may not be very clear. So far around 55-60 PWNe have been registered applying different types of observations at different wavelength (spanning in radio and X-ray) (Kaspi, Roberts, and Harding, 2004).

The Crab nebula is a very well studied object at all wavelengths for this reason its intensity is often used as a unit reference (Crab nebula energy flux:  $2.4 \times 10^{-8}$  erg cm<sup>-2</sup> s<sup>-1</sup>). The Crab pulsar has a frequency  $\nu = 30.2$  Hz (spin-down period  $P = 33.1$  ms), and a characteristic magnetic field of  $B = 7.6 \times 10^{12}$  G (Kou and Tong, 2015). It emits  $\gamma$ -rays up to TeV band, which are most likely produced from inverse Compton scattering of soft photons fields inside the nebula. However, the hadronic component is not excluded since both scenarios appear to be plausible. The protons obtained from neutron decays occurring inside the nebula are trapped by the Crab Nebula magnetic field and accumulate inside it producing gamma-rays and neutrinos in collisions with the matter in the nebula. Neutrons decaying outside the Crab Nebula contribute to the Galactic cosmic rays (Bednarek and Protheroe, 1997). Vela X PWN, is an active pulsar with associated nebula, and due to its intense luminosity the hadronic scenario is very plausible and is supposed to be one of the most plausible observable neutrino sources. However, due to its position in the sky, is not

directly observable by IceCube which is located in the Southern hemisphere, while experiments such as KM3NeT could potentially detect events from Vela X PWN.

In the following we will assume the PWN distribution function in the Galaxy as the one of pulsars (Lorimer et al., 2006); the distribution of pulsars and PWNe are expected to be very similar due to their shared production process, so we rely on this reasonable assumption for our computations.

## Chapter 3

# High-Energy Neutrino and Gamma-ray detectors

The field of TeV astronomy is rapidly evolving thanks to data obtained by many recent experiments. Imaging Atmospheric Cherenkov Telescopes (IACT), such as H.E.S.S., MAGIC and VERITAS, and Air-Shower surface Arrays, such as ARGO-YBJ, Milagro and HAWC, provided a detailed description of Galactic  $\gamma$ -ray emission in the energy range 0.1 – 100 TeV. Large scale diffusion emission from different regions of the Galactic plane has been measured by H.E.S.S., ARGO-YBJ, HAWC, and Milagro while catalogues of sources have been recently produced by H.E.S.S and HAWC. In the case of the IACT and surface arrays, the Earth's atmosphere is used as detection medium, making available a collection area of many hundreds of square meters. This enables IACT instruments to detect gamma-ray photons in an energy regime inaccessible to space-based instruments.

At lower energies, in the 1 - 100 GeV range, the Large Area Telescope (LAT) on board the Fermi Gamma-ray Space Telescope observes a large number of sources. The last released catalogue collects 1556 hard sources (Ajello et al., 2017). All the LAT hard-source catalogues have been crucial in providing promising candidates for detection by IACTs, enabling the search for plausible  $\gamma$ -ray counterparts of IceCube high-energy neutrinos. The 3FHL catalogue offers an excellent opportunity to relate observations from space and those that will be possible in the near future from the ground.

At larger energies, from 60 TeV up to tens of PeV, IceCube, the largest neutrino telescope is observing astrophysical neutrinos. Neutrinos are elusive particles, having small cross section and low interaction probability. The main purpose in the construction of a telescope therefore is to possibly maximize the interaction probability by increasing the interaction volume and/or the density of the interaction medium. However, this is not the only problem to overcome. A large impact on the discernment of astrophysical signal is given by the ability to identify the background component. For high-energy neutrinos this is entirely constituted by muons and neutrinos produced by the interaction of CR in the atmosphere. In order to shield the apparatus from a large part of background they are often built under the ground at several hundreds of meters below the surface, or also deep in the sea water.

This chapter is focused on the description of all the main experimental facilities that observe the sky at TeV energies and the results of which are useful for our discussion. We briefly illustrate their apparatus. Then we show the interesting measurements reported at present days to which we will largely refer for our comparisons and our analysis of next chapters.

## 3.1 IceCube

IceCube is the world's largest Neutrino observatory. It is located in the South Pole and is the first detector of its kind: it was built in the Antarctic ice, buried under the surface. It extends for a volume of about  $1 \text{ km}^3$ , with a total mass of a Gigaton. Its construction was completed in December 2010 and it has now been operating in its full setup since 2011.

IceCube energy range of detection goes from slightly below few TeV to tens of PeV. One of the main purposes of the experiment is to observe interactions of neutrinos produced by catastrophic events such as exploding stars, gamma-ray bursts and other phenomena involving neutron stars and black holes. However, the detector also includes a surface array called "IceTop" and a densely instrumented inner zone called "Deep Core": two equipments that make the facility suitable for other purposes such as the study of cosmic rays, neutrino oscillations, dark matter and search for sterile neutrino. IceCube is a Cherenkov detector provided of a multitude of digital optical modules called "DOMs" located on a regular grid that covers all its volume. Each DOM is composed by a Photo-multiplier Tube (PMT) and a suite of electronic boards assemblies. The main detection process is based on the observation of Cherenkov light emitted by electrically-charged secondary particles produced in the interactions with nucleons of the ice atoms. Travelling faster than the speed of light in ice they produce a Cherenkov cone of light that is collected and registered by the DOMs.

The in-ice elements of IceCube are 86 strings, each 2540 meters long, inserted vertically into 86 boreholes which are set at 125 m apart from one another, covering an hexagonal grid on the surface. Each string has 60 DOMs attached, with a total of 5160 modules. The DOMs are situated from 1450 meters to 2450 meters in depth and they are set to a vertical distance of 17 meters from each other. The whole scheme of the IceCube composition is shown in Fig. 3.1.

The Deep Core sub-detector is the central volume composed by six strings deployed with a different and denser configuration. This zone can observe interactions below the energy of 100 GeV and is designated to the study of neutrino oscillation phenomena with the possibility to determine the mass hierarchy.

### 3.1.1 Event topology

Events seen by IceCube are classified into three topologies according to their spatial spreading in the detector: *showers*, *tracks*, and *double-bangs*.

- **Showers**

At the TeV energies the primary neutrino interaction channel is deep-inelastic scattering with nuclei in the detector material. Electrons (or positrons) and hadrons that propagate in a medium lose energy mainly through electro-photonic and hadronic cascades respectively. In general, cascades are produced in both neutral (NC) and charged-current (CC) interactions, since in all these cases a shower of hadrons is created at the neutrino interaction vertex. Moreover, in charged-current interactions, this shower is accompanied by an outgoing charged lepton. When the lepton is an electron (meaning in CC interactions of electronic neutrinos), may also lose energy rapidly and itself trigger another overlaid shower very close to the first one (Aartsen et al., 2014). Events that show a cascade-shape predominance are simply identified as "showers". Due

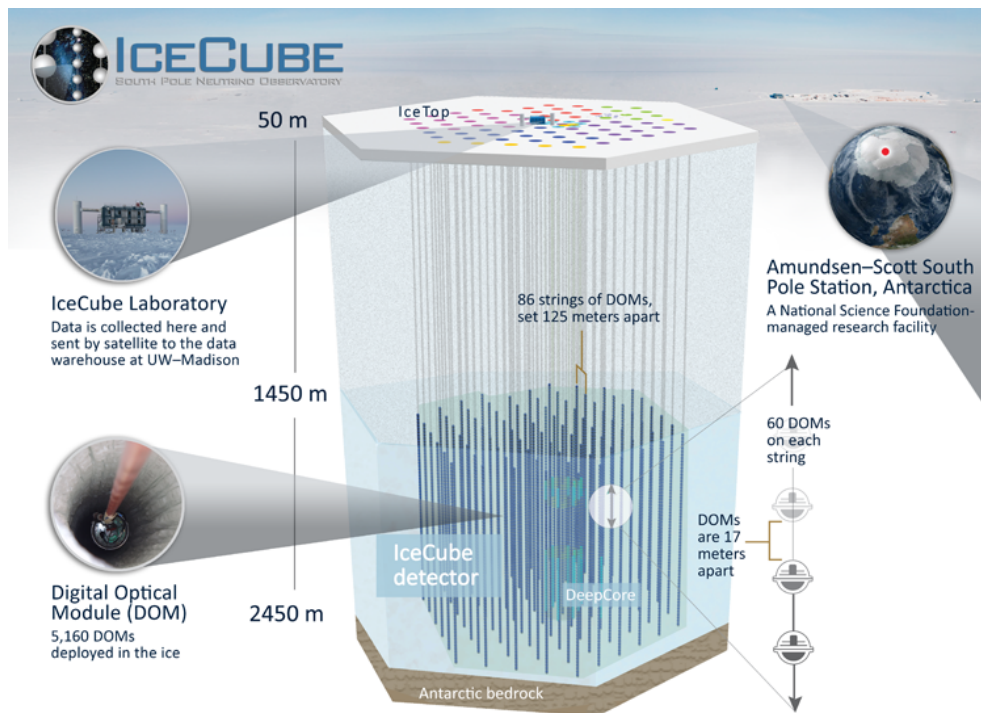


FIGURE 3.1: IceCube in-ice structure. Credit: *IceCube website*.

to the typically broad cascade spreading this kind of event has a nearly spherical geometry.

- **Tracks**

When an event shows a visible muon track is identified as a "track" event. Tracks are the signatures for muonic neutrinos and muonic antineutrinos interactions. In particular, a muon (of whatever charge) generated in neutrino (or antineutrino) CC interaction leaves a track in the detector since it loses energy mainly by ionization and does not produce an electromagnetic cascade. Despite their instability, at the IceCube energies of measurement, muon leptons are able to travel few kilometers before decaying. Muons produced by initial neutrinos with PeV energies have indeed a range in ice of  $\sim 10$  kilometers which is 10 times larger than the linear dimension of the IceCube detector. If the interaction vertex is contained within the volume, in these kind of events is also visible a shower-like component due to the hadronic shower which appears along with the track-like one (see event examples in Fig. 3.2).

- **Double-Bang**

Tauonic neutrinos interactions produce showers as well, but, when a  $\tau$ -lepton is produced in CC interaction, it has the possibility of decaying in both the lighter leptons  $e$  and  $\mu$ , or in the semi-leptonic branches. At energies above 50 TeV, the range in ice of the  $\tau$  is order of 10 m, hence a  $\tau$  produced inside the active volume has an high probability to also decay inside it. The tauonic interaction would hence be characterized by the so called "double-bang" topology: a pattern in which the two different vertices (the one of the first interaction and the other of the decay) should be observable and is therefore discernable from the other two topologies. Note that there is also another condition on the observability of this kind of event, i.e. that the distance traveled by the  $\tau$

before decaying is larger than the distance between DOMs. If this is the case the modules are able to identify and separate the two cascade starting points, otherwise it would be registered as a single shower event.

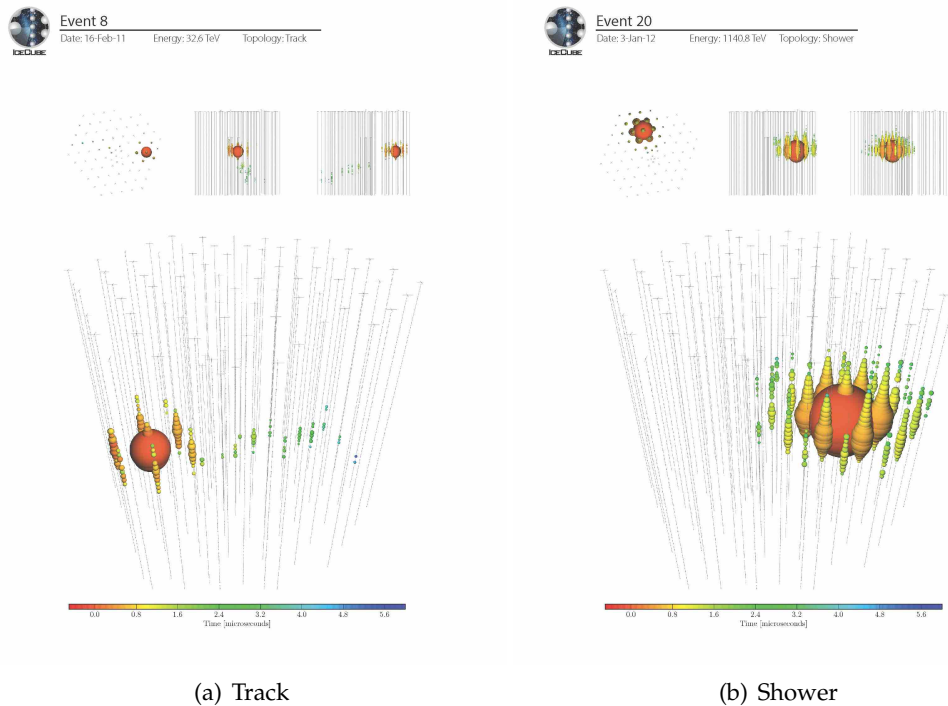


FIGURE 3.2: Two real events observed in the first period of data taking. Figures taken from Aartsen et al., 2013.

Fig. 3.2 shows two events registered in the first three years of data taking: track-like (left), shower-like (right). These two events are well distinguishable, however, since a track which starts inside the volume is always accompanied by a shower, some shapes might be ambiguous.

For an observed event has to be reconstructed both the deposited energy and the arrival direction in addition to its topology. The track arrival direction is much more well-defined than the direction of the shower, so the experiment angular resolution is different according to the topology considered. IceCube can reconstruct arrival directions with an uncertainty of  $1^\circ$  degree for tracks and  $15^\circ$  for showers. The energy deposited inside of the detector is also different depending on the process. Deposited energy is proportional to the integrated path length that each particle covers when is over the Cherenkov threshold. Electronic neutrino CC processes that occur inside the detector produce two showers (electrophotonic and hadronic) in the volume, depositing the whole initial energy inside it. This is very advantageous since, assuming the nucleus in the medium at rest, we can directly know the initial neutrino energy, and in this case the only limitation is given by the detector energy resolution. The detector resolution for starting  $\nu_e$  events at 100 TeV is 8%. This is not the case of CC muonic interactions. The total energy is divided in the shower and the track. The tracks gives us only partial information about the energy of muons, since they escape the active volume of detection. Neutral current interactions of every flavor, instead, produce neutrinos that get about  $\frac{3}{4}$  of the initial energy and that are not detectable. So this energy reconstruction results to be more complicated. To

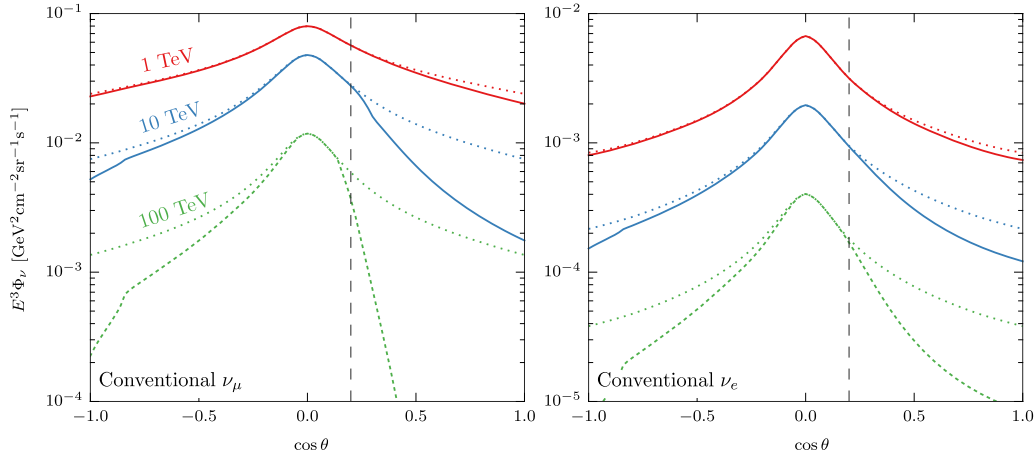


FIGURE 3.3: The observable fluxes are suppressed in the Northern sky ( $\cos \theta \leq 0.2$ , to the left of the vertical dashed line) by absorption in the Earth (at  $\cos \theta < -0.8$  we see a major absorption in correspondence of the much denser core), and in the Southern sky ( $\cos \theta > 0.2$ , to the right of the line) by self-veto by accompanying muons. Figure taken from Aartsen et al., 2015b.

give some quantitative perspective, in general it has been calculated that neutral currents deposit 23% of the total energy, whereas charged current events deposit 97% (Aartsen et al., 2014).

In addition, the reason why for CC interactions the energy observed is lower than 100% is that, while electromagnetic showers deposit all their energy in the detector (with the condition that the vertex is well contained in the volume), hadronic showers have a lower light efficiency, namely 89% at 100 TeV. This is because in a hadronic production there is a percentage of neutral population (mainly  $\pi_0$ ) that do not produce Cherenkov effect.

### 3.1.2 Background

The background in IceCube rises entirely from atmospheric activity and it's composed by atmospheric neutrinos and muons. Muons generated in atmosphere above the Northern hemisphere interact inside the Earth and therefore they are not able to reach the IceCube detector. The atmospheric neutrino flux produced in the Northern hemisphere, yet suffering of absorption effects, due to the lower cross section has a lower probability to interact and therefore is more likely to reach the opposite side of the planet surface. For these reasons, the majority of muon background is produced in the sky above Antarctica (Southern sky), hence muons direction is mainly vertically and from the top down oriented. Otherwise, atmospheric neutrinos can reach from all directions since they can also be generated in the atmosphere above the Northern Hemisphere, travel across the Earth and be detected in the IceCube volume.

The procedure for elimination of muonic neutrino background applied in the Southern hemisphere is the so called "self-veto". It consists in discarding the muon neutrino produced along with the atmospheric muon by vetoing the muon itself. In other words, when a neutrino event is seen along with an incoming muon, the event is discarded since it has a high probability to have been produced in the same decay that produced the muon, hence it is likely for it to have atmospheric origin. Note that

this exact procedure can also be applied to the electronic neutrino that is produced in the same muonic decay.

Fig. 3.3 shows the suppression of the atmospheric  $\nu_\mu$  e  $\nu_e$ , which is the combination of the Earth shielding effect and the self-veto procedure on the muon neutrinos. They are functions of the zenith angle: negative values of  $\cos \theta$  are in the Northern Hemisphere and positive in the Southern. The fluxes are computed for different energy values: 1, 10, 100 TeV. The solid lines show the passing fluxes after the suppression effect and veto application, and the dotted lines show the original not absorbed and not-vetoed fluxes. For what we just said, in the North the suppression is given by the absorption of the Earth, whereas the veto mechanism take place in the South.

For what concerns the main processes that produce the atmospheric background, neutrinos and muons are produced in the hadronic interactions of cosmic rays (CR) with nuclei which are present in the atmosphere and that produce  $\pi$ -mesons. So the background is mainly generated from  $\pi^+$  and  $\pi^-$  decays. In addition, there is also a minor presence of  $K$  mesons, they follow the same decays of pions but in addition there's a further channel for  $K^+$  and  $K^-$  that contributes to the total neutrino flux:

$$K^+ \rightarrow \pi^0 + e^+ + \nu_e; \quad (3.1)$$

$$K^- \rightarrow \pi^0 + e^- + \bar{\nu}_e. \quad (3.2)$$

This channel represents the 5% of the  $K$  decays and slightly varies the total flavor ratio which will not be exactly  $(\frac{1}{3} : \frac{2}{3} : 0)$  but will have a slightly larger presence of electronic flavor.

At higher energies we also have a component given by the decays of the heavier charm-mesons such as  $D^+$ ,  $D^-$ ,  $D^0$ , etc., this is called the 'prompt signal'. The heavy mesons decays contribute to the whole flavor fraction with  $\nu_e$  and  $\nu_\mu$  in equal parts:  $(\frac{1}{2} : \frac{1}{2} : 0)$ . At this energy, atmospheric neutrinos do not oscillate because the oscillation wavelength is much larger than the distance traveled before reaching the detector. Hence, it is notable to observe that in case a tau event is registered, this has to have extraterrestrial origins and do not belong to the atmospheric background signal.

### 3.1.3 HESE dataset

In the High-Energy Starting Events (HESE) sample are collected all events with the interaction point well contained inside the volume in order to suppress the muon background. All the events with tracks originated outside the volume are discarded. The negative outcome of this restriction, is that a great part of the total event yield has to be excluded because we are limiting the active volume only to the IceCube volume. However, the utility is that the energy threshold of observation can be lowered, because low-energy non-atmospheric tracks cannot risk being confused with atmospheric ones, permitting to collect a larger low-energy population. Secondly it permits to observe the Southern sky which is where the Galactic centre is and is therefore a region of high interest.

For this purpose IceCube is equipped with a veto region. Fig.3.4 shows the vertical and horizontal sections of the IceCube volume where the shaded area represents the portion that acts as veto. In the left figure we can note an opaque zone which is 80 meters thick, situated in the middle of the volume. This region is composed by impure ice contaminated by dust, and therefore it cannot be used for detection. The selection process requires that an event has fewer than three of its first 250 photoelectrons detected in the veto and in addition it requires to produce at least 6000

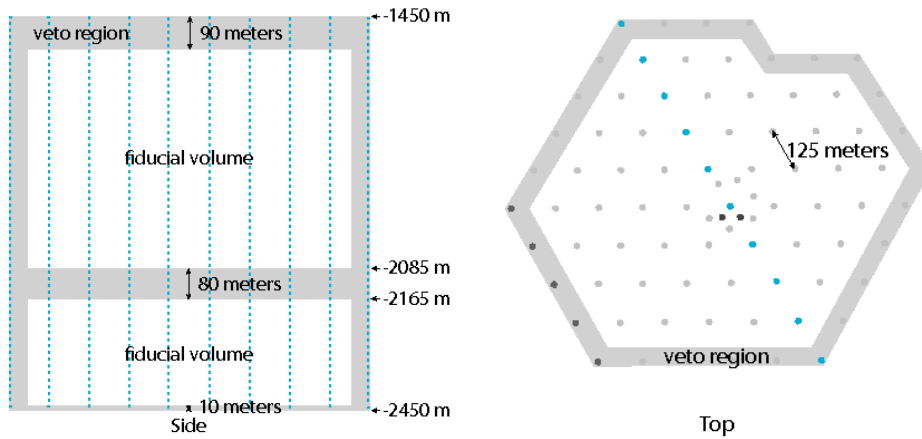


FIGURE 3.4: IceCube lateral section (left) and horizontal section (right). Figure taken from Aartsen et al., 2013. The gray area is the veto region. In the left panel the shaded 80 meters area situated in the middle represents the impure layer that cannot be used for detection.

photoelectrons overall (corresponding to about 30 TeV). This second condition is imposed in order to assure that the statistical fluctuations on the total light yield is low enough for entering muons to produce enough light in the veto volume. This allows to have a veto effect for neutrinos too ("self-veto"). This process successfully eliminates about 99.999% of the atmospheric muons and about 70% of atmospheric neutrinos generated along with their parent muons in the Southern Hemisphere, but since the efficiency of the veto varies with the energy this is valid for 100 TeV, however it may not be as efficient at different energies. Furthermore this selection allows IceCube to have approximately equal sensitivity to each flavor, to each arrival direction and to each event topology.

As we can see from Figure 3.3, both the self-veto process and the absorption effect are more efficient the higher the energy, so at our energies of interest we have the best suppression.

In the 7.5 years of published data (Abbasi et al., 2020b), IceCube collected 102 HESE events. These are divided into: 27 track events generated in  $\nu_\mu$ -nucleon charged-current interactions; 71 shower events (either electromagnetic or hadronic) generated in both  $\nu_e$  and  $\nu_\tau$  charged-current as well as neutral-current interactions of any flavor; and 4 double bangs candidates. In particular, of these events, 60 have deposited energies above 60 TeV, among which there are 2 double cascades. Of these, one has a high probability of originating from a  $\nu_\tau$  interaction (Abbasi et al., 2020a), while for the other event, the tauonic origin is simply favored with respect to a  $\nu_e$  or  $\nu_\mu$  origin.

The 7.5-year HESE events constitute  $\sim 5\sigma$  excess over the expected atmospheric background thus clearly pointing toward an extraterrestrial origin. However, contributions to the sample from CR showers produced in the Earth's atmosphere are a small but not negligible. 1.5% atmospheric muons and 16% atmospheric neutrinos are estimated above 60 TeV. Assuming a flux with full flavour mixing and equal amount of neutrinos and antineutrinos, the astrophysical neutrino spectrum is compatible with an unbroken power law. The best fit values for the all flavor HESE flux

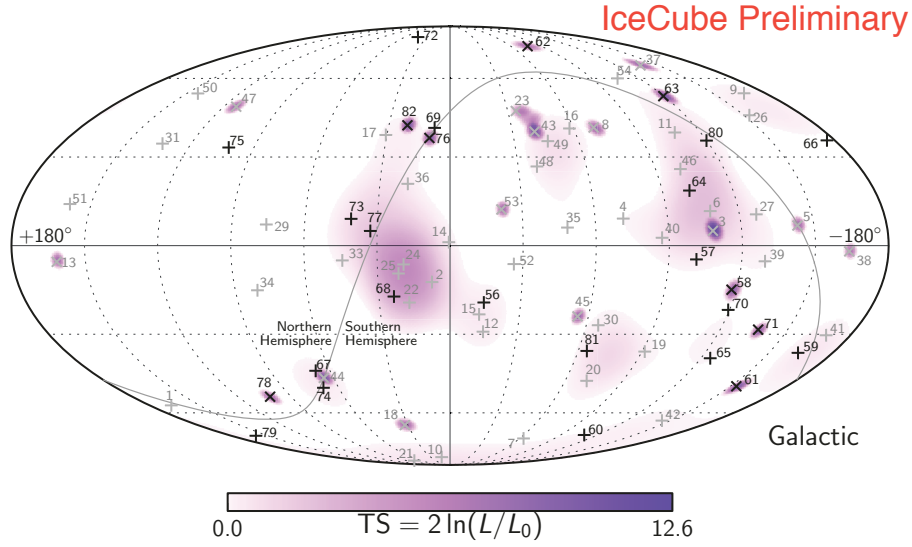


FIGURE 3.5: Correlation map of 6-years HESE events. Figure taken from Collaboration, 2017. Arrival directions of the events in galactic coordinates. Shower-like events are marked with a + and those containing tracks with a ×. Colors show the test statistics (TS) for the point-source clustering test at each location.

at 100 TeV ( $\Phi_0$ ), and the spectral index ( $\gamma$ ) are:

$$\Phi_0 = (6.37^{+0.49}_{-0.54}) \times 10^{-18} \text{ GeV}^{-1} \text{ s}^{-1} \text{ cm}^{-2} \text{ sr}^{-1}, \quad \gamma = 2.87^{+0.20}_{-0.19}.$$

The last source correlation analysis is referred to the 6-years analysis (with 82 events) (Collaboration, 2017), where no significant clustering was found (Fig. 3.5).

### 3.1.4 Through-going muons

The Earth shields the atmospheric particles coming from the Northern Hemisphere and the absorbing power of the Earth has major efficiency at higher energies. Since it extends the active volume giving the possibility to collect a higher statistic it is advantageous to consider incoming signals of events arisen externally (mainly from the bottom) of interactions between neutrinos and the Earth. These events are generated by upward going muons induced by charged current (CC) interaction of muonic neutrinos crossing the Earth. To be detected, a neutrino must produce a muon with sufficient range to reach the detector. It is referred to this sample with the name of “through-going muons”.

The 8-year through-going muons data sample contains about 350.000 neutrino events and, as estimated by the best fit above 10 TeV, almost 1000 of them are extraterrestrial neutrinos (Collaboration, 2017). It constitutes  $6.7\sigma$  significance over the atmospheric-only hypothesis. When modeled as an isotropic power-law flux normalized at 100 TeV, this yields the bestfit values of:

$$\Phi_{0,\mu} = (1.01^{+0.26}_{-0.23}) \times 10^{-18} \text{ GeV}^{-1} \text{ s}^{-1} \text{ cm}^{-2} \text{ sr}^{-1}, \quad \gamma = 2.19 \pm 0.1.$$

No obvious correlation with astrophysical sources has been found (Fig. 3.6). The spectrum is harder than for starting-events, and the spectral discrepancy between the two data-sets previously observed was confirmed by the last data release. Assuming an unbroken power-law fit, the tension between the through-going muons

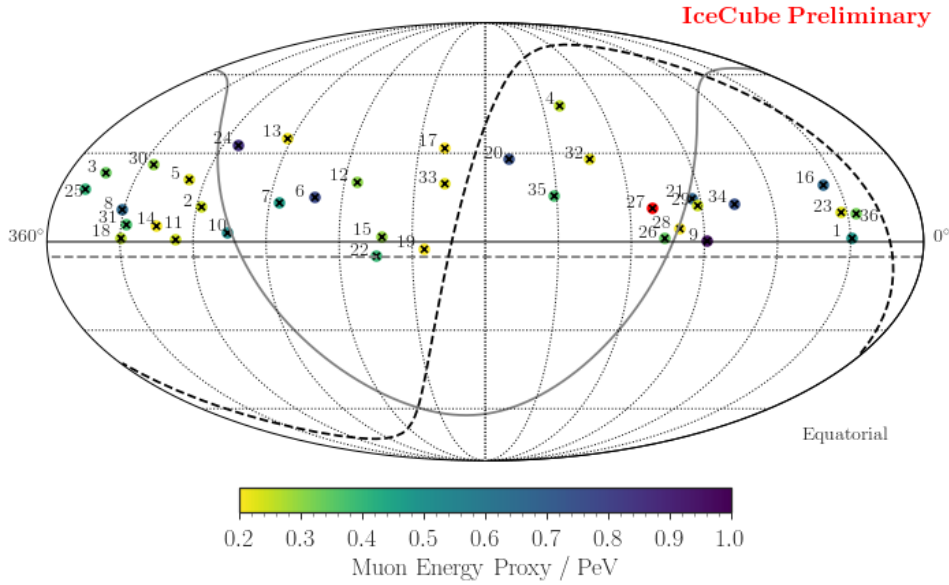


FIGURE 3.6: Reconstructed arrival directions of observed events with estimated muon energies above 200 TeV. The color indicates the energy. The solid gray line indicates the galactic plane and the dashed black line the supergalactic plane. Figure taken from Collaboration, 2017.

data and the global HESE IceCube signal fit (that takes into account all atmospheric fluxes as well) is confirmed with a  $3\sigma$  confidence level. This suggests a possible existence of a spectral feature for the astrophysical flux. Currently, this is still a matter of study and will be surely addressed in the future updated publications.

## 3.2 ANTARES

The largest underwater neutrino telescope is the ANTARES detector which is located 40 km off the Southern coast of France in the Mediterranean Sea. It consists of a three-dimensional array of PMTs. Like IceCube, also the ANTARES neutrino detection is based on the observation of Cherenkov light induced in the medium by relativistic charged particles. The position, time, and collected charge of the signals detected by the PMTs are used to infer the direction and energy of the incident neutrino.

Being built in the Mediterranean sea, ANTARES has good exposure to the Southern sky. This, its effective area, and good angular resolution has allowed the detector to produce the best limits on neutrino emission from point-like objects at low declinations (Adrián-Martínez et al., 2014). The 90% confidence level upper limits on the muon neutrino flux normalization vary between  $(3.5 - 5.1) \times 10^{-8} \text{ GeV cm}^{-2}\text{s}^{-1}$ , depending on the location of the source.

A search for neutrinos from the central region of the Galactic Plane is presented in Adrian-Martinez et al., 2016. No excess of events has been observed, and limits on the contribution from this possible source to the astrophysical neutrino signal observed by IceCube have been set as a function of spectral index. For a neutrino flux  $\propto E^{-2.5}$  is excluded at 90% c.l. that 3 or more events from the 3 years IceCube HESE sample are originating from the central region of the Galactic plane.

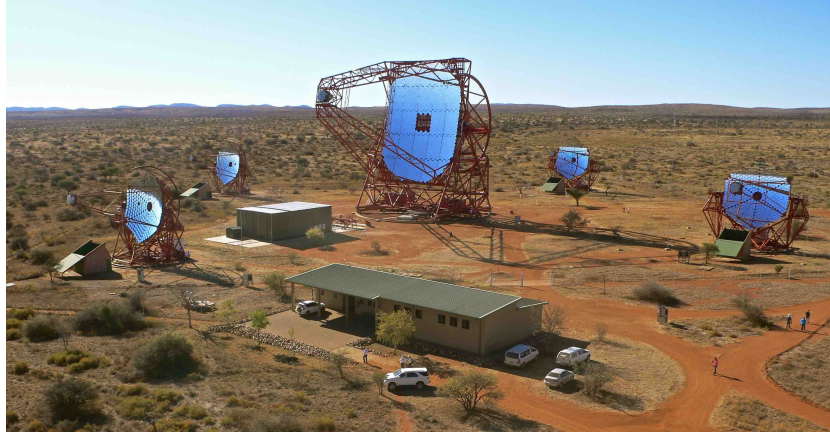


FIGURE 3.7: H.E.S.S. observatory site in Namibia. Credit: Wikipedia (*H.E.S.S. gamma-ray experiment five telescope array*).

### 3.3 H.E.S.S.

The High Energy Spectroscopic System (H.E.S.S.) observatory is located at an altitude of 1800 m above sea level in the Khomas highland of Namibia. It is composed of an array of five imaging atmospheric Cherenkov telescopes (IACTs). It detects Cherenkov light emitted by charged particles in electromagnetic extensive air showers that occur in the atmosphere. The showers are initiated when a primary photon of sufficient energy enters Earth's atmosphere.

The array consists of four small telescopes under 12 m in diameter arranged in a square built apart from each other at 120 m. They were activated in the first phase of the experiment (H.E.S.S. Phase I). In 2012, a fifth much larger telescope with a 28 m mirror was constructed in the centre of the array to launch the second phase of the experiment (H.E.S.S. Phase II, see Fig. 3.7). All telescopes are built with tessellated mirrors that cover a total area of 107 m<sup>2</sup>, and have cameras consisting of 960 photo-multipliers. The most complete survey, which is the one that we are studying in this work, is obtained only using the four telescopes.

The total field of view covered is of 5° and they are therefore well suited for sky surveys. The energy threshold of the four-telescope array is roughly 200 GeV at zenith and increases with increasing zenith angle. The reconstruction of the arrival direction and energy of the primary photon can be made with respective accuracy of  $\sim 0.08^\circ$  and  $\sim 15\%$ .

#### 3.3.1 H.E.S.S. Galactic Plane Survey and diffuse measurement

The H.E.S.S. Galactic plane survey (HGPS), at present represents the deepest and most comprehensive survey of the inner Milky Way Galaxy undertaken in very high-energy  $\gamma$ -rays. For this reason it is of high interest for our research. The range of energies covered spans from 100 GeV to 100 TeV. The HGPS data set was taken in the period from January 2004 to January 2013. H.E.S.S. acquired this data-set by pointing the IACT array to a given position in the sky for a nominal duration of 28 min (referred to as an observation run). The H.E.S.S. Galactic Plane Survey (HGPS) catalogue includes 78 VHE sources observed in the longitude range  $-110^\circ \leq l \leq 60^\circ$  and for latitudes  $|b| < 3^\circ$ , measured with an angular resolution of  $0.08^\circ$  and a sensitivity for point-like objects  $\simeq 1.5\% \Phi_{\text{CRAB}}$  (with  $\Phi_{\text{CRAB}} = 2.26 \times 10^{-11} \text{ cm}^{-2} \text{ s}^{-1}$  the flux of the Crab Nebula) (Abdalla et al., 2018a). The general procedure followed

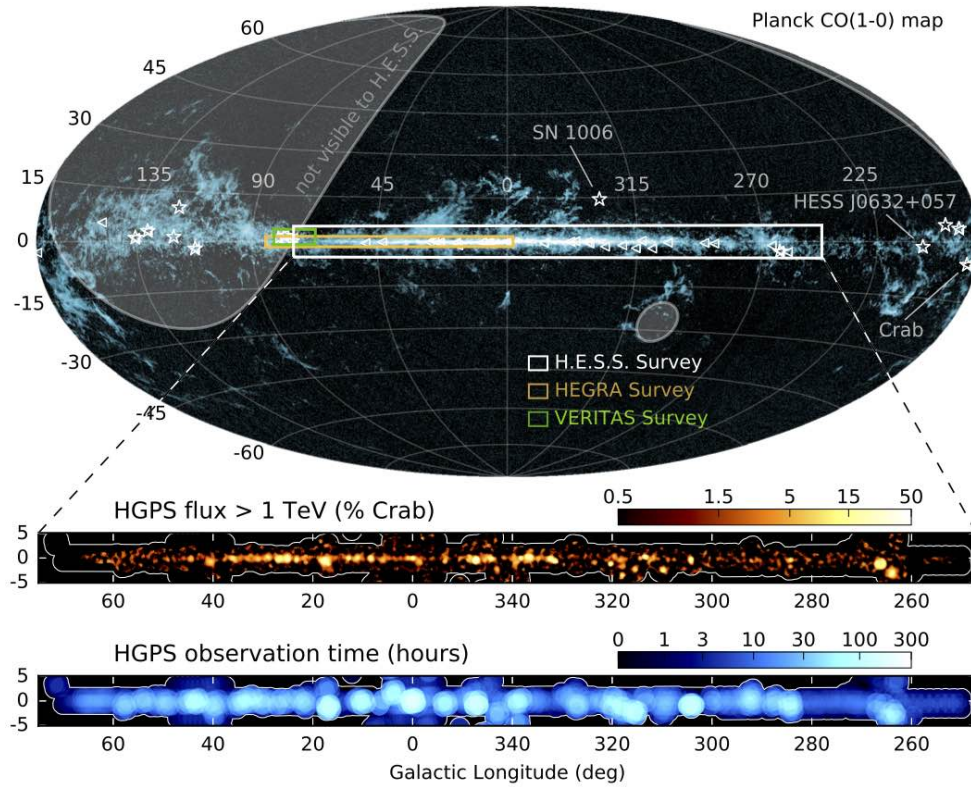


FIGURE 3.8: Illustration of HGPS region superimposed on an all-sky image of Planck CO(1-0) data ((Ptuskin and Zirakashvili, 2005)) in Galactic coordinates. Figure taken from Abdalla et al., 2018a. See Abdalla et al., 2018a for all details.

for individuating the sources is by subtracting the background in order to extract the gamma-ray event candidates. This is performed by using the adaptive ring method in which this subtraction is performed within circular regions of variable correlation radii ( $R_c$ ).

The integral flux above 1 TeV of each source is obtained from the morphology fit of flux maps, assuming a power-law spectrum with index 2.3. Tests were performed to determine the impact of this latter assumption and showed that, on average, flux variations are less than 5% if the assumed spectral index is varied by  $\pm 0.2$ . The values in the released flux maps should be interpreted as the flux of a potential source, assuming a spectrum, that is centered on a given pixel position in the map and fully enclosed within  $R_c$ . Figure 3.8 shows the flux map computed with  $R_c = 0.4^\circ$ .

The sensitivity of the H.E.S.S. detector is an issue widely examined by the collaboration and which is extensively relevant for our studies. The first interesting description is shown in Fig. 3.9 where the detectable HGPS source integral fluxes ( $E > 1$  TeV) is compared with the sizes dimension. Here is shown the approximate flux sensitivity limit of the HGPS as a function of source size. One can see that the sensitivity worsens as the source size increases. In other words in order to detect extended sources they have to produce large fluxes, while for point-like sources the flux threshold of detection can be lowered. The collaboration therefore concludes that the HGPS can be considered complete down to  $\sim 10\%$  of the Crab flux for sources with an extension  $< 0.7^\circ$ , while for smaller sources ( $< 0.1^\circ$ ), the HGPS achieves completeness at a few % of the Crab flux.

The source size is one of the major effects that influence the HGPS sensitivity but

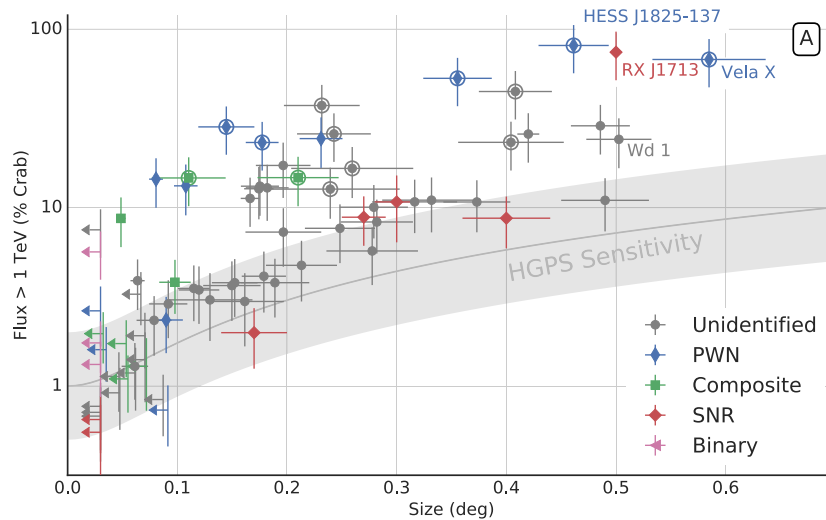


FIGURE 3.9: Integral source flux ( $E > 1$  TeV) vs. source size scatter plot with colors representing the different classes of firmly identified sources. Figure taken from Abdalla et al., 2018a.

is not the only one. Other effects that reduce the effective sensitivity or completeness limit of HGPS are the detection threshold, the large-scale emission model, and source confusion. In Fig. 3.10 is shown how the sensitivity of the H.E.S.S. observatory changes accordingly to distance and luminosity for point-like sources. Under the assumption of point-sources the profile appears non regular and this is the reason why it is difficult to define a simple valid description of the sensitivity profile even without including a variable source size. The H.E.S.S. sensitivity horizon is plotted for two fixed values of luminosity:  $10^{34} \text{ erg s}^{-1}$  (blue line), and  $10^{33} \text{ erg s}^{-1}$  (brown line). In particular we see that assuming a point-like source with  $10^{33} \text{ erg s}^{-1}$ , H.E.S.S. is able to resolve it only if it is located inside the horizon otherwise it will remain unresolved and its flux will be registered as a diffuse emission. We see that the average radius of detection is  $\sim 2$  kpc for point sources of luminosity  $10^{33} \text{ erg s}^{-1}$ , and  $\sim 7.3$  kpc for  $10^{34} \text{ erg s}^{-1}$ . We can therefore expect that only a small fraction of the Galaxy is resolved and thus to have a relevant contribution of unresolved to the total diffuse signal.

The H.E.S.S. collaboration also performs an investigation of diffuse emission related to those regions where no  $\gamma$ -ray sources are detected (Abramowski et al., 2014). The results presented are in the range of Galactic longitude and latitude:  $-75^\circ < l < 60^\circ$  and  $-2^\circ < b < 2^\circ$ , where the exposure of the HGPS is largest. The overall average of the energy threshold of the analysis is roughly 250 GeV. Standard analysis cuts reduce the background and guarantee good quality of the event reconstruction. The diffuse estimation is obtained by two different techniques of subtraction. The collaboration performs a first background subtraction on the total signal in order to remove systematic experimental effects. This is developed by subtracting to the total signal the background obtained from the same field of view, in regions of no known  $\gamma$ -ray sources. The region defined as region of background is the one with latitudes comprised in  $-1.2^\circ < b < -2^\circ$  and  $1.2^\circ < b < 2^\circ$ . The total emission from the Galactic plane is therefore obtained as the excess with respect to the average signal at latitudes exceeding  $|b| = 1.2^\circ$  (Abramowski et al., 2014). The diffuse signal is then obtained by subtracting single sources emission, these are represented by the black areas in the upper plot of Fig. 3.11. White regions in the upper panel show the diffuse analysis regions (DAR) obtained after the subtractions,

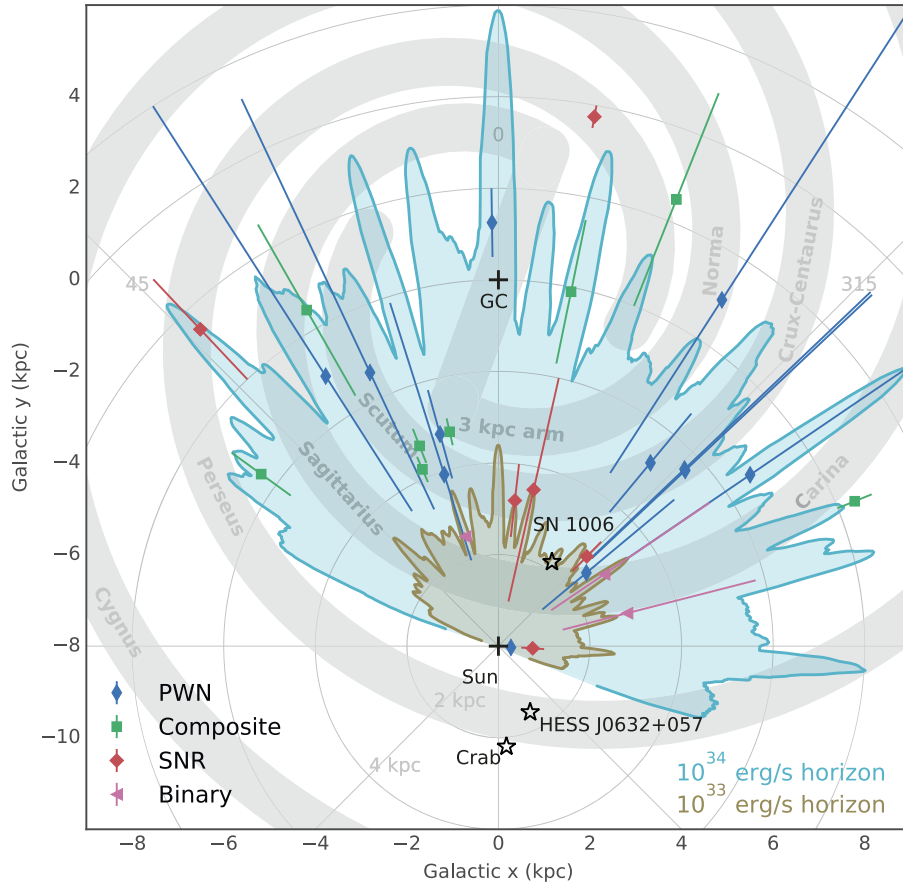


FIGURE 3.10: Illustration of the location of identified H.E.S.S. sources in the Galaxy with respect to HGPS completeness (sensitivity limits). The spiral arms are the gray bars. The HGPS horizons for source luminosities of  $10^{33}$  and  $10^{34}$  erg/s are depicted by light blue and light brown lines (and shaded regions therein), respectively. Figure taken from Abdalla et al., 2018a.

while the horizontal dashed lines mark the region  $-1.2^\circ < b < 1.2^\circ$ . The middle panel represents the longitudinal profile of the Galactic Plane over a latitude range of  $-2^\circ < b < 2^\circ$ . The black crosses represent the differential flux data at 1 TeV including sources. While the red solid line is the minimal 1 TeV  $\gamma$ -ray emission from hadronic interactions, estimated using  $H$  and  $H_2$  data and a solar-like cosmic-ray spectrum. In the bottom panel is finally reported only the diffuse emission given by the black crosses. The rest of the plot is the same as the middle one. The red dashed line includes a nuclear enhancement factor of 2.1 that takes into account nucleon-nucleon interactions (besides pp). The first notable characteristic of these data points is that their distribution is strongly influenced by the shape of the black regions of the upper plot, meaning by the sources positions and extensions. This is in fact rather common at these ultra high energies, where the distinction between source and diffuse contribution becomes indeed more blurry. Moreover, the method used by the collaboration for overall background subtraction appears to be rather insensitive to large-scale emission with modest variation in latitudinal intensity because such signals are subtracted along with the background. This is, for instance, the case of the inverse Compton emission, which is estimated to be subtracted at 95% through this procedure.

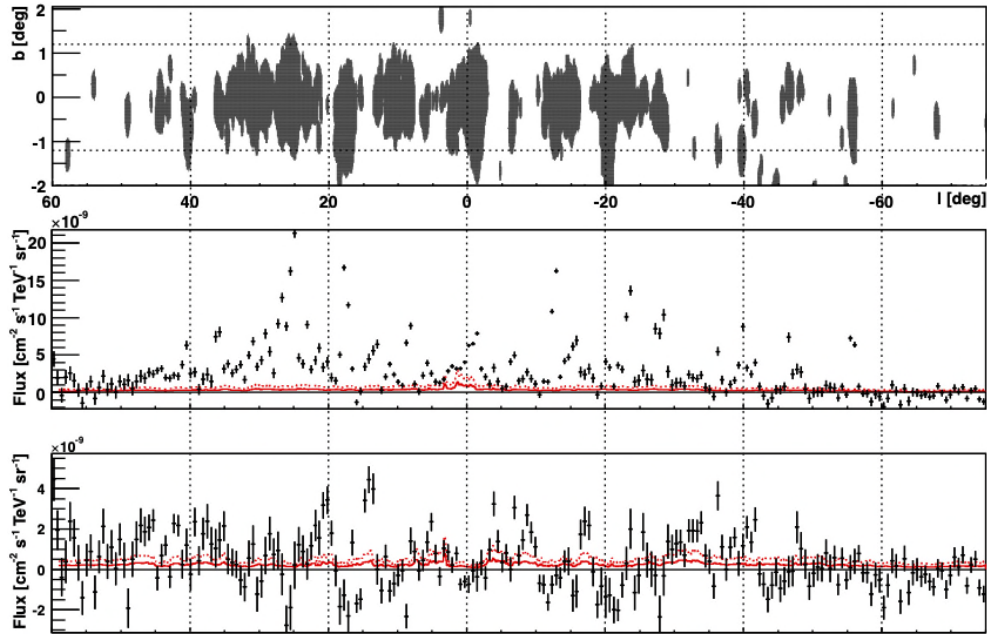


FIGURE 3.11: Upper plot: the white regions depict the diffuse analysis region (DAR). Black are regions of significant  $\gamma$ -ray emission. The horizontal dashed lines mark the latitudes:  $b = -1.2^\circ$  and  $b = 1.2^\circ$ . Middle plot: black crosses indicate the longitudinal profile of the differential flux data at 1 TeV in  $|b| < 2^\circ$  including known sources. Red solid line represent the minimal hadronic  $\gamma$ -ray emission expected in the same region. Bottom panel: same as middle panel but without the source contribution. Figure taken from Abramowski et al., 2014.

### 3.4 HAWC

The High-Altitude Water Cherenkov (HAWC) detector is located in the saddle point between two peaks at around 5000 m of altitude, in the Mexican national park Pico de Orizaba. It was completed in March 2015. The HAWC experiment is built upon the previous gamma-ray detector Milagro which we will discuss in Sec. 3.17. Like Milagro, HAWC is a Cherenkov observatory composed of water tanks used to reconstruct air showers produced by gamma-rays in the atmosphere. The detector contains 300 tanks, with a total of 1200 photomultipliers (PMTs): 3 peripheral and 1 central PMT tube per tank. To reduce the noise, each tank is optically insulated and so is each PMTs between tanks. This is a relevant consideration at high altitudes, where the flux of low-energy cosmic rays is large. Since the shape of their electromagnetic showers have very different footprints, cosmic rays can be discriminated from gamma rays by observing the pattern of triggered PMTs in the detector. The experiment has the ability to reject  $> 99\%$  of cosmic-ray showers at energies above roughly 3 TeV. The removal of cosmic-ray events is a substantial improvement over Milagro, where 10% of the cosmic ray showers survive in the data even for cuts at 50 TeV. The HAWC observatory has a flux sensitivity of  $\sim 5 - 10\%$  of the flux of the Crab Nebula. The sensitivity, however, changes along with the source declination.

Being HAWC a surface array, its observation is based on detection of air shower particles that reach ground level, allowing it to operate continuously and observe an instantaneous field of view (FoV) of  $> 1.5$  sr. As we will see, other two surface arrays telescopes ARGO-YBJ and Milagro have previously conducted the same VHE survey as HAWC. However the sensitivity of HAWC, thanks to a combination of



FIGURE 3.12: HAWC observatory in the national park Pico de Orizaba, Mexico (*The High-Altitude Water Cherenkov Gamma-Ray Observatory*).

large size, high elevation, and unique background rejection capability, is better by more than an order of magnitude.

### 3.4.1 Catalogue

The 2HWC catalogue collects the results of the first source search realized with the complete HAWC detector starting in 2015 and after 507 days of data-taking (Abeysekara et al., 2017b). The peak sensitivity of this survey lies around 10 TeV, depending on the source spectrum. A total of 39 sources were detected, 16 of which are found more than one degree away from any previously reported TeV source. Seven of the detected sources may be associated with pulsar wind nebulae, two with supernova remnants, two with blazars, and the remaining 23 have no firm identification yet. The source list includes the position measurement, spectrum measurement, and respective uncertainties. The HAWC experiment reports the longitudinal gamma-ray profile in the angular region  $0^\circ < l < 180^\circ$  and  $|b| < 2^\circ$ , for a photon median energy  $E_\gamma = 7$  TeV (Zhou, Rho, and Vianello, 2018).

Analyzing the main processes performed by the collaboration in the development of the catalogue, the first step after the measurements collection, is the event selection and reconstruction. In this phase is operated the hadron/photon separation in order to subtract the cosmic ray background. The event maps are simply represented by histograms of the arrival direction of the reconstructed events, in the equatorial coordinate system. The observational sky contains regions that produce strong gamma-ray fluxes. As they would bias the background estimate, they are excluded from the computation. These regions cover the Crab Nebula, the two Markarians, the Geminga region and, a region of  $\pm 3^\circ$  around the inner Galactic Plane.

The collaboration constructs event source maps according to a test statistic computation. The final map is computed from the ratio of the likelihood that a source is present and the null hypotheses that the observed event population is attributable to background alone. After the first step of defining the source location and size, the source energy-spectrum is fitted using a simple power law dependence with fixed index. The reference energy considered by the collaboration is 7 TeV.

In Fig.3.13 are represented the map of gamma-ray sources found in an extensive sky region of the observational window comprised in  $44^\circ < l < 4^\circ$  and  $|b| < 6^\circ$ . Each source is represented by a white small circle with labels located below. The different colours represent contour lines of the TS map values. The TS values correspond to point sources hypothesis with a spectral index of  $-2.7$ . The green contour lines indicate values of different values of  $\sqrt{TS}$ . The source listed in TeVCat are represented with black squares and labels located above.

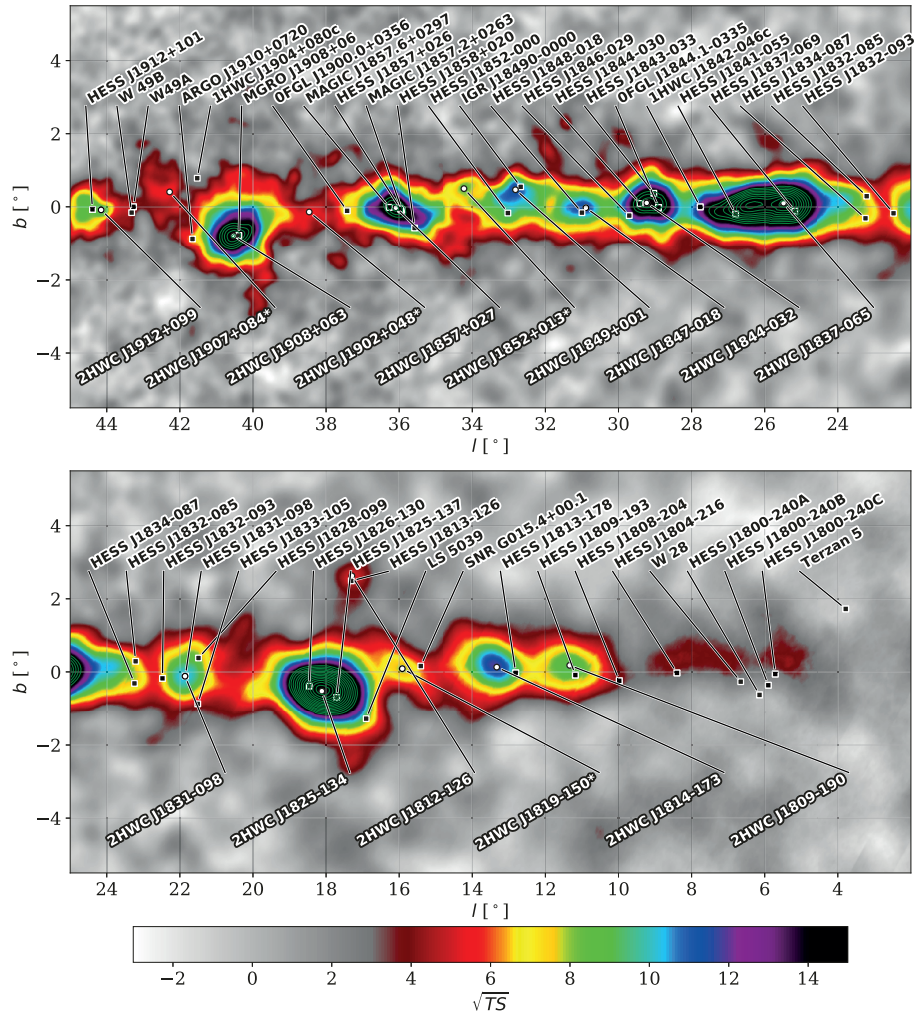


FIGURE 3.13: HAWC sources in part of the inner Galactic Plane region, in Galactic coordinates:  $44^\circ < l < 4^\circ$  and  $|b| < 6^\circ$ . Figure taken from Abeysekara et al., 2017b.

### 3.5 ARGO-YBJ

ARGO-YBJ is a “full coverage” air shower array detector dedicated to gamma-ray astronomy and cosmic ray studies. It is located at the Yangbajing Cosmic Ray Laboratory (4300 meters a. s. l., Tibet, China).

ARGO-YBJ detector is composed of a single layer of Resistive Plate Chambers (RPCs) covering a surface of  $74 \times 78$  meters. The whole coverage is divided in 130 groups of 12 adjoining RPCs called “clusters”. In order to extend the experimental area and therefore have a better reconstruction of the shower fronts, 23 additional



FIGURE 3.14: ARGO-YBJ (Astrophysical Radiation with Ground-based Observatory at YangBaJing): the Yangbajing observatory in Tibet where the experiment ARGO-YBJ is located. Credit *INFN website: ARGO-YBJ*.

clusters are placed around the central area. The total active area of the experiment is  $110 \times 110$  meters squared. The space-time unit of the detector is composed of 8 neighboring RPC readout strips and is called “pad”. Air showers are triggered by requiring a number of hits greater than 20 within a 150 ns time window, giving an average trigger rate of about 3.5 kHz with a dead time of 4%.

The installation of the whole detector was completed in the spring of 2007, the data taking lasted from November of the same year until 2013.

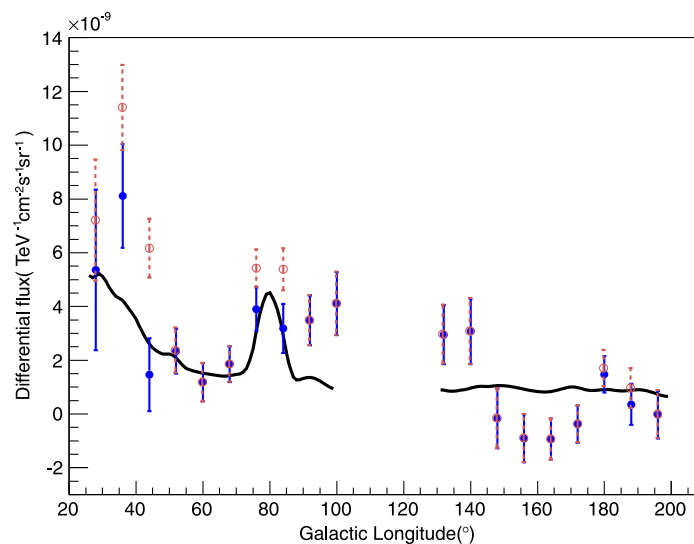


FIGURE 3.15: Figure taken from Bartoli et al., 2015. Galactic longitude profile of the diffuse gamma-ray emission in the Galactic latitude interval  $|b| < 5^\circ$  at an energy of 600 GeV obtained from the ARGO-YBJ data. The filled circles show the results after masking the sources, while the open circles show the results without the masking. The solid line represents the value quoted by the Fermi-DGE model at the same energy, smeared out with the ARGO-YBJ PSF (see Bartoli et al., 2015).

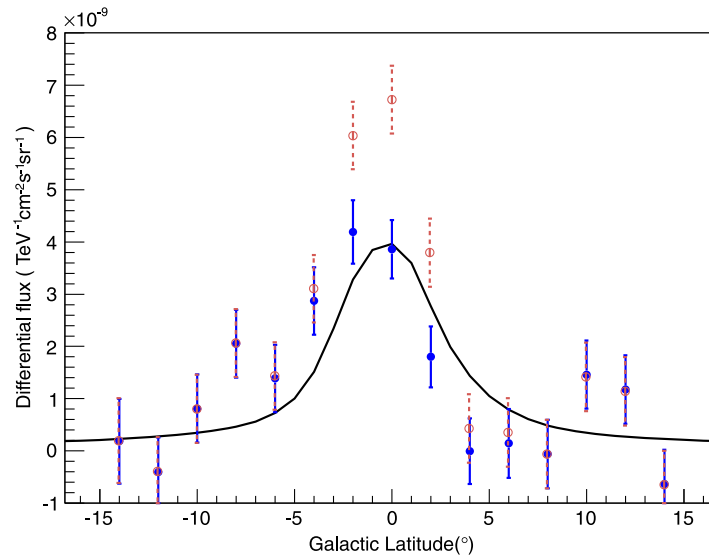


FIGURE 3.16: Figure taken from Bartoli et al., 2015. Galactic latitude profile of the diffuse gamma-ray emission in the Galactic longitude interval  $25^\circ < l < 100^\circ$  at an energy of 600 GeV obtained from the ARGO-YBJ data. See legend in Fig.3.15.

### 3.5.1 Results

For each event the collaboration performed a space-time reconstruction of the shower front, including the position of the core, the incident direction of the primary particle, and the energy reconstruction (Bartoli et al., 2015). The shower core position is obtained by using a maximum likelihood method for fitting the lateral particle density distribution of the shower. Both the primary energy and the angular resolution depend on the number of hit pads. However, due to the large fluctuations in the shower development in the atmosphere and to its partial sampling with the limited detector area, the number of particles at ground level cannot be considered an accurate estimator of the primary energy. The energy spectrum is evaluated by studying the global number of hit pads distribution for a single event, and comparing it to simulations obtained with different test spectra in order to establish the one that best fits the data.

The Argo-YBJ experiment measures the total gamma-ray emission in the longitudinal region  $40^\circ < l < 100^\circ$  and latitudes  $|b| < 5^\circ$  for  $E_\gamma = 600$  GeV (Bartoli et al., 2015). See Fig. ??, where the longitudinal and latitudinal distributions of the diffuse gamma-ray flux obtained at an energy of 600 GeV are reported.

## 3.6 Milagro

Milagro (Multiple Institution Los Alamos Gamma Ray Observatory) is a water Cherenkov detector active until 2008, for the detection of extensive air showers produced by high-energy gamma-rays. It is situated in the Jemez Mountains near Los Alamos, New Mexico at the Fenton Hill Observatory site at an altitude of 2630 meters.

It consists of a man made pond of dimensions 80 meters, 60 meters, and 8 meters deep, lined on the bottom, filled with water, and covered on top (Fig. 3.17). In the water was located a weighted grid of PMTs tied together at anchor lines, which was laid to the bottom of the pond and that floats up to fixed positions.



FIGURE 3.17: Milagro detector on Jemez Mountains near Los Alamos, New Mexico. Credit: <https://www.lanl.gov>.

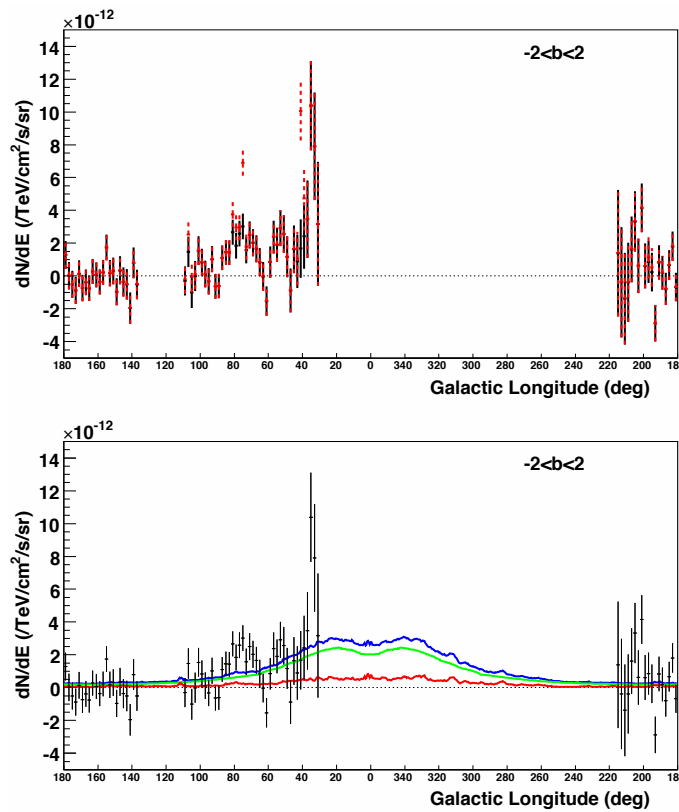


FIGURE 3.18: Galactic longitude profile of the gamma-ray emission around 15 TeV in the Galactic plane as measured by Milagro. Upper plot: Red data points – no subtraction of source contributions, black data points – after subtraction. Lower plot: Source-subtracted profile overlaid with prediction of the optimized GALPROP model – the red line is the pion contribution, the green line the IC, and the blue line is the total flux prediction integrated in the latitude range  $\pm 2^\circ$ . Figure taken from Abdo et al., 2008a.

An outrigger array was added in 2003 and provided a longer lever arm to reconstruct events and improved the angular resolution of the detector from  $\sim 0.75^\circ$  to

$\sim 0.45^\circ$ . Milagro can observe the overhead sky with a large field of view of 2 sr. Due to its high duty cycle it can monitor the sky continuously, these characteristics make it well-suited for measuring diffuse emission. Its construction started in 1999 and ended in 2001, year of starting of data-taking. Milagro was active for seven years during which collected interesting observations such as the cosmic ray distribution anisotropy observed both at large and intermediate ( $\sim 10^\circ$ ) angular scale (*Proceedings, 30th International Cosmic Ray Conference (ICRC 2007) 2007*, Abdo et al., 2008b).

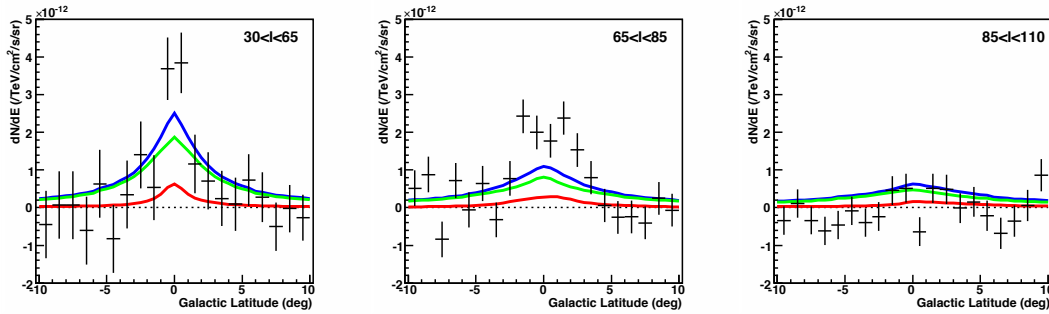


FIGURE 3.19: Source-subtracted Galactic latitude profile of the gamma-ray emission around 15 TeV in the inner Galaxy (left plot), in the Cygnus region (middle plot), and in the region above Cygnus (right plot) as measured by Milagro (points with errors) and predicted by the optimized GALPROP model. The colors are as above. Figure taken from Abdo et al., 2008a.

### 3.6.1 Results

The total seven years dataset collected by Milagro contains  $2.2 \times 10^{11}$  events most of which are due to hadronic cosmic rays. The experiment is able to reconstruct both arrival direction and energy of the initial particle that generated each of the showers. The time difference between observations by different PMTs getting hit is used to determine the arrival angle of the shower which in turn gives the arrival direction of the primary. The amount of Cherenkov light detected by the PMTs can be used to get a measure of the primary particle energy.

The background rejection process is used to differentiate hadronic air showers from electromagnetic showers and it is based on the ability to detect the energetic particles in an extensive air shower. In order to do so, the collaboration uses the method of "direct integration" by calculating a background map using events over a 2 hrs time interval. The detailed process is described in Atkins et al., 2003.

Milagro provides the total gamma-ray emission observed at the reference energy  $E_\gamma = 15$  TeV, for longitudes  $30^\circ < l < 110^\circ$  and  $136^\circ < l < 216^\circ$  and for latitudes  $|b| < 10^\circ$  (Abdo et al., 2008a). In Fig. 3.18 and 3.19 are reported respectively the longitudinal and latitude distribution of the  $\gamma$ -ray emission around 15 TeV in the Galactic plane (Abdo et al., 2008a). The upper panel of Fig. 3.18 shows the distribution of the total flux (red data points with dashed error bars), while black data points are obtained after subtraction of the source contribution. In the lower plot instead is represented the source subtracted profile along with the prediction of the pion contribution (red line), IC contribution (green line), and total flux prediction between the latitude interval  $|b| < 2^\circ$ ; all three are obtained using the GALPROP code. The region of longitude  $-144^\circ < l < 29^\circ$  is below the Milagro horizon so it appears empty, while the region  $111^\circ < l < 135^\circ$  is excluded because the analysis method is insensitive there. Fig. 3.19 shows the source-subtracted latitudinal distributions

of gamma emission in the latitudinal interval  $\pm 10^\circ$ , for three longitudinal regions:  $30^\circ < l < 65^\circ$  (inner Galaxy);  $65^\circ < l < 85^\circ$  (Cygnus region);  $85^\circ < l < 110^\circ$  (above Cygnus region). The black points with error-bars are the data while the curves are the GALPROP predicted emissions as above.

### 3.7 Future generation of detectors

The Cherenkov Telescope Array (CTA) (CTA, 2018) will be one of the land-based gamma-ray telescopes, however, because of its advance it will be the first of its kind. It will be the major global observatory for very high energy gamma-ray astronomy over the next decade and beyond. Covering a wide range of energies from 20 GeV to 300 TeV, its scientific potential is the broadest of all land-based Cherenkov detectors of gamma-rays. Among its purposes there are understanding sources and role of relativistic cosmic particles, search for dark matter, investigation on physical processes of neutron stars and black holes. Moreover, being able to cover the whole sky, it will maximize the potential to observe the rarest phenomena such as nearby supernovae, gamma-ray bursts or gravitational wave transients.

The observatory will be constituted by arrays of IACTs divided on two sites: Northern and Southern, in order to have a full sky coverage. Three classes of telescopes are planned (Fig. 3.20). In the Southern CTA it is intended to cover a large range of energies and observe the Galactic centre so it will be provided with 99 telescopes of all three categories. The Northern will be focused on higher energies and extragalactic sources and will include only the largest telescopes for a total of 19.

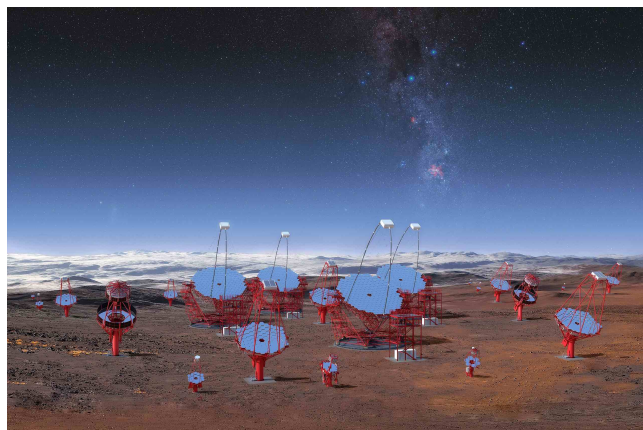


FIGURE 3.20: CTA prototype that shows all three classes of telescopes planned. Credit: *CTA/M-A. Besel/IAC (G.P. Diaz)/ESO*

The angular resolution of CTA will approach 1 arc-minute at high energies. This will allow to obtain a detailed imaging of a large number of gamma-ray sources which will widely extend our present catalogues and refine current observations on already present sources.

Many are the questions that still need to be answered regarding neutrinos, and especially cosmic neutrinos. IceCube-Gen2 is a planned neutrino observatory of next generation whose aim is to provide an unprecedented view of the high-energy universe, taking neutrino astronomy to new levels of discovery. In the next generation the whole instrumentation already deployed will be doubled in order to achieve a tenfold increase in volume to about 10 cubic kilometers and aiming at an order of

magnitude increase in neutrino detection rates. Construction of the extended observatory is estimated to require 6 years, with completion and full operation at the end of the next decade.

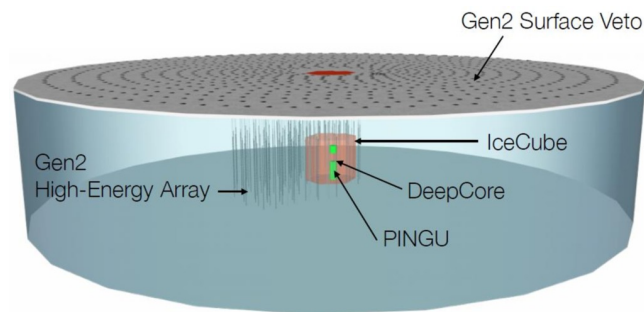


FIGURE 3.21: Schematic view of IceCube Gen-2, comprising the existing IceCube array with its densely equipped inner region DeepCore, the high-energy array of Gen2, the super-densely equipped PINGU sub-detector, and an extended surface array (Spiering, 2018).

Another development of the IceCube-Gen2 detector include the radio detection technique of neutrinos. Many experimental efforts have advanced this technique in the past two decades. They include the ANITA experiment (a balloon-borne radio detector), as well as experimental efforts in Antarctic ice, namely the Askaryan Radio Array (ARA) at the South Pole, and the ARIANNA detector on the Ross Ice Shelf (Anker et al., 2020).

Other interesting results on high-energy neutrinos are expected also from the future research infrastructure KM3NeT. The telescopes will have detector volumes between megaton and several cubic kilometres of clear sea water. Located in the deepest seas of the Mediterranean, KM3NeT will contribute to the research of the properties of neutrinos such as the mass hierarchy. Furthermore, with the ARCA telescope, KM3NeT scientists will search for neutrinos from distant astrophysical sources such as supernovae, gamma-ray bursts or colliding stars (KM3NeT).

## Chapter 4

# Diffuse Galactic emission

The diffuse Galactic component of high-energy gammas and neutrinos rises from hadronic interactions between cosmic rays (CR) and the gas contained in the Galaxy. The calculation of the diffuse fluxes are, however, affected by the high uncertainty related to the cosmic rays density distribution. A good knowledge of the cosmic rays distribution and spectrum in all the regions of the Galaxy where the gas density is not negligible is, indeed, required to obtain a reliable prediction of the diffuse component.

So far we don't have an evidence of Galactic neutrino signal, not from sources nor diffuse. The IceCube collaboration estimates the Galactic high-energy component to contribute not more than 14% to the total neutrino flux which is instead dominated by extragalactic production (Aartsen et al., 2017).

Recently Fermi-LAT instrument has reported a detailed picture of the entire gamma-ray sky in the multi-GeV domain (Ackermann et al., 2012; Acero et al., 2016) that can be compared with expectations obtained by modelling CR propagation in the Galaxy. Recent analyses pointed out that the spectral distribution of CR may depend on the galactocentric distance. The possibility of a progressive large-scale hardening towards the inner Galaxy was considered in Gaggero et al., 2015b and confirmed by two different analyses (Acero et al., 2016; Yang, Aharonian, and Evoli, 2016) of the Fermi-LAT data. While, a very recent work (Aharonian et al., 2018) argues that CR hardening is not a global large-scale effect but may be the result of local enhancements of CR density in giant molecular clouds.

In any case, the hypothesis that CR spectral index in different regions of the Galaxy is lower (in modulus) than the local value could clearly have a dramatic effect at TeV energies and above. It would enhance the expected HE emission with respect to standard expectations and, moreover, it would produce a different angular distribution of HE photons and neutrinos from the Galactic plane with respect to lower energy observations. It is thus important to compare predictions obtained in this assumption with present observational constraints.

In this Chapter we will present the model used for the calculation of the high energy Galactic diffuse flux of neutrinos and gamma-rays. First of all we will point out our four hypothesized scenarios related to the cosmic ray distribution in the Galaxy. The first two scenarios ("standard cases") assumes that the CR flux scales proportionally to the distribution of the CR sources in the Galaxy. While the energy spectrum is assumed being constant in the Galaxy and therefore directly constrained by the one measured at the Earth position. In the other two hypotheses ("hardening cases") we consider the CR density being dependent from the sources distribution, as in the first two, and in addition we consider the spectral index being dependent on the galactocentric distance. Under these assumptions we estimate the HE diffuse neutrino flux and the HE diffuse gamma flux. Finally we compare the results obtained with the

data provided by different HE gamma detectors providing interesting constraints on the CR distribution.

This Chapter is based on the original paper Cataldo et al., 2019.

## 4.1 Diffuse emission

The diffuse emission by hadronic interaction is one of the main sources of neutrino and gamma-ray production in the Galactic disk. It gives a significant contribution to the total fluxes of neutrinos and gammas at many orders of energies, and it could also become dominant over the total Galactic source contribution. We present here the results of our work Cataldo et al., 2019 where we estimate this component of the gamma-ray Galactic flux and we use the same models to estimate the neutrino counterpart. The general expressions for the diffuse fluxes are<sup>1</sup>:

$$\varphi_\nu^{\text{diff}}(E_\nu, \hat{n}_\nu) = \frac{1}{3} \sum_{\ell=e,\mu,\tau} \left[ \int dE \frac{d\sigma_{\nu_\ell}(E, E_\nu)}{dE_\nu} \int dl \varphi_{\text{CR}}(E, \vec{r}_\odot + l\hat{n}_\nu) n_{\text{H}}(\vec{r}_\odot + l\hat{n}_\nu) \right]; \quad (4.1)$$

$$\varphi_\gamma^{\text{diff}}(E_\gamma, \hat{n}_\gamma) = \int dE \frac{d\sigma_\gamma(E, E_\gamma)}{dE_\gamma} \int dl \varphi_{\text{CR}}(E, \vec{r}_\odot + l\hat{n}_\gamma) n_{\text{H}}(\vec{r}_\odot + l\hat{n}_\gamma); \quad (4.2)$$

where  $E_\nu, E_\gamma$  and  $\hat{n}_\nu, \hat{n}_\gamma$  indicate the neutrino and gamma energy and arrival direction, respectively.  $d\sigma_{\nu_\ell}/dE_\nu, d\sigma_\gamma/dE_\gamma$  are the differential cross sections already presented in (1.17) and (1.32). The first one is the differential cross section for production of neutrinos  $\nu_\ell$  and antineutrinos  $\bar{\nu}_\ell$  by a nucleon of energy  $E$  in nucleon-nucleon collision, and the same goes for gamma cross-section. The function  $\varphi_{\text{CR}}(E, \vec{r})$  represents the differential CR flux,  $n_{\text{H}}(\vec{r})$  is the gas density distribution, and  $r_\odot = 8.5$  kpc is the position of the Sun respect to the center of the Galaxy. In the above relation, we assumed that, due to neutrino oscillation, the neutrino flux at Earth is equally distributed among the three different flavours, so Eq.(4.1) represents the single flavor flux. This approximation is valid at few % accuracy and as discussed in Sec.1.1.2 it is completely adequate for our purposes. The Galactic distribution of the gas density,  $n_{\text{H}}(\vec{r})$ , is assumed with a cylindrical symmetry and is taken from the public GALPROP code (*GALPROP*) as described in Sec. 2.0.1. The distribution is given as a sum of atomic ( $H$ ), and molecular ( $H_2$ ) hydrogen and, yet subdominant, also takes into account the contribution of Helium.

An estimation of the neutrino diffuse flux was already proposed in Pagliaroli, Evoli, and Villante, 2016. Here we present a different phenomenological description of the problem by changing the models for cosmic ray distribution in the Galaxy. The aim of this work is to test expectations for Galactic HE neutrinos and gamma-rays in the TeV domain against different observational results. In order to do so we give a complete estimation of the gamma-ray and neutrino fluxes by also discussing the contribution of pointlike and extended sources when comparing to observational data.

### 4.1.1 Cosmic-ray distribution

The cosmic-ray (CR) total density distribution and spectrum are strictly related to their propagation in the Galaxy. After their production, cosmic-rays travel in the Galactic magnetic fields which have both a small scale and large scale structure.

<sup>1</sup>From now on, we use the symbol  $\varphi$  for angle-differential fluxes and  $\Phi$  for angle-integrated fluxes.

Charged particles are sensitive to both local and global properties of the magnetic field and this results in a random walk motion which could be modeled by a diffusive regime of propagation.

In Pagliaroli, Evoli, and Villante, 2016 are considered three cases used to modelize the CR distribution, called *A*, *B*, *C*. It is firstly assumed that CR distribution is homogeneous in the Galaxy (*Case A*), that it follows the distribution of galactic CR sources (*Case B*), and than that it has a spectral index that depends on the galactocentric distance (*Case C*). In this work instead we use four different models based on four different assumptions on the cosmic-ray distribution in the Galaxy by introducing several improvements.

We define the 4 cases following the CR nucleon flux described in Pagliaroli, Evoli, and Villante, 2016. For the first two cases, to which we will refer as *standard*, this is given as the product of a function of position and a function of nucleon energy. So it is expressed by:

$$\varphi_{\text{CR}}(E, \vec{r}) = \varphi_{\text{CR},\odot}(E) g(\vec{r}). \quad (4.3)$$

The term  $\varphi_{\text{CR},\odot}(E)$  is the local spectrum of cosmic rays (so the one observed at the Sun position), and  $g(\vec{r})$  is an adimensional function (normalized to one at the Sun position  $\vec{r}_{\odot}$ ) introduced to describe the spatial distribution of CR. For the definition of this latter function, the distribution of CR sources is assumed to follow the Supernova Remnants (SNRs) number density parameterization given by Green, 2015 and reported in Eq.(2.3). Then, in order to take into account the propagation, we solve a 3D isotropic diffusion equation with constant diffusion coefficient and stationary CRs injection with 2 different assumptions for the diffusion length:  $R = 1$  kpc and  $R = \infty$  kpc, defining the first two *standard* scenarios. In the first case, CRs are confined very close to their sources, while in the second case the CRs are propagated in the whole Galaxy.

The factorized expression of Eq.(4.3) is based on the assumption that the cosmic ray energy spectrum is uniform in every region of the Galaxy. There is a large class of models that are based on this assumption which in general is true whether the following conditions are satisfied (Lipari and Vernetto, 2018):

- All components of CR are in a stationary state;
- The spectrum of CR is not significantly distorted by the contributions of near sources;
- Averaged in time, the spectra generated by the CR sources of the Galaxy have a space independent shape;
- The diffusion coefficient that describes the propagation of CR in the Galaxy, has the same rigidity dependence in all positions of the Galaxy;
- The largest CR losses are due to the escape from the Galaxy;
- The CR energy losses have to be negligible during their propagation.

One of the most useful implication of the factorization is that since the spectral shape of CR is identical for the overall Galaxy, this can be constrained directly from observations in the local proximity of the Earth.

Otherwise, whether one or more of the previous conditions are not met, the total CR distribution cannot be factorized in its energy and spatial dependence making the computations more complicated. It is, indeed, conceivable that CR diffusion, due to a stronger star forming activity and peculiar magnetic field, behaves differently

in the inner Galactic region. Several anomalies observed in the gamma-ray diffuse emission support this possibility. First of all, the Milagro excess which still has unclear origins. Milagro measured a large gamma-ray flux coming from the inner region of the Galactic plane at 15 TeV median energy (Abdo et al., 2008a) which is not reproduced by the conventional CR distribution models (Gaggero et al., 2015b). Furthermore the already mentioned Fermi-LAT diffuse gamma-ray results at lower energies that are notably underestimated by simpler models. Consequent analysis on the Fermi-LAT measurements suggest an evidence of the hardening of the cosmic-ray spectrum with galactocentric distance (Acero et al., 2016; Yang, Aharonian, and Evoli, 2016). We implemented this possibility by defining a position dependent spectral index ( $\Delta(\vec{r})$ ) that follows the trend observed at GeV energies by these analysis. This is obtained starting from the first two standard cases, with the introduction of a third function  $h(E, \vec{r})$  defined as:

$$h(E, \vec{r}) = \left( \frac{E}{\bar{E}} \right)^{\Delta(\vec{r})}; \quad (4.4)$$

with  $\bar{E} = 20$  GeV. The total CR distribution, for the additional 2 cases (that we will call *hardening* cases), will be therefore defined as:

$$\varphi_{\text{CR}}(E, \vec{r}) = \varphi_{\text{CR}, \odot}(E) g(\vec{r}) h(E, \vec{r}). \quad (4.5)$$

Each single component of the energy and spatial distribution of the cosmic-rays is described in detail in the following.

Beside Pagliaroli, Evoli, and Villante, 2016, a similar approach for the estimation of the Galactic diffuse can be found in Lipari and Vernetto, 2018 where the diffuse gamma-ray flux is estimated up to PeV energies including also absorption effects. While in Gaggero et al., 2015a is proposed a phenomenological scenario ( $\text{KRA}_\gamma$ ) in order to reproduce in all regions the diffuse observed by Fermi-LAT. We propose an improvement with respect to previous calculations by considering more realistic descriptions of CR distribution. Furthermore, we present a new analysis with the aim of testing different CR distributions through comparisons of Galactic HE gamma-ray and neutrino emission against several existing observational data-sets in the TeV domain.

#### Local CR spectrum: $\varphi_{\text{CR}, \odot}(E)$

We describe the local CR nucleon flux  $\varphi_{\text{CR}, \odot}(E)$  according to the data driven parameterization Dembinski et al., 2018 that relies as little as possible on theoretical assumptions. In this reference the fit is found by combining measurements at several energy orders. Since the CR spectrum spans over 11 orders a common picture needs to be pieced together from many data sets. At lower energies of magnitude, below 100 TeV, the fit relies on satellite and balloon experiments measurements that report the flux per element. While at energies above 100 TeV, the ground-based experiments take over and report the all-particle flux up to  $10^8$  TeV. In Dembinski et al., 2018 the data-driven model, called the Global Spline Fit (GSF) is used to parameterize the latest and most detailed measurements of the cosmic-ray flux and its composition from 0.01 TeV to  $10^8$  TeV, combining direct and air-shower observations. The GSF only assumes that the flux is smoothly varying and otherwise relies only on the available data. In Fig. 4.1 is reported the all-particle flux given by the global fit (black thick solid line), the flux contributed by protons (red line solid line), helium (yellow dashed line), the oxygen group (gray dash-dotted line), and the iron group

(blue dotted line). We observe several features in the overall spectrum obtained, which follow the measured spectral variations: an unnamed dip around 5 TeV, the first and second knees around 3 PeV and 100 PeV respectively, the ankle around 8 EeV, a slight hardening around 20 PeV, and finally the so-called "toe" around 60 EeV.

In the energy range of interest for the present analysis, that roughly corresponds to  $E \simeq 10 \times E_\gamma \sim 10 - 200$  TeV, the total nucleon flux is lower than the broken-power law parameterization (Ahlers et al., 2016) adopted in our previous calculation (Pagliaroli, Evoli, and Villante, 2016) by  $\sim 12\%$  ( $\sim 30\%$ ) at  $E \simeq 10$  TeV ( $E \simeq 100$  TeV).

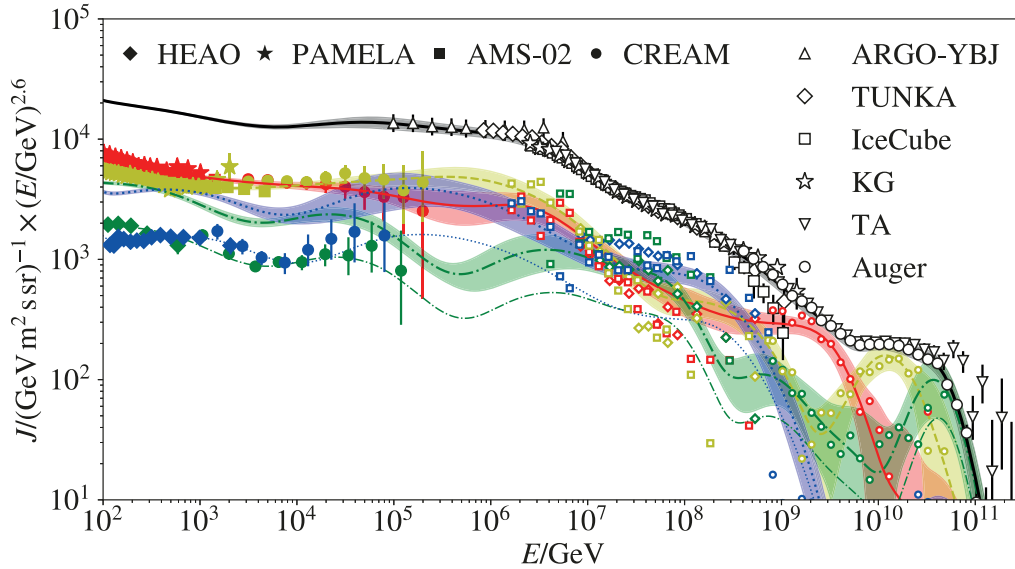


FIGURE 4.1: All-particle flux (black thick solid line), the flux contributed by protons (red line solid line), helium (yellow dashed line), oxygen (gray dash-dotted line), and iron (blue dotted line). Bands around the model lines show a variation of one standard deviation. Error bars represent combined statistical and systematic uncertainties. Data points of composition measurements from air-showers are not shown without error bars for clarity. TA stands for Telescope Array, KG for KASCADE-Grande. Figure taken from Dembinski et al., 2018.

### Spatial function: $g(\vec{r})$

The uncertainty on the definition of the CR distribution in the Galaxy is not only spectrum related but partially affects the spatial distribution as well. The definition of the total CR flux density is strictly linked to the Galactic  $\gamma$ -ray flux. In particular, the gamma-ray emissivity (defined as the gamma-ray flux per Hydrogen atom) constitutes a proxy of the cosmic-ray flux radial density. Several analysis on the Fermi-LAT gamma-ray measurements have been performed according to different methods in order to derive the emissivity distribution (Acero et al., 2016; Yang, Aharonian, and Evoli, 2016; Pothast et al., 2018). The dots in Fig.4.2 show the values of the CR distribution for energies  $\simeq 20$  GeV (Acero et al., 2016) and the emissivity integrated above 1 GeV (Yang, Aharonian, and Evoli, 2016; Pothast et al., 2018), resulting from the aforementioned analyses (respectively black, green, and red). They are all normalized to 1 at the Sun position, and are plotted as a function of cylindrical radius values obtained dividing the Galaxy into annuli starting from the center.

The results, yet similar for many radii, appear not fully consistent especially for low galactocentric distances.

In order to cover this uncertainty our estimation provides two different models for the function  $g(\vec{r})$  which describes the spatial distribution of Galactic cosmic rays. First we analyze how this function is calculated and then we define the two models. The function  $g(\vec{r})$  is determined by the distribution of the CR sources in the Galaxy  $f_S(\vec{r})$  and by the propagation of CR in the Galactic magnetic field. In Pagliaroli, Evoli, and Villante, 2016, are considered two extreme assumptions (*Case A* and *B*) which correspond to a completely mixed scenario (i.e. a uniform CR gas:  $g(\vec{r}) \equiv 1$ ) and to the opposite assumption of CRs being confined very close to their sources, respectively. In this work we consider a different phenomenological description. We define the function  $g(\vec{r})$  by solving the 3D isotropic diffusion equation with constant diffusion coefficient  $D$  and stationary CR injection  $S(E, \vec{r})$ :

$$\frac{\partial n(E, \vec{r}, t)}{\partial t} = D\nabla^2 n(E, \vec{r}, t) + S(E, \vec{r}); \quad (4.6)$$

with:

$$n(E, \vec{r}, t) dE d^3r : \text{ number of protons in } (E, E, dE), (\vec{r}, \vec{r} + d^3r); \quad (4.7)$$

$$S(E, \vec{r}) dE d^3r : \text{ number of produced protons in } (E, E, dE), (\vec{r}, \vec{r} + d^3r). \quad (4.8)$$

The solution is obtained through the Green Function indicated with  $G(\vec{r}, t)$  which, for the correspondent homogeneous differential equation, is a 3D Gaussian with variance  $\sigma^2 = 2Dt$ :

$$G(\vec{r}, t) = \frac{1}{(4\pi Dt)^{3/2}} \exp\left(-\frac{r^2}{4Dt}\right). \quad (4.9)$$

So the complete solution is given by:

$$n(E, \vec{r}) = \int d^3x S(E, \vec{r} - \vec{x}) \int_0^{t_G} d\tau \frac{1}{(4\pi D\tau)^{3/2}} \exp\left(-\frac{x^2}{4D\tau}\right); \quad (4.10)$$

with  $\vec{x}, \tau$  spatial and time variables of integration. The time  $t_G$  represents the integration time which is the age of the Galaxy. By defining the variable  $\gamma = |\vec{x}|/\sqrt{2D\tau}$ , and  $R = \sqrt{2Dt_G}$ , is easy to show that the final solution for the CR proton density in the Galaxy is:

$$n(E, \vec{r}) = \int d^3x S(E, \vec{r} - \vec{x}) \frac{\mathcal{F}(|\vec{x}|/R)}{|\vec{x}|}; \quad (4.11)$$

with the function  $\mathcal{F}(|\vec{x}|/R)$  defined as follows:

$$\mathcal{F}(v) \equiv \int_v^\infty d\gamma \frac{1}{\sqrt{2\pi}} \exp(-\gamma^2/2). \quad (4.12)$$

At this point, we assume the CR source density distribution to follow the Supernova Remnants (SNR) number density parameterization given by Green, 2015:  $f_S(\vec{r})$ , and finally, we define the function  $g(\vec{r})$  as:

$$g(\vec{r}) = \frac{1}{\mathcal{N}} \int d^3x f_S(\vec{r} - \vec{x}) \frac{\mathcal{F}(|\vec{x}|/R)}{|\vec{x}|}; \quad (4.13)$$

where  $\mathcal{N}$  is a normalization constant given by:

$$\mathcal{N} = \int d^3x f_S(\vec{r}_\odot - \vec{x}) \frac{\mathcal{F}(|\vec{x}|/R)}{|\vec{x}|}. \quad (4.14)$$

The function  $g(\vec{r})$  is therefore obtained as the convolution of the source distribution with a kernel that is inversely proportional to source distance below a fixed smearing radius  $R$  while it is exponentially suppressed for larger distances. In this context, the smearing parameter  $R$  represents the diffusion length  $R = \sqrt{2D t_G}$ .

The functions  $g(\vec{r})$  calculated for different smearing radii:  $R = 1, 3, 5, 10, \infty$  kpc are shown as a function of the galactocentric distance by the black lines in Fig.4.2. They are compared with the CR density at  $E \simeq 20$  GeV and the  $\gamma$ -ray emissivity integrated above  $E_\gamma = 1$  GeV obtained from Fermi-LAT data in Acero et al., 2016; Yang, Aharonian, and Evoli, 2016; Pothast et al., 2018. While we believe that the data show a clear trend as a function of  $r$ , we think that they still do not allow to discard any of the proposed curves. We thus consider the two extreme assumptions  $R = 1$  kpc and  $R = \infty$ , corresponding to the thick black lines in Fig.4.2, in order to encompass a large range of possibilities and to provide a conservative estimate of the uncertainty in the gamma-ray flux connected with different descriptions of the CR spatial distribution in the Galaxy. Note that since the assumed smearing length  $R$  is larger than the thickness of the Galactic disk, we neglect in both cases the variation of the CR flux along the Galactic latitudinal axis. In other words, we assume  $g(r, z) \simeq g(r, 0)$  in the disk, where we used Galactic cylindrical coordinates.

In the first case ( $R = 1$  kpc) the obtained function  $g(\vec{r})$  is very close to the SNR distribution (Green, 2015) given by the blue dashed line in Fig.4.2. However, differently from the SNR distribution, it does not vanish at the Galactic center, as it is naturally expected due to CR propagation. In the outer regions of the Galaxy, the function  $g(\vec{r})$  drops faster than the CR density. For this reason, we neglect the variations of  $g(\vec{r})$  and we assume that it is constant for  $r \geq 10$  kpc.

In the second case ( $R = \infty$ ) the function  $g(\vec{r})$  is quite close to the CR distribution predicted by the GALPROP code (GALPROP), shown with orange dashed line in Fig.4.2. The function  $g(\vec{r})$  describes quite well the observational results a part from few points at  $r \simeq 3$  kpc and very close to the Galactic center. However, in this region that contains the Galactic bulge different studies find different results. Indeed, the most challenging issue from both the observational and modeling point of view is that there is large degeneracy between the different gamma-ray production components in the Galactic center region (Pothast et al., 2018). So the results in this region are in general less reliable.

### Spectral index: $\Delta(\vec{r})$

As already introduced, in the function of Eq.(4.4):  $h(E, r) = (E/\bar{E})^{\Delta(\vec{r})}$  is included the spatial dependence of the spectral index. For the pivot value is chosen  $\bar{E} = 20$  GeV assuming that for  $E > \bar{E}$  the spectral variation begins to be evident. Moreover this is justified by the observation in Recchia, Blasi, and Morlino, 2016 that around few tens of GeV the CR distribution of Acero et al., 2016 (normalized to 1 at the Sun position) roughly follows the function  $g(\vec{r})$ .

Concerning the spectral index function  $\Delta(\vec{r})$  in our models this is appropriately

defined in order to follow the CR spectral hardening in the inner Galaxy. The function in Galactic cylindrical coordinates<sup>2</sup> is:

$$\Delta(r, z) = \Delta_0 \left(1 - \frac{r}{r_\odot}\right); \quad (4.15)$$

with  $r_\odot = 8.5$  kpc. This choice is equivalent to what is done by Gaggero et al., 2015a; Gaggero et al., 2015b; Gaggero et al., 2017 in their phenomenological CR propagation model characterized by radially dependent transport properties. In order to define the value of the parameter  $\Delta_0$  our aim is to reproduce the value reported in Yang, Aharonian, and Evoli, 2016; Pothast et al., 2018, where the spectral index  $\alpha$  of the parent CR reported in figure, is obtained converting the value of gamma emission associated to  $\pi_0$  decay  $\alpha_\gamma$  by using the relation in Kappes et al., 2007 presented in Sec.1.4:  $\alpha \simeq \alpha_\gamma - 0.1$ . The numerical parameter  $\Delta_0$  physically corresponds to the difference between the CR spectral index at the Sun position,  $\alpha_\odot \simeq 2.7$  at  $E = 20$  GeV, and its value close to the Galactic center. This number is taken as  $\Delta_0 = 0.3$  since this assumption allows us to reproduce the trend with  $r$  observed by Acero et al., 2016; Yang, Aharonian, and Evoli, 2016; Pothast et al., 2018 for  $r \leq 10$  kpc, as it is shown in the lower panel of Fig.4.2. In more external regions, the evidence for a variation of CR energy distribution is much weaker and we assume that  $\Delta(r)$  is constant, as shown by the black solid line in Fig.4.2.

### 4.1.2 Results

Our results for the diffuse HE gamma-ray flux produced by the interaction of CR with the gas contained in the Galactic disk at  $E_\gamma = 1$  TeV are plotted as function of the Galactic longitude  $l$  (at the fixed latitude  $b = 0$ ) in upper plot of Fig.4.3; the latitudinal distribution obtained for  $l = 0$  is plotted in the lower plot of Fig.4.3. The same plots for diffuse HE neutrino flux at 100 TeV, are shown in 4.4 (up: longitudinal distribution, bottom: latitudinal distribution). In both plots: blue lines are obtained by assuming that the CR spectrum is independent from the position in the Galaxy ("standard" scenario) while red lines implement CR spectral hardening in the inner Galaxy, as described above ("hardening" scenario). Solid and dashed lines in (each group) are obtained by assuming that the CR spatial distribution is described by the function  $g(\vec{r})$  given in Eq.(4.13) with smearing radius equal to  $R = 1$  kpc and  $R = \infty$ , respectively.

The angle-integrated gamma-ray flux at 1 TeV is equal to  $\Phi_\gamma = (7.0 - 8.0) \times 10^{-13} \text{ cm}^{-2} \text{ s}^{-1} \text{ GeV}^{-1}$  in the standard scenario and  $\Phi_\gamma = (8.4 - 10.4) \times 10^{-13} \text{ cm}^{-2} \text{ s}^{-1} \text{ GeV}^{-1}$  in the hardening scenario, with upper and lower bounds corresponding to  $R = 1$  kpc and  $R = \infty$ , respectively. The angle-integrated neutrino flux (single flavour) at 100 TeV is  $\Phi_\nu = (1.0 - 1.2) \times 10^{-18} \text{ cm}^{-2} \text{ s}^{-1} \text{ GeV}^{-1}$  for standard cases, obtained for  $R = 1$  kpc and  $R = \infty$ , respectively. While for the angle-integrated fluxes at 100 TeV with hardening we obtain:  $\Phi_\nu = (1.5 - 2.2) \times 10^{-18} \text{ cm}^{-2} \text{ s}^{-1} \text{ GeV}^{-1}$  for  $R = 1$  kpc and  $R = \infty$ , respectively.

The inclusion of CR hardening increases the integrated flux by 1.2 – 1.3 for gammas and 1.5 – 1.8 for neutrinos. The exact enhancement factor is dependent on the assumed CR spatial distribution. Even if the effect on the total flux is relatively small, a CR hardening may be responsible for a much more significant increase of

<sup>2</sup>We indicate with  $(r, z)$  the Galactic cylindrical coordinates. While with  $(r, b, l)$  we will indicate the spherical coordinates centered in the Sun position, with  $b$ , and  $l$  being the Galactic latitude and longitude respectively.

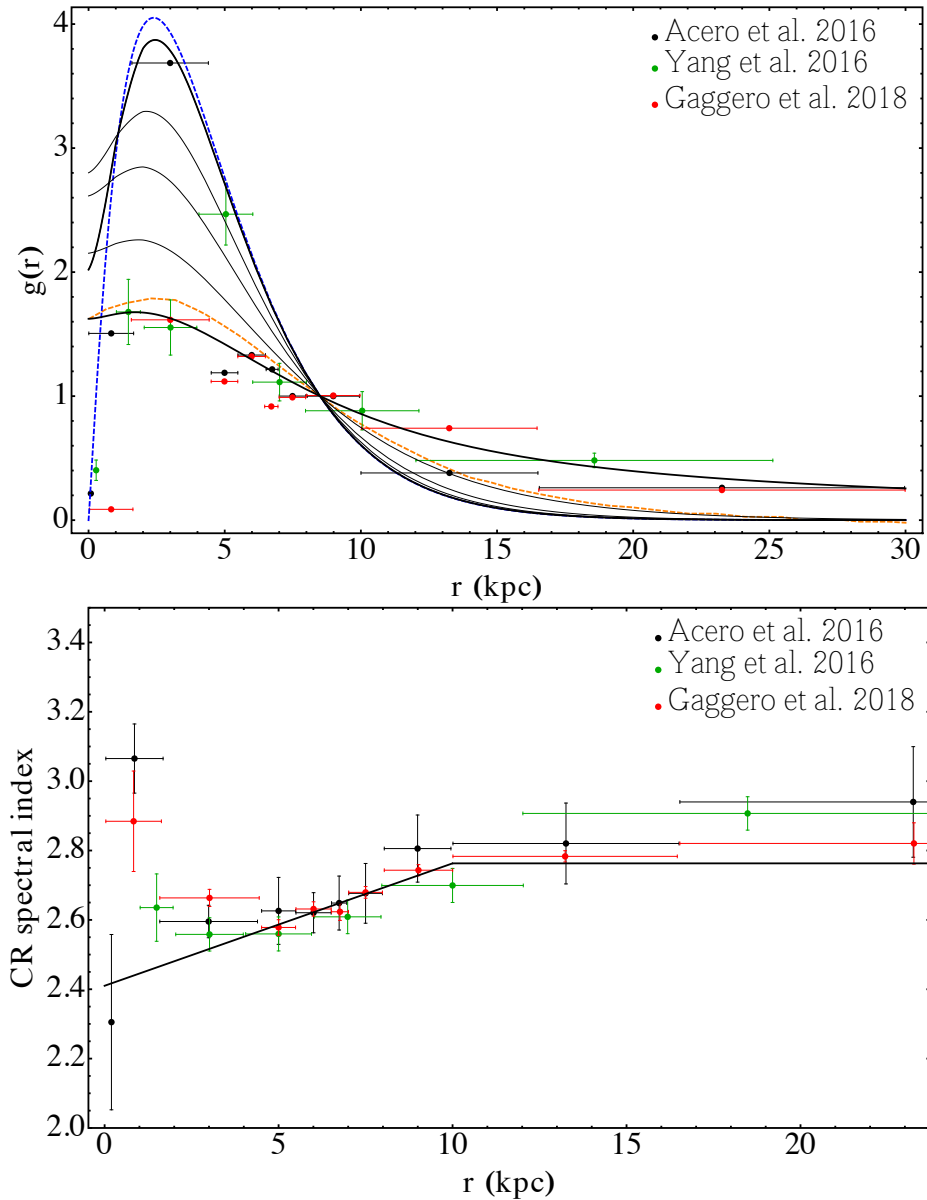


FIGURE 4.2: **Upper Panel:** The black lines show the functions  $g(\mathbf{r})$  obtained from Eq.(4.13) for different smearing radii  $R$ . Going from top to bottom at  $r \simeq 2$  kpc, the different lines correspond to  $R = 1, 3, 5, 10, \infty$  kpc, respectively. The data points show the CR density at  $E \simeq 20$  GeV Acero et al., 2016 (normalized to one at the Sun position) and the  $\gamma$ -ray emissivity above  $E_\gamma = 1$  GeV (Yang, Aharonian, and Evoli, 2016; Pothast et al., 2018), as a function of the galactocentric distance obtained from Fermi-LAT data. **Lower Panel:** The black line gives the spectral index of CR at  $E_{\text{CR}} = 20$  GeV adopted in this calculation. The data points show the CR spectral index obtained as a function of the galactocentric distance from Fermi-LAT data in Acero et al., 2016; Yang, Aharonian, and Evoli, 2016; Pothast et al., 2018.

Figure taken from Cataldo et al., 2019.

the flux in the central region  $-60^\circ \leq l \leq 60^\circ$ . We see indeed from Fig.4.3 and 4.4 that the enhancement factor can be as large as  $\sim 2$  for gammas and  $\sim 6$  for neutrinos in the direction of the Galactic center. These factors, are larger than the uncertainty

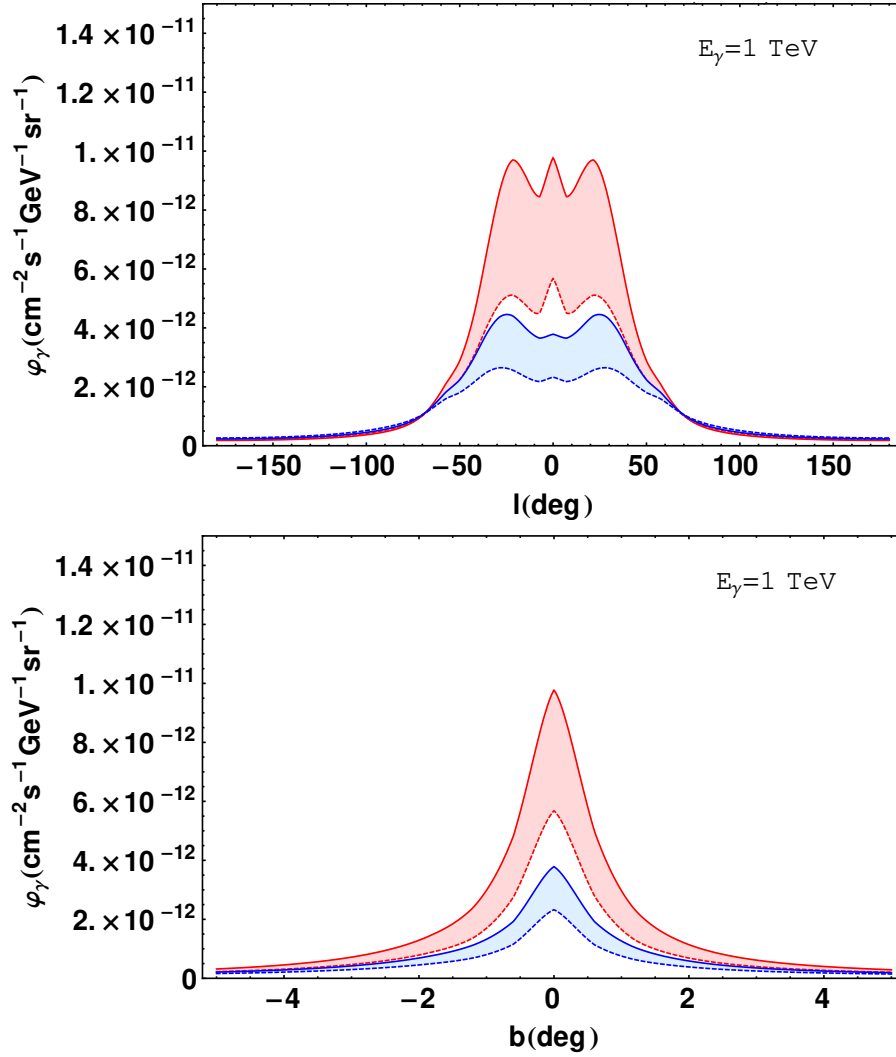


FIGURE 4.3: The diffuse HE gamma-ray flux at  $E_\gamma = 1 \text{ TeV}$  as a function of the Galactic longitude  $l$  (for  $b = 0$ ) (upper panel), and Galactic latitude for  $l = 0$  (lower panel) obtained by assuming that the CR spectrum is position-independent (blue lines) and by implementing CR spectral hardening in the inner Galaxy (red lines) as described by Eqs.(4.4),(4.15). Solid and dashed lines (in each group) are obtained by assuming that the CR spatial distribution follows that of SNR with smearing radius  $R = 1 \text{ kpc}$  and  $R = \infty$ , respectively. Plots obtained with results published in Cataldo et al., 2019.

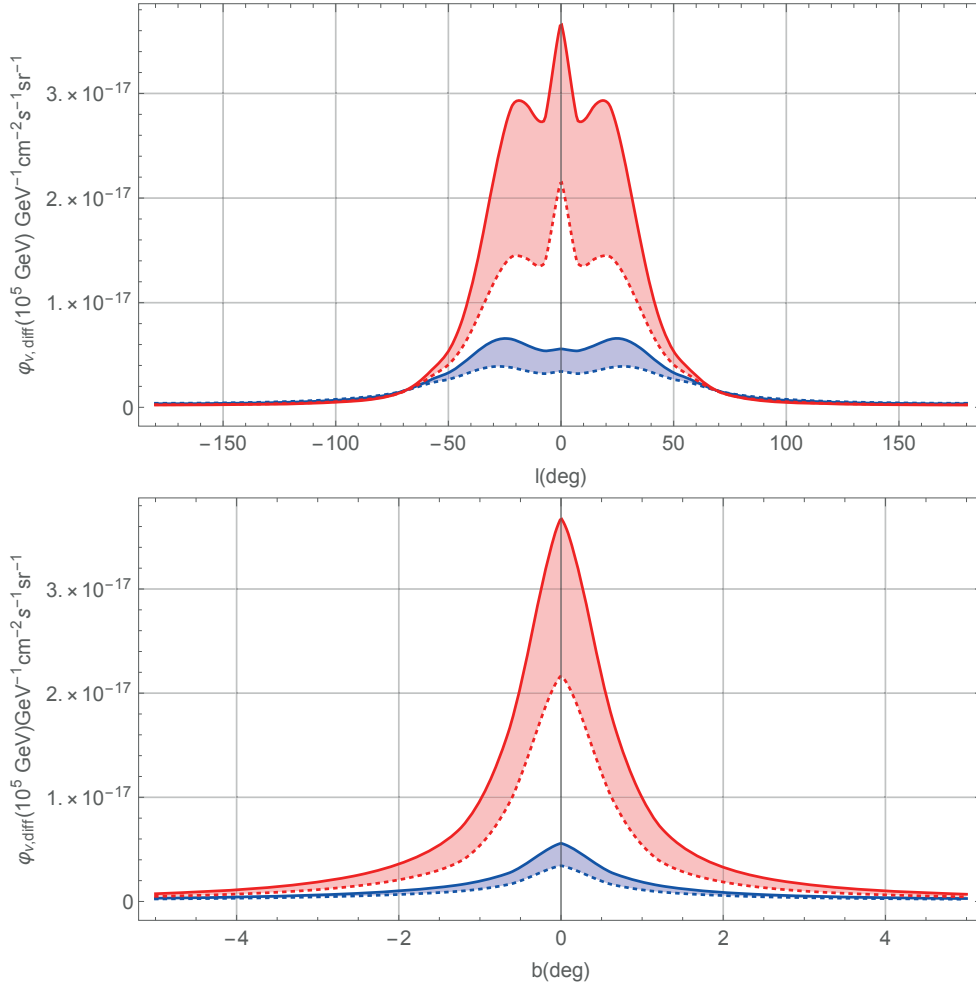


FIGURE 4.4: The diffuse HE neutrino flux at  $E_\gamma = 100$  TeV as a function of Galactic longitude for  $b = 0$  (upper panel), and latitude for  $l = 0$  (lower panel) obtained by assuming that the CR spectrum is position-independent (blue lines) and by implementing CR spectral hardening in the inner Galaxy (red lines) as described by Eqs.(4.4),(4.15). Solid and dashed lines (in each group) are obtained by assuming that the CR spatial distribution follows that of SNR with smearing radius  $R = 1$  kpc and  $R = \infty$ , respectively.

in the flux due to CR spatial distribution that we conservatively represent as the width of the coloured bands in the figure. Additional uncertainty sources are the normalization of the local CR flux at our energies of interest; the distribution of gas in the Galaxy for which we use the same input as *GALPROP*. All these are expected to produce a total error smaller than the difference between red and blue lines in the figure, suggesting that effects of CR hardening can be probed by TeV scale gamma-ray observations of the Galactic central region.

## 4.2 Resolved source contribution

At energies in the TeV range and at the low Galactic latitudes, a measurement of the large-scale diffuse  $\gamma$ -ray emission appears challenging regarding sensitivity and analysis methodology. The emissions of both diffuse CR interactions and sources appear comparable and therefore is difficult to isolate one component from the other. Considering for instance the diffuse estimation given by the H.E.S.S. collaboration (Sec.3.3.1), this appears strongly depending on the source distribution (Fig.3.11). The estimation difficulties are also due to a high presence of extended TeV sources which are more problematic to be resolved due to the applied background subtraction method (Abramowski et al., 2014) and are therefore more easily assimilated to the large-scale diffuse emission. For this reason, a direct comparison between our diffuse models and the diffuse measurements at these energies is not the best possible procedure given such a biased estimation of the diffuse from experimental observations. We therefore construct a complete model that includes both contributions of interstellar emission and sources and we compare it with the total flux observed by the various experiments.

The total flux of HE neutrinos and gammas produced in our Galaxy can be written respectively as:

$$\varphi_{\nu,\text{tot}} = \varphi_{\nu,\text{diff}} + \varphi_{\nu,S}; \quad (4.16)$$

$$\varphi_{\gamma,\text{tot}} = \varphi_{\gamma,\text{diff}} + \varphi_{\gamma,S} + \varphi_{\gamma,\text{IC}}; \quad (4.17)$$

where  $\varphi_{\nu,\text{diff}}$  and  $\varphi_{\gamma,\text{diff}}$  are the diffuse fluxes;  $\varphi_{\nu,S}$ ,  $\varphi_{\gamma,S}$  is the flux produced by sources and  $\varphi_{\gamma,\text{IC}}$  indicates the contribution due to inverse Compton emission by diffuse HE electrons. The diffuse emission is calculated as described in the previous Section. With the term 'sources', we refer here to all the contributions produced within or close to an acceleration site by freshly accelerated particles that potentially have (a part from cut-off effects) harder spectra than the diffuse component. For the source flux we decided to use the the HESS-GPS catalogue (Abdalla et al., 2018a) (already introduced in the previous Chapter). The experiment H.E.S.S. is the most useful for our studies for many reasons that will be clarified along the discussion in this and the next Chapters. For the purpose of this treatment we chose the HGPS because it is focused on the central Galactic region, i.e. for  $-60^\circ < l < 60^\circ$ , where the effect of the hardening is more pronounced and can be therefore tested.

Due to the largest length scale of electron interaction respect to protons, the inverse Compton emission from the Galactic disk is assumed to be extended to larger latitudes. Hence, the background subtraction method operated by the H.E.S.S. collaboration is expected to provide an exclusion of the 95% of IC TeV production. Thus, we do not include the IC contribution in our estimation.

The HGPS includes 78 VHE sources observed in the longitude range  $-110^\circ \leq l \leq 60^\circ$  and latitudes  $|b| < 3^\circ$ , measured with an angular resolution of  $0.08^\circ$  and a

sensitivity  $\lesssim 1.5\%$  Crab flux for point-like objects. Nevertheless, we need to always keep in mind that the H.E.S.S. sensitivity profile varies according to flux and source-size and that the catalogue can be considered complete only for sources with flux ( $> 1$  TeV) above  $\Phi_{\text{th}} = 10\% \Phi_{\text{CRAB}}$  (Sec.3.3.1). This must be taken into account for our estimation and future comparisons when defining the term  $\varphi_{\gamma,S}$  which, more precisely, constitutes the sum of the resolved source flux plus an unresolved source contribution. We will refer to the flux produced by *resolved* gamma-ray sources, with  $\varphi_{\gamma,S}^{(r)}$  which in this treatment is evaluated by using the H.E.S.S. survey.

In the catalogue, extended sources are described with Gaussian profiles in  $l$  and in  $b$ , centered at the source coordinates and with size  $\sigma$  reported in the catalogue. The source spectrum is calculated in the energy range  $0.1 \leq E_{\gamma} \leq 100$  TeV by using a power law or a power-law with an exponential cutoff with best-fit parameters reported in the online material of Abdalla et al., 2018a.

We start from these gamma-ray observations, and convert them into neutrino source contribution:  $\varphi_{\nu,S}$  under the hadronic hypothesis and by using the relations reported in Eqs.(1.56), (1.57), (1.58), (1.59) of Chapter 1. We will define the source term starting from the gamma-ray resolved flux, however, how we will see, a possible introduction of an additional neutrino flux coming from unresolved gamma-ray flux could only strengthen our results in the neutrino sky.

We consider the spectral parameters given by the HGPS catalogue and obtain the spectral parameters for each source of neutrinos, and finally we compute each source flux. This procedure is done assuming that all conditions listed in Sec.1.4 are satisfied for all sources considered. Except for the first one, all of the requirements can be considered in fact valid for all sources collected in the HGPS catalogue (Kappes et al., 2007). Since the majority of the sources observed by H.E.S.S. are not yet identified, we know very little on their nature and therefore we do not know the dominant processes occurring inside them. For this reason we assume to give a maximal estimation for the neutrino source contribution. We assume indeed that the limit condition of a fully hadronic production is verified for every source considered, and we convert the gamma-ray source fluxes into neutrino fluxes under this hypothesis.

Fig.4.5 shows the longitudinal distribution of gamma-ray sources (upper panel) and of the obtained neutrino sources (lower panel) in the longitudinal range  $-60^{\circ} < l < 60^{\circ}$  for  $b = 0$ . Each neutrino source is spatially expressed by a Gaussian in the  $l$  and  $b$  coordinates, centered in the gamma-ray source position, with width equal to the width of the corresponding gamma-ray source, given in the catalogue. Both plots are obtained at the fixed energy of 1 TeV.

### 4.3 Comparisons

The sum of the gamma-ray flux produced by diffuse component and resolved sources provides a lower estimate of the total gamma-ray emission that can be compared with the observational determinations of the total gamma-ray flux at TeV energies obtained by H.E.S.S. (Abramowski et al., 2014), HAWC (zhou2017lgv), Argo-YBJ (Bartoli et al., 2015) and Milagro (Abdo et al., 2008a).

The gamma-sky comparison is reported in Fig.4.7. The four experiments have different observation windows, angular resolutions and median observation energies, as it is indicated in the figure. In particular, the H.E.S.S. Galactic Plane Survey (Abramowski et al., 2014) (first panel from the top of Fig.4.7) measures the profile of gamma-ray emission, averaged for latitudes  $|b| < 2^{\circ}$ , in the longitude range

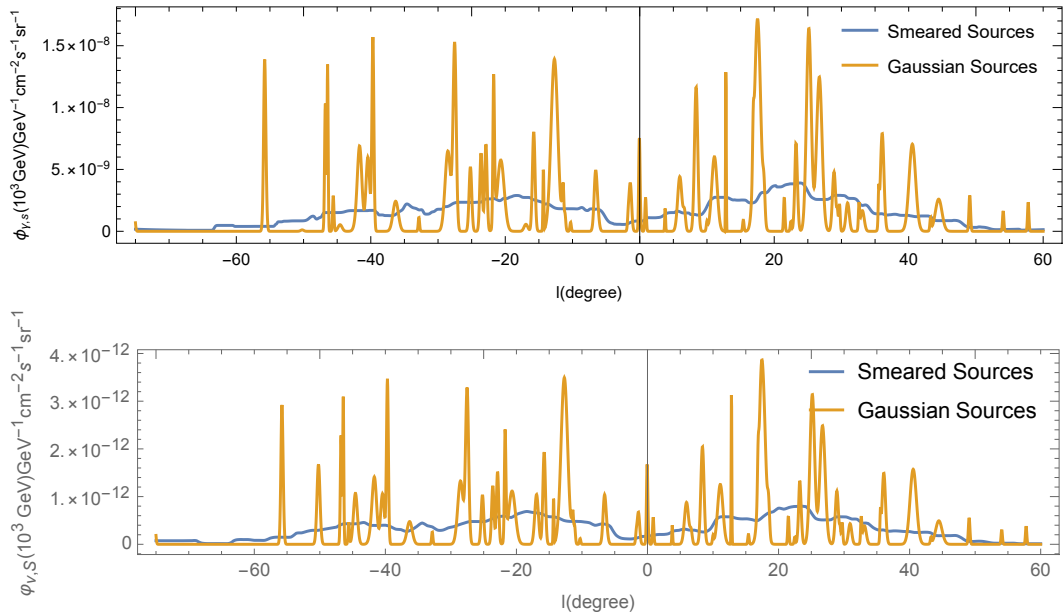


FIGURE 4.5: Upper panel: HGPS gamma-ray sources as parameterized in Abdalla et al., 2018b; lower panel: corresponding neutrino sources in the hypothesis of a dominant hadronic regime.

$-75^\circ < l < 60^\circ$ , for a photon median energy  $E_\gamma = 1$  TeV. The data are provided in angular bins  $\delta l \sim 0.6^\circ$ . In order to remove possible background contributions, the total emission from the Galactic plane is obtained by H.E.S.S. as the excess with respect to the average signal at absolute latitudes  $|b| \geq 1.2^\circ$  (Abramowski et al., 2014). We apply the same background reduction procedure to our predictions. For each considered case, we report in the figure the excess along the Galactic plane (i.e. in the region  $|b| < 1.2^\circ$ ) with respect to the average emission in the region  $1.2^\circ < |b| < 2^\circ$ .

The HAWC experiment recently presented the preliminary longitudinal gamma-ray profile in the angular region  $0^\circ < l < 60^\circ$  for a photon median energy  $E_\gamma = 7$  TeV (second panel in Fig.4.7). The emission is averaged over Galactic latitudes  $|b| < 2^\circ$  and it is provided in angular bins  $\delta l \sim 2^\circ$  (zhou2017lgy). The Argo-YBJ experiment measures the total gamma-ray emission in the overlapping longitudinal range  $25^\circ < l < 60^\circ$  for  $E_\gamma = 600$  GeV (third panel of Fig.4.7). The measured flux is averaged over Galactic latitudes  $|b| < 5^\circ$  and the data are presented in longitudinal bins  $\delta l \sim 8^\circ$  (Bartoli et al., 2015). At higher energy,  $E_\gamma = 15$  TeV, the Milagro experiment reports the total gamma-ray emission in the region  $30^\circ < l < 60^\circ$  (lower panel of Fig.4.7). The observed flux is averaged over Galactic latitudes  $|b| < 2^\circ$  and it is provided in angular bins  $\delta l \sim 2^\circ$  (Abdo et al., 2008a).

In order to facilitate the comparison among the different measurements, we rebinned the data from H.E.S.S., HAWC and Milagro over longitudinal bins  $\delta l \sim 10^\circ$  that are comparable with Argo-YBJ angular resolution. The re-binning procedure is also done to avoid large fluctuations of the signal thus making visually clear the excess (or the deficit) of the observed flux with respect to our predictions. It should be noted that our calculations of the diffuse gamma-ray component are intended to describe the main features of the interstellar emission, but they are not expected to reproduce the small angular scales fluctuations of the observed signal, being based on (relatively) smooth gas and CR distributions. The data points obtained after the re-binning procedure are reported in Fig.4.7. They are located in the bin midpoint and

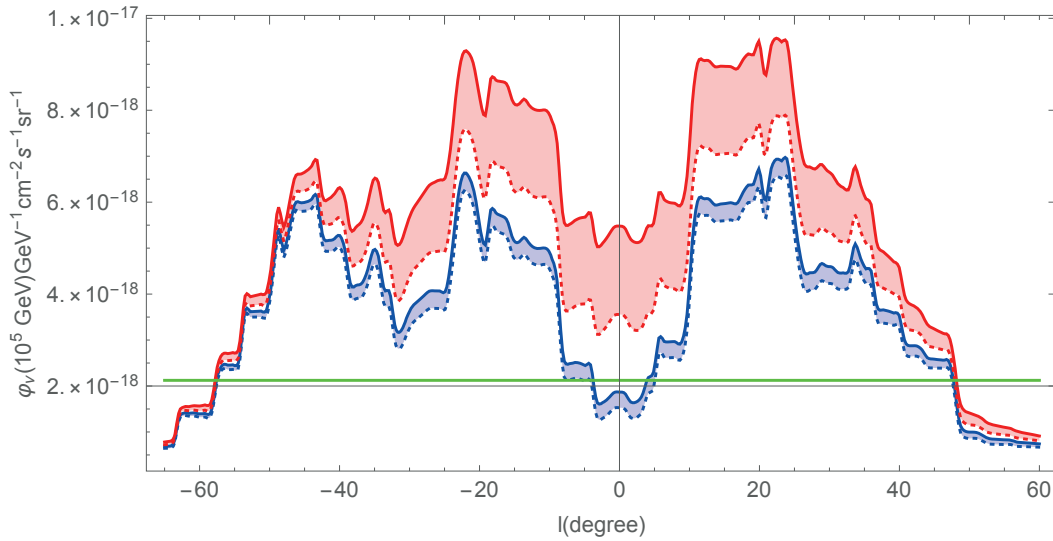


FIGURE 4.6: Longitudinal distribution of total neutrino flux at 100 TeV, in the range  $-65^\circ < l < 60^\circ$  ( $b = 0$ ), obtained for the 4 cases. Blue lines: standard cases, red lines: hardening cases. Solid and dotted lines correspond to the two diffusion radii  $R = 1$  kpc, and  $R = \infty$  respectively. The green line represents the isotropic fit of the HESE signal measured by IceCube (Abbasi et al., 2020b).

have vertical error bars that include systematic and statistical errors of the measured fluxes. The two errors are summed in quadrature and correspond to a total uncertainty equal to 30% for H.E.S.S. Abdalla et al., 2018a, 50% for HAWC zhou2017lgv, 27% for Argo Bartoli et al., 2015 and 36% for Milagro Abdo et al., 2008a. The grey dashed lines (not given for Argo-YBJ) are obtained by performing a moving average of the experimental data with the previously discussed  $\delta l$  and are intended to show the longitudinal dependence of the total galactic emission measured by each experiment.

The red and blue curves displayed in Fig.4.7 give the sum of the gamma-ray flux produced by sources in H.E.S.S. catalogue and diffuse emission, averaged in the Galactic latitudinal windows considered by each experiment and then smeared in longitudinal bins  $\delta l = 10^\circ$  for H.E.S.S., HAWC and Milagro and  $\delta l = 8^\circ$  for Argo-YBJ. The red lines take into account CR spectral hardening hypothesis while blue lines correspond to the standard assumption. Solid and dashed lines are obtained (in both cases) by assuming that the CR spatial distribution follows that of SNRs with smearing radius equal to  $R = 1$  kpc and  $R = \infty$  (see Eq.(4.13)), respectively. The green dotted lines in the various panels show the contribution to the total flux which is only ascribed to sources resolved by H.E.S.S.

In order to discuss the behaviour of our gamma-ray predictions as a function of energy, we select the observation window  $30^\circ < l < 60^\circ$  and  $-2^\circ < b < 2^\circ$  where all the experiments are sensitive. In this region, we compare the gamma-ray fluxes obtained in this work with the measured ones at different energies. The results are reported in Fig.4.8.

We compare the total neutrino flux as defined in Eq.(4.16) with the IceCube results (Abbasi et al., 2020b). The neutrino comparison is reported in Fig.4.6. We show the comparison with the isotropic fit of the 7.5 years HESE data set from the last release (Abbasi et al., 2020b). We decided to use the HESE events for the spatial comparison since this is data set sensible to the sky region that includes the Galactic

center, hence the region of our interest. Again, in order to facilitate the comparison, the source flux is obtained applying a re-binning of the data over longitudinal bins of  $15^\circ$  (Fig.4.5), comparable with the angular resolution of showers (dominant topology among starting events).

Finally, in Fig.4.9 we compare the spectra of integrated fluxes on the overall sky with the spectra obtained for the two IceCube data sets: HESE and through-going muons.

## 4.4 Discussion

The main conclusions that we can infer from the neutrino comparisons shown in Fig.4.6 and 4.9 are the following.

- Our total Galactic neutrino flux integrated over the whole sky, regardless the model considered, gives a subdominant contribution respect to the total signal. This is expected since the still missing evidence for the Galactic contribution in the IceCube signal which is predominantly extragalactic. For the overall integrated fluxes we obtain that the standard scenario is  $\sim 4 - 4.5\%$  of the isotropic astrophysical flux, while introducing the hardening the percentage is  $\sim 6 - 8\%$  according to the spatial CR diffusion considered ( $R = 1$  kpc and  $R = \infty$  respectively). This is in agreement with the upper limit given by the collaboration:  $< 14\%$  (Aartsen et al., 2017).
- However, there is a portion of the sky that includes the Galactic center where the model flux appears to exceed the isotropic signal. This is true for every model considered, both standard and with hardening, as shown in Fig.4.6 where we report the longitudinal distribution (for  $b = 0$ ) of the fluxes of our models compared with the isotropic HESE signal (green line).
- In Fig.4.9, where the spectra of the angle integrated fluxes are shown, again we see how the IceCube signal is significantly higher than the diffuse Galactic flux predicted even assuming an harder emission from the central part of the Galaxy.

Finally, our model can be considered approximately equivalent to the  $KRA_\gamma$  model by Gaggero et al., 2015b, Gaggero et al., 2017, since it includes the same spectral dependence and a more data-driven expression of the local CR spectrum. We can expect therefore comparable constraints on our model as obtained in Albert et al., 2018 by the joint likelihood test performed using seven years IceCube track data and ten years of ANTARES track and shower data.

In the following are listed the most remarkable conclusions that can be derived from the gamma-ray comparisons of Fig.4.7 and 4.8 where the main features of the gamma-ray signal in the TeV domain are reproduced by our model both as function of the observation angle and energy.

- According to our estimates, the emission from resolved sources accounts for a large fraction of the total flux in the TeV domain. In the angular ranges indicated in Fig.4.7, the gamma-ray sources included in the HESS-GPS catalogue are responsible for 30%, 46%, 44%, 44% of the total signal observed by Argo-YBJ, HESS, HAWC and Milagro, respectively.

- Another interesting feature that emerges is that the gamma-ray flux from the Galactic plane at 1 TeV is not symmetric with respect to Galactic center, being the flux observed by H.E.S.S. in the longitude range  $0^\circ \leq l \leq 60^\circ$  about 30% larger than that observed in  $-60^\circ \leq l \leq 0^\circ$ . This asymmetry is partially reproduced by our calculations as a result of the inclusion of resolved sources. In our model, diffuse emission is indeed invariant with respect to  $l \rightarrow -l$  transformation, being based on cylindrically symmetric gas and CR distribution. In order to reproduce the observed difference, one should break cylindrical symmetry, including e.g. a 3D gas distribution and/or the effects of molecular clouds (Aharonian et al., 2018).
- The comparison between theoretical predictions and observational data allows us to obtain interesting constraints on the CR distribution. Indeed, the predicted fluxes in the presence of CR hardening saturate or exceed the observed signal in certain regions of the sky. In particular, the largest prediction considered, which is obtained by including CR spectral hardening and by assuming that the CR spatial distribution follows that of SNR with  $R = 1$  kpc smearing radius (red solid lines), account for 95%, 104%, 104% and 118% of the total signal observed by Argo-YBJ, HESS, HAWC and Milagro in the angular ranges indicated in Fig. 4.7, respectively. This is hardly acceptable on physical basis considering that the calculated flux provides a lower limit for the total gamma-ray emission and an additional non negligible contribution is expected to be provided by non-resolved sources and IC.

## 4.5 Unresolved sources

Due to the more detailed and extensive information provided by current detectors, for the gamma-ray messenger we can proceed with a more refined study which for neutrinos instead is not possible with present data. For gamma-rays we give indeed estimation of the unresolved source contribution to the diffuse emission measured by the H.E.S.S. detector in its observational window.

At TeV energies, we naturally expect that unresolved sources account for a relevant fraction of the total gamma-ray signal because a small portion of the Galaxy is resolved by the H.E.S.S. observatory while sources are expected to be distributed in the entire Galaxy. It is e.g. discussed in Abdalla et al., 2018a (and in our Sec. 3.3.1) that point-like objects with intrinsic luminosity above 1 TeV equal to  $L = 10^{34}$  erg s<sup>-1</sup> can be observed up to a median distance  $\bar{D} \sim 7$  kpc. The observational horizon can be, however, much smaller (up to a factor 3) for extended sources.

As already mentioned, the total flux produced by sources should include also the contribution due to very faint and/or extended sources that are not resolved by H.E.S.S. We can express the total source contribution as:

$$\varphi_{\gamma,S} = \varphi_{\gamma,S}^{(r)} (1 + \eta); \quad (4.18)$$

where the parameter  $\eta$ , that depends in principle on the observation direction and energy, quantifies the relative contribution of unresolved objects to the total source flux. Observing Fig. 3.9 we can assume that the H.E.S.S. sensitivity limit for extended objects is  $\simeq 10\%$  of the CRAB flux ( $\Phi_{\text{CRAB}} = 2.26 \cdot 10^{-11}$  cm<sup>-2</sup> s<sup>-1</sup>) integrated above 1 TeV (Abdalla et al., 2018a). As stated from the collaboration, indeed, above this flux threshold ( $\Phi_{\text{th}} = 10\% \Phi_{\text{CRAB}}$ ) the catalogue can be considered complete (Abdalla et

al., 2018a). By taking this into account we can provide an estimate of the  $\eta$  parameter as a function of the assumed sources intrinsic luminosity  $L$ .

Taking the Crab emission spectrum as a reference, a source at a distance  $D$  with intrinsic luminosity  $L$  ( $> 1$  TeV) produces a flux at Earth given by:

$$\Phi = \Phi_{\text{CRAB}} (L/L_{\text{CRAB}}) (D/D_{\text{CRAB}})^{-2}; \quad (4.19)$$

where  $L_{\text{CRAB}} = 5 \cdot 10^{34} \text{ erg s}^{-1}$  and  $D_{\text{CRAB}} = 2 \text{ kpc}$  are the Crab nebula luminosity and distance, respectively. The produced flux is larger than  $\Phi_{\text{th}}$  only if the source distance is  $D \leq \bar{D}(L)$  where:

$$\bar{D}(L) \equiv 6.3 \text{ kpc} \sqrt{L/L_{\text{CRAB}}}. \quad (4.20)$$

The above estimate confirms that a relatively small region of the Galaxy is fully resolved by H.E.S.S., even if sources are assumed to be very luminous.

In the assumption of fixed source intrinsic luminosity  $L$ , the cumulative contribution of sources to the gamma-ray flux for  $E_\gamma \geq 1$  TeV observed from the direction  $\hat{n}$  can be calculated as:

$$\varphi_{\gamma,S}(\hat{n}, L) = \Phi_{\text{th}} \bar{D}(L)^2 \int_0^\infty dl f_S(\vec{r}_\odot + \hat{n}l); \quad (4.21)$$

where  $f_S(\vec{r})$  represents the source distribution in the Galaxy. The total flux can be divided in two contributions, "fully resolved" and "partially resolved" sources. In this second category are considered all sources with flux below the threshold. The contribution of fully resolved sources with  $\Phi \geq \Phi_{\text{th}}$  can be calculated as:

$$\varphi_{\gamma,S}^{(fr)}(\hat{n}, L) = \Phi_{\text{th}} \bar{D}(L)^2 \int_0^{\bar{D}(L)} dl f_S(\vec{r}_\odot + \hat{n}l); \quad (4.22)$$

i.e. by the integral extended from 0 to the maximum distance  $\bar{D}(L)$  at which the source is observable. Following this prescription, the flux from sources with  $\Phi \leq \Phi_{\text{th}}$ , that maybe are not resolved being very faint and/or extended, is instead given by:

$$\varphi_{\gamma,S}^{(pr)}(\hat{n}, L) = \Phi_{\text{th}} \bar{D}(L)^2 \int_{\bar{D}(L)}^\infty dl f_S(\vec{r}_\odot + \hat{n}l). \quad (4.23)$$

Since the cutoff distance  $\bar{D}(L)$  can be relatively small with respect to the Galactic scales, we expect that the ratio  $\varphi^{(pr)}/\varphi^{(fr)}$  may be large, in particular when looking at small Galactic latitudes where the source density along the line-of-sight is not expected to vanish for large distances. In order to estimate the relevance of "partially resolved" contribution, we calculate the ratio:

$$\mathcal{R}(L) = \frac{\Phi_S^{(pr)}(L)}{\Phi_S^{(fr)}(L)}; \quad (4.24)$$

where the fluxes:

$$\begin{aligned} \Phi_S^{(pr)}(L) &\equiv \int_{\Delta\Omega} d\Omega \varphi_{\gamma,S}^{(pr)}(\hat{n}, L); \\ \Phi_S^{(fr)}(L) &\equiv \int_{\Delta\Omega} d\Omega \varphi_{\gamma,S}^{(fr)}(\hat{n}, L); \end{aligned}$$

give the "partially resolved" and "fully resolved" source emission integrated over the

angular region  $\Delta\Omega$  defined as  $-60^\circ \leq l \leq 60^\circ$  and  $-3^\circ \leq b \leq 3^\circ$ . If we take  $L = L_{\text{CRAB}}$  and we assume that the source distribution  $f_S(\vec{r})$  is proportional to the SNR number density given in Green, 2015, we obtain  $\mathcal{R} = 0.9$ . By considering a uniform cylindrical source distribution with radius  $r = 15$  kpc and thickness  $H = 0.2$  kpc, we obtain  $\mathcal{R} = 0.8$ .

The above results can be used to estimate the contribution to total gamma-ray flux by sources unresolved by H.E.S.S. In the angular region  $\Delta\Omega$ , the H.E.S.S. experiment observes 29 sources with fluxes larger than  $\Phi_{\text{th}} = 10\% \Phi_{\text{CRAB}}$ , corresponding to a "fully resolved" flux  $\Phi_S^{(fr)} = 7.0 \Phi_{\text{CRAB}}$ . This represents a fraction  $\omega = 0.84$  of the cumulative resolved flux  $\Phi_S^{(r)}$  that includes 42 additional sources with  $\Phi \leq \Phi_{\text{th}}$ . Taking this into account and considering that the total source flux  $\Phi_{\gamma,S}$  is given by the sum of fully resolved and partially resolved contribution, we obtain:

$$\Phi_{\gamma,S} = \Phi_{\gamma,S}^{(r)}(1 + \eta); \quad (4.25)$$

where the parameter  $(1 + \eta) \equiv \omega + \omega\mathcal{R}$  is defined as in Eq.(4.18) and can be relatively large. If we take  $L = L_{\text{CRAB}}$  we obtain  $\eta \simeq 0.6$ .

So the integrated contribution of unresolved sources in the angular region  $|l| \leq 60^\circ$  and  $|b| \leq 3^\circ$  is found to be  $\eta \simeq 60\%$  of the resolved signal, if we assume that source distribution is proportional to the SNR number density Green, 2015 and sources have intrinsic luminosity  $L = L_{\text{CRAB}}$ . Moreover, the parameter  $\eta$  is a decreasing function of  $L$ , i.e. larger values for  $\eta$  are obtained for smaller sources intrinsic luminosity, since the horizon for resolved sources decreases (see Eq.(4.20)) and thus a smaller portion of the Galaxy is probed by H.E.S.S. We thus understand that the above value represents a lower limit of the luminosity-averaged contribution unless the source luminosity distribution extends well above  $L_{\text{CRAB}}$ .

Despite the large uncertainty, the above estimate allows us to conclude that resolved and unresolved sources plausibly give comparable contributions to the total gamma-ray resolved signal, in substantial agreement with results presented by Egberts, 2018. However, the unresolved prediction cannot be obtained as a function of the observation direction and energy. For this reason, we do not include the unresolved sources contribution when comparing of observational data of Argo-YBJ, H.E.S.S., HAWC and Milagro experiments with our theoretical estimates.

We can however compare the expected percentages. If we consider the lowest prediction in the presence of CR spectral hardening, that is obtained by considering a smooth CR space distribution (i.e. with a smearing radius  $R = \infty$ ) and corresponds to the red dashed lines in Fig.4.7, we obtain that  $\eta$  should be lower than 0.92, 0.51, 0.45 and 0.14 in the angular ranges and at the gamma-ray energies probed by Argo-YBJ, H.E.S.S., HAWC and Milagro, respectively.

The obtained limits for unresolved sources contribution can be compared with the expected values for  $\eta$ . In the HGPS observational window, we obtained  $\eta \sim 0.6$  for HE gamma-ray sources distributed as SNRs and with intrinsic luminosity ( $> 1$  TeV) comparable to that of Crab nebula. In conclusion, by comparing the estimated value for  $\eta$  with the constraint  $\eta \leq 0.51$  that is obtained from H.E.S.S. data, we are lead to state that a potential tension exists between the CR spectral hardening hypothesis and observational results, unless we assume HE gamma-ray sources to have a relatively large intrinsic luminosity, greater than or comparable to that of Crab nebula.

The estimation of unresolved source contribution, although challenging, provides insights for further in-dept population studies. This result represents indeed

the starting-point for our next work.

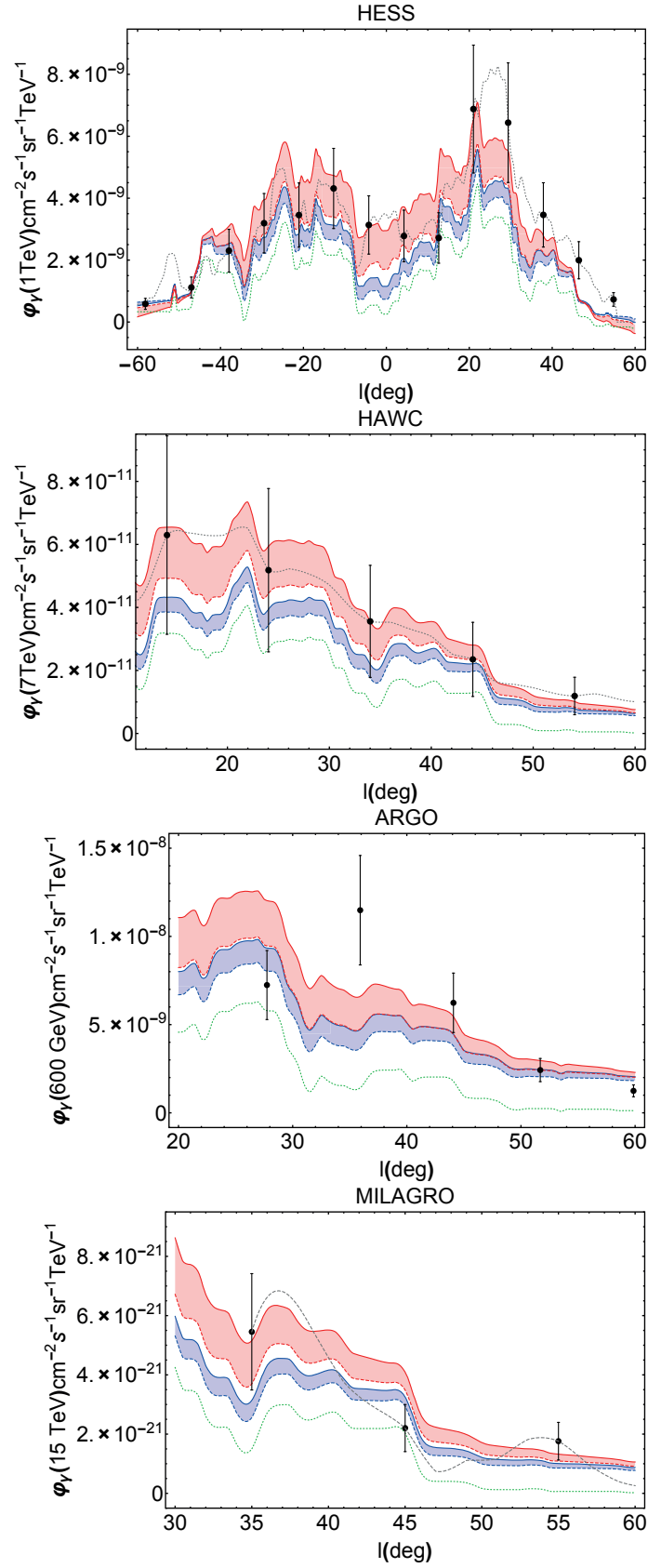


FIGURE 4.7: The total gamma fluxes predicted as a function of the Galactic longitude  $l$  following the same color prescription as in Fig.4.3. The green dotted line represents the contribution of resolved sources. For a detailed description of the plots see the text. Figure taken from Cataldo et al., 2019.

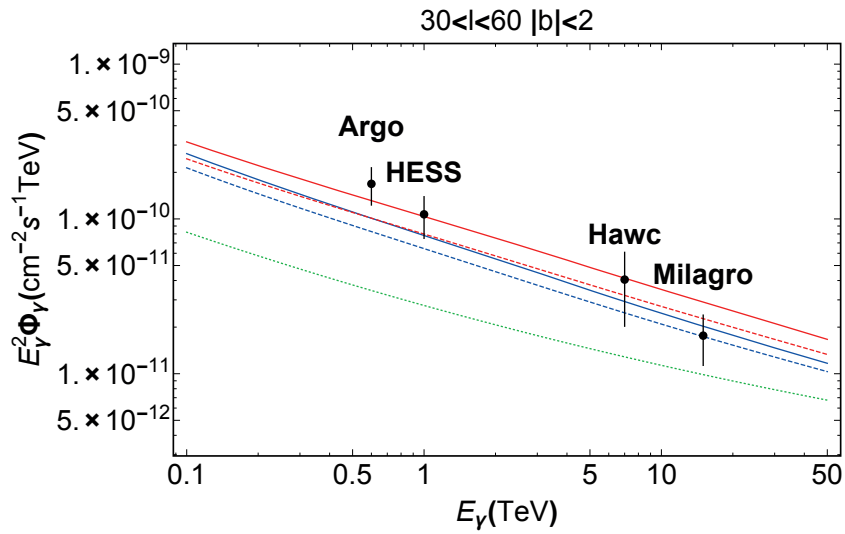


FIGURE 4.8: The total gamma flux as a function of the energy for the four different cases considered. The same quantity as measured by H.E.S.S., HAWC, Argo-YBJ and Milagro is also displayed for a comparison. The green dotted line represents the contribution due to resolved sources. Figure taken from Cataldo et al., 2019

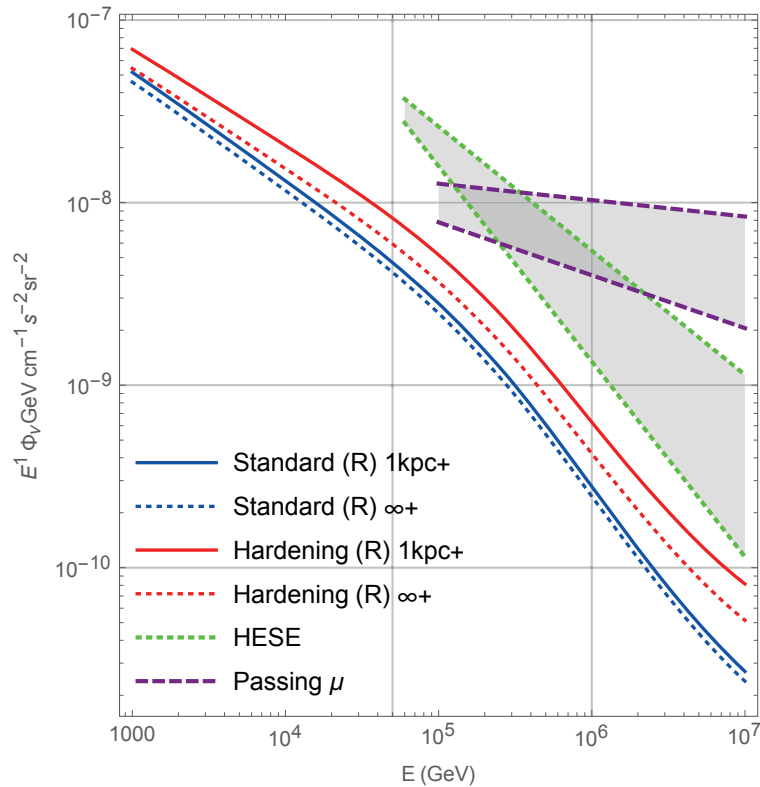


FIGURE 4.9: The total neutrino flux as a function of the energy for the different cases. The same quantity as measured by IceCube for starting events and through-going muons events is displayed in green and purple respectively.

## Chapter 5

# Source contribution to the VHE Galactic emission

One of the main conclusions inferred from our previous work is that the unresolved Galactic sources at TeV energies may have a relevant contribution to the total Galactic gamma-ray emission. In this Chapter we provide a refinement of this estimation by performing a population study of the H.E.S.S. Galactic Plane Survey. However, we can infer much more information from this catalogue so this work led us to several more interesting developments.

Even if the knowledge of our Galaxy in the TeV domain has greatly progressed, several questions remain unsolved. For instance, in most cases, we are not able to determine whether the observed TeV gamma-ray signals are produced by leptonic or hadronic mechanisms. This limits the possibility to use the gamma-neutrino connection, implied by hadronic production, to estimate the neutrino signal from gamma-ray observed sources. In addition, although different astrophysical objects, such as Supernova Remnants (SNRs) and Pulsar Wind Nebulae (PWNe), can generate TeV  $\gamma$ -rays, we still don't know which (if any) class of sources dominates the Galactic emission. Recent observations of Geminga and PSR B0656+14 by Milagro (Abdo et al., 2009) and HAWC (Abeysekara et al., 2017a), provided evidence for a new class of objects powered by pulsar activity, the so-called "TeV halos", that could potentially explain a large fraction of bright TeV sources observed in the sky (Sudoh, Linden, and Beacom, 2019).

We perform our study with the goal of also addressing some of these open issues. We analyze the flux, latitude and longitude distributions of sources detected by H.E.S.S. in order to infer the properties of the TeV source population. To avoid selection effects, we include in our analysis the brightest sources with a flux above 1 TeV larger than 10% of the CRAB flux. By performing a general analysis based on suitable assumptions for the source space and luminosity distributions, we show that the HGPS data permit to estimate with relatively good accuracy general properties of the Milky Way. We give indeed the total Milky Way luminosity produced by TeV sources and the total Galactic flux due to both resolved and unresolved sources in the H.E.S.S. observational window (OW). Finally, this allows us to quantify the contribution of unresolved sources to the total flux, confirming our first estimation that unresolved contribution is possibly the dominant component of the large-scale diffuse signal observed at TeV by H.E.S.S. (Abramowski et al., 2014) and Milagro (Atkins et al., 2005). Our analysis of the TeV source population improves and complements previous discussions on the subject, such as e.g. the one provided by Casanova and Dingus, 2008, by considering different aspects and an original approach and by taking advantage of more recent observational data.

This Chapter is based on the original paper Cataldo et al., 2020.

## 5.1 Why H.E.S.S.?

In the observational window probed by the telescope H.E.S.S. ( $-110^\circ \leq l \leq 60^\circ$ ,  $|b| < 3^\circ$ ) and above its flux threshold ( $\sim 1.5\% \Phi_{\text{CRAB}}$ ), the catalogue contains 78 VHE gamma-ray sources with a spectrum of emission extending above 1 TeV (Abdalla et al., 2018a). The flux, longitudinal, and latitudinal distributions of the sources collected are represented by the histograms in Fig. 5.1. The blue blocks are all 78 sources reported in the HGPS, while the magenta ones show the sources observed with flux above the threshold  $\Phi_{\text{th}} = 10\% \Phi_{\text{CRAB}}$  used for our analysis. Above this threshold the catalogue can be considered essentially complete, as it is discussed in Abdalla et al., 2018b and explained in Chapter 3. This sample consists of 32 sources with the following identification: 3 firmly associated with SNRs (Vela Junior, RCW 86, RX J1713.7-3946), 2 objects showing evidence of both shell and nebular emission which we refer to as "composite", 8 associated with PWNe, and 19 unidentified, (Fig. 5.2).

There are several reasons why the HGPS is the best choice for our studies. At energies of our interest, H.E.S.S. provides the most complete catalogue of gamma-ray Galactic sources (see also Sec. 3.3.1). Indeed, this telescope covers an angular region that is focused on the Galactic disk and contains the Galactic center. This region of the sky contains most of potential sources located in the Galactic plane, if we assume the source distribution to be parameterized as SNR or PWN distributions presented in Green, 2015 and Lorimer et al., 2006, respectively (and described in this thesis in Sec. 2.1.1 and 2.1.3). Indeed by integrating the source distribution over the total observational window covered by H.E.S.S. we obtain a value which is around  $\sim 0.8$  (see Eq. (5.22)). This is true for both the distributions, if normalized to 1 over the total sky.

If we consider the other HE gamma-ray telescopes introduced in Chapter 3 their observational window have instead a smaller coverage on the Galactic disk. The HAWC experiment provides the longitudinal gamma-ray profile in the angular region  $0^\circ < l < 180^\circ$  and  $|b| < 2^\circ$ , for a photon median energy  $E_\gamma = 7$  TeV (Zhou, Rho, and Vianello, 2018). The Argo-YBJ experiment measures the total gamma-ray emission in the longitudinal region  $40^\circ < l < 100^\circ$  and latitudes  $|b| < 5^\circ$  for  $E_\gamma = 600$  GeV (Bartoli et al., 2015). At higher energy,  $E_\gamma = 15$  TeV, the Milagro experiment reports the total gamma-ray emission for longitudes  $30^\circ < l < 110^\circ$  and  $136^\circ < l < 216^\circ$  and for latitudes  $|b| < 10^\circ$  (Abdo et al., 2008a). Considering the same source distributions, the sky regions probed by Milagro, Argo-YBJ, and HAWC contain a smaller fraction of the potential sources in the Galactic plane, equal to  $\simeq 20\%$ ,  $\simeq 20\%$ , and  $\simeq 40\%$ , respectively. In conclusion, the H.E.S.S. Galactic Plane Survey (HGPS) is the best choice for our purposes since it provides optimal sky coverage to perform Galactic population studies.

Another interesting characteristic of the HGPS is the sensitivity analysis provided. As already described in Sec. 3.3.1, the lowest threshold for point-like sources is  $\sim 1.5\%$  of the Crab flux although the sensitivity varies with source size, flux, and position. However, the collaboration assumes completeness of the catalogue over the threshold: 10% of Crab flux for sources with size  $< 1^\circ$ . Meaning that, if small enough, all sources that produce a photon flux above 1 TeV larger than  $10\% \Phi_{\text{CRAB}}$  are supposed to be observable by the detector despite their position in the Galaxy and their angular dimension. As we didn't want to make any prior assumption on the sensitivity of the instrument, we decided to limit our population study only to the sample considered complete, which therefore contains the brightest sources. Moreover, we assume all sources in our model to be below the size threshold of  $1^\circ$

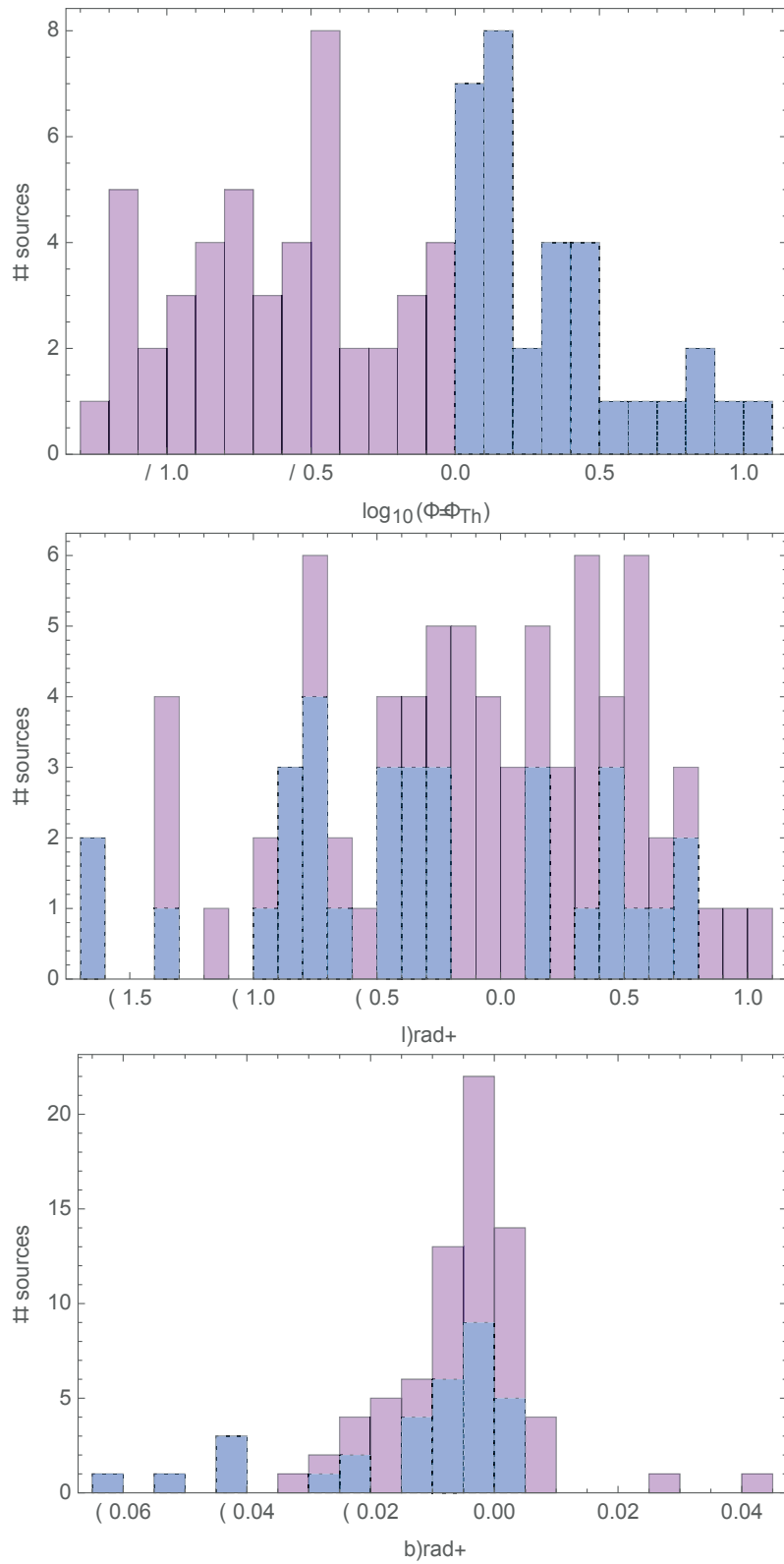


FIGURE 5.1: Histograms of flux, longitude, latitude distributions in the HGPS. Blue blocks: over-threshold sources; pink blocks: below-threshold sources.

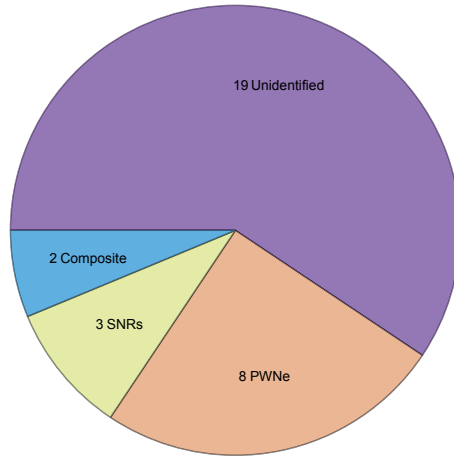


FIGURE 5.2: Pie chart of the identification of 32 sources observed by H.E.S.S. above the flux threshold.

and under this value we perform our analysis in full generality without being forced to hypothesize a prescribed physical dimension for the sources because the angular extension does not discriminate the possible identification. Then, in Sec.5.7 we test the possibility of an exception that consists in very close and very extended sources that cover angular regions larger than  $\sim 1^\circ$  and could escape detection due to background subtraction procedure employed by H.E.S.S. We check that this situation is unlikely and, thus, in most of the cases does not affect our constraints.

## 5.2 Model

The luminosity function of a generic ensemble of sources is defined by the equation:

$$\frac{dN}{d^3r dL} = \rho(\vec{r}) Y(L); \quad (5.1)$$

where the  $\rho(\vec{r})$  is the spatial distribution and  $Y(L)$  is the intrinsic luminosity distribution. To model the flux observed by the H.E.S.S. telescope we need to define the two functions  $\rho(\vec{r})$  and  $Y(L)$  for potential TeV Galactic gamma-ray sources. In this case  $L$  represents the gamma-ray intrinsic luminosity value obtained integrating on the energy range 1 – 100 TeV which is the one probed by H.E.S.S.

In our reference case the spatial distribution is assumed to follow the Galactic distribution of pulsars. As already introduced in Chapter 2 this is well approximated by the function given by Lorimer et al., 2006 of Eq.(2.4). In particular, our spatial distribution  $\rho(r, z)$  (showed in Fig.5.3) is assumed proportional to the one by Lorimer et al., 2006 and conventionally normalized to one when integrated in the entire Galaxy. So along the cylindrical coordinates  $r$  and  $z$  is:

$$\rho(r, z) \propto \left(\frac{r}{r_\odot}\right)^{\alpha_p} \exp\left(-\beta_p \frac{r - r_\odot}{r_\odot}\right) \exp\left(-\frac{|z|}{H}\right). \quad (5.2)$$

For our model we use the parameter values  $\alpha_p = 1.9$  and  $\beta_p = 5$ , obtained in Lorimer et al., 2006 by fitting a sample of pulsars using a model that takes into account a spiral-arm modelling of the Galaxy. While for the  $z$  axis we assumed an exponential scaling with a value  $H = 0.2$  kpc for the disk thickness.

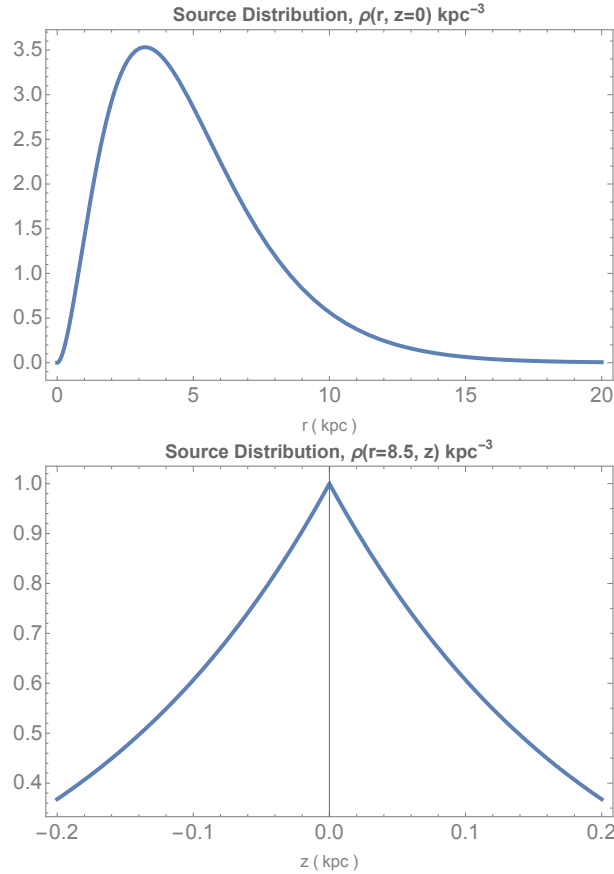


FIGURE 5.3: Galactic pulsar distribution in cylindrical coordinates as in Lorimer et al., 2006, with a disk thickness  $H = 200$  pc.

The intrinsic luminosity function is assumed as a power-law:

$$Y(L) = \frac{\mathcal{N}}{L_{\max}} \left( \frac{L}{L_{\max}} \right)^{-\alpha}; \quad (5.3)$$

that extends in the luminosity range  $L_{\min} \leq L \leq L_{\max}$ . In our study we assume a value  $\alpha = 1.5$  as working hypothesis, since this value can be motivated in the context of a population of gamma-emitting sources connected with pulsar activity, i.e. Pulsar Wind Nebulae (PWNe) and/or TeV halos, as it will be more clear in the next Chapter in which we will physically justify this choice. Other options for the power-law index  $\alpha$  (and other assumptions in the analysis) will be considered later on in order to test the stability of our results.

The number  $\mathcal{N}$  represents the normalization of the function  $Y(L)$  obtained at high-luminosity. It physically represents the number of sources with luminosity  $L_{\max}$  in the logarithmic luminosity interval  $d \ln(L)$ , since the logarithmic luminosity distribution is:

$$\frac{dN}{d \ln L} = \mathcal{N} \frac{L}{L_{\max}} \left( \frac{L}{L_{\max}} \right)^{-\alpha}; \quad (5.4)$$

and for  $L = L_{\max}$  is equal to  $\mathcal{N}$ .

The last necessary ingredient to predict the expected signal in H.E.S.S. is the relationship between the intrinsic luminosity of sources  $L$  and the flux produced at

Earth, that can be generally written as:

$$\Phi = \frac{L}{4\pi r^2 \langle E \rangle}; \quad (5.5)$$

where  $r$  is the source distance, and  $\langle E \rangle$  is the average energy of photons emitted in the range 1 – 100 TeV. In the HGPS the integral flux above 1 TeV of each source is obtained from the morphology fit of flux maps, assuming a power-law spectrum with index  $\beta = 2.3$  for all of them. This value is compatible with the average spectral index obtained by fitting HGPS sources by using a power law or a power-law with an exponential cutoff in the energy range  $0.2 \text{ TeV} \leq E_\gamma \leq 100 \text{ TeV}$  (see Sec.3.3.1). In order to be consistent with this procedure, we adopt the same assumption to describe the spectrum of Galactic sources in the TeV domain i.e. we assume that all sources can be described by a power-law in energy with spectral index  $\beta = 2.3$ . So the average energy  $\langle E \rangle$  corresponds to:

$$\langle E \rangle = \frac{\int_{1\text{TeV}}^{100\text{TeV}} dE E \left(\frac{E}{1\text{TeV}}\right)^{-2.3}}{\int_{1\text{TeV}}^{100\text{TeV}} dE \left(\frac{E}{1\text{TeV}}\right)^{-2.3}} = 3.25 \text{ TeV}. \quad (5.6)$$

### 5.2.1 Cumulative flux of H.E.S.S. sources

In order to further check the validity of our final results, one of the distributions that we will compare is the flux distribution  $dN/d\Phi$ . This can be calculated as:

$$\frac{dN}{d\Phi} = \int_0^{D(L_{\max}, \Phi)} dr 4\pi r^4 \langle E \rangle Y(4\pi r^2 \langle E \rangle \Phi) \bar{\rho}(r); \quad (5.7)$$

where we used the flux-luminosity relation in Eq.(5.5) that gives:  $L = \Phi r^2 4\pi \langle E \rangle$ . The function:

$$\bar{\rho}(r) \equiv \int_{\text{OW}} d\Omega \rho(r, \vec{n}); \quad (5.8)$$

represents the source spatial distribution integrated over the longitude and latitude intervals probed by H.E.S.S. Note that the integration in Eq.(5.7) is limited to the distance range  $r \leq D(L_{\max}, \Phi)$ . In particular the generic function:

$$D(L, \Phi) \equiv \sqrt{\frac{L}{4\pi \langle E \rangle \Phi}}; \quad (5.9)$$

represents the distance below which a source with intrinsic luminosity  $L$  produces a flux larger than  $\Phi$ . Substituting the luminosity function  $Y(\Phi r^2 4\pi \langle E \rangle)$  with the one chosen for our calculations, Eq.(5.3), we obtain the following:

$$\frac{dN}{d\Phi} = \frac{\mathcal{N}}{L_{\max}^{1-\alpha}} \int_0^{D(L_{\max}, \Phi)} dr (4\pi \langle E \rangle)^{1-\alpha} r^{4-2\alpha} \Phi^{-\alpha} \bar{\rho}(r). \quad (5.10)$$

The function  $dN/d\Phi$  can be calculated analytically in the two limit cases  $L_{\max} \rightarrow \infty$  and  $L_{\max} \rightarrow 0$ . For  $L_{\max} \rightarrow \infty$ , the upper limit of the integration goes to infinite as well:  $D(L_{\max}, \Phi) \rightarrow \infty$ . In this case the integral is independent from  $\Phi$  and the function becomes:

$$\frac{dN}{d\Phi} = \mathcal{N} L_{\max}^{\alpha-1} \Phi^{-\alpha} (4\pi \langle E \rangle)^{1-\alpha} \int_0^\infty dr r^{4-2\alpha} \bar{\rho}(r); \quad (5.11)$$

here the integral is only dependent on the coordinate  $r$  and is therefore a constant. The dependence on  $\Phi$  is only given by the term  $\Phi^{-\alpha}$ . The cumulative function  $N(\Phi)$  is the flux integral and represents the total number of sources above a flux  $\Phi$ . In this case is therefore:

$$N(\Phi) \propto \Phi^{-\alpha+1}. \quad (5.12)$$

For the second limit case  $L_{\max} \rightarrow 0$ , hence for  $D(L_{\max}, \Phi) \rightarrow 0$ , the integral over  $r$  is extended to a small region where the distribution function  $\bar{\rho}(r)$  can be considered constant and equal to its value at  $r = 0$ , i.e. in this case we assume  $\bar{\rho}(r) \simeq \bar{\rho}(0)$ . We thus obtain:

$$\begin{aligned} \frac{dN}{d\Phi} &\simeq (4\pi\langle E \rangle)^{1-\alpha} \bar{\rho}(0) \mathcal{N} L_{\max}^{\alpha-1} \Phi^{-\alpha} \int_0^{D(L_{\max}, \Phi)} dr r^{4-2\alpha} \\ &= (4\pi\langle E \rangle)^{1-\alpha} \bar{\rho}(0) \mathcal{N} L_{\max}^{\alpha-1} \Phi^{-\alpha} \left. \frac{r^{5-2\alpha}}{5-2\alpha} \right|_0^{D(L_{\max}, \Phi)} = \\ &= \bar{\rho}(0) \left( \frac{\mathcal{N}}{5-2\alpha} \right) \left( \frac{L_{\max}}{4\pi\langle E \rangle} \right)^{\frac{3}{2}} \Phi^{-\frac{5}{2}}. \end{aligned} \quad (5.13)$$

The behaviour of  $dN/d\Phi$  as a function of  $\Phi$  is therefore independent from the index  $\alpha$  considered and is proportional to  $\Phi^{-\frac{5}{2}}$ . The dependence on the flux of the cumulative function will be therefore independent from  $\alpha$  as well and will be:

$$N(\Phi) \propto \Phi^{-\frac{5}{2}}. \quad (5.14)$$

The two analytical limits for the cumulative flux distribution  $N(\Phi)$  are reported in Fig. 5.5 by the two smooth lines and compared with the cumulative distribution obtained by the HGPS data given by the gray histogram. In particular, the magenta dot-dashed line is the function of Eq.(5.14) obtained for  $L_{\max} \rightarrow 0$ , while the blue dotted line is the function (5.12) obtained for  $L_{\max} \rightarrow \infty$ .

### 5.3 Unbinned Likelihood

Flux, latitude, and longitude distributions of the sources observed in HGPS are fitted by using an unbinned likelihood with the goal of constraining the source luminosity distribution. By fixing the value of  $\alpha = 1.5$  for our reference case, our model has the two free parameters:  $L_{\max}$  and  $\mathcal{N}$ . In order to determine the maximal luminosity  $L_{\max}$  and the normalization  $\mathcal{N}$  of the luminosity function, see Eq.(5.3), we use the maximum Likelihood technique. The H.E.S.S. catalogue contains Galactic coordinates  $(b_i, l_i)$ , the observed fluxes  $\Phi_i$  in the energy range 1 – 100 TeV and the respective uncertainty  $\delta\Phi_i$  for each source.

Given this data set we define an unbinned Likelihood function  $\mathcal{L}$ , according to:

$$\log \mathcal{L} = -\mu_{\text{tot}} + \sum_i \log(\mu_i); \quad (5.15)$$

where  $\mu_{\text{tot}}$  represents the number of expected sources, while  $\mu_i$  is the probability to observe an object with coordinates  $(b_i, l_i)$  and measured flux  $\Phi_i$ . These quantities are calculated by considering that the source distribution per unit of flux  $\Phi$  and solid angle  $d\Omega$  is given by:

$$\mu(b, l, \Phi) = \int dr 4\pi r^4 \langle E \rangle Y(4\pi r^2 \langle E \rangle \Phi) \rho(r, b, l); \quad (5.16)$$

with the functions  $Y(L)$  and  $\rho(\vec{r})$  defined in Sec. 5.2. The parameter  $\mu_{\text{tot}}$  is obtained by integrating the function  $\mu(b, l, \Phi)$  in the H.E.S.S. observational window and in the flux range  $\Phi \geq 0.1\Phi_{\text{CRAB}}$  (since we only consider the limited sample of sources over the threshold) and is equivalent to the cumulative function already described. While the coefficients  $\mu_i$  are obtained as:

$$\mu_i = \int d\Phi \mu(b_i, l_i, \Phi) P(\Phi_i, \Phi, \delta\Phi_i); \quad (5.17)$$

where the function  $P(\Phi_i, \Phi, \sigma)$  represents the probability that the *measured* flux  $\Phi_i$  is obtained for a source emitting the *real* flux  $\Phi$ . We assume that this can be described by a Gaussian with a dispersion  $\sigma$  equal to the uncertainty of the measured flux, i.e.

$$P(\Phi_i, \Phi, \delta\Phi_i) = \frac{1}{\sqrt{2\pi\delta\Phi_i^2}} \exp\left[-\frac{(\Phi - \Phi_i)^2}{2\delta\Phi_i^2}\right]. \quad (5.18)$$

Finally, the best fit values and the allowed regions for the parameters in our analysis are obtained by studying the  $\chi^2$  behaviour, defined according to:

$$\chi^2 = -2 \log \mathcal{L}. \quad (5.19)$$

## 5.4 Best-fit values

The best fit values and the allowed regions for the maximal luminosity  $L_{\text{max}}$  and the normalization  $\mathcal{N}$  of the source luminosity distribution are shown in Fig. 5.4. We obtain:

$$\begin{aligned} L_{\text{max}} &= 4.9_{-2.1}^{+3.0} \times 10^{35} \text{ ergs/s}; \\ \mathcal{N} &= 17_{-6}^{+14}; \end{aligned} \quad (5.20)$$

where the quoted uncertainties correspond to  $1\sigma$  confidence level (CL). The constraint on the maximal luminosity can be also expressed as  $L_{\text{max}} = 13_{-6}^{+8} L_{\text{CRAB}}$  by considering that the Crab luminosity (above 1 TeV) is  $L_{\text{CRAB}} = 3.8 \cdot 10^{34} \text{ ergs/sec}$ . The above results are obtained for our reference case where we assume that the source distribution is proportional to that of pulsars given by Lorimer et al., 2006, the disk thickness is  $H = 0.2 \text{ kpc}$ , and the power-law index of the luminosity distribution is  $\alpha = 1.5$ . Moreover, for our fit we include 29 HPGS sources neglecting the 3 sources which are firmly identified as SNRs. This is motivated by the possible interpretation of our results in terms of a population of fading sources powered by pulsar activity that we discuss in the next chapter.

The obtained bounds are connected with specific features of the H.E.S.S. data. The constraint on the maximal luminosity essentially originates from the flux distribution of HGPS sources, as can be understood by looking at Fig. 5.5 where we compare the cumulative number  $N(\Phi)$  of observed sources with flux larger than  $\Phi$ , with the predictions obtained for different  $L_{\text{max}}$  values. The theoretical calculations are normalized in such a way that the expected number of sources with  $\Phi \geq 0.1\Phi_{\text{CRAB}}$  is equal to the observational value  $N_{\text{obs}} = 29$ . This corresponds to moving along the cyan dashed line in Fig. 5.4 that maximizes the likelihood for each assumed  $L_{\text{max}}$ . The black line in Fig. 5.5 corresponds to the best fit value  $L_{\text{max}} = 13 L_{\text{CRAB}}$  and, as it is evident from the plot, well reproduces the flux distribution in the range above the threshold:  $\Phi \geq 0.1\Phi_{\text{CRAB}}$ , considered in our analysis.

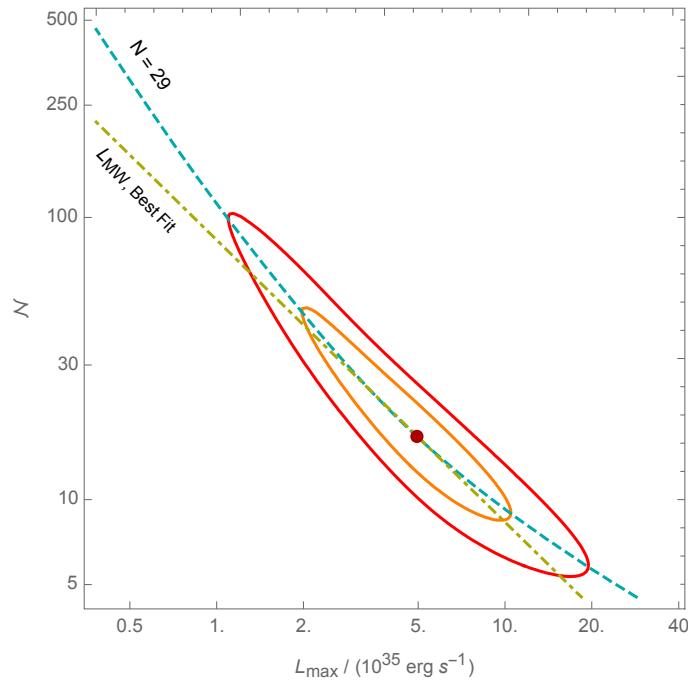


FIGURE 5.4: The best fit and the 1 and 2  $\sigma$  allowed regions for the maximal luminosity  $L_{\max}$  and the normalization  $\mathcal{N}$  of the luminosity distribution of Galactic TeV sources. The dot represents the best fit value. The olive line corresponds to constant values of the total Milky Way luminosity, calculated according to Eq.(5.21). Figure taken from Cataldo et al., 2020.

For comparison, we also show with a red dashed line the expected behaviour of  $N(\Phi)$  for  $L_{\max} = 30 L_{\text{CRAB}}$ . This value is disfavoured at  $\sim 2\sigma$  level by HGPS data because it predicts presence of sources with flux above the threshold too high which are in fact not observed.

A more complete understanding of the above points can be obtained by considering the magenta dot-dashed line and the blue dotted line in Fig.5.5 that correspond to the limiting cases  $L_{\max} \rightarrow 0$  and  $L_{\max} \rightarrow \infty$ , respectively. The limit  $L_{\max} \rightarrow 0$  represents the scenario in which all sources have a very low luminosity, therefore, the detector is able to resolve only a small surrounding region, being the far away sources too faint to produce a detectable flux. In this case indeed the number of under-threshold sources grows and is the largest obtained in the plot. The limit  $L_{\max} \rightarrow \infty$ , instead, corresponds to the possibility for the detector to investigate the whole Milky Way in all its extension. Both these curves are not acceptable since the first limit estimates a lower flux respect to the data over the threshold, while the second predicts a larger flux which is in fact not observed. As discussed in Sec.5.2.1 the cumulative distribution scales as  $N(\Phi) \propto \Phi^{1-\alpha}$  when  $L_{\max} \rightarrow \infty$ . When  $L_{\max} \rightarrow 0$ , one instead obtains  $dN/d\Phi \propto \Phi^{-5/2}$ , predicting  $N(\Phi) \propto \Phi^{-3/2}$  independently from the assumed source luminosity function. The cumulative distribution of sources observed by H.E.S.S. has a different behaviour with respect to both cases and thus it requires a specific  $L_{\max}$  value in order to be reproduced. The possibility to determine  $L_{\max}$  from the flux distribution automatically implies the ability to fit the normalization  $\mathcal{N}$  of the source luminosity function by considering the additional constraint provided by the total number of observed sources, as it is understood by looking at the cyan dashed line in Fig.5.4.

## 5.5 Total flux and total luminosity of the Milky Way

In our analysis, we determine the maximal luminosity  $L_{\max}$  and the normalization  $\mathcal{N}$  of the luminosity function by fitting H.E.S.S. observational results. The determination of  $L_{\max}$  and  $\mathcal{N}$  allows us to estimate the total TeV luminosity produced by the considered population in the entire Galaxy. This is given by:

$$L_{\text{MW}} = \int_{L_{\min}}^{L_{\max}} dL L \frac{\mathcal{N}}{L_{\max}} \left( \frac{L}{L_{\max}} \right)^{-\alpha};$$

$$L_{\text{MW}} = \int_{\Delta}^1 d\ell L_{\max} \mathcal{N} (\ell)^{-\alpha+1};$$

with  $\ell = L/L_{\max}$ :

$$L_{\text{MW}} = \frac{\mathcal{N} L_{\max}}{(2-\alpha)} [1 - \Delta^{\alpha-2}]; \quad (5.21)$$

where  $\Delta \equiv L_{\max}/L_{\min}$ . The minimal luminosity  $L_{\min}$  cannot be constrained by H.E.S.S. observations. However, its value marginally affects the quantities considered in this paper, provided that  $\Delta \gg 1$ , i.e.  $L_{\max} \gg L_{\min}$ . Unless otherwise specified, we quote the results obtained for  $\Delta \rightarrow \infty$  that can be easily recalculated by using the above equation, if other values are considered.

By using Eqs.(5.1, 5.3, 5.5), we can also calculate the flux at Earth produced by all sources (resolved and not resolved) included in the H.E.S.S. observational window (OW). This can be expressed as:

$$\Phi_{\text{tot}} = \int_{\text{OW}} d^3r \rho(\vec{r}) \int_{L_{\min}}^{L_{\max}} dL \Phi(L, r) \frac{\mathcal{N}}{L_{\max}} \left( \frac{L}{L_{\max}} \right)^{-\alpha};$$

$$= \int_{\text{OW}} d^3r \rho(\mathbf{r}) \int_{L_{\min}}^{L_{\max}} dL \frac{L}{4\pi r^2 \langle E \rangle} \frac{\mathcal{N}}{L_{\max}} \left( \frac{L}{L_{\max}} \right)^{-\alpha}.$$

At this point it is useful to define the parameter  $\xi$  as:

$$\xi \equiv \int_{\text{OW}} d^3r \rho(\vec{r}) = 0.812; \quad (5.22)$$

which represents the fraction of sources of the considered population which are included in the H.E.S.S. observational window. Using the quantity  $\langle r^{-2} \rangle$  which is the average value of their inverse square distance:

$$\langle r^{-2} \rangle \equiv \frac{1}{\xi} \int_{\text{OW}} d^3r \rho(\vec{r}) r^{-2} = 0.0176 \text{ kpc}^{-2}; \quad (5.23)$$

we obtain a useful definition for the total Milky Way flux:

$$\Phi_{\text{tot}} = \xi \frac{L_{\text{MW}}}{4\pi \langle E \rangle} \langle r^{-2} \rangle. \quad (5.24)$$

While the above values  $\xi$  and  $\langle r^{-2} \rangle$  are specific for HGPS survey (and for the adopted source spatial distribution  $\rho(\vec{r})$ ), Eq.(5.24) has a general validity. It can be used to evaluate the expected flux in a generic telescope and for an arbitrary source distribution, provided that the corresponding  $\xi$  and  $\langle r^{-2} \rangle$  are coherently calculated.

In conclusion, by using Eqs.(5.21) and (5.24), we obtain a determination of the total luminosity of the Galaxy in the energy range 1 – 100 TeV and of the total flux (in the same energy range) produced by sources in the H.E.S.S. observational window.

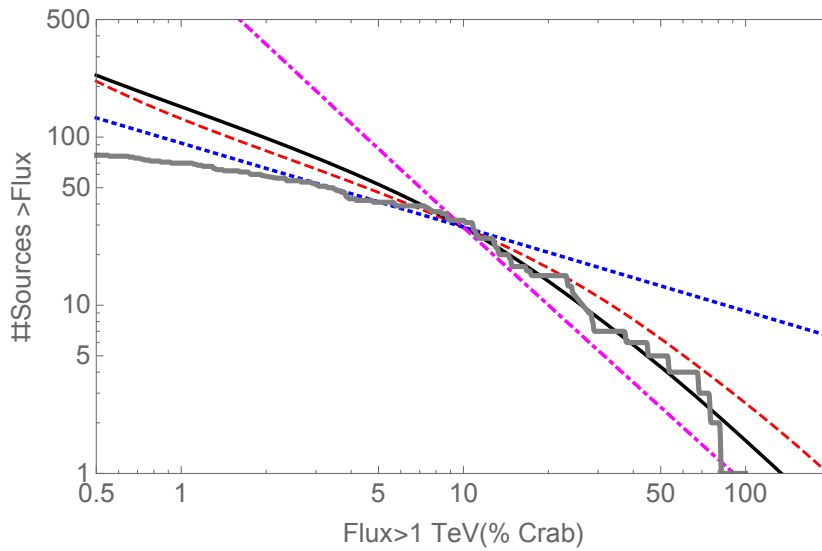


FIGURE 5.5: The cumulative distribution of the HGPS sources (gray line) compared with expectations for different values of the maximal luminosity  $L_{\max}$ . The black line is obtained for the best-fit values in Eq.(5.20), the magenta dot-dashed line and the blue dotted one are obtained for the limit cases of  $L_{\max} \rightarrow 0$  and  $L_{\max} \rightarrow \infty$ , respectively, while the red dashed line shows an intermediate case of  $L_{\max} = 30 \times L_{\text{CRAB}}$ . Figure taken from Cataldo et al., 2020.

We get:

$$\begin{aligned} L_{\text{MW}} &= 1.7_{-0.4}^{+0.5} \times 10^{37} \text{ ergs sec}^{-1}; \\ \Phi_{\text{tot}} &= 3.8_{-1.0}^{+1.0} \times 10^{-10} \text{ cm}^{-2} \text{ sec}^{-1}; \end{aligned} \quad (5.25)$$

that correspond to  $L_{\text{MW}} = 445_{-112}^{+138} L_{\text{CRAB}}$  and  $\Phi_{\text{tot}} = 16.8_{-3.5}^{+4.4} \Phi_{\text{CRAB}}$  in CRAB units. We note that the uncertainties on these quantities are relatively small because they are proportional to the product  $\mathcal{N} L_{\max}$  that is well constrained by observational data, as it is also understood by considering the green dot-dashed line in Fig.5.4. The total TeV luminosity is only a factor  $\sim 4$  smaller than that obtained in the energy range 1 – 100 GeV by fitting the Fermi-LAT 3FGL (Ajello et al., 2017) and 1FHL (Ackermann et al., 2013) catalogues.

## 5.6 Unresolved source contribution

The total flux at the Earth  $\Phi_{\text{tot}} = 16.8_{-3.5}^{+4.4} \Phi_{\text{CRAB}}$  should be compared with the cumulative emission produced by all the 78 resolved sources in the HGPS catalogue:

$$\Phi_{\text{HGPS}} = 10.4 \Phi_{\text{CRAB}}; \quad (5.26)$$

We obtain by subtraction the unresolved flux:

$$\Phi_{\text{NR}} = 6.4_{-3.5}^{+4.4} \Phi_{\text{CRAB}}; \quad (5.27)$$

which is due to sources in the considered population that are too faint to be identified by H.E.S.S. We see that the unresolved emission  $\Phi_{\text{NR}}$  is relatively large, compared

to the resolved source contribution. This is naturally expected because the observational horizon for H.E.S.S. is limited, while sources are expected to be distributed everywhere in the Galaxy. Comparing the unresolved flux to the resolved source flux this is more than the 60%:  $\Phi_{\text{NR}} \simeq 0.6 \Phi_{\text{HGPS}}$ , while it represents the 38% of the total flux measured by H.E.S.S. given by the resolved flux and the diffuse contribution. As we can see from Fig.5.5, the unresolved contribution, i.e. the number of sources expected below the flux threshold, is well constrained by our best fit. We also tested this value by changing the assumption on our model (see the next Section).

We can conclude that our result is in perfect agreement with our preliminary estimation of the unresolved source component given in Chapter 4 (Cataldo et al., 2019), and obtained following a different approach, giving therefore confirmation to its validity.

In Steppa and Egberts, 2020 is presented an estimation of the same quantity by following a different population study of the HGPS. They show a value of the unresolved flux 13 – 32% of the total flux measured by H.E.S.S., which is comparable with our  $\sim 38\%$  fraction.

## 5.7 Robustness of results

In the following we discuss the stability of our results with respect to the assumptions adopted in our analysis. In Table 5.1 we consider different scenarios modifying the hypotheses with respect to the reference case (e.g. the space distribution, the disk thickness, the source physical dimension, the power-law index of the luminosity distribution, etc.). In Table 5.1, for each case we give the best-fit results and the  $1\sigma$  allowed regions for the source luminosity function parameters ( $\mathcal{N}$  and  $L_{\text{max}}$ ), the total TeV luminosity of the Galaxy  $L_{\text{MW}}$ , the total flux produced at Earth  $\Phi_{\text{tot}}$ , and the level of agreement with data expressed in terms of the  $\Delta\chi^2$  with respect to our reference case.

Firstly, we illustrate the variation of the best fits and results by considering all 32 sources observed over the threshold. The inclusion of the three sources firmly identified as SNRs in the HPGS catalogue (case labelled as  $N_{\text{obs}} = 32$  in Tab. 5.1) does not alter our conclusions, marginally affecting the maximal luminosity  $L_{\text{max}}$  and increasing by less than 10% the normalization  $\mathcal{N}$  of the source luminosity distribution.

The second test performed is on the spatial source distribution. As a preliminary test, we consider a uniform distribution in the Galactic plane up to a distance  $r = 15$  kpc and with a thickness  $H = 50$  pc. In this case the total luminosity becomes  $2.4 \times 10^{37} \text{ ergs}^{-1}$  and  $\Delta\chi^2 = -1.1$ , so it appears favoured. This is especially due to the narrower disk assumed respect to our reference case ( $H = 200$  pc). However, a flat distribution does not represent the most physical scenario and is not reported in the table. Then we assume, instead of the pulsar distribution by Lorimer et al., 2006, a function that follows the SNR distribution in the Galaxy as parameterized by Green, 2015. The new distribution function has the same shape of the Green, 2015 function and is normalized to 1. As it is evident from the results labelled as "SNR", no significant effects are produced by assuming that the sources are distributed following the SNR distribution function, they are indeed quite similar in shape and we imposed the same normalization. A different situation is found when changing the thickness of the disk  $H$ . We test two smaller values of this parameter:  $H = 0.1$  kpc, and  $H = 0.05$  kpc.

The results of our analysis appear to be slightly modified when we reduce the thickness of the Galactic disk from our reference choice. The total Milky Way luminosity has a variation of  $\sim 27\%$  respect to our reference case while the variation of the total flux is  $\sim 17\%$ . However, the quality of the fit substantially improves with respect to our reference choice ( $\Delta\chi^2 \simeq -7$  and  $\Delta\chi^2 \simeq -10.5$ ) the more the disk thickness is reduced ( $H = 0.1$  kpc and  $H = 0.05$  kpc, respectively). The HGPS data-set is better fitted by a narrower Galactic disk. This is due to the fact that the latitudinal distribution of HGPS sources is quite narrow, having a rms latitude of  $0.017$  rad, as it expected for a population of young sources connected with the site of past core-collapse supernova explosions. See the bottom panel of Fig. 5.1 where the latitudinal distribution of the sources in the catalogue is shown. In particular, this information can be used in favor of a fading source population, as young pulsar wind nebulae, not old enough to drift off the Galactic plane (Abdalla et al., 2018b). This specific hypothesis and its implications will be further discussed in the next chapter.

Moreover, we remove the point-like assumption that we made, by assuming all sources to have a physical dimension  $d$ . This implies that there is a minimal distance below which sources cannot be observed because they have large angular dimension. This condition is implemented as:

$$r \geq \frac{d}{\theta_{\max}} = r_{\min}; \quad (5.28)$$

where  $\theta_{\max} \sim 1^\circ$  is the maximal angular dimension that can be probed by H.E.S.S. We consider two possible values  $d = 20$  pc and  $d = 40$  pc. We see that our results are not modified in this assumption. Our constraints are not affected unless one assumes that the majority of the observed sources have an extension much larger than  $few \times 10$  pc. In conclusion, the obtained results may be applied to extended gamma-ray sources, provided that they have dimension that do not exceed  $\sim 40$  pc.

We also check possible variation of the source spectral index in the range  $2.2 < \beta < 2.4$ . We notice that our results are not modified. In particular, the total Milky Way luminosity has a maximum variation of  $\sim 10\%$  respect to the Ref. case while the total flux remains almost the same. We do not consider larger variations on this parameter because different values are less compatible with the observed data sample (Abdalla et al., 2018a).

Finally, we consider the effects produced by a variation of the power index  $\alpha$  of the luminosity distribution by considering two cases:  $\alpha = 1.3$ ,  $\alpha = 1.8$ . We obtain a  $\sim 10\%$  decrease ( $\sim 50\%$  increase) of the TeV Milky way luminosity and of the total flux at Earth for  $\alpha = 1.3$  ( $\alpha = 1.8$ ), with a small preference for the case with power law index 1.3.

In general, the total flux is slightly more stable than the total luminosity with respect to variations of  $\beta$  and  $\rho(r)$  as a consequence of the fact that HGPS data directly constrain the fluxes (and not the luminosity values) of observed sources. In conclusion, the cumulative source contribution to the Milky Way luminosity in the  $1 - 100$  TeV range and to the total  $\gamma$ -ray flux in the H.E.S.S. OW are included in the ranges:  $L_{\text{MW}} = (1.2 - 2.5) \times 10^{37}$  erg s $^{-1}$ ,  $\Phi_{\text{tot}} = (3.5 - 5.9) \times 10^{-10}$  cm $^{-2}$  s $^{-1}$ , showing that the Milky Way luminosity and the total  $\gamma$ -ray flux can be constrained within a factor of 2.1 and 1.7 respectively by present observational data.

|                       | $\log_{10} \frac{L_{\max}}{\text{erg s}^{-1}}$ | $\mathcal{N}$     | $\log_{10} \frac{L_{\text{MW}}}{\text{erg s}^{-1}}$ | $\Phi_{\text{tot}}$ | $\Delta\chi^2$ |
|-----------------------|--|-------------------|---|---------------------|----------------|
| Ref.                  | $35.69^{+0.21}_{-0.28}$                        | $17^{+14}_{-6}$   | $37.22^{+0.12}_{-0.13}$                             | $3.8^{+1.0}_{-1.0}$ | —              |
| SNR                   | $35.69^{+0.22}_{-0.25}$                        | $18^{+15}_{-7}$   | $37.23^{+0.12}_{-0.13}$                             | $3.8^{+1.0}_{-1.0}$ | 1.4            |
| $H = 0.1$ kpc         | $35.65^{+0.22}_{-0.27}$                        | $15^{+14.5}_{-6}$ | $37.13^{+0.12}_{-0.13}$                             | $5.0^{+0.4}_{-2.0}$ | −7.3           |
| $H = 0.05$ kpc        | $35.34^{+0.26}_{-0.19}$                        | $28^{+19}_{-13}$  | $37.08^{+0.12}_{-0.13}$                             | $4.4^{+1.3}_{-0.9}$ | −10.5          |
| $d = 20$ pc           | $35.69^{+0.20}_{-0.26}$                        | $17^{+16}_{-6}$   | $37.23^{+0.12}_{-0.13}$                             | $3.9^{+0.8}_{-1.0}$ | −0.2           |
| $d = 40$ pc           | $35.67^{+0.20}_{-0.25}$                        | $20^{+20}_{-8}$   | $37.28^{+0.12}_{-0.13}$                             | $4.4^{+1.2}_{-1.1}$ | −1.8           |
| $\alpha = 1.3$        | $35.61^{+0.18}_{-0.27}$                        | $25^{+24}_{-8.5}$ | $37.17^{+0.12}_{-0.13}$                             | $3.5^{+1.1}_{-0.9}$ | 0.0            |
| $\alpha = 1.8$        | $35.83^{+0.29}_{-0.24}$                        | $7^{+6}_{-4}$     | $37.39^{+0.11}_{-0.13}$                             | $5.9^{+1.8}_{-0.1}$ | 0.5            |
| $N_{\text{obs}} = 32$ | $35.71^{+0.22}_{-0.24}$                        | $18^{+14}_{-7}$   | $37.26^{+0.12}_{-0.12}$                             | $4.2^{+1.3}_{-1.0}$ | —              |

TABLE 5.1: The best fit values and the  $1\sigma$  allowed ranges for the maximal luminosity ( $L_{\max}$ ); the normalization factor of the luminosity function ( $\mathcal{N}$ ); the total TeV Milky Way luminosity ( $L_{\text{MW}}$ ); the total flux in the H.E.S.S. OW ( $\Phi_{\text{tot}}$ , expressed in  $10^{-10} \text{ cm}^{-2} \text{ s}^{-1}$ ). The different cases are described in the text. The  $\Delta\chi^2$  is calculated respect to our reference case (first row in the table.)

## 5.8 Final considerations

Recently the H.E.S.S. observatory has completed the first systematic survey of the Galactic plane in the very high-energy domain. Remarkably, the astrophysical nature of the majority of detected sources is still unknown. In our paper Cataldo et al., 2020, we present a novel analysis of flux, longitude, and latitude distributions of the brightest sources ( $\Phi \geq 10\% \Phi_{\text{CRAB}}$ ) of the HGPS catalogue showing that the luminosity distribution of Galactic TeV sources can be effectively constrained.

More precisely, by assuming that the luminosity function is described by a power-law (Eq.(5.3)) we extract the source maximal luminosity  $L_{\max} = 4.9^{+3.0}_{-2.1} \times 10^{35} \text{ erg s}^{-1}$  and the high-luminosity normalization of the source distribution  $\mathcal{N} = 17^{+14}_{-6}$  by fitting HGPS data. This approach is original and different from previous studies on the subject (Casanova and Dingus, 2008) where the value of the maximal luminosity is instead assumed "a priori". This allows us to determine the total Milky Way luminosity  $L_{\text{MW}} = 1.7^{+0.5}_{-0.4} \times 10^{37} \text{ erg s}^{-1}$  in the energy range 1 – 100 TeV and the total Galactic flux in the H.E.S.S. OW given by  $\Phi_{\text{tot}} = 3.8^{+1.0}_{-1.0} \times 10^{-10} \text{ cm}^{-2} \text{ s}^{-1}$ . The luminosity  $L_{\text{MW}}$  is only a factor  $\sim 4$  smaller than that obtained in the energy range 1 – 100 GeV by fitting Fermi-LAT 3FGL and 1FHL catalogue.

Moreover, our total luminosity appears compatible with the range given in Steppa and Egberts, 2020 and obtained for energy in the range 1-10 TeV. The values from the paper can be reported in the energies (1 – 100) TeV by using the assumed source spectrum  $E^{-2.4}$ , and the range becomes  $7.1 \times 10^{36} - 3.1 \times 10^{37} \text{ erg/s}$ , depending on the spatial model. In particular for the PWN distribution, the one we assumed in our reference model, the total luminosity is  $(1.2 \pm 0.1) \times 10^{37} \text{ erg/s}$  that is in good agreement with what we obtained, i.e.  $1.7^{+0.5}_{-0.4} \times 10^{37} \text{ erg/s}$ . The same can be done in order to compare the total fluxes. Scaling our value in the energy range (1 – 10) TeV and to the whole Galaxy we get:  $\Phi_{\text{tot}} = (4 \pm 1) \times 10^{-10} \text{ cm}^{-2} \text{ s}^{-1}$ , which compared with the total flux due to sources derived for the PWN model  $(7.7 \pm 1.9) \times 10^{-10} \text{ cm}^{-2} \text{ s}^{-1}$ , appears smaller. However, it can be increased considering a power law index  $\alpha = 1.8$  for the luminosity distribution, closer to the one in Steppa and Egberts, 2020.

In addition, the total source flux is relatively large, implying that unresolved source contribution is not negligible (about 60% of the resolved signal measured by H.E.S.S., and the  $\sim 38\%$  of the total signal observed) and potentially responsible for a large fraction of the diffuse large-scale gamma-ray signal observed by H.E.S.S. This could have important implications for the interpretation of current observations of other experiments in the TeV domain. The unresolved contribution can e.g. explain the excess reported by Milagro at 15 TeV (Atkins et al., 2005). Our results can be also used to investigate the capability of future experiments, like e.g. CTA, to probe the Galactic TeV source population.

In the following chapter we will see how our population study can be applied to a particular kind of sources in order to estimate some overall properties of the total Galactic population. We will analyze the hypothesis in which the signal observed by the experiment H.E.S.S. is dominated by fading sources powered by pulsar activity and we will infer general properties of the Galactic pulsar population.



## Chapter 6

# Galactic TeV population of pulsar-powered sources

As briefly discussed in the previous chapter the total catalogue collected by H.E.S.S. is composed of 78 TeV sources. Twelve are firmly identified Pulsar Wind Nebulae, 8 Supernova Remnants, 3 binaries, 8 composite sources, yet most of the remaining sources are instead not identified (36) or not even physically associated to any of other emission counterparts (11). By the association criteria used by the collaboration, which are principally based on positional correlation, the nature of almost half of sources (46%) appears not yet clear. One of the most likely scenario proposed is that a large part of unidentified sources are in fact pulsar wind nebulae in which the central pulsar is not observable due to a radio beam misalignment. Indeed, since obviously there is not a preferred direction of emission for pulsars, it is expected that only a small fraction of them are able to point directly to the Earth and be therefore detected.

There are also evidences of a population of gamma-ray emitting objects that have been called "TeV-halos", the properties of which are still for most part uncertain. TeV-halos have been firstly observed by the Milagro detector, and then confirmed in a subsequent data release by HAWC in 2017 (Abeysekara et al., 2017b). They appear as largely extended objects that produce non-hadronic gamma-ray emission in the TeV domain by being powered by pulsar activity. TeV-halos could potentially explain a large fraction of bright TeV sources observed in the Sky (Sudoh, Linden, and Beacom, 2019) so their contribution is very interesting to investigate.

In the first part of our work presented in Chapter 5, we made a general study of the catalogue without making any particular assumption on the nature of the sources. On the other hand, in this Chapter we consider to test the hypothesis that all bright sources observed by H.E.S.S. (which are not firmly identified as SNRs) are *fading sources* powered by pulsar activity, e.g. PWNe and/or TeV halos, and in this category are also counted the composite sources that have a PWN-like emission. We apply our population study presented in Chapter 5 to the above particular assumption on the nature of the sources considered and, by making this, we are able to give an estimation of general properties of the total pulsar population of the Milky Way. We then discuss the constraints on the pulsar properties that have been found, namely the initial spin period and magnetic field, that are obtained by HGPS data.

This Chapter is based on the original paper Cataldo et al., 2020.

### 6.1 Pulsar powered sources

In this section we analyze more in detail the pulsar powered sources observed at TeV energies in our Galaxy, i.e. pulsar wind nebulae and the new discovered TeV halos.

Then we describe the basic model used for the pulsar evolution and its energy loss mechanism that also powers PWNe and TeV halos.

### 6.1.1 From PWN to TeV-halo

Milagro observations revealed extended TeV  $\gamma$ -ray emission surrounding the nearby Geminga pulsar. The HAWC detector has confirmed these observations around Geminga (Abdo et al., 2009) and has detected a further similar emission surrounding another nearby pulsar, PSR B0656+14, also called "Monogem pulsar" (Thorsett et al., 2003). While in Linden et al., 2017 is shown that 13 more extended TeV sources of 2HWC catalog are coincident with pulsars. In addition, the H.E.S.S. observatory has detected more TeV  $\gamma$ -ray sources coincident with pulsars or pulsar wind nebulae (PWNe) (Abdalla et al., 2018a), and they find that their extension is significantly larger than expected from PWN theory. Hydrodynamical simulations predict indeed a typical PWN size on the order of 1 pc (Gaensler and Slane, 2006). These TeV sources appear very bright with a luminosity  $\sim 10^{32}$  erg s $^{-1}$ , and present hard spectra  $\sim E^{-2.2}$ . They also appear spatially extended covering regions of radius around  $\sim 25$  pc. These extended TeV sources appear morphologically and dynamically distinct from PWNe detected in X-ray and radio observations, and are predicted as a generic feature of pulsar emission. They take the name of "TeV-halos".

Their emission is interpreted as the result of electrons and positrons interacting with the ambient interstellar radiation field outside the PWN, the leptonic origin is suggested by the lack of gas-correlated emission. TeV halos are defined as the gamma-ray emission related to the presence of an over-density of relativistic electrons around a source/acceleration-site, in a zone in which the source itself does not dominate the dynamics or composition of the interstellar medium (Giacinti et al., 2020). According to the above definition, halos may exist only around PWN whose electrons and positrons have started to escape into the surrounding unperturbed ISM. Within the halo region, multi-TeV gamma-rays are produced by the inverse-Compton scattering of ambient photons by  $\sim 10$  TeV electrons and positrons accelerated by the pulsar wind termination shock. The fact that the size of the TeV halo is significantly larger than the X-ray emission indicates that the electrons and positrons responsible for TeV halo emission have already escaped the PWN and are interacting with the interstellar radiation field. Moreover, note that due to their morphology the electronic diffusion in TeV-halos should be significantly suppressed respect to the intergalactic medium. Therefore TeV-halos can be considered as the first direct proof of an inhibited diffusivity around Galactic sources. An interesting model for the diffusivity in TeV-halos has been proposed in Evoli, Linden, and Morlino, 2018.

In Fig.6.1 is schematically shown the evolution stages that occur from the PWN formation and take to the TeV-halo birth (Giacinti et al., 2020).

The first stage (1) that represents early times,  $t \lesssim 10$  kyr is shown in the upper left panel. Inside the volume delimited by the contact discontinuity ("CD") there is the PWN (blue area) which is still contained inside the SNR (green external line). Therefore the electrons that are responsible for the TeV gamma-ray emission of the nebula are thought to be confined as well. In this phase the relativistic electron-positron wind that surrounds the PWN, inflates a nebula inside the parent SNR. The forward shock ("FS") made by the ejecta from the supernova expands in the surrounding interstellar material (ISM). Subsequently, there is the formation of a reverse shock (indicated as "RS") made by the braking of the ejected material (see Sec. 2.1.3) which in this phase have not reached the inner PWN yet. The SNR forward



the configuration we can see the tail of the PWN trained behind the pulsar. At this stage, high-energy electrons escape into the surrounding ISM, and may, only then, form a halo. As shown in the inset that shows an enlargement of the region around the head of the nebula, there are several high-energy electrons that can escape into the surrounding ISM. This is further confirmed by observations in the X-ray of the bow-shocks.

The third is the only stage where the TeV emission can be considered as a “TeV halo”. So we can easily expect that only older PWN, with ages  $> 100$  years can have developed a TeV halo in the recent part of their life. The two pulsars Geminga and PSR B0656+14, for which the halo has been observed, are indeed both in the stage 3 of their evolution, which confirms this theory.

For the emission by TeV halo in our model we will simply consider the same evolution considered for PWNe, since they are both powered by pulsar activity. Although they energetically evolve the same way, one of the main differences is their size: PWNe TeV emission has a size at least one order of magnitude smaller than the emission by halo. This will be also considered in our model for which we will accordingly verify the stability of our results.

### 6.1.2 Magnetic dipole model for pulsars

Due to their characteristics one of the most used models to study pulsars evolution is the magnetic dipole approximation. From measurements of the two observables, i.e. the period of rotation and its derivative, are inferred several evolution characteristics of pulsars such as their spin-down power  $\dot{E}$ , luminosity, spin-down time scale  $\tau_0$ , characteristic age  $\tau_c$ . The energy outflow of the pulsar is decaying continually at a rate determined by  $\tau_0$ , following an evolution which appears similar to that expected from a magnetic dipole. Here we derive the main evolution equation that we will use in the following. In the magnetic dipole approximation for pulsars it is assumed that the neutron star rotates in vacuum with a frequency  $\nu(t)$  that varies in time and possesses a magnetic dipole moment  $\vec{\mu}$  oriented with a fixed angle  $\theta$  respect to the rotation axis. Observations have found that almost all pulsars (except accreting X-ray pulsars in binary systems) are spinning down. For such a configuration, the magnetic momentum of the star is related to the pure magnetic dipole field  $B$  as:

$$\vec{\mu} = \frac{BR^3}{2}(\vec{e}_{\parallel} \cos \theta + \vec{e}_{\perp} \sin \theta \cos \Omega t + \vec{e}'_{\perp} \sin \theta \sin \Omega t); \quad (6.1)$$

where  $R$  is the radius of the star, while  $\vec{e}_{\parallel}$  is the unit vector oriented parallel to the rotation axis, and the other two  $\vec{e}_{\perp}$  and  $\vec{e}'_{\perp}$  are unit vectors mutually orthogonal and orthogonal to  $\vec{e}_{\parallel}$ . The modulus of  $\vec{\mu}$  is therefore:

$$|\vec{\mu}| = \frac{BR^3}{2}. \quad (6.2)$$

This configuration has a magnetic dipole varying with time and therefore radiates energy at a rate:

$$\dot{E} = -\frac{2}{3c^3}|\ddot{\vec{\mu}}|^2. \quad (6.3)$$

We can obtain the dependence of the spin-down power  $\dot{E}(t)$  from the angular velocity  $\Omega(t)$ :

$$\dot{E}(t) = -\frac{B^2 R^6 \sin^2 \theta}{6c^3} \Omega^4(t). \quad (6.4)$$

This energy is emitted at expenses of the kinetic rotational energy of the pulsar which is given by:

$$E(t) = \frac{1}{2} I \Omega^2(t); \quad (6.5)$$

where  $I$  is the momentum of inertia. Deriving we obtain the dependence of  $\dot{\Omega}$  by its primitive  $\Omega$ :

$$\dot{E}(t) = I \Omega(t) \dot{\Omega}(t); \quad (6.6)$$

$$\dot{\Omega}(t) = \frac{\dot{E}(t)}{I \Omega(t)}. \quad (6.7)$$

Substituting the expression (6.4) in (6.7) we get:

$$\dot{\Omega}(t) = -\frac{BR^6 \sin^2 \theta}{6Ic^3} \Omega^3(t). \quad (6.8)$$

In this expression the index  $n = 3$  is called "braking index" and its value can be inferred for several pulsars. The numbers obtained observatively, as predictable, do not reproduce exactly the value 3 since the magnetic dipole model represents a simplification of what actually occurs inside a pulsar. Usually the values obtained experimentally are lower. We can indeed generalize this expression to a generic value  $n$ :

$$\dot{\Omega}(t) = -k \Omega(t)^n. \quad (6.9)$$

So from Eq. (6.4) the spin-down evolution is a power-law with index  $n + 1$ :

$$\dot{E}(t) = -k' \Omega(t)^{n+1}; \quad (6.10)$$

where the constants  $k$  and  $k'$  are defined by the particular model considered, and for the case of magnetic dipole are:

$$k = \frac{BR^6 \sin^2 \theta}{6Ic^3}; \quad (6.11)$$

$$k' = \frac{B^2 R^6 \sin^2 \theta}{6c^3}; \quad (6.12)$$

and in this case are linked by:  $k' = B I k$ . By integrating Eq.(6.9) we obtain:

$$\Omega(t) = \Omega_0 \left(1 + \frac{t}{\tau_0}\right)^{-\frac{1}{n-1}}; \quad (6.13)$$

where the initial value of the frequency at the time  $t = 0$  is indicated with  $\Omega_0$ , and where the initial spin-down characteristic timescale  $\tau_0$  of the evolution is defined as:

$$\tau_0 = \frac{\Omega_0^{1-n}}{k(n-1)}. \quad (6.14)$$

From Eqs.(6.10) and (6.13) we obtain therefore:

$$\dot{E}(t) = \dot{E}_0 \left(1 + \frac{t}{\tau_0}\right)^{-\frac{n+1}{n-1}}; \quad (6.15)$$

where  $\dot{E}_0$  is the spin-down rate at the time  $t = 0$ . Eq.(6.15) represents the general expression of the spin-down power evolution in time obtained for a pulsar with a generic braking index  $n$ .

To date all measured pulsars braking indices, including the Crab pulsar (Lyne et al., 2015) are smaller than three. For example the Crab pulsar has a braking index of  $n = 2.51 \pm 0.01$  (Lyne, Pritchard, and Graham Smith, 1993). It means that the slow down process is faster than what hypothesized in the magnetic dipole model. So there are additional physical processes needed to describe the slow down of the pulsar. For instance, some work has suggested that a significant amount of rotational kinetic energy in young neutron stars may be carried away by gravitational waves generated by unstable oscillations (Andersson, Kokkotas, and Schutz, 1999, Ho and Lai, 2000). Other mechanisms have been proposed to explain the braking index observations, e.g. the pulsar wind model, (Xu and Qiao, 2001, Wu, Xu, and Gil, 2003, Contopoulos and Spitkovsky, 2006, Yue, Xu, and Zhu, 2007), a changing magnetic field strength (Chen and Li, 2006, Espinoza et al., 2011), a changing inclination angle (Lyne et al. 2013). Unfortunately, these models are either not always consistent with observations or cannot simulate the long-term evolution of pulsars.

### 6.1.3 Gamma emission of pulsar-powered sources

A PWN is usually considered to be a calorimetrical, dynamical object around a pulsar. The PWN stores and displays the radiative output of the pulsar during tens of kiloyears while at the same time undergoing a substantial dynamical evolution inside the host SNR. So the energy outflow of the pulsar determines the energy injection history of a PWN. In our model we will assume the injection evolution dictated by an average braking index  $n = 3$ , so for a simple dipole model without any other energy dispersion mechanisms. So for a braking index value  $n = 3$  the spin-down power is:

$$\dot{E}(t) = \dot{E}_0 \left(1 + \frac{t}{\tau}\right)^{-2}; \quad (6.16)$$

where  $\tau$  is the spin-down timescale that for our work we will assume constant ( $\tau = \tau_0$ );  $\dot{E}_0$  is the initial spin-down power. PWN indeed will be generated and will start emitting after a time  $t_0$  from the birth of pulsar, which represents as a matter of fact the birth time of the PWN which may not coincide with the birth time of its pulsar. We are only interested in pulsar powered sources as TeV sources so we want to define a time variable useful for our purposes. We decide to use the simple assumption for which the birth time coincides with the start of the TeV emission. This means that for the sources in our model the time coordinate  $t$  simply represents  $t = t_{\text{present}} - t_0$ , where  $t_{\text{present}}$  is the current time at the source. Moreover, we define  $T_d$  as the total duration of TeV emission, with  $t \leq T_d$ .

For the luminosity emitted by a TeV source powered by a pulsar, is reasonable to assume that it is proportional to the pulsar spin-down power, i.e.:

$$L(t) = \lambda \dot{E}(t); \quad (6.17)$$

where  $\lambda (\leq 1)$  it is determined by the conversion of the spin-down energy into  $e^\pm$  pairs (that can be very efficient, see e.g. Sudoh, Linden, and Beacom, 2019; Manconi, Di Mauro, and Donato, 2020) and by the subsequent production of TeV photons. Moreover, in the most generic case in which this parameter is dependent on time the generic expression for the luminosity is  $L(t) = \lambda(t) \dot{E}(t)$ ,

The possibility of  $\lambda$  being correlated to the spin-down power, is suggested by the results of Abdalla et al., 2018b. By studying a sample of PWNe in the HPGS catalogue, the collaboration found a mild but stable correlation of luminosity with pulsar spin-down power as:

$$L = \lambda \dot{E} \propto \dot{E}^{1+\delta}; \quad (6.18)$$

with  $1 + \delta = 0.59 \pm 0.21$ . This can be derived defining a time dependent efficiency  $\lambda(t)$  by using the value  $\lambda_0$  referred to initial efficiency of TeV emission:

$$\lambda(t) = \lambda_0 \left( \frac{\dot{E}(t)}{\dot{E}_0} \right)^\delta. \quad (6.19)$$

Substituting into the luminosity expression we obtain:

$$L(t) = \lambda_0 \dot{E}_0^{-\delta} \dot{E}(t)^{1+\delta}; \quad (6.20)$$

which can be written as:

$$L(t) = L_{\max} \left( 1 + \frac{t}{\tau} \right)^{-\gamma}. \quad (6.21)$$

Where  $L_{\max}$  is the initial luminosity, and  $\gamma = 2(\delta + 1) \simeq 1.2$ . This possibility will be also evaluated in our model, see Sec.6.4. The term  $\lambda$  can be highly uncertain and we will better discuss later its variation and possible values. However, the simplest consideration that can be done is that  $\lambda$  is constant in time. Under this assumption between the luminosity and the spin-down power there is a simple relation and they have the same index,  $\gamma = 2$ :

$$L(t) = L_{\max} \left( 1 + \frac{t}{\tau} \right)^{-2}; \quad (6.22)$$

where the initial luminosity is simply expressed by:

$$L_{\max} = \lambda \dot{E}_0. \quad (6.23)$$

Typical values for luminosity and other parameters of PWNe such as characteristic age  $\tau_c$ , position  $d$ , spin-down power  $\dot{E}$  are collected by H.E.S.S in Abdalla et al., 2018b and listed in Table 6.2. The table is restricted to all firmly identified PWNe for which the corresponding pulsar has been detected and timed. Note that from the values of  $\dot{E}$  and  $L$  one can easily calculate the  $\lambda$  fractions if assumed constant. The lowest value registered from the catalogue is the one of J1303-631 for which  $\lambda \simeq 5 \times 10^{-2}$ .

## 6.2 Model in the fading-source interpretation

We discuss the results obtained in the previous chapter in the context of a fading source population powered by pulsar activity. In this hypothesis we give the new expression of the luminosity function and the free parameters of the model, which are now dependent on variables physically linked to these type of sources.

| HGPS name                 | ATNF name  | Canonical name                     | $\lg \dot{E}$ | $\tau_c$<br>(kyr) | $d$<br>(kpc) | PSR offset<br>(pc) | $\Gamma$        | $R_{\text{PWN}}$<br>(pc) | $L_{1-10 \text{ TeV}}$<br>( $10^{33} \text{ erg s}^{-1}$ ) |
|---------------------------|------------|------------------------------------|---------------|-------------------|--------------|--------------------|-----------------|--------------------------|--|
| J1813-178 <sup>[1]</sup>  | J1813-1749 |                                    | 37.75         | 5.60              | 4.70         | < 2                | $2.07 \pm 0.05$ | $4.0 \pm 0.3$            | $19.0 \pm 1.5$   |
| J1833-105                 | J1833-1034 | G21.5-0.9 <sup>[2]</sup>           | 37.53         | 4.85              | 4.10         | < 2                | $2.42 \pm 0.19$ | < 4                      | $2.6 \pm 0.5$  |
| J1514-591                 | B1509-58   | MSH 15-52 <sup>[3]</sup>           | 37.23         | 1.56              | 4.40         | < 4                | $2.26 \pm 0.03$ | $11.1 \pm 2.0$           | $52.1 \pm 1.8$   |
| J1930+188                 | J1930+1852 | G54.1+0.3 <sup>[4]</sup>           | 37.08         | 2.89              | 7.00         | < 10               | $2.6 \pm 0.3$   | < 9                      | $5.5 \pm 1.8$  |
| J1420-607                 | J1420-6048 | Kookaburra (K2) <sup>[5]</sup>     | 37.00         | 13.0              | 5.61         | $5.1 \pm 1.2$      | $2.20 \pm 0.05$ | $7.9 \pm 0.6$            | $44 \pm 3$   |
| J1849-000                 | J1849-0001 | IGR J18490-0000 <sup>[6]</sup>     | 36.99         | 42.9              | 7.00         | < 10               | $1.97 \pm 0.09$ | $11.0 \pm 1.9$           | $12 \pm 2$   |
| J1846-029                 | J1846-0258 | Kes 75 <sup>[2]</sup>              | 36.91         | 0.728             | 5.80         | < 2                | $2.41 \pm 0.09$ | < 3                      | $6.0 \pm 0.7$  |
| J0835-455                 | B0833-45   | Vela X <sup>[7]</sup>              | 36.84         | 11.3              | 0.280        | $2.37 \pm 0.18$    | $1.89 \pm 0.03$ | $2.9 \pm 0.3$            | $0.83 \pm 0.11^*$  |
| J1837-069 <sup>[8]</sup>  | J1838-0655 |                                    | 36.74         | 22.7              | 6.60         | $17 \pm 3$         | $2.54 \pm 0.04$ | $41 \pm 4$               | $204 \pm 8$  |
| J1418-609                 | J1418-6058 | Kookaburra (Rabbit) <sup>[5]</sup> | 36.69         | 10.3              | 5.00         | $7.3 \pm 1.5$      | $2.26 \pm 0.05$ | $9.4 \pm 0.9$            | $31 \pm 3$   |
| J1356-645 <sup>[9]</sup>  | J1357-6429 |                                    | 36.49         | 7.31              | 2.50         | $5.5 \pm 1.4$      | $2.20 \pm 0.08$ | $10.1 \pm 0.9$           | $14.7 \pm 1.4$   |
| J1825-137 <sup>[10]</sup> | B1823-13   |                                    | 36.45         | 21.4              | 3.93         | $33 \pm 6$         | $2.38 \pm 0.03$ | $32 \pm 2$               | $116 \pm 4$  |
| J1119-614                 | J1119-6127 | G292.2-0.5 <sup>[11]</sup>         | 36.36         | 1.61              | 8.40         | < 11               | $2.64 \pm 0.12$ | $14 \pm 2$               | $23 \pm 4$   |
| J1303-631 <sup>[12]</sup> | J1301-6305 |                                    | 36.23         | 11.0              | 6.65         | $20.5 \pm 1.8$     | $2.33 \pm 0.02$ | $20.6 \pm 1.7$           | $96 \pm 5$   |

FIGURE 6.2: Table taken from Abdalla et al., 2018b that collects HGPS sources considered as firmly identified pulsar wind nebulae. The sources are sorted by decreasing  $\dot{E}$ .  $\lg \dot{E}$  stands for  $\log_{10}(E/\text{erg s}^{-1})$ ,  $\tau_c$  is the pulsar characteristic age,  $d$  is the pulsar distance,  $R_{\text{PWN}}$  is the 1-sigma Gaussian extension, and  $L_{1-10 \text{ TeV}}$  is the TeV luminosity.

The luminosity distribution given in Eq.(5.3) can be naturally obtained by assuming a population of *fading* sources with intrinsic luminosity that decreases over a time scale  $\tau$  according to the already derived expression of Eq.(6.22). As already mentioned,  $L_{\text{max}}$  is the initial luminosity and, given the definition of  $T_d$ , the  $L_{\text{min}} = L(T_d)$  is the minimum TeV luminosity that the source will reach during its lifetime. So, in other words, we can indicate the time  $t_0$  as the birth time of a fading source that, at present time, has reached a luminosity  $L = L(t)$ . Therefore, the interval time of formation  $dt_0$  of sources with luminosity within the interval  $L, L + dL$  is:

$$dt_0 = \frac{dt_0}{dL} dL. \quad (6.24)$$

The luminosity function is given by the number of sources  $dN$  in that interval of luminosity, i.e.:

$$Y(L) = \frac{dN}{dL} = \frac{dN}{dt_0} \frac{dt_0}{dL}. \quad (6.25)$$

Assuming that the birth-rate  $\mathcal{R}$  of these sources in the Galaxy is constant in time:

$$\frac{dN}{dt} = \mathcal{R}; \quad (6.26)$$

what is left to calculate is the derivative  $dt_0/dL$  from Eq.(6.22). This is obtained from:

$$t_0(L) = t_{\text{present}} - \tau \left[ \left( \frac{L}{L_{\text{max}}} \right)^{-\frac{1}{\gamma}} - 1 \right]; \quad (6.27)$$

$$\frac{dt_0}{dL} = \frac{\tau}{\gamma L_{\text{max}}} \left( \frac{L}{L_{\text{max}}} \right)^{-\frac{1}{\gamma}-1}. \quad (6.28)$$

In conclusion, by calling  $\alpha = 1/\gamma + 1$ , the luminosity function  $Y(L)$  is given by:

$$Y(L) = \frac{\mathcal{R} \tau (\alpha - 1)}{L_{\text{max}}} \left( \frac{L}{L_{\text{max}}} \right)^{-\alpha}. \quad (6.29)$$

Under this assumption, we can now reinterpret the free parameters of our model. In particular, the normalization factor of the luminosity distribution is:

$$\mathcal{N} = \mathcal{R} \tau (\alpha - 1); \quad (6.30)$$

and has a precise physical meaning. It basically represents the total number of *young* sources in the Galaxy that had not enough time to lose their initial luminosity and that are expected to be more easily detected by H.E.S.S.. Note that, for a fixed  $\alpha$ , the observational determination of  $\mathcal{N}$  can be converted into a bound on the fading timescale  $\tau$ , if the source formation rate is known.

The above description can be applied to potential TeV sources in the Galaxy, such as PWNe (Gaensler and Slane, 2006) or TeV Halos (Linden and Buckman, 2018), which are connected with the explosion of core-collapse SN and the formation of a pulsar. The birth rate of these objects can be assumed proportional to that of SN explosions in our Galaxy, i.e.  $\mathcal{R}_{\text{SN}} = 0.019 \text{ yr}^{-1}$  as measured by Diehl et al., 2006. We thus write  $\mathcal{R} = \varepsilon \mathcal{R}_{\text{SN}}$  assuming  $\varepsilon = 1$  for simplicity, unless otherwise specified.

As seen at the beginning of this section, for energy loss dominated by magnetic dipole radiation (braking index  $n = 3$ ), we can compute the initial spin-down power  $\dot{E}_0$  and the characteristic spin-down time scale  $\tau_0$  as functions of the frequency. Now, knowing that  $\Omega = 2\pi/P$  and therefore  $\Omega_0 = 2\pi/P_0$ , we obtain:

$$\begin{aligned} \dot{E}_0 &= \frac{8\pi^4 B_0^2 R^6}{3c^3 P_0^4}; \\ \tau_0 &= \frac{3Ic^3 P_0^2}{4\pi^2 B_0^2 R^6}; \end{aligned} \quad (6.31)$$

where  $P_0$  is the initial spin period and  $B_0$  is the magnetic field that in our model is assumed constant (Shapiro and Teukolsky, 1983). While the term  $\sin^2 \theta$  in Eqs.(6.11)(6.12) is substituted with its average over the angle  $\langle \sin^2 \theta \rangle = 1/2$ . Moreover, the values for the inertial momentum and the pulsar radius are  $I = 1.4 \cdot 10^{45} \text{ g cm}^2$ ,  $R = 12 \text{ km}$  (Lattimer and Prakash, 2007) respectively. This implies that the fading timescale is determined by the pulsar spin-down time scale, i.e.  $\tau = \tau_0$ .

Moreover, as already mentioned, if the efficiency of TeV emission (i.e. the fraction of energy converted in TeV gamma-rays) does not depend on time, the exponent in Eq.(6.22) is simply the exponent in Eq.(6.15):

$$\lambda \simeq \text{const} \implies \gamma = 2. \quad (6.32)$$

Note that this motivates our working hypothesis already introduced in Sec.5 that the luminosity distribution scales as  $Y(L) \propto L^{-1.5}$ . Nevertheless, the parameter  $\lambda$  is highly uncertain. The values obtained for firmly identified PWNe in the HPGS catalogue fall between  $5 \times 10^{-5}$  and  $6 \times 10^{-2}$ , see Tab.6.2. For comparison, the value  $\lambda \sim 3 \times 10^{-3}$  is obtained in Linden and Buckman, 2018 by studying the TeV  $\gamma$ -ray emission of Geminga. In this work, we consider  $\lambda$  as a free parameter, taking the value  $\lambda = 10^{-3}$  as a reference in numerical calculations.

Finally, we also consider a variable value of  $\lambda$  as in Eq.(6.19) (Abdalla et al., 2018b), for which we obtained a value  $\gamma \simeq 1.2$ . In this case the source luminosity function is  $Y(L) \propto L^{-1.8}$ . This scenario is discussed in our analysis and, as we will see, does not introduce relevant changes in our conclusions.

For our results we decided to use two variables directly linked to the initial characteristics of the Galactic pulsar population: the average initial spin period  $P_0$  and the average magnetic field  $B_0$ . We will give our results in terms of  $P_0$  and  $B_0$  instead of  $L_{\max}$  and  $\tau$  as done for the generic model of Chapter 5. They can be derived inverting Eqs.(6.31), and remembering that  $\tau = \tau_0$  and that  $L_{\max} = \lambda \dot{E}_0$ . We obtain:

$$P_0 = \sqrt{\frac{\lambda 2\pi^2 I}{\tau L_{\max}}}; \quad (6.33)$$

$$B_0 = \sqrt{\frac{\lambda 3c^3 I^2}{\tau^2 2R^6 L_{\max}}}. \quad (6.34)$$

Finally,  $P_0$  and  $B_0$  can be determined from  $L_{\max}$  and  $\tau$  substituting all known values of the parameters:

$$\begin{aligned} \frac{P_0}{1 \text{ ms}} &= 94 \left(\frac{\lambda}{10^{-3}}\right)^{1/2} \left(\frac{\tau}{10^4 \text{ yr}}\right)^{-1/2} \left(\frac{L_{\max}}{10^{34} \text{ erg s}^{-1}}\right)^{-1/2}; \\ \frac{B_0}{10^{12} \text{ G}} &= 5.2 \left(\frac{\lambda}{10^{-3}}\right)^{1/2} \left(\frac{\tau}{10^4 \text{ yr}}\right)^{-1} \left(\frac{L_{\max}}{10^{34} \text{ erg s}^{-1}}\right)^{-1/2}. \end{aligned} \quad (6.35)$$

### 6.3 $P_0$ and $B_0$ dispersion

We consider the effects of dispersion of the initial period and magnetic field around reference values indicated as  $\tilde{P}_0$  and  $\tilde{B}_0$ ; which in turn implies a dispersion in  $L_{\max}$  and  $\tau$ .

We call  $h(p)$  and  $g(b)$  the functions that describe the probability distributions of initial period and magnetic field respectively; with  $p = P_0/\tilde{P}_0$ ,  $b = B_0/\tilde{B}_0$ . We assume that these functions can be modelled as Gaussian distributions in  $\log_{10}(p)$  and  $\log_{10}(b)$ , centered in zero and having widths given by  $\sigma_{\log P} = \log_{10}(f_p)$  and  $\sigma_{\log B} = \log_{10}(f_b)$ , with the parameters  $f_p$  and  $f_b$  defined in the next section. The two distributions are:

$$h(p) = \frac{1}{\sqrt{2\pi\sigma_{\log P}^2}} \exp\left(-\frac{\log_{10}^2(p)}{2\sigma_{\log P}^2}\right); \quad (6.36)$$

$$g(b) = \frac{1}{\sqrt{2\pi\sigma_{\log B}^2}} \exp\left(-\frac{\log_{10}^2(b)}{2\sigma_{\log B}^2}\right). \quad (6.37)$$

The source luminosity function can be obtained by integrating Eq.(6.29), calculated by assuming  $\tau = \tau_0(B_0, P_0)$  and  $L_{\max} = \lambda \dot{E}_0(B_0, P_0)$ , over  $B_0$  and  $P_0$  probability distributions. Substituting the variables  $p, b$  this is:

$$Y(L) = \int dp \int db h(p) g(b) Y(L, p, b). \quad (6.38)$$

Using Eqs.(6.31) we rewrite  $\tau$ , and  $L_{\max}$  in terms of the new variables  $p, b$ :

$$\tau(p, b) = \tilde{\tau} p^2 b^{-2}; \quad (6.39)$$

$$L_{\max}(p, b) = \tilde{L} p^4 b^2; \quad (6.40)$$

where  $\tilde{\tau} \equiv \tau_0(\tilde{B}_0, \tilde{P}_0)$  and  $\tilde{L} \equiv L_{\max}(\tilde{B}_0, \tilde{P}_0) = \lambda \dot{E}_0(\tilde{B}_0, \tilde{P}_0)$  are the spin-down timescale and maximal luminosity for the central values  $\tilde{P}_0$  and  $\tilde{B}_0$ . Under this assumption, the parameters  $\tilde{\tau}$  and  $\tilde{L}$  represent the central values of the log-normal (correlated) distributions of  $\tau$  and  $L_{\max}$  that are obtained as a result of the introduction of  $P_0$  and  $B_0$  dispersion. After our computations, the luminosity distribution becomes:

$$Y(L) = \frac{R \tilde{\tau} (\alpha - 1)}{\tilde{L}} \left( \frac{L}{\tilde{L}} \right)^{-\alpha} G \left( \frac{L}{\tilde{L}} \right); \quad (6.41)$$

valid for a generic value of  $\alpha$ . The obtained luminosity function differs from Eq.(6.29) for the presence of the function  $G(L/\tilde{L})$  that is defined according to:

$$G(x) \equiv \int dp h(p) p^{6-4\alpha} \int db g(b) b^{2\alpha-4} \Theta \left( p^{-4} b^2 - x \right). \quad (6.42)$$

For our reference case  $\alpha = 1.5$  the function  $G(x)$  becomes:

$$G(x) = \int dp h(p) \int db \frac{g(b)}{b} \Theta \left( p^{-4} b^2 - x \right); \quad (6.43)$$

We solved these integrals computationally and in the same way we found new solutions for the best fit parameters for fixed values of standard deviations:  $\sigma_{\log P}$  and  $\sigma_{\log B}$ .

## 6.4 Results

The best fit values obtained in Chapter 5 can be interpreted in terms of the new variables. If we consider a fading source population connected with the explosion of core-collapse SNe, we can convert the limits on the normalization parameter  $\mathcal{N}$  of the source luminosity function into a determination of the fading time-scale  $\tau$  through the relationship  $\mathcal{N} = \mathcal{R} \tau (\alpha - 1)$ . By assuming that the source formation rate  $\mathcal{R}$  is approximately equal to the SN rate  $\mathcal{R}_{\text{SN}} = 0.019 \text{ yr}^{-1}$ , we get a best fit value of the spin-down time scale:

$$\tau = 1.8_{-0.6}^{+1.5} \times 10^3 \text{ yr}; \quad (6.44)$$

for our reference case, that corresponds to the orange solid line in the left panel of Fig.6.4. Similar values are obtained in the other cases, as reported in Tab.6.1.

In the assumption that the observed objects are PWNe and/or TeV halos which are powered by the formation and the subsequent spin-down of a pulsar, the above value can be used to determine through Eqs.(6.35) the initial period  $P_0$  and magnetic field  $B_0$  of the considered population. We get the constraints:

$$\begin{aligned} P_0 &= 33.5_{-4.3}^{+5.4} \text{ ms} \times \left( \frac{\lambda}{10^{-3}} \right)^{1/2}; \\ B_0 &= 4.3 (1 \pm 0.45) 10^{12} \text{ G} \times \left( \frac{\lambda}{10^{-3}} \right)^{1/2}; \end{aligned} \quad (6.45)$$

that correspond to the orange solid line in the right panel of Fig.6.4. The small uncertainty for the period  $P_0$  is connected with the fact that this quantity is determined by the product  $L_{\max} \tau$  which is relatively well determined by observational data, being the possible variations of  $L_{\max}$  and  $\tau$  anti-correlated.

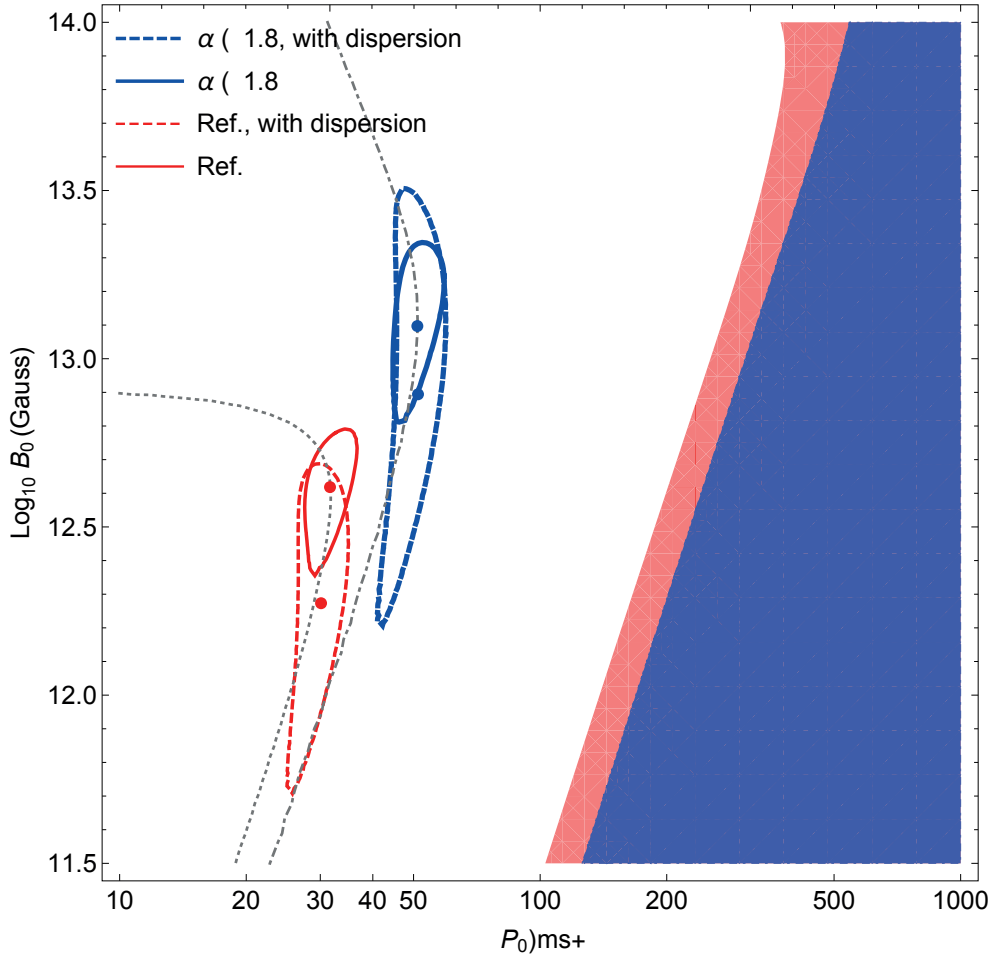


FIGURE 6.3: The best fit and the 1 and  $2\sigma$  allowed regions in the plane  $(P_0, B_0)$ , calculated in the assumption that the fraction of pulsar spin-down energy converted to TeV emission is  $\lambda = 10^{-3}$ . The shaded regions correspond to  $N(0.1\Phi_{\text{CRAB}}) \leq 10$  in the assumption  $\lambda = 5 \times 10^{-2}$ . Figure taken from Cataldo et al., 2020.

|                | $\log_{10} \frac{L_{\text{max}}}{\text{erg s}^{-1}}$ | $\mathcal{N}$     | $\tau$              | $\log_{10} B_0$         | $P_0$                | $\Delta\chi^2$ |
|----------------|--|-------------------|---------------------|-------------------------|----------------------|----------------|
| Ref.           | $35.69^{+0.21}_{-0.28}$                              | $17^{+14}_{-6}$   | $1.8^{+1.5}_{-0.6}$ | $12.62^{+0.17}_{-0.26}$ | $31.7^{+5.0}_{-4.0}$ | —              |
| SNR            | $35.69^{+0.22}_{-0.25}$                              | $18^{+15}_{-7}$   | $1.8^{+1.6}_{-0.7}$ | $12.60^{+0.17}_{-0.26}$ | $31.2^{+4.9}_{-4.0}$ | 1.4            |
| $H = 0.1$ kpc  | $35.65^{+0.22}_{-0.27}$                              | $15^{+14.5}_{-6}$ | $1.6^{+1.5}_{-0.6}$ | $12.68^{+0.17}_{-0.25}$ | $35.1^{+5.6}_{-4.6}$ | -7.3           |
| $H = 0.05$ kpc | $35.34^{+0.26}_{-0.19}$                              | $28^{+19}_{-13}$  | $2.9^{+2.0}_{-1.4}$ | $12.57^{+0.23}_{-0.26}$ | $36.7^{+3.7}_{-3.3}$ | -10.5          |
| $d = 20$ pc    | $35.69^{+0.20}_{-0.26}$                              | $17^{+16}_{-6}$   | $1.9^{+1.9}_{-0.7}$ | $12.60^{+0.17}_{-0.29}$ | $31.2^{+4.9}_{-3.9}$ | -0.2           |
| $d = 40$ pc    | $35.67^{+0.20}_{-0.25}$                              | $20^{+20}_{-8}$   | $2.2^{+2.0}_{-0.8}$ | $12.54^{+0.18}_{-0.28}$ | $29.5^{+4.7}_{-4.0}$ | -1.8           |
| $\alpha = 1.3$ | $35.61^{+0.18}_{-0.27}$                              | $25^{+24}_{-8.5}$ | $4.3^{+4.3}_{-1.5}$ | $12.26^{+0.16}_{-0.23}$ | $21.8^{+3.5}_{-2.8}$ | 0.0            |
| $\alpha = 1.8$ | $35.83^{+0.29}_{-0.24}$                              | $7^{+6}_{-4}$     | $0.5^{+0.4}_{-0.2}$ | $13.10^{+0.24}_{-0.26}$ | $51.1^{+8.1}_{-6.4}$ | 0.5            |

TABLE 6.1: The same as Table 5.1 but with best fit values and the  $1\sigma$  allowed ranges for the magnetic field of pulsars  $B_0$  (in Gauss and expressed logarithmically), and the spin-down period  $P_0$  in ms; the fading timescale  $\tau$  is expressed in ky. The different cases are described in the text in Chapter 5.

We note that the inferred magnetic field agrees with the value  $\log_{10}(B_0/1\text{G}) \simeq 12.65$  obtained by pulsar population studies (Faucher-Giguere and Kaspi, 2006). The

inferred period is consistent with the value  $P_0 \sim 50$  ms obtained in Watters and Romani, 2011 by studying  $\gamma$ -ray pulsar population. The value  $P_0 \sim 300$  ms that is obtained from pulsar radio observation (Faucher-Giguere and Kaspi, 2006) is instead excluded by our analysis, unless one assumes that a very large fraction  $\lambda \sim 10^{-1}$  of the spin-down power is converted to TeV  $\gamma$ -ray emission.

The above results are obtained under the assumption that all the sources in the HGPS catalogue with flux  $\Phi \geq 0.1\Phi_{\text{CRAB}}$  (except those firmly identified as SNRs) are powered by pulsar activity. A conservative upper bound for the period  $P_0$  can be obtained by considering that no less than 10 of these sources have to be necessarily included in this population, being firmly identified as PWNe or Composite Sources (Fig.5.2). The lines  $N(0.1\Phi_{\text{CRAB}}) = \text{const}$ , corresponding to a fixed number of sources above the adopted flux threshold  $0.1\Phi_{\text{CRAB}}$  are shown by the gray dashed lines in the planes  $(L_{\text{max}}, \tau)$  and  $(P_0, B_0)$  in Fig.6.4. It can be shown analytically (see Sec.5.2) that  $N(\Phi)$  scales as:

$$N(\Phi) \propto \tau L_{\text{max}}^{3/2} \propto B_0 P_0^{-4} \lambda^{3/2};$$

for the limiting case  $L_{\text{max}} \rightarrow 0$ , while it scales as:

$$N(\Phi) \propto \tau L_{\text{max}}^{\alpha-1} \propto B_0^{2\alpha-4} P_0^{6-4\alpha} \lambda^{\alpha-1};$$

for  $L_{\text{max}} \rightarrow \infty$ . If  $1 < \alpha < 2$ , the condition  $N(\Phi) = \text{const}$  always individuates a maximum allowed period  $P_0$  (at the transition between the above regimes) whose specific value depends on the fraction  $\lambda$  of the pulsar spin-down energy that is converted to TeV  $\gamma$ -ray emission. In particular, the red shaded area in Fig.6.4 can be excluded because it corresponds to  $N(0.1\Phi_{\text{CRAB}}) \leq 10$  and to the relatively large value  $\lambda = 5 \times 10^{-2}$ . This allows us to obtain the bound  $P_0 \leq 500$  ms that can be strengthened if an upper limit for the magnetic field  $B_0 \leq 10^{14}$  G is introduced.

In order to test stability of the constraints given in Eq.(6.45), we repeat our calculation for the case  $\alpha = 1.8$  obtained by assuming that  $\lambda$  is correlated with the spin-down power as suggested by Abdalla et al., 2018b. In this case, the fading time scale is  $\tau = 0.5_{-0.2}^{+0.4} \times 10^3$  y, while the initial period and magnetic field are given by:

$$\begin{aligned} P_0 &= 51.0_{-6.4}^{+8.1} \text{ ms} \times \left( \frac{\lambda_0}{10^{-3}} \right)^{1/2}; \\ B_0 &= 12.7_{-5.8}^{+9.6} 10^{12} \text{ G} \times \left( \frac{\lambda_0}{10^{-3}} \right)^{1/2}. \end{aligned} \quad (6.46)$$

The above results are shown by the blue solid line in Fig. 6.3 where they are compared with those obtained in the reference case ( $\alpha = 1.5$ ).

As a further test, we hypothesize that the initial pulsar periods and magnetic fields are not univocally determined but have log-normal dispersion around preferred values  $\tilde{P}_0$  and  $\tilde{B}_0$  with widths  $\sigma_{\log P} = \log_{10}(f_p)$  and  $\sigma_{\log B} = \log_{10}(f_b)$ . The constraints on  $\tilde{P}_0$  and  $\tilde{B}_0$  that are obtained by choosing  $f_p = \sqrt{2}$  and  $f_b = 2$ , are displayed by the dashed red and blue lines in Fig.6.3. We see that the inferred value for  $\tilde{P}_0$  is basically insensitive to assumed dispersion while the preferred magnetic field  $\tilde{B}_0$  is slightly reduced with respect to the reference case, as a consequence of the high-luminosity tail of the source luminosity function that is obtained by assuming  $f_p \neq 0$  and  $f_b \neq 0$ .

Summarizing, the results displayed in Fig.6.3 show that the bounds on the initial period and magnetic field do not critically depend on the adopted assumptions, being  $P_0$  constrained to the narrow range 25 – 60 ms for  $\lambda = 10^{-3}$ . The fact that the inferred values for  $B_0$  and  $P_0$  are consistent with expectations justifies the working assumption that a large fraction of bright sources observed by H.E.S.S. belongs to a population of young pulsars, and supports the hypothesis, formulated e.g. by Linden and Buckman, 2018 and Sudoh, Linden, and Beacom, 2019, that PWNe and/or TeV halos could produce the majority of TeV bright sources in the Sky. On the contrary, the large values for the initial period  $P_0 \sim 300$  ms which is obtained from radio pulsar studies (Faucher-Giguere and Kaspi, 2006), can explain the HGPS results only if we assume that a limited fraction of observed sources belong to the considered population and/or a consistent fraction of the spin-down energy is converted into TeV  $\gamma$ -ray emission. By using the reference value  $\lambda = 10^{-3}$ , we obtain only  $\sim 1$  source above the adopted flux threshold  $0.1\Phi_{\text{CRAB}}$ . In order to reproduce the 10 sources firmly identified as pulsars, we have to assume  $\lambda = 1.6 \times 10^{-2}$ , while to predict all the 29 sources observed by H.E.S.S. the value of the efficiency  $\lambda$  has to be as large as  $\sim 5 \times 10^{-2}$ .

As a further check of this point, we calculate the expected number of sources in the H.E.S.S. observational window by using the  $P_0$  and  $B_0$  distributions obtained by Faucher-Giguere and Kaspi, 2006 from pulsar radio observations, i.e. a gaussian centered in  $P_0 = 300$  ms with standard deviation  $\sigma_P = 150$  ms, and a log-normal centered in  $\log B_0 = 12.65$  with standard deviation  $\sigma_{\log B} = 0.55$ . We obtained  $P_0 = 30.1^{+4.8}_{-3.7}$  ms,  $\log_{10} B_0 = 12.27^{+0.38}_{-0.52}$ .

Finally, it is interesting to see how the result would change in case of a population composed only of TeV halos. Based on a birth process for TeV halos as the one described in Sec.6.1.1 following Giacinti et al., 2020, we can modelize the energy evolution as in (Sudoh, Linden, and Beacom, 2019). They assume a spin-down power for TeV halos equal to Eq.(6.16) but valid only for a certain time  $t > T_{\min}$  since they emit starting from a  $T_{\min} \neq 0$ . We consider this scenario by introducing a variation on the birth rate respect to the one assumed for our reference case ( $\mathcal{R} = \mathcal{R}_{\text{SN}}$ ). The birth rate for TeV halos is assumed lower by a fraction  $\epsilon (< 1)$ :  $\mathcal{R}_{\text{halo}} = \epsilon\mathcal{R}$ . In this assumption, the TeV halo luminosity function has the same expression as Eq.(6.29) but we obtain that  $L_{\max}$  is replaced by the luminosity  $L(T_{\min})$  evaluated at time  $t = T_{\min}$  from Eq.(6.22), and the spin-down time  $\tau$  is substituted by  $\epsilon(\tau + T_{\min})$ . As a consequence, the same functional form can be used to fit the data, obtaining the same best fit points but with a different interpretation. In particular, in order to have the maximal luminosity value ( $13 L_{\text{Crab}}$ ) at a later time  $T_{\min}$  (instead of  $t = 0$ ), we have to assume the sources to be initially more energetic, implying therefore a smaller initial spin-down period  $P_0$ . We indeed evaluated how the best fit parameters for  $B_0$  and  $P_0$  would change according to the fraction  $\epsilon$  obtaining values proportional to  $\epsilon$  and  $\sqrt{\epsilon}$  respectively.

This kind of interpretation is however obtained by assuming that the TeV sky is only populated by TeV-halos which start to emit at TeV energies at the time of their birth. It is more conservative to assume that sources powered by pulsar activity can also emit as Pulsar Wind Nebulae at earlier times. So the most plausible situation is obtained assuming that the population of PWNe emits TeV gammas and, after an average time  $T_{\min}$  a fraction of them develops a TeV-halo which continues to emit by losing energy with the same law (Giacinti et al., 2020). This is what we considered for our population study, and in this case our calculation is not sensible to  $T_{\min}$  and the interpretation doesn't change.

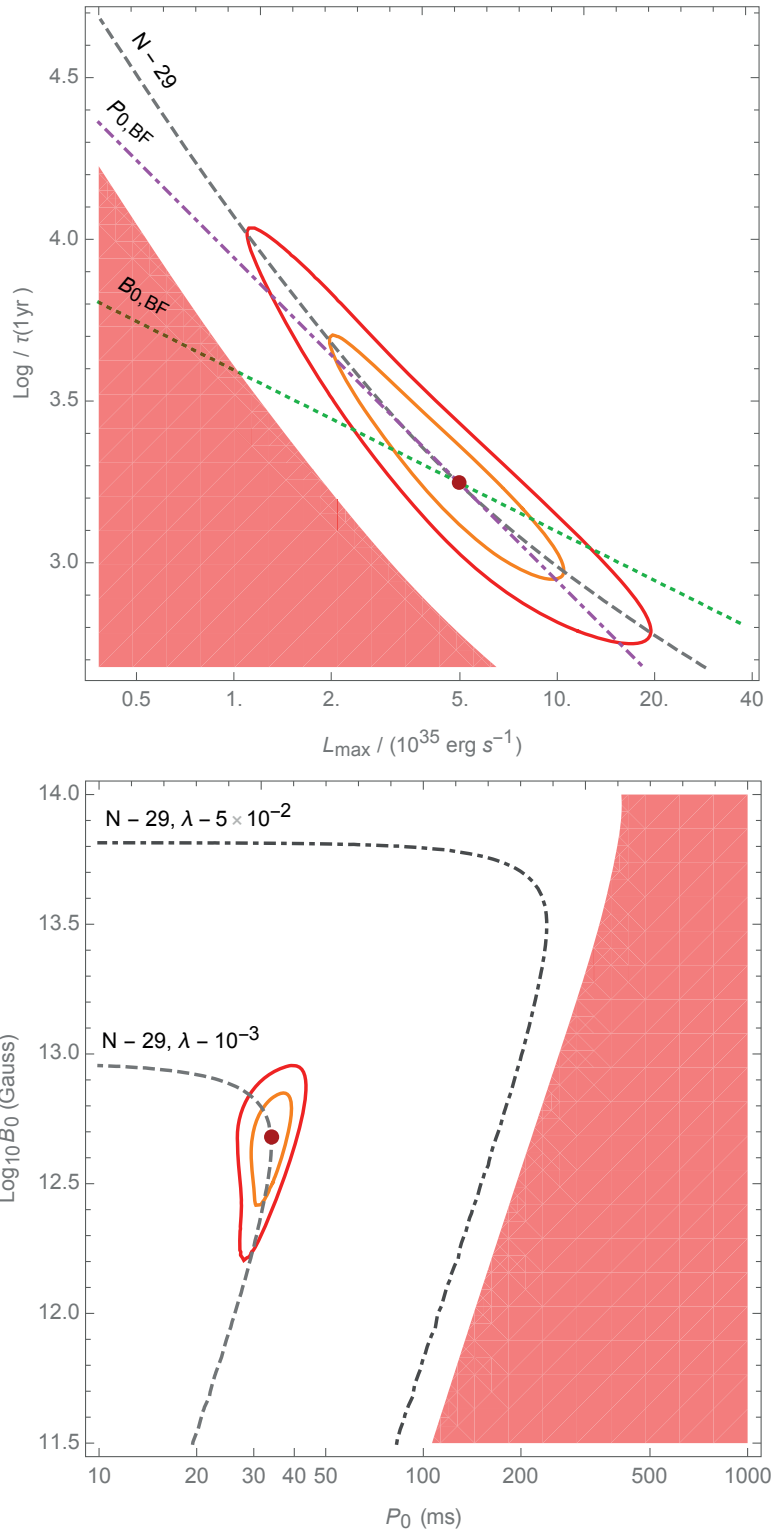


FIGURE 6.4: Upper panel: the best fit and the  $1\sigma$  and  $2\sigma$  allowed regions in the plane  $(L_{\text{max}}, \tau)$ . Lower panel: the best fit and the  $1\sigma$  and  $2\sigma$  allowed regions in the plane  $(P_0, B_0)$ , calculated in the assumption that  $\lambda = 10^{-3}$ . In both panels the red shaded area is excluded by the data because corresponds to  $N(0.1\Phi_{\text{CRAB}}) \leq 10$  in the assumption of  $\lambda = 5 \times 10^{-2}$  which is a large value for the fraction of pulsar spin-down energy converted to TeV emission. Figure taken from Cataldo et al., 2020.

Moreover, let's note that the dominance of TeV halo sources in our population sample would introduce a dominance of extended sources. In Chapter 5 we also consider this possibility and we do not register any change in the results obtained for a population of extended sources. We show that this doesn't change for sources with sizes up to 40 pc which is larger than the measured sizes of currently observed TeV halos.

## 6.5 Conclusions

After studying the HGPS data sample of brightest sources observed in the Galactic plane, we made an assumption on the nature of the sources in the catalogue. We consider the possibility that the bright sources observed by H.E.S.S., which are not firmly identified as SNRs, are powered by pulsar activity, like e.g. PWNe and TeV halos. We apply our previously presented model to this particular reasonable situation. We evaluate the constraints on the physical properties of the pulsar population that follow from this hypothesis. For our reference case, assuming that the fraction of the pulsar spin-down energy converted in TeV photons is  $\lambda = 10^{-3}$ , we obtain the best-fit values  $P_0 = 33.5_{-4.3}^{+5.4}$  ms and  $B_0 = 4.32 (1 \pm 0.45) 10^{12}$  G, the initial spin period and magnetic field, respectively. The above constraints are consistent with the  $B_0$  values obtained in Faucher-Giguere and Kaspi, 2006 and  $P_0$  constrains described in Watters and Romani, 2011 by studying the gamma-ray pulsar population.

Finally, by considering that 10 sources in HGPS catalogue have been firmly identified as PWNe and considering  $\lambda \leq 5 \times 10^{-2}$  as an upper bound for efficiency of TeV emission, we obtain that the initial spin-down period of the considered pulsar population is constrained to be  $P_0 \leq 500$  ms.

Here we present also the properties of the newly discovered sources of TeV halos for which many branches of investigation are still open. Our model embraces also the possibility of the presence of TeV halos in the population sample. Here we give some interesting considerations on the TeV halo sources and we also examine our results in terms of a population only made of TeV halos. We show that our results are stable and can provide interesting constraints also in this case.

## Chapter 7

# Conclusions

Large part of this work is dedicated to exploring the connection of neutrinos and gammas by using a multimessenger approach. Both are indeed produced in hadronic interactions which occur in the Milky Way. Due to their peculiar properties represent crucial probes for the study of the innermost parts of the Galaxy. Both neutrinos and gamma-rays, being electromagnetically neutral, do not get deflected in magnetic fields. So have the useful property of preserving their production direction. Neutrinos due to their weak interaction capability are not absorbed in their path towards the Earth. The same stands also for VHE gamma-rays, which are in good approximation only negligibly absorbed. For these reasons we can perform a parallel study of both the messengers by jointly constructing models for their estimation. However, due to the larger variety of available experimental information, the most stringent constraints on our models come especially from the gamma-ray sky.

In our first work (presented in Chapter 4) we focus on the diffuse component. We present updated calculations of the diffuse emission produced by the interaction of CRs with the gas contained in the Galactic disk considering also the possibility of CR spectral hardening in the inner Galaxy as recently emerged from the analysis of Fermi-LAT data at lower energies. Firstly, we fix constraints on the Galactic contribution to the total IceCube neutrino signal obtaining a fraction  $\sim 8\% - 12\%$  according to the scenario considered. These values are compatible with the upper limit of  $\sim 14\%$  given by the collaboration.

Although due to the low statistic the Galactic component is not observed yet, we demonstrate that there is a portion of the sky that includes the Galactic center where the model flux appears to exceed the isotropic signal. So we define the region of interest to investigate to potentially observe the Galactic flux component. Moreover, we show that interesting constraints on the CR distribution in the Galaxy can be obtained by comparing the total gamma-ray flux due to the diffuse interstellar emission plus the cumulative contribution of point-like and extended sources in H.E.S.S.-GPS catalogue with the total flux measured by Argo-YBJ, H.E.S.S., HAWC and Milagro experiments. Indeed, our largest prediction for the diffuse emission which is obtained by assuming that the CR density follows that of SNR (with  $R = 1\text{ kpc}$  smearing radius) and by considering CR spectral hardening in the inner Galaxy, seems to be excluded by present observational data. Stronger constraints can be obtained by taking into account the contribution to the observed signal provided by gamma-ray sources non resolved by H.E.S.S. This is naturally expected to be non negligible but is affected by large uncertainties. The CR spectral hardening hypothesis would be ruled out globally (i.e. even if a smooth CR spatial distribution with  $R = \infty$  is assumed), if the non resolved contribution is demonstrated to be larger than  $\sim 50\%$  of the resolved component.

Being the unresolved contribution a remarkable component of the total, we focused on refining its estimation in our second work. This took us to a development of

our investigation and to more interesting results. We present a novel analysis of the flux, longitude and latitude distributions of the brightest sources ( $\Phi \geq 10\% \Phi_{\text{CRAB}}$ ) of the HGPS showing that the luminosity distribution of Galactic TeV sources can be effectively constrained. This allows us to determine the total Milky Way luminosity  $L_{\text{MW}} = 1.7_{-0.4}^{+0.5} \times 10^{37} \text{ erg s}^{-1}$  in the energy range 1 – 100 TeV and the total Galactic flux in the H.E.S.S. observational window given by  $\Phi_{\text{tot}} = 3.8_{-1.0}^{+1.0} \times 10^{-10} \text{ cm}^{-2} \text{ s}^{-1}$ . The total source flux is relatively large, confirming that unresolved source contribution is not negligible (about 60% of the resolved signal measured by H.E.S.S.) and potentially responsible for a large fraction of the diffuse large-scale gamma-ray signal observed by H.E.S.S. This could have important implications for the interpretation of current observations of other experiments in the TeV domain. The unresolved contribution can e.g. explain the excess reported by Milagro at 15 TeV (Atkins et al., 2005). Our results can be also used to investigate the capability of future experiments, like e.g. CTA, to probe the Galactic TeV source population.

Chapter 6 is dedicated to an interesting development of our work. We consider the possibility that the bright sources observed by H.E.S.S., which are not firmly identified as SNRs, are powered by pulsar activity, like e.g. PWNe and TeV halos. We evaluate the constraints on the physical properties of the pulsar population that follow from this hypothesis. Assuming that the fraction of the pulsar spin-down energy converted in TeV photons is  $\lambda = 10^{-3}$ , we obtain the best-fit values  $P_0 = 33.5_{-4.3}^{+5.4} \text{ ms}$  and  $B_0 = 4.32 (1 \pm 0.45) 10^{12} \text{ G}$ , the initial spin period and magnetic field, respectively. The above constraints are consistent with the  $B_0$  values obtained in Faucher-Giguere and Kaspi, 2006 and  $P_0$  constrains described in Watters and Romani, 2011 by studying the gamma-ray pulsar population.

Finally, by considering that 10 sources in HGPS catalogue have been firmly identified as PWNe and considering  $\lambda \leq 5 \times 10^{-2}$  as an upper bound for efficiency of TeV emission, we obtain that the initial spin-down period of the considered pulsar population is constrained to be  $P_0 \leq 500 \text{ ms}$ .

# Bibliography

- Aartsen, M. G. et al. (2013). “Evidence for High-Energy Extraterrestrial Neutrinos at the IceCube Detector”. In: *Science* 342, p. 1242856. DOI: [10.1126/science.1242856](https://doi.org/10.1126/science.1242856). arXiv: [1311.5238](https://arxiv.org/abs/1311.5238) [astro-ph.HE].
- Aartsen, M. G. et al. (2014). “Energy reconstruction methods in the IceCube neutrino telescope”. In: *Journal of Instrumentation* 9.03, P03009–P03009. ISSN: 1748-0221. DOI: [10.1088/1748-0221/9/03/p03009](https://doi.org/10.1088/1748-0221/9/03/p03009). URL: <http://dx.doi.org/10.1088/1748-0221/9/03/P03009>.
- Aartsen, M. G. et al. (2015a). “A Combined Maximum-Likelihood Analysis of the High-Energy Astrophysical Neutrino Flux Measured With IceCube”. In: *The Astrophysical Journal* 809.1, p. 98. ISSN: 1538-4357. DOI: [10.1088/0004-637x/809/1/98](https://doi.org/10.1088/0004-637x/809/1/98). URL: <http://dx.doi.org/10.1088/0004-637x/809/1/98>.
- Aartsen, M. G. et al. (2017). “Constraints on Galactic Neutrino Emission with Seven Years of IceCube Data”. In: arXiv: [1707.03416](https://arxiv.org/abs/1707.03416) [astro-ph.HE].
- Aartsen, M.G. et al. (2015b). “Atmospheric and astrophysical neutrinos above 1 TeV interacting in IceCube”. In: *Physical Review D* 91.2. ISSN: 1550-2368. DOI: [10.1103/PhysRevD.91.022001](https://doi.org/10.1103/PhysRevD.91.022001). URL: <http://dx.doi.org/10.1103/PhysRevD.91.022001>.
- Abbasi, R. et al. (Nov. 2020a). “Measurement of Astrophysical Tau Neutrinos in IceCube’s High-Energy Starting Events”. In: arXiv: [2011.03561](https://arxiv.org/abs/2011.03561) [hep-ex].
- (Nov. 2020b). “The IceCube high-energy starting event sample: Description and flux characterization with 7.5 years of data”. In: arXiv: [2011.03545](https://arxiv.org/abs/2011.03545) [astro-ph.HE].
- Abdalla, H. et al. (2018a). “The H.E.S.S. Galactic plane survey”. In: *Astron. Astrophys.* 612, A1. DOI: [10.1051/0004-6361/201732098](https://doi.org/10.1051/0004-6361/201732098). arXiv: [1804.02432](https://arxiv.org/abs/1804.02432) [astro-ph.HE].
- (2018b). “The population of TeV pulsar wind nebulae in the H.E.S.S. Galactic Plane Survey”. In: *Astron. Astrophys.* 612, A2. DOI: [10.1051/0004-6361/201629377](https://doi.org/10.1051/0004-6361/201629377). arXiv: [1702.08280](https://arxiv.org/abs/1702.08280) [astro-ph.HE].
- Abdo, A. A. et al. (2008a). “A Measurement of the Spatial Distribution of Diffuse TeV Gamma Ray Emission from the Galactic Plane with Milagro”. In: *Astrophys. J.* 688, pp. 1078–1083. DOI: [10.1086/592213](https://doi.org/10.1086/592213). arXiv: [0805.0417](https://arxiv.org/abs/0805.0417) [astro-ph].
- Abdo, A.A. et al. (2008b). “Discovery of Localized Regions of Excess 10-TeV Cosmic Rays”. In: *Phys. Rev. Lett.* 101, p. 221101. DOI: [10.1103/PhysRevLett.101.221101](https://doi.org/10.1103/PhysRevLett.101.221101). arXiv: [0801.3827](https://arxiv.org/abs/0801.3827) [astro-ph].
- (2009). “Milagro Observations of TeV Emission from Galactic Sources in the Fermi Bright Source List”. In: *Astrophys. J. Lett.* 700. [Erratum: *Astrophys.J.Lett.* 703, L185 (2009), Erratum: *Astrophys.J.* 703, L185 (2009)], pp. L127–L131. DOI: [10.1088/0004-637x/700/2/L127](https://doi.org/10.1088/0004-637x/700/2/L127). arXiv: [0904.1018](https://arxiv.org/abs/0904.1018) [astro-ph.HE].
- Abeysekara, A. U. et al. (2016). “Search for TeV Gamma-Ray Emission from Point-Like Sources in the Inner Galactic Plane with a Partial Configuration of the HAWC Observatory”. In: *The Astrophysical Journal* 817.1, p. 3. DOI: [10.3847/0004-637x/817/1/3](https://doi.org/10.3847/0004-637x/817/1/3).
- Abeysekara, A.U. et al. (2017a). “Extended gamma-ray sources around pulsars constrain the origin of the positron flux at Earth”. In: *Science* 358.6365, pp. 911–914. DOI: [10.1126/science.aan4880](https://doi.org/10.1126/science.aan4880). arXiv: [1711.06223](https://arxiv.org/abs/1711.06223) [astro-ph.HE].

- Abeyssekara, A.U. et al. (2017b). “The 2HWC HAWC Observatory Gamma Ray Catalog”. In: *Astrophys. J.* 843.1, p. 40. DOI: [10 . 3847 / 1538 - 4357 / aa7556](https://doi.org/10.3847/1538-4357/aa7556). arXiv: [1702.02992](https://arxiv.org/abs/1702.02992) [astro-ph.HE].
- Abramowski, A. et al. (2014). “Diffuse Galactic gamma-ray emission with H.E.S.S”. In: *Phys. Rev. D* 90.12, p. 122007. DOI: [10 . 1103 / PhysRevD . 90 . 122007](https://doi.org/10.1103/PhysRevD.90.122007). arXiv: [1411.7568](https://arxiv.org/abs/1411.7568) [astro-ph.HE].
- (2016). “Acceleration of petaelectronvolt protons in the Galactic Centre”. In: *Nature* 531, p. 476. DOI: [10 . 1038/nature17147](https://doi.org/10.1038/nature17147). arXiv: [1603.07730](https://arxiv.org/abs/1603.07730) [astro-ph.HE].
- Acero, F. et al. (2016). “Development of the Model of Galactic Interstellar Emission for Standard Point-Source Analysis of Fermi Large Area Telescope Data”. In: *Astrophys. J. Suppl.* 223.2, p. 26. DOI: [10 . 3847 / 0067 - 0049 / 223 / 2 / 26](https://doi.org/10.3847/0067-0049/223/2/26). arXiv: [1602.07246](https://arxiv.org/abs/1602.07246) [astro-ph.HE].
- Acharya, S. et al. (2018). “ $\pi^0$  and  $\eta$  meson production in proton-proton collisions at  $\sqrt{s} = 8$  TeV”. In: *Eur. Phys. J. C* 78.3, p. 263. DOI: [10 . 1140/epjc/s10052-018-5612-8](https://doi.org/10.1140/epjc/s10052-018-5612-8). arXiv: [1708.08745](https://arxiv.org/abs/1708.08745) [hep-ex].
- Ackermann, M. et al. (2012). “Fermi-LAT Observations of the Diffuse Gamma-Ray Emission: Implications for Cosmic Rays and the Interstellar Medium”. In: *Astrophys. J.* 750, p. 3. DOI: [10 . 1088 / 0004 - 637X / 750 / 1 / 3](https://doi.org/10.1088/0004-637X/750/1/3). arXiv: [1202 . 4039](https://arxiv.org/abs/1202.4039) [astro-ph.HE].
- (2013). “The First Fermi-LAT Catalog of Sources Above 10 GeV”. In: *Astrophys. J. Suppl.* 209, p. 34. DOI: [10 . 1088 / 0067 - 0049 / 209 / 2 / 34](https://doi.org/10.1088/0067-0049/209/2/34). arXiv: [1306 . 6772](https://arxiv.org/abs/1306.6772) [astro-ph.IM].
- Adrian-Martinez, S. et al. (2016). “Constraints on the neutrino emission from the Galactic Ridge with the ANTARES telescope”. In: *Phys. Lett.* B760, pp. 143–148. DOI: [10.1016/j.physletb.2016.06.051](https://doi.org/10.1016/j.physletb.2016.06.051). arXiv: [1602.03036](https://arxiv.org/abs/1602.03036) [astro-ph.HE].
- Adrián-Martínez, S. et al. (2014). “Searches for Point-like and extended neutrino sources close to the Galactic Centre using the ANTARES neutrino Telescope”. In: *The Astrophysical Journal* 786.1, p. L5. ISSN: 2041-8213. DOI: [10 . 1088 / 2041 - 8205 / 786 / 1 / L5](https://doi.org/10.1088/2041-8205/786/1/L5). URL: <http://dx.doi.org/10.1088/2041-8205/786/1/L5>.
- Aharonian, F. et al. (2018). “Probing the “Sea” of Galactic Cosmic Rays with Fermi-LAT”. In: arXiv: [1811.12118](https://arxiv.org/abs/1811.12118) [astro-ph.HE].
- Ahlers, M. and K. Murase (2014). “Probing the Galactic origin of the IceCube excess with gamma rays”. In: *Physical Review D* 90.2. ISSN: 1550-2368. DOI: [10 . 1103 / physrevd.90.023010](https://doi.org/10.1103/PhysRevD.90.023010). URL: <http://dx.doi.org/10.1103/PhysRevD.90.023010>.
- Ahlers, M. et al. (2016). “Galactic neutrinos in the TeV to PeV range”. In: *Phys. Rev. D* 93.1, p. 013009. DOI: [10 . 1103 / PhysRevD . 93 . 013009](https://doi.org/10.1103/PhysRevD.93.013009). arXiv: [1505 . 03156](https://arxiv.org/abs/1505.03156) [hep-ph].
- Ajello, M. et al. (2017). “3FHL: The Third Catalog of Hard Fermi-LAT Sources”. In: *Astrophys. J. Suppl.* 232.2, p. 18. DOI: [10 . 3847 / 1538 - 4365 / aa8221](https://doi.org/10.3847/1538-4365/aa8221). arXiv: [1702 . 00664](https://arxiv.org/abs/1702.00664) [astro-ph.HE].
- Albert, A. et al. (2018). “Joint Constraints on Galactic Diffuse Neutrino Emission from the ANTARES and IceCube Neutrino Telescopes”. In: *Astrophys. J. Lett.* 868.2, p. L20. DOI: [10 . 3847 / 2041 - 8213 / aaecef](https://doi.org/10.3847/2041-8213/aaecef). arXiv: [1808.03531](https://arxiv.org/abs/1808.03531) [astro-ph.HE].
- Andersson, N., K. Kokkotas, and B. F Schutz (1999). “Gravitational radiation limit on the spin of young neutron stars”. In: *The Astrophysical Journal* 510.2, p. 846.
- Anker, A. et al. (2020). *White Paper: ARIANNA-200 high energy neutrino telescope*. arXiv: [2004.09841](https://arxiv.org/abs/2004.09841) [astro-ph.IM].
- Atkins, R. et al. (2003). “Observation of TeV Gamma Rays from the Crab Nebula with Milagro Using a New Background Rejection Technique”. In: *The Astrophysical Journal* 595.2, 803–811. ISSN: 1538-4357. DOI: [10 . 1086 / 377498](https://doi.org/10.1086/377498). URL: <http://dx.doi.org/10.1086/377498>.

- Atkins, R. et al. (2005). "Evidence for TeV gamma-ray emission from the galactic plane". In: *Phys. Rev. Lett.* 95, p. 251103. DOI: [10.1103/PhysRevLett.95.251103](https://doi.org/10.1103/PhysRevLett.95.251103). arXiv: [astro-ph/0502303](https://arxiv.org/abs/astro-ph/0502303).
- ATNF. <https://www.atnf.csiro.au/research/pulsar/psrcat/>.
- Bartoli, B. et al. (June 2015). "Study of the Diffuse Gamma-ray Emission From the Galactic Plane With ARGO-YBJ". In: *Astrophys. J.* 806, p. 20. DOI: [10.1088/0004-637X/806/1/20](https://doi.org/10.1088/0004-637X/806/1/20). arXiv: [1507.06758](https://arxiv.org/abs/1507.06758) [astro-ph.IM].
- Bednarek, W. and R. J. Protheroe (1997). "Gamma Rays and Neutrinos from the Crab Nebula Produced by Pulsar Accelerated Nuclei". In: *Physical Review Letters* 79.14, 2616–2619. ISSN: 1079-7114. DOI: [10.1103/physrevlett.79.2616](https://doi.org/10.1103/physrevlett.79.2616). URL: <http://dx.doi.org/10.1103/PhysRevLett.79.2616>.
- Bellini, G. et al. (2014). "Neutrino Oscillations". In: *Advances in High Energy Physics* 2014, 1–28. ISSN: 1687-7365. DOI: [10.1155/2014/191960](https://doi.org/10.1155/2014/191960). URL: <http://dx.doi.org/10.1155/2014/191960>.
- Blumenthal, G.R. and R.J. Gould (1970). "Bremsstrahlung, synchrotron radiation, and compton scattering of high-energy electrons traversing dilute gases". In: *Rev. Mod. Phys.* 42, pp. 237–270. DOI: [10.1103/RevModPhys.42.237](https://doi.org/10.1103/RevModPhys.42.237).
- Boer, W. de et al. (Sept. 2015). "Evidence for a hadronic origin of the Fermi Bubbles and the Galactic Excess". In: arXiv: [1509.05310](https://arxiv.org/abs/1509.05310) [astro-ph.HE].
- Burgay, M. et al. (Mar. 2006). "The Parkes High-Latitude pulsar survey". In: *Monthly Notices of the Royal Astronomical Society* 368.1, pp. 283–292.
- Casanova, S. and B. L. Dingus (2008). "Constraints on the TeV source population and its contribution to the galactic diffuse TeV emission". In: *Astropart. Phys.* 29, pp. 63–69. DOI: [10.1016/j.astropartphys.2007.11.008](https://doi.org/10.1016/j.astropartphys.2007.11.008). arXiv: [0711.2753](https://arxiv.org/abs/0711.2753) [astro-ph].
- Cataldo, M. et al. (2019). "Probing galactic cosmic ray distribution with TeV gamma-ray sky". In: *JCAP* 12, p. 050. DOI: [10.1088/1475-7516/2019/12/050](https://doi.org/10.1088/1475-7516/2019/12/050). arXiv: [1904.03894](https://arxiv.org/abs/1904.03894) [astro-ph.HE].
- Cataldo, M. et al. (2020). "The TeV Gamma-Ray Luminosity of the Milky Way and the Contribution of H.E.S.S. Unresolved Sources to Very High Energy Diffuse Emission". In: *The Astrophysical Journal* 904.2, p. 85. DOI: [10.3847/1538-4357/abc0ee](https://doi.org/10.3847/1538-4357/abc0ee). URL: <https://doi.org/10.3847/1538-4357/abc0ee>.
- Chen, W. C. and X. D. Li (2006). "Why the braking indices of young pulsars are less than 3?" In: *Astronomy & Astrophysics* 450.1, pp. L1–L4.
- Collaboration, IceCube (2017). "The IceCube Neutrino Observatory - Contributions to ICRC 2017 Part II: Properties of the Atmospheric and Astrophysical Neutrino Flux". In: arXiv: [1710.01191](https://arxiv.org/abs/1710.01191) [astro-ph.HE].
- Contopoulos, I. and A. Spitkovsky (2006). "Revised pulsar spin-down". In: *The Astrophysical Journal* 643.2, p. 1139.
- Costantini, M. L. and F. Vissani (2005). "Expected neutrino signal from supernova remnant RX J1713.7-3946 and flavor oscillations". In: *Astropart. Phys.* 23, pp. 477–485. DOI: [10.1016/j.astropartphys.2005.03.003](https://doi.org/10.1016/j.astropartphys.2005.03.003). arXiv: [astro-ph/0411761](https://arxiv.org/abs/astro-ph/0411761).
- Crocker, R. M. and F. Aharonian (2011). "The Fermi Bubbles: Giant, Multi-Billion-Year-Old Reservoirs of Galactic Center Cosmic Rays". In: *Phys. Rev. Lett.* 106, p. 101102. DOI: [10.1103/PhysRevLett.106.101102](https://doi.org/10.1103/PhysRevLett.106.101102). arXiv: [1008.2658](https://arxiv.org/abs/1008.2658) [astro-ph.GA].
- CTA, Consortium (2018). "Science with the Cherenkov Telescope Array". In: DOI: [10.1142/10986](https://doi.org/10.1142/10986). URL: <http://dx.doi.org/10.1142/10986>.
- CTA/M-A. Besel/IAC (G.P. Diaz)/ESO. [https://www.eso.org/public/italy/images/eso1841a/D.Lorimer's catalogue](https://www.eso.org/public/italy/images/eso1841a/D.Lorimer's%20catalogue). <http://astro.phys.wvu.edu/GalacticMSPs/GalacticMSPs.txt>.

- Dembinski, H. P. et al. (2018). “Data-driven model of the cosmic-ray flux and mass composition from 10 GeV to  $10^{11}$  GeV”. In: *PoS ICRC2017*. [35,533(2017)], p. 533. DOI: [10.22323/1.301.0533](https://doi.org/10.22323/1.301.0533). arXiv: [1711.11432](https://arxiv.org/abs/1711.11432) [astro-ph.HE].
- Diehl, R. et al. (2006). “Radioactive Al-26 and massive stars in the galaxy”. In: *Nature* 439, pp. 45–47. DOI: [10.1038/nature04364](https://doi.org/10.1038/nature04364). arXiv: [astro-ph/0601015](https://arxiv.org/abs/astro-ph/0601015).
- Egberts, K. (2018). “Unresolved sources in the Galactic diffuse gamma-ray emission at TeV energies”. In: *PoS ICRC2017*, p. 684. DOI: [10.22323/1.301.0684](https://doi.org/10.22323/1.301.0684).
- Erlykin, A. D. and A.W. Wolfendale (2005). “The origin of cosmic rays”. In: *J. Phys. G* 31, pp. 1475–1498. DOI: [10.1088/0954-3899/31/12/009](https://doi.org/10.1088/0954-3899/31/12/009). arXiv: [astro-ph/0510016](https://arxiv.org/abs/astro-ph/0510016).
- Espinoza, C. M. et al. (2011). “The braking index of PSR J1734–3333 and the magnetar population”. In: *The Astrophysical Journal Letters* 741.1, p. L13.
- Evoli, Carmelo, Tim Linden, and Giovanni Morlino (2018). “Self-generated cosmic-ray confinement in TeV halos: Implications for TeV  $\gamma$ -ray emission and the positron excess”. In: *Phys. Rev. D* 98.6, p. 063017. DOI: [10.1103/PhysRevD.98.063017](https://doi.org/10.1103/PhysRevD.98.063017). arXiv: [1807.09263](https://arxiv.org/abs/1807.09263) [astro-ph.HE].
- Faucher-Giguere, C.A. and V. M. Kaspi (2006). “Birth and evolution of isolated radio pulsars”. In: *Astrophys. J.* 643, pp. 332–355. DOI: [10.1086/501516](https://doi.org/10.1086/501516). arXiv: [astro-ph/0512585](https://arxiv.org/abs/astro-ph/0512585).
- Ferrière, K. M. (2001). “The interstellar environment of our galaxy”. In: *Reviews of Modern Physics* 73.4, 1031–1066. ISSN: 1539-0756. DOI: [10.1103/revmodphys.73.1031](https://doi.org/10.1103/revmodphys.73.1031). URL: <http://dx.doi.org/10.1103/RevModPhys.73.1031>.
- Finkbeiner, D. P. (2004). “Microwave Interstellar Medium Emission Observed by the Wilkinson Microwave Anisotropy Probe”. In: *The Astrophysical Journal* 614.1, 186–193. ISSN: 1538-4357. DOI: [10.1086/423482](https://doi.org/10.1086/423482). URL: <http://dx.doi.org/10.1086/423482>.
- Gaensler, B. M. and P. O. Slane (2006). “The Evolution and Structure of Pulsar Wind Nebulae”. In: *Annual Review of Astronomy and Astrophysics* 44.1, 17–47. ISSN: 1545-4282. DOI: [10.1146/annurev.astro.44.051905.092528](https://doi.org/10.1146/annurev.astro.44.051905.092528). URL: <http://dx.doi.org/10.1146/annurev.astro.44.051905.092528>.
- Gaggero, D. et al. (2015a). “Gamma-ray sky points to radial gradients in cosmic-ray transport”. In: *Phys. Rev. D* 91.8, p. 083012. DOI: [10.1103/PhysRevD.91.083012](https://doi.org/10.1103/PhysRevD.91.083012). arXiv: [1411.7623](https://arxiv.org/abs/1411.7623) [astro-ph.HE].
- Gaggero, D. et al. (2015b). “The gamma-ray and neutrino sky: A consistent picture of Fermi-LAT, Milagro, and IceCube results”. In: *Astrophys. J.* 815.2, p. L25. DOI: [10.1088/2041-8205/815/2/L25](https://doi.org/10.1088/2041-8205/815/2/L25). arXiv: [1504.00227](https://arxiv.org/abs/1504.00227) [astro-ph.HE].
- Gaggero, D. et al. (2017). “Diffuse cosmic rays shining in the Galactic center: A novel interpretation of H.E.S.S. and Fermi-LAT gamma-ray data”. In: *Phys. Rev. Lett.* 119.3, p. 031101. DOI: [10.1103/PhysRevLett.119.031101](https://doi.org/10.1103/PhysRevLett.119.031101). arXiv: [1702.01124](https://arxiv.org/abs/1702.01124) [astro-ph.HE].
- Gaisser, T. K., R. Engel, and E. Resconi (June 2016). *Cosmic Rays and Particle Physics: 2nd Edition*. Cambridge University Press. ISBN: 978-0-521-01646-9. GALPROP. <https://galprop.stanford.edu>.
- Giacinti, G. et al. (2020). “On the TeV Halo Fraction in gamma-ray bright Pulsar Wind Nebulae”. In: *Astron. Astrophys.* 636, A113. DOI: [10.1051/0004-6361/201936505](https://doi.org/10.1051/0004-6361/201936505). arXiv: [1907.12121](https://arxiv.org/abs/1907.12121) [astro-ph.HE].
- Ginzburg, V. L. and S. I. Syrovatskii (1964). *The Origin of Cosmic Rays. The Science of Microfabrication*. New York: Macmillan.
- Green, D. A. (2014). *A catalogue of 294 Galactic supernova remnants*. arXiv: [1409.0637](https://arxiv.org/abs/1409.0637) [astro-ph.HE].

- Green, D.A. (2015). "Constraints on the distribution of supernova remnants with Galactocentric radius". In: *Mon. Not. Roy. Astron. Soc.* 454.2, pp. 1517–1524. DOI: [10.1093/mnras/stv1885](https://doi.org/10.1093/mnras/stv1885). arXiv: 1508.02931 [astro-ph.HE].
- Gupta, A. et al. (2012). "A huge reservoir of ionized gas around the Milky Way: Accounting for the Missing Mass?" In: *The Astrophysical Journal* 756.1, p. L8. ISSN: 2041-8213. DOI: [10.1088/2041-8205/756/1/L8](https://doi.org/10.1088/2041-8205/756/1/L8). URL: <http://dx.doi.org/10.1088/2041-8205/756/1/L8>.
- H.E.S.S. gamma-ray experiment five telescope array*. <https://commons.wikimedia.org/w/index.php?curid=61288242>.
- Ho, W. C. G. and D. Lai (2000). "r-Mode oscillations and spin-down of young rotating magnetic neutron stars". In: *The Astrophysical Journal* 543.1, p. 386. *IceCube website*. <https://icecube.wisc.edu>. *INFN website: ARGO-YBJ*. <https://home.infn.it/it/approfondimenti/esperimenti/1371-argo>.
- Kappes, A. et al. (2007). "Potential Neutrino Signals from Galactic Gamma-Ray Sources". In: *Astrophys. J.* 656. [Erratum: *Astrophys. J.* 661, 1348 (2007)], pp. 870–896. DOI: [10.1086/508936](https://doi.org/10.1086/508936), [10.1086/518161](https://doi.org/10.1086/518161). arXiv: [astro-ph/0607286](https://arxiv.org/abs/astro-ph/0607286) [astro-ph].
- Kaspi, V. M. (2010). "Grand Unification in Neutron Stars". In: *Proc. Nat. Acad. Sci.* 107, pp. 7147–7152. DOI: [10.1073/pnas.1000812107](https://doi.org/10.1073/pnas.1000812107). arXiv: 1005.0876 [astro-ph.HE].
- Kaspi, V. M., M. S.E. Roberts, and A. K. Harding (Feb. 2004). "Isolated neutron stars". In: arXiv: [astro-ph/0402136](https://arxiv.org/abs/astro-ph/0402136).
- Kataoka, J. et al. (2013). "Suzaku Observations of the Diffuse X-ray Emission Across the Fermi Bubbles' Edges". In: *The Astrophysical Journal* 779.1, p. 57. ISSN: 1538-4357. DOI: [10.1088/0004-637x/779/1/57](https://doi.org/10.1088/0004-637x/779/1/57). URL: <http://dx.doi.org/10.1088/0004-637x/779/1/57>.
- Kataoka, J. et al. (2018). "X-Ray and Gamma-Ray Observations of the Fermi Bubbles and NPS/Loop I Structures". In: *Galaxies* 6.1, p. 27. ISSN: 2075-4434. DOI: [10.3390/galaxies6010027](https://doi.org/10.3390/galaxies6010027). URL: <http://dx.doi.org/10.3390/galaxies6010027>.
- Kelner, S. R. and F. A. Aharonian (2008). "Energy spectra of gamma rays, electrons, and neutrinos produced at interactions of relativistic protons with low energy radiation". In: *Physical Review D* 78.3. ISSN: 1550-2368. DOI: [10.1103/physrevd.78.034013](https://doi.org/10.1103/physrevd.78.034013). URL: <http://dx.doi.org/10.1103/PhysRevD.78.034013>.
- Kelner, S.R., Felex A. Aharonian, and V.V. Bugayov (2006). "Energy spectra of gamma-rays, electrons and neutrinos produced at proton-proton interactions in the very high energy regime". In: *Phys. Rev. D* 74. [Erratum: *Phys. Rev. D* 79, 039901 (2009)], p. 034018. DOI: [10.1103/PhysRevD.74.034018](https://doi.org/10.1103/PhysRevD.74.034018). arXiv: [astro-ph/0606058](https://arxiv.org/abs/astro-ph/0606058). *KM3NeT*. <https://www.km3net.org>.
- Kou, F. F. and H. Tong (2015). "Rotational evolution of the Crab pulsar in the wind braking model". In: *Monthly Notices of the Royal Astronomical Society* 450.2, 1990–1998. ISSN: 0035-8711. DOI: [10.1093/mnras/stv734](https://doi.org/10.1093/mnras/stv734). URL: <http://dx.doi.org/10.1093/mnras/stv734>.
- LAT-Detected Gamma-Ray Pulsars*. <https://confluence.slac.stanford.edu/display/GLAMCOG/Public+List+of+LAT-Detected+Gamma-Ray+Pulsars>.
- Lattimer, J. M. and M. Prakash (2007). "Neutron Star Observations: Prognosis for Equation of State Constraints". In: *Phys. Rept.* 442, pp. 109–165. DOI: [10.1016/j.physrep.2007.02.003](https://doi.org/10.1016/j.physrep.2007.02.003). arXiv: [astro-ph/0612440](https://arxiv.org/abs/astro-ph/0612440).
- Linden, T. and B. J. Buckman (2018). "Pulsar TeV Halos Explain the Diffuse TeV Excess Observed by Milagro". In: *Phys. Rev. Lett.* 120.12, p. 121101. DOI: [10.1103/PhysRevLett.120.121101](https://doi.org/10.1103/PhysRevLett.120.121101). arXiv: 1707.01905 [astro-ph.HE].

- Linden, T. et al. (2017). "Using HAWC to discover invisible pulsars". In: *Physical Review D* 96.10. ISSN: 2470-0029. DOI: [10.1103/physrevd.96.103016](https://doi.org/10.1103/PhysRevD.96.103016). URL: <http://dx.doi.org/10.1103/PhysRevD.96.103016>.
- Lipari, P. (2006). "Perspectives of High Energy Neutrino Astronomy". In: *Nucl. Instrum. Meth. A* 567. Ed. by E. Migneco et al., pp. 405–417. DOI: [10.1016/j.nima.2006.05.249](https://doi.org/10.1016/j.nima.2006.05.249). arXiv: [astro-ph/0605535](https://arxiv.org/abs/astro-ph/0605535).
- Lipari, P. and S. Vernetto (2018). "Diffuse Galactic gamma ray flux at very high energy". In: *Phys. Rev. D* 98.4, p. 043003. DOI: [10.1103/PhysRevD.98.043003](https://doi.org/10.1103/PhysRevD.98.043003). arXiv: [1804.10116](https://arxiv.org/abs/1804.10116) [[astro-ph.HE](#)].
- Lorimer, D.R. et al. (2006). "The Parkes multibeam pulsar survey: VI. Discovery and timing of 142 pulsars and a Galactic population analysis". In: *Mon. Not. Roy. Astron. Soc.* 372, pp. 777–800. DOI: [10.1111/j.1365-2966.2006.10887.x](https://doi.org/10.1111/j.1365-2966.2006.10887.x). arXiv: [astro-ph/0607640](https://arxiv.org/abs/astro-ph/0607640).
- Lyne, A. et al. (2015). "45 years of rotation of the Crab pulsar". In: *Mon. Not. Roy. Astron. Soc.* 446, pp. 857–864. DOI: [10.1093/mnras/stu2118](https://doi.org/10.1093/mnras/stu2118). arXiv: [1410.0886](https://arxiv.org/abs/1410.0886) [[astro-ph.HE](#)].
- Lyne, A. G., R. S. Pritchard, and F. Graham Smith (1993). "23 years of Crab pulsar rotational history". In: *Monthly Notices of the Royal Astronomical Society* 265.4, pp. 1003–1012.
- Manconi, S., M. Di Mauro, and F. Donato (Jan. 2020). "Contribution of pulsars to cosmic-ray positrons in light of recent observation of inverse-Compton halos". In: arXiv: [2001.09985](https://arxiv.org/abs/2001.09985) [[astro-ph.HE](#)].
- Pagliaroli, G., C. Evoli, and F. L. Villante (2016). "Expectations for high energy diffuse galactic neutrinos for different cosmic ray distributions". In: *JCAP* 1611.11, p. 004. DOI: [10.1088/1475-7516/2016/11/004](https://doi.org/10.1088/1475-7516/2016/11/004). arXiv: [1606.04489](https://arxiv.org/abs/1606.04489) [[astro-ph.HE](#)].
- Palladino, A. et al. (2015). "What is the Flavor of the Cosmic Neutrinos Seen by Ice-Cube?" In: *Physical Review Letters* 114.17. ISSN: 1079-7114. DOI: [10.1103/physrevlett.114.171101](https://doi.org/10.1103/physrevlett.114.171101). URL: <http://dx.doi.org/10.1103/PhysRevLett.114.171101>.
- Pothen, M. et al. (2018). "On the progressive hardening of the cosmic-ray proton spectrum in the inner Galaxy". In: *JCAP* 1810.10, p. 045. DOI: [10.1088/1475-7516/2018/10/045](https://doi.org/10.1088/1475-7516/2018/10/045). arXiv: [1807.04554](https://arxiv.org/abs/1807.04554) [[astro-ph.HE](#)].
- Proceedings, 30th International Cosmic Ray Conference (ICRC 2007)* (July 2007). Merida, Mexico: Yucatan Autonoma Univ.
- Ptuskin, V. S. and V. N. Zirakashvili (2005). "On the spectrum of high-energy cosmic rays produced by supernova remnants in the presence of strong cosmic-ray streaming instability and wave dissipation". In: *Astronomy Astrophysics* 429.3, 755–765. ISSN: 1432-0746. DOI: [10.1051/0004-6361:20041517](https://doi.org/10.1051/0004-6361:20041517). URL: <http://dx.doi.org/10.1051/0004-6361:20041517>.
- Recchia, S., P. Blasi, and G. Morlino (2016). "On the radial distribution of Galactic cosmic rays". In: *Mon. Not. Roy. Astron. Soc.* 462.1, pp. L88–L92. DOI: [10.1093/mnrasl/slw136](https://doi.org/10.1093/mnrasl/slw136). arXiv: [1604.07682](https://arxiv.org/abs/1604.07682) [[astro-ph.HE](#)].
- Shapiro, S.L. and S.A. Teukolsky (1983). *Black holes, white dwarfs, and neutron stars: The physics of compact objects*. ISBN: 978-0-471-87316-7.
- Slane, Patrick (2017). "Pulsar Wind Nebulae". In: *Handbook of Supernovae*, 2159–2179. DOI: [10.1007/978-3-319-21846-5\\_95](https://doi.org/10.1007/978-3-319-21846-5_95). URL: [http://dx.doi.org/10.1007/978-3-319-21846-5\\_95](http://dx.doi.org/10.1007/978-3-319-21846-5_95).
- Spiering, C. (2018). "High Energy Neutrino Astronomy: Where Do We Stand, Where Do We Go?" In: *Physics of Particles and Nuclei* 49.4, 497–507. ISSN: 1531-8559. DOI: [10.1134/s1063779618040536](https://doi.org/10.1134/s1063779618040536). URL: <http://dx.doi.org/10.1134/S1063779618040536>.

- Steppa, C. and K. Egberts (2020). "Modelling the Galactic very-high-energy -ray source population". In: *Astronomy Astrophysics* 643, A137. ISSN: 1432-0746. DOI: [10.1051/0004-6361/202038172](https://doi.org/10.1051/0004-6361/202038172). URL: <http://dx.doi.org/10.1051/0004-6361/202038172>.
- Su, M., T. R. Slatyer, and D. P. Finkbeiner (2010). "Giant Gamma-ray Bubbles from Fermi-LAT: AGN Activity or Bipolar Galactic Wind?" In: *Astrophys. J.* 724, pp. 1044–1082. DOI: [10.1088/0004-637X/724/2/1044](https://doi.org/10.1088/0004-637X/724/2/1044). arXiv: [1005.5480](https://arxiv.org/abs/1005.5480) [astro-ph.HE].
- Sudoh, T., T. Linden, and J. F. Beacom (2019). "TeV Halos are Everywhere: Prospects for New Discoveries". In: *Phys. Rev. D* 100.4, p. 043016. DOI: [10.1103/PhysRevD.100.043016](https://doi.org/10.1103/PhysRevD.100.043016). arXiv: [1902.08203](https://arxiv.org/abs/1902.08203) [astro-ph.HE].
- Taylor, A. M., S. Gabici, and F. Aharonian (2014). "Galactic halo origin of the neutrinos detected by IceCube". In: *Phys. Rev. D* 89.10, p. 103003. DOI: [10.1103/PhysRevD.89.103003](https://doi.org/10.1103/PhysRevD.89.103003). arXiv: [1403.3206](https://arxiv.org/abs/1403.3206) [astro-ph.HE].
- The High-Altitude Water Cherenkov Gamma-Ray Observatory*. <https://www.hawc-observatory.org>.
- Thorsett, S. E. et al. (2003). "Pulsar PSR B0656+14, the Monogem Ring, and the Origin of the "Knee" in the Primary Cosmic-Ray Spectrum". In: *The Astrophysical Journal* 592.2, L71–L73. ISSN: 1538-4357. DOI: [10.1086/377682](https://doi.org/10.1086/377682). URL: <http://dx.doi.org/10.1086/377682>.
- Vernetto, S. and P. Lipari (2016). "Absorption of very high energy gamma rays in the Milky Way". In: *Phys. Rev. D* 94.6, p. 063009. DOI: [10.1103/PhysRevD.94.063009](https://doi.org/10.1103/PhysRevD.94.063009). arXiv: [1608.01587](https://arxiv.org/abs/1608.01587) [astro-ph.HE].
- Villante, F.L. and F. Vissani (2008). "How precisely neutrino emission from supernova remnants can be constrained by gamma ray observations?" In: *Phys. Rev. D* 78, p. 103007. DOI: [10.1103/PhysRevD.78.103007](https://doi.org/10.1103/PhysRevD.78.103007). arXiv: [0807.4151](https://arxiv.org/abs/0807.4151) [astro-ph].
- Vissani, F., G. Pagliaroli, and F. L. Villante (2013). "The fraction of muon tracks in cosmic neutrinos". In: *JCAP* 09, p. 017. DOI: [10.1088/1475-7516/2013/09/017](https://doi.org/10.1088/1475-7516/2013/09/017). arXiv: [1306.0211](https://arxiv.org/abs/1306.0211) [astro-ph.HE].
- Watters, K. P. and R. W. Romani (2011). "The Galactic Population of Young Gamma-ray Pulsars". In: *Astrophys. J.* 727, p. 123. DOI: [10.1088/0004-637X/727/2/123](https://doi.org/10.1088/0004-637X/727/2/123). arXiv: [1009.5305](https://arxiv.org/abs/1009.5305) [astro-ph.HE].
- Weiler, K. W. and N. Panagia (1978). "Are Crab-type Supernova Remnants (Plerions) Short-lived?" In: eprint: "<https://ui.adsabs.harvard.edu/abs/1978A&A...70..419W/abstract>".
- Wu, F., R. X. Xu, and J. Gil (2003). "The braking indices in pulsar emission models". In: *Astronomy & Astrophysics* 409.2, pp. 641–645.
- Xu, R. X. and G. J. Qiao (2001). "Pulsar braking index: A test of emission models?" In: *The Astrophysical Journal Letters* 561.1, p. L85.
- Yang, R., F. Aharonian, and C. Evoli (2016). "Radial distribution of the diffuse -ray emissivity in the Galactic disk". In: *Phys. Rev. D* 93.12, p. 123007. DOI: [10.1103/PhysRevD.93.123007](https://doi.org/10.1103/PhysRevD.93.123007). arXiv: [1602.04710](https://arxiv.org/abs/1602.04710) [astro-ph.HE].
- Yue, Y. L., R. X. Xu, and W. W. Zhu (2007). "What can the braking indices tell us about the nature of pulsars?" In: *Advances in Space Research* 40.10, pp. 1491–1497.
- Zhou, H., C. D. Rho, and G. Vianello (2018). "Probing Galactic Diffuse TeV Gamma-Ray Emission with the HAWC Observatory". In: *PoS ICRC2017*, p. 689. DOI: [10.22323/1.301.0689](https://doi.org/10.22323/1.301.0689). arXiv: [1709.03619](https://arxiv.org/abs/1709.03619) [astro-ph.HE].